



HAL
open science

Réduction de modèle et contrôle en boucle fermée d'écoulements de type oscillateur et amplificateur de bruit

Alexandre Barbagallo

► **To cite this version:**

Alexandre Barbagallo. Réduction de modèle et contrôle en boucle fermée d'écoulements de type oscillateur et amplificateur de bruit. Mécanique des fluides [physics.class-ph]. Ecole Polytechnique X, 2011. Français. NNT: . pastel-00654930

HAL Id: pastel-00654930

<https://pastel.hal.science/pastel-00654930>

Submitted on 23 Dec 2011

HAL is a multi-disciplinary open access archive for the deposit and dissemination of scientific research documents, whether they are published or not. The documents may come from teaching and research institutions in France or abroad, or from public or private research centers.

L'archive ouverte pluridisciplinaire **HAL**, est destinée au dépôt et à la diffusion de documents scientifiques de niveau recherche, publiés ou non, émanant des établissements d'enseignement et de recherche français ou étrangers, des laboratoires publics ou privés.

THÈSE DE DOCTORAT
DE L'ÉCOLE POLYTECHNIQUE

présentée par

Alexandre Barbagallo

pour obtenir le titre de

Docteur de l'École Polytechnique

Spécialité : Mécanique

**Model reduction and closed-loop control
of oscillator and noise-amplifier flows**

*Réduction de modèle et contrôle en boucle fermée
d'écoulements de type oscillateur
et amplificateur de bruit*

soutenue le 14 janvier 2011

devant le jury composé de :

M. Dwight Barkley	
M. Laurent Cordier	
M. François Gallaire	<i>Rapporteur</i>
M. Angelo Iollo	<i>Rapporteur</i>
M. Lionel Mathelin	
M. Peter J. Schmid	<i>Directeur de thèse</i>
M. Denis Sipp	<i>Encadrant</i>

Résumé : Ce travail est consacré au contrôle en boucle fermée des perturbations se développant linéairement dans des écoulements laminaires et incompressibles de types oscillateurs et amplificateurs de bruit. La loi de contrôle, calculée selon la théorie du contrôle LQG, est basée sur un modèle d'ordre réduit de l'écoulement obtenu par projection de Petrov-Galerkin.

La stabilisation d'un écoulement de cavité de type oscillateur est traitée dans une première partie. Il est montré que la totalité de la partie instable de l'écoulement (les modes globaux instables) ainsi que la relation entrée-sortie (action de l'actionneur sur le capteur) de la partie stable doivent être captées par le modèle réduit afin de stabiliser le système. Les modes globaux, modes POD et modes BPOD sont successivement évalués comme bases de projection pour modéliser la partie stable. Les modes globaux ne parviennent pas à reproduire le comportement entrée-sortie de la partie stable et par conséquent ne peuvent stabiliser l'écoulement que lorsque l'instabilité du système est initialement faible (nombre de Reynolds proche de la criticité). En revanche, les modes POD et plus particulièrement BPOD sont capable d'extraire la dynamique entrée-sortie stable et permettent de stabiliser efficacement l'écoulement.

La seconde partie de ce travail est consacrée à la réduction de l'amplification des perturbations sur une marche descendante. L'influence de la localisation du capteur et de la fonctionnelle de coût sur la performance du compensateur est étudiée. Il est montré que la troncature du modèle réduit peut rendre le système bouclé instable. Finalement, la possibilité de contrôler une simulation non-linéaire avec un modèle linéaire est évaluée.

Mots clés : stabilité globale, contrôle d'écoulement, contrôle LQG, réduction de modèle, modes globaux, modes POD, modes BPOD.

Summary : This work deals with the closed-loop control of disturbances which develop linearly in laminar and incompressible flows. The control of both oscillator and amplifier flows is assessed. We consider a LQG control strategy in which the control law is computed using a reduced-order model of the flow. This reduced-order model is obtained by a Petrov-Galerkin projection.

The first part is devoted to the stabilization of an open cavity flow which behaves as an oscillator. It is shown that the unstable subspace of the flow (the unstable global modes) and the input-output behaviour between the actuator and the sensor of the stable subspace must be captured by the reduced-order model to stabilize the system. Global modes, POD modes and BPOD modes are successively evaluated as projection bases to construct a reduced-order model of the stable part of the flow. It appears that global modes are not able to reproduce the input-output behaviour of the stable part of the flow and subsequently may only stabilize the flow if the instability is very weak (close to the criticality). On the contrary, reduced-order models based on POD modes and BPOD modes efficiently extract the input-output dynamic of the stable subspace and are successful to stabilize the flow.

The second part of this work is dedicated to the reduction of the disturbances' amplification on a backward facing step. The influence of the sensor's location and of the cost functional on the performance of the compensator is studied. It is shown that the truncation of the reduced-order model may lead to an unstable closed-loop system. Finally, the possibility to control a non-linear simulation using a linear compensator is evaluated.

Key words : global stability, flow control, LQG control, model reduction, global modes, POD modes, BPOD modes.



Remerciements

Cette thèse a été effectuée lors d'une collaboration entre le Département d'Aérodynamique Fondamentale et Expérimentale (DAFE) de l'ONERA et le Laboratoire d'Hydrodynamique (LadHyX) de l'Ecole Polytechnique. Je suis infiniment reconnaissant à Laurent Jacquin, directeur du DAFE, et à Patrick Huerre, directeur du LadHyX, de m'avoir accueilli au sein de leurs laboratoires.

Je remercie les rapporteurs de cette thèse, François Gallaire et Angelo Iollo, pour leur étude approfondie du manuscrit ainsi que les membres du jury : Dwight Barkley, Laurent Cordier et Lionel Mathelin.

Je tiens à remercier particulièrement Denis Sipp qui a encadré cette thèse à l'ONERA. Je te remercie pour ta disponibilité, ton écoute attentive et ta persévérance à répondre à mes nombreuses questions. J'ai beaucoup apprécié ces innombrables heures où tu m'as fait partager ta passion pour la mécanique des fluides et ton enthousiasme à comprendre et résoudre des problèmes scientifiques. Je suis conscient que ce travail ne serait pas ce qu'il est sans ton implication quotidienne. Grâce à toi, ces trois années resteront à jamais dans ma mémoire.

Un grand merci à Peter Schmid qui a dirigé cette thèse. J'ai beaucoup apprécié ta bonne humeur et ta simplicité qui m'a mis à l'aise dès notre première rencontre. Ce travail est aussi très redevable à ton vaste champ de connaissances. Nos discussions au café Daguerre resteront gravées comme quelques uns des meilleurs souvenirs de cette thèse. Merci également pour ton implication lors de mon rapatriement d'Allemagne.

Je remercie enfin Jean-Christophe Robinet avec qui j'ai collaboré sur la dernière partie de ces travaux.

Ces trois années ont été très agréables grâce à la bonne ambiance qui règne à l'ONERA et au LadHyX.

Je remercie chaleureusement tous les ingénieurs et techniciens du DAFE, ainsi que Dominique et Claire. Merci aux doctorants et stagiaires du DAFE pour leur soutien et leur bonne humeur : Samuel, Olivier, Vincent, Benjamin, Sarah, Gregory, Aurélien, Sami, Laurence, Benoît, Philippe, Sébastien et Jean-Yves, ainsi qu'à tous les stagiaires que j'ai pu rencontrer.

Mes passages au LadHyX, bien que trop peu nombreux, ont toujours été très plaisants. L'atmosphère décontractée instaurée par les doctorants, post-doctorants et chercheurs y est excellente. Merci particulièrement à Xavier, Cristobal, Fulvio, Miguel, Gianluca, Joran, John, Yongyun, Diego, Junho, Pierre, Madiha, Maria-Luisa, Frédérick, Christoph, Shehryar, Mathieu, Rémi, Elena, Julien, Arnaud, Joseph, Lutz, François et Charles.

Je tiens enfin à remercier très chaleureusement mes collègues allemands qui m'ont accueilli à Munich et soutenu lors de mon séjour à l'« UniBw ». Un très grand merci à Christoph, Jan, Olivier et Julius.

Pour finir, je souhaite remercier mes amis parisiens Benoit et Julian pour leur présence durant ces trois années (merci à Julian pour m'avoir hébergé si souvent chez lui).

Enfin, je remercie du fond du cœur ma famille pour son soutien continu et pour m'avoir toujours donné les moyens de concrétiser mes objectifs.

Table des matières

I Model reduction and closed-loop control of oscillator and noise-amplifier flows	1
1 Introduction	3
1.1 Flow unsteadiness	3
1.1.1 Flow unsteadiness in industrial applications	3
1.1.2 Hydrodynamic instabilities	4
1.1.2.1 Oscillators	4
1.1.2.2 Noise amplifiers	5
1.2 Control	6
1.2.1 Various control strategies	6
1.2.2 Linear Quadratic Gaussian control	7
1.2.2.1 Application of LQG controllers to simplified flow systems	8
1.3 Model reduction	9
1.3.1 Galerkin projection	9
1.3.1.1 Global modes	10
1.3.1.2 Proper Orthogonal Decomposition Modes	10
1.3.1.3 Balanced Proper Orthogonal Decomposition Modes	10
2 Summary of the articles	13
2.1 Article 1	13
2.2 Article 2	16
2.3 Article 3	19
3 Conclusions and future work	23
3.1 Summary of the results	23
3.2 Future work	25
References	27
II Articles	35
4 Article 1	
Closed-loop control of an open cavity flow using reduced-order models	37
5 Article 2	
Input-output measures for model reduction and closed-loop control : application to global modes	89
6 Article 3	
Closed-loop control of amplifier flows	117

Première partie

**Model reduction and closed-loop
control of oscillator and
noise-amplifier flows**

1 Introduction

1.1 Flow unsteadiness

Although flow unsteadiness usually results in magnificent phenomena to observe (see figure 1.1), it is often prejudicial in engineering applications. This thesis is devoted to the design and evaluation of control strategies which aim at suppressing unsteady perturbations and ultimately return to a stationary flow.

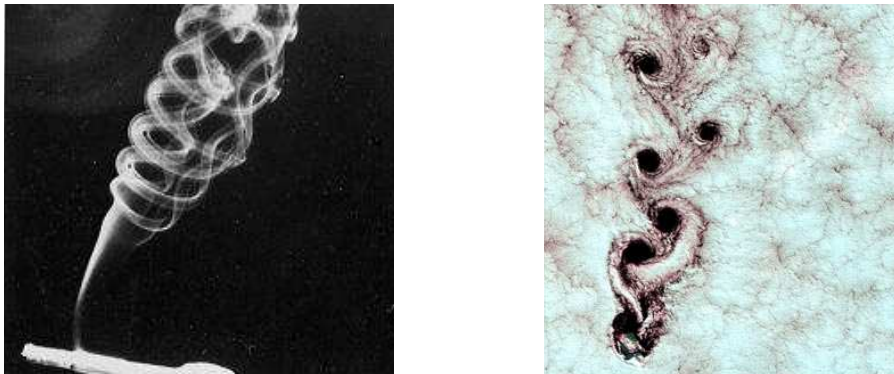


FIGURE 1.1 – Left : cigarette smoke subject to buoyancy effects. After Perry & Lim [75]. Right : Von Karmann vortex street in the atmosphere triggered by the flow over an island. (NASA picture).

1.1.1 Flow unsteadiness in industrial applications

In day-to-day situations, we are surrounded by air with unsteady behavior. For example, the smoke of a cigarette which rises under the buoyancy effect (see figure 1.1 left) is subject to various flow instabilities which render the prediction of its trajectory almost impossible. In the aerospace industry, and more generally in engineering domains related to fluid mechanics, the flows can also exhibit erratic behaviors. This behavior can be desired : in combustion chambers an enhanced mixing results in a better combustion ; but may also be detrimental to the correct functioning of the system. When an airplane is flying at cruise conditions the flow accelerates on the suction side of the wing and creates a stationary shock. If the angle of attack suddenly increases (for example to avoid a collision with another aircraft) the shock will start to oscillate and may trigger some structural modes of the aircraft. This phenomenon, known as shock buffeting (see Jacquin et al. [52]), is dangerous for the airplane safety and reduces the flight envelope of commercial airplanes. In order to reduce the electromagnetic detection of modern military airplanes, the engine compressor is fed with external air through a curved air intake (see figure 1.2). Due to strong adverse pressure gradients, the flow separates, creating a shear layer which amplifies incoming perturbations and results in large vortical structures which impact the compressor and diminish the performance of the engine.

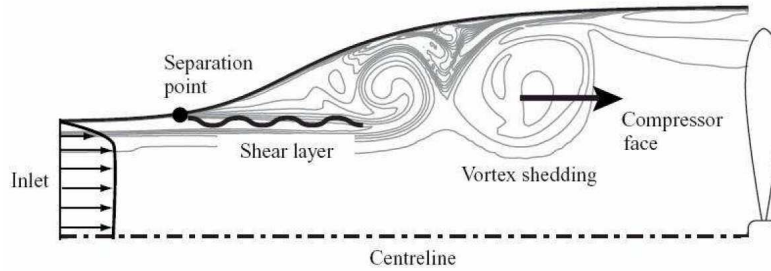


FIGURE 1.2 – Sketch of the creation of perturbations in an air intake.

These few examples are taken from the aerospace industry and therefore associated with high velocities and turbulent flow conditions. However, similar flow unsteadiness may be encountered at lower Reynolds numbers and for laminar flows. Since laminar flows are less complex and thus better understood than turbulent flows, the flow control techniques considered in this thesis will be evaluated using laminar test cases. In addition, the perturbations described in the previous examples are much larger than the typical turbulence length scales. Therefore, as suggested in Sipp et al. [85], it is likely that the techniques developed in this thesis for laminar flows may also be extended successfully to turbulent flow conditions by augmenting the Navier-Stokes equations with one or more turbulence model equations.

1.1.2 Hydrodynamic instabilities

Turbulent flows are by definition unsteady. On the contrary, laminar flows may be either stationary or unsteady. Hydrodynamic stability theory is the field which analyses how and when the flow changes from a stationary state, usually referred to as a base flow, to an unsteady behavior (perturbed flow). In the flow configurations of interest in this thesis, the parameter which governs the transition between the stationary and unsteady states, referred to as the control parameter, is the Reynolds number. This parameter quantifies the relative importance of inertial forces and viscous forces. For low Reynolds numbers, the stabilizing forces due to the viscous effects are predominant and would damp any external perturbations in the flow. As the Reynolds number increases, the inertial forces become more important, allowing unsteadiness in the flow. In this case it is instructive to distinguish flows which behave as oscillators and flows which act as noise-amplifiers (Huerre & Rossi [46]).

1.1.2.1 Oscillators

Oscillator flows are characterized by a self-sustained beating of the flow at a particular frequency. The usual mechanism leading to an oscillator behavior consists in an exponential amplification of any perturbation of the flow field followed by its saturation due to non-linear effects. In other words, when the control parameter is increased above a critical value the flow is subject to a Hopf bifurcation and bifurcates from a stationary solution to a limit cycle. At this point, no external perturbations are necessary to keep alive the oscillatory motion of the flow; this mechanism is intrinsic to the flow.

Oscillator behavior is well predicted by a global stability analysis (see Jackson [51] for the first analysis in the case of a cylinder flow). Global stability computations have first been computed on simple academic configurations : cylinder flow (Noack & Eckelmann [73]), backward-facing step (Barkley et al. [12], Marquet et al. [68]), separated flows (Gallaire et al. [36], Akervik et al. [4], Ehrenstein & Gallaire [31]). More recently, global stability analysis of complex geometries have been considered : transonic flow over a wing (Crouch et al. [27]), compressible flow over a swept leading edge (Mack et al. [67] and Mack & Schmid [66]) and a three-dimensionnal

jet in crossflow (Bagheri et al. [10]). Additional details are available in the review articles of Theofilis [89] and Chomaz [25].



FIGURE 1.3 – Supercritical flow over an open cavity at $Re_L = 11\,150$ (aspect ratio $H/L = 1.5$). After Basley et al. [13].

The test case which will be representative of oscillator flow behavior in this thesis is the incompressible flow over an open cavity. This flow is shown in figure 1.3 by smoke-visualization for a Reynolds number $Re_L = 11\,150$ (based on the freestream velocity and the length L of the cavity) and a cavity aspect ratio $L/H = 1.5$ (H is the height of the cavity). This figure is taken from Basley et al. [13]. On top, the high velocity flow is visualized by bright colors. Due to viscous effects, this flow drags along the fluid inside the cavity into a solid rotation. The main vortex inside the recirculation zone is noticeable due to smaller vortices located between the downstream edge and the bottom of the cavity. This recirculation zone is separated from the main flow by an unstable shear-layer. The perturbations are amplified by the Kelvin-Helmholtz instability during their convection along the shear layer and emerge as vortical structures. When these structures impact the downstream edge of the cavity, the sensitivity zone of the shear-layer located at the upstream edge of the cavity is triggered, creating new perturbations which are again amplified along the shear-layer (see Rockwell & Naudascher [78], Gharib & Roshko [40] and Faure et al. [35]). This feedback loop is responsible for the self-sustained nature of the perturbations. The oscillator behavior of this flow by means of global stability theory analysis has been treated by Sipp & Lebedev [84] for a two-dimensional incompressible flow and by Brès & Colonius [20] for a three-dimensional compressible flow. Note that the compressible cavity flow has been extensively studied (see original article of Rossiter [79] and recent review by Rowley & Williams [81]).

1.1.2.2 Noise amplifiers

In some cases, an unsteady flow behavior which does not exhibit an organized and coherent motion is observed. The length scales and frequencies of the detected perturbations have a broad range and only exist if the flow is perturbed by an external noise source. Therefore these flows are referred to as noise-amplifier flows and the mechanism leading to the emergence of discernible structures is extrinsic. It is worth mentioning that a global stability analysis is not capable of describing this flow behavior since it would result in a globally stable system. Therefore these flows are preferably studied using the resolvent operator which highlights the transient amplification of perturbations in such systems (see Sipp et al. [85]).

The prototypical configuration considered in this thesis is the incompressible flow over a backward facing step. In figure 1.4 this flow is shown for a Reynolds number $Re = 1050$ based on the freestream velocity and the step height, using Laser Induced Fluorescence visualiza-

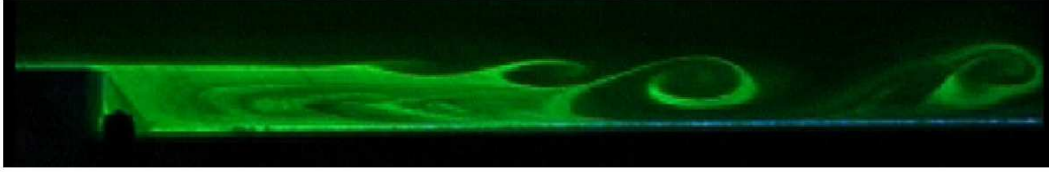


FIGURE 1.4 – Flow over a backward-facing step at $Re_H = 1050$. After Aider [2].

tions. The figure is taken from Aider [2]. On top, the freestream flow separates from the wall at the step. A recirculation bubble behind the step is visualized in green. As in the cavity, the Kelvin-Helmholtz instability is responsible for the amplification of disturbances along the shear-layer. In this case, the roll-up of vortices is particularly visible. However at sufficiently low Reynolds number the vortices are convected downstream without triggering new perturbations. As a result, this flow case requires external noise, e.g. a slightly perturbed incoming flow, to maintain unsteadiness. The noise amplifier behavior of backward-facing steps has been extensively studied in the literature (Barkley et al. [12], Beaudoin et al. [14], Blackburn et al. [19], Marquet et al. [68]). These studies particularly emphasize the superposition of a strong amplifier behavior as well the bifurcation to a steady 3D state.

1.2 Control

Flow unsteadiness limits the life expectancy of engineering systems by structural excitations, increases the acoustic pollution by generating noise or may directly affect the system's safety (shock buffeting). It is therefore of pivotal importance to deliver robust and efficient flow control techniques to design engineers.

1.2.1 Various control strategies

Flow control can be defined as the modification of a natural flow behavior towards a desired flow state. To achieve flow control, two distinct strategies have been considered (see Rowley & Williams [81]). The first, referred to as *passive control*, consists in a modification of the flow without adding energy to the system. On the contrary, *active control* techniques are characterized by an energy input.

Passive control strategies basically come down to a modification of the geometry aiming at changing the mean flow (see review by Choi et al. [24]). This geometric modification can also be achieved by adding a fixed device at a location where the flow is sensitive : in Strykowski & Sreenivasan [88], the vortex shedding behind a cylinder has been suppressed for Reynolds numbers close to the critical Reynolds number ($47 < Re < 60$) by adding a small control cylinder in a region close to the separation point. Note that the sensitivity regions of this flow have been recovered by Giannetti & Luchini [41] and Marquet et al. [69] using tools from global stability theory. At high Reynolds numbers, the noise of a transonic cavity has been reduced by placing a small control cylinder at the upstream edge of the cavity (see Illy et al. [50]). Passive control strategies are easy to implement due to the absence of moving devices (actuators). However, this implies that the control is designed for a specific flow configuration and cannot adapt to possible changes in the flow state. In addition, the geometric modifications or placement of these control devices are usually obtained by trial-and-error or require a good expertise in the flow case to be controlled, in particular, the knowledge of the physical mechanisms leading to the unwanted situation and of the sensitivity regions of the flow. For example, to prevent the formation of large vortical structures in air intakes, one possible solution would be to suppress the recirculation zone. Recirculation zones are created by the separation of low momentum

streamlines close to the wall. In case of a strong adverse pressure gradient the inertial forces are too weak compared to the opposing force created by the adverse pressure gradient and the flow separates. This phenomenon may be suppressed by transferring high momentum fluid into the lower part of the boundary layer using, for example, vortices which are created by vortex generators (Gardarin [39], Duriez [29]) or roughness elements (Pujals et al. [77]).

Contrary to the passive control strategies, active control strategies require energy and may adapt to flow changes. Examples of active control devices are : moving flaps (such as high lift devices on a wing) or actuators which inject fluid (jets) or momentum (plasma actuators) into the flow. In their simplest form, these actuators are governed by a steady motion (see Joslin [54] for an application to laminar flow control), a periodic control law (see review by Greenblatt & Wygnanski [42]) or a predefined control law. However, more advanced strategies use measurements extracted in real time from the flow to produce a relevant control action. To this end, tools coming from control theory such as optimal control have recently been considered to perform flow control and are considered in this thesis. Details about optimal control applied to fluid mechanics can be found in Kim & Bewley [55].

1.2.2 Linear Quadratic Gaussian control

In this thesis, we consider the Linear Quadratic Gaussian (LQG) control framework to suppress, or at least reduce, the perturbations which develop in oscillator and noise-amplifier systems. LQG control computes a control law based on a Linear description of the system in order to minimize a Quadratic cost functional, the system being driven by Gaussian noise. A preliminary step is therefore to choose a set of actuators to act on the flow, a set of sensors to extract real time information from the flow and to define a linear state-space model representative of the system of interest (although the Navier-Stokes equations are non-linear). This is generally overcome by studying the early stages of development of the perturbations to be controlled since for small perturbations nonlinearities are negligible. Therefore a correct model may be obtained by linearizing the equations around a base flow (solution of the steady non-linear Navier-Stokes equations). LQG control consists in computing a so-called compensator which takes as input one or many measurements of the system and returns the control law which governs the actuators. Standard references about optimal control are Burl [21] and Zhou [93].

A sketch representing the key elements of the compensated system is displayed in figure 1.5. In this sketch, the plant represents the system to be controlled. In the most general case, the plant is initialized by the flow state $\mathbf{X}(t_0)$ and subject to external noise which mimics for example incoming perturbations. The sensor extracts a measurement from the state $\mathbf{X}(t)$ which is given to the compensator. A control law is then computed to determine the temporal behavior of the actuator and eventually control the plant. The compensator is composed of two distinct components : a controller and an estimator, which may be designed independently (see separation principle in Burl [21]).

The controller and estimator are computed based on a linear model of the plant. The controller provides to the actuator a control law $u(t) = \mathbf{K}\mathbf{X}(t)$ given by the multiplication of the state $\mathbf{X}(t)$ and the so-called control gain matrix \mathbf{K} . This matrix is computed by solving a Riccati matrix equation (see Burl [21]) and minimizes a quadratic cost functional. In flow control applications this cost functional is usually taken as the sum of the state energy (or the measurement energy) and the energy of the control, a control cost parameter being used to give more emphasis to the state energy or to the control cost (see Kim & Bewley [55]). However, other cost functionals are possible (see Lee et al. [59] and Min & Choi [70]). The input of the controller is the state of the system which is usually not a quantity available in experiments, therefore an estimation of the flow state is required. The estimator has the task of computing an estimated state (\mathbf{Y} in figure 1.5) which is subsequently used by the controller. The estimated flow state is computed using the time history of the measurement and of the

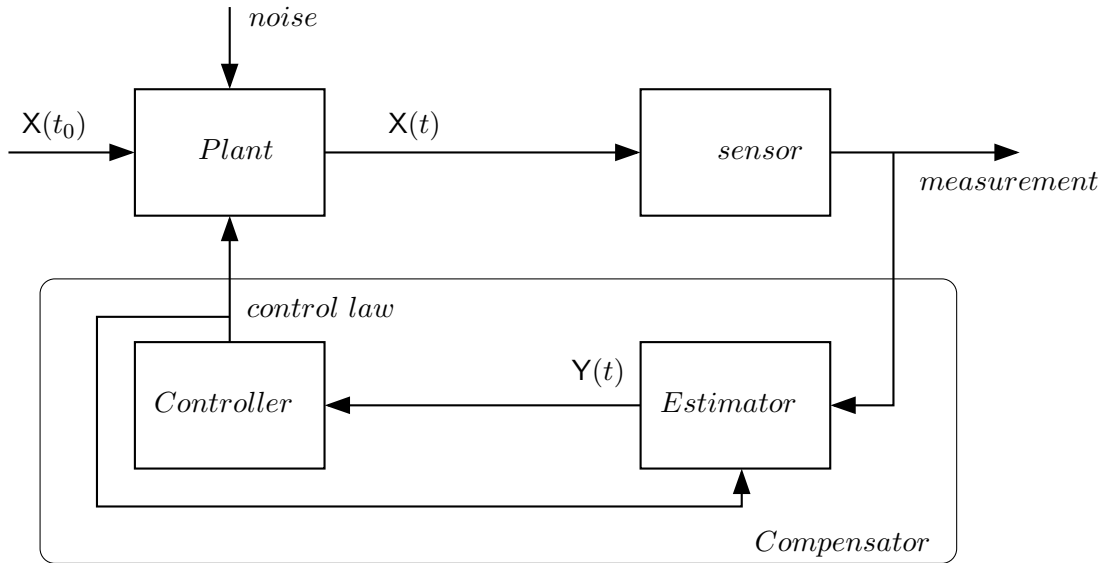


FIGURE 1.5 – Sketch of a typical Linear Quadratic Gaussian control setup.

control law. Similarly to the controller, the estimator is based on a linear description of the system and aims at minimizing the error between the flow state and the estimated state. The computation of the estimator also relies on the solution of a Riccati matrix equation.

1.2.2.1 Application of LQG controllers to simplified flow systems

The application of LQG compensators to fluid mechanics necessitates the solution of two Riccati matrix equations involved in the computation of the controller and estimator. These equations have the drawback of being computationally tractable only for systems of moderate dimensions ($\approx 10^3$). However, typical hydrodynamic problems are usually characterized by a wide range of length scales which have to be properly captured to accurately solve the Navier-Stokes equations. This implies that the linear system which is directly extracted from the discretization of the linearized numerical simulation has a very high number of degrees of freedom (10^5 or 10^6 for two or three-dimensional configurations). For that reason, LQG compensators have first been applied to simplified generic configurations. The control of channel flow has been widely considered since Fourier transformations can be applied in the streamwise and spanwise directions and the problem becomes one-dimensional. The stabilization of both supercritical and subcritical channel flows for particular spanwise and streamwise wavenumbers was obtained by Bewley & Liu [18] and the performance of the compensator was compared to the proportional integral control of Joshi et al. [53]. Since all wavenumbers decouple in frequency space, it is possible to compute the control for each wavenumber (centralized approach) and recover the control law in physical space (decentralized approach) using an inverse Fourier transform (see Bewley [17]). This strategy is adopted in Högberg et al. [43]. Finally, the ability of LQG controllers to control the transient growth of a linearized channel flow was studied by Lim & Kim [60]. The decentralized approach was also considered to control spatially developing boundary layers in Högberg & Henningson [44] using full-state control (the entire state is directly extracted from the simulation without referring to the estimator) and in Chevalier et al. [23] using LQG compensators. Finally, the one-dimensional Ginzburg-Landau equation has been considered as a benchmark for optimal control evaluation in subcritical and supercritical cases (see Lauga & Bewley [56],[57],[58] and Bagheri et al. [9]) and for the optimal placement of actuators and sensors in a supercritical case in Chen et al. [22].

When the geometry becomes more complicated (absence of invariant directions), Fourier transformations cannot be applied and one-dimensional models can no longer be obtained. In

this case, a reduced-order model of the flow becomes mandatory for the computation of the compensator.

1.3 Model reduction

As mentioned previously, an accurate solution of the Navier-Stokes equations requires a accurate discretization in order to resolve the smaller length scales of the problem. However, as acknowledged by Kim & Bewley [55], the compensator design does not require such a complete description of the system but only the dynamics from the actuator to the sensor. This dynamics obviously depends on the number of actuators and sensors considered, but is generally rather low-dimensional compared to the full discretization and may be easily captured by a reduced-order model. In addition, in order to compute a control law in real time, the compensator should have a reaction time similar to the phenomena to be controlled. This again leads to a reduced-order model.

Two major strategies are available to arrive at a reduced-order model : system identification techniques and projection techniques. System identification has the advantage of relying only on data arising from simulations or experiments and is therefore easily applicable. After having defined actuators and sensors, this technique consists of identifying the coefficients of the reduced-order model. Many strategies are available for the computation of these coefficients such as the "autoregression with exogenous input" (ARX) considered in Huang & Kim [45] or the Eigensystem Realisation Algorithm described in Ma et al. [65]. As already mentioned, the main benefit of such techniques is that no a priori knowledge about the actuators, sensors and dynamics of the system is required. Extensive details on system identification techniques are given in Ljung [61]; some applications to cavity flows may be found in Rowley & Williams [81].

A related technique consists in defining a theoretical representation of the system which can subsequently be calibrated using data from simulations or experiments. For example in Rowley et al. [82] and Illingworth [49], a resonant cavity has been modeled by a superposition of independent transfer functions, each representing different physical mechanisms : shear-layer, scattering, acoustics, receptivity; to which are added a model for the actuator and for the sensor. Note that this strategy relies on a solid understanding of the physical problem at hand, which is not always accessible.

1.3.1 Galerkin projection

The technique which will be considered in this thesis to arrive at a state-space model of the flow belongs to the category of projection techniques. The starting point of this method is : (i) a high-dimensional state-space model arising from the discretization of the linearized Navier-Stokes equations with actuators and sensors (see Kim & Bewley [55]) and (ii) a set of vectors, called the reduced basis, which span the subspace onto which the dynamics will be projected. The high-dimensional system is then projected onto the reduced basis using a Galerkin projection (or Petrov-Galerkin projection in case of a bi-orthogonal basis). This results in a reduced-order model whose size is equal to the dimension of the projection basis. In this thesis we only consider linear reduced-order models since we are interested in the dynamics of small perturbations which are superposed on a specific base flow. In this case, the Navier-Stokes equations linearized about this base flow accurately represent the problem. However, non-linear models may also be obtained using a Galerkin projection if the non-linear dynamics is studied, e.g. the vortex shedding behind a bluff body (see section on POD modes).

The projection subspace has a great influence on the dynamics returned by the model and its choice is of pivotal importance in this technique. In this thesis, three different projection bases have been considered.

1.3.1.1 Global modes

Reduced-order models may be obtained by projecting the high-dimensional system onto global modes. The global modes are the eigenvectors of the linearized Navier-Stokes operator (see Sipp et al. [85]). Initially, these modes have been computed during global stability analyses as the spatial structures associated to the stable or unstable eigenvalues (see §1.1.2.1 and references therein). Since the global modes are often non-orthogonal (see Cossu & Chomaz [26]), an adjoint basis is required for the projection step. This adjoint basis is composed of the adjoint global modes, i.e. the eigenvalues of the adjoint linearized Navier-Stokes operator. A reduced-order model is obtained by projecting onto a reduced set of global modes, for example the least stable ones. Such models have been used, in particular for the computation of optimal growth (Ehrenstein & Gallaire [30], Akervik et al. [3], Ehrenstein & Gallaire [32], Alizard & Robinet [5]).

By construction, global modes are related to the dynamics of the flow of interest without any information about actuators and sensors. For that reason and due to the difficulty of computing many global modes, their efficiency as a projection basis for control-oriented reduced-order models is still questionable. Closed-loop control using such reduced-order models have been studied in Akervik et al. [4] and recently in Ehrenstein et al. [33].

1.3.1.2 Proper Orthogonal Decomposition Modes

Proper Orthogonal Decomposition (POD) is one of the most popular technique in fluid mechanics to obtain a reduced-order model. This technique consists of constructing a reduced basis such that the approximation of a particular dataset which spans a high-dimensional space is represented on the reduced basis in an optimal manner. The term “optimal” refers to the fact that the error between the original dataset and its projection onto the reduced dataset is minimal based on the energy norm.

This method was first used in fluid mechanics by Lumley [63] to extract the coherent structures in turbulent flows. It is particularly attractive since it does not require any knowledge of the flow but relies only on the dataset of interest. However, this method turns into solving an eigenvalue problem whose size is equal to the number of degrees of freedom of the high-dimensional system. A technique referred to as the snapshot method (Sirovich [87]) allows to reduce the problem to an eigenvalue problem whose size is equal to the number of snapshots, resulting in a computationally tractable method. For example, this method has been considered for the description of a boundary layer flow in Aubry et al. [7] and a channel flow in Podvin & Lumley [76]. However, reduced-order models obtained by a Galerkin projection onto POD modes may be unstable (Ma & Karniadakis [64]). Therefore, improvements of these models were obtained by adding “shift modes” and stability modes (Noack et al. [72]), a pressure term (Noack et al. [74]), a spectral viscosity (S. Sirisup and G. E. Karniadakis [86]) or by calibrating the model coefficients (Galetti et al. [38]). In order to perform flow control, efforts have been made to include the effects of actuators in the flow (Galetti et al. [37], Weller et al. [91], Luchtenburg et al. [62]). Finally, flow control results based on reduced-order models designed with POD modes may be found in Bergmann et al. [16], Bergmann & Cordier [15], Weller et al. [90] and in the experimental work of Samimy et al. [83]. Note that in our study, the POD basis is computed using snapshots from the impulse response of the linearized Navier-Stokes operator. A similar technique was considered in Ilak & Rowley [48] and Bagheri et al. [8] and [10].

1.3.1.3 Balanced Proper Orthogonal Decomposition Modes

Balanced Proper Orthogonal Decomposition is a model reduction technique linked to a method from control theory called “balanced truncation” (see Moore [71]). Having defined a state-space model including actuators and sensors, this method relies on the notions of control-

lability and observability. Controllability refers to the ability of a state to be influenced by the actuators; observability refers to the capacity of a state to be measured by the sensors. As recognized in control theory, only the states which are both highly controllable and observable are required for control design. For this reason, the general idea of balanced truncation is to retain only the states which are highly controllable and observable. These modes correspond to the eigenvalues with highest amplitudes of the product of the so-called controllability and observability Gramians (see Antoulas [6]). These gramians are obtained by solving two Lyapunov equations which, similarly to Riccati equations, cannot be solved computationally for systems of high dimensions. Therefore, the strict application of balanced truncation is limited to simple one-dimensional problems (see Farrel & Ioannou [34] and Bagheri et al. [9]).

A breakthrough in this technique was achieved recently by Willcox & Peraire [92] who showed that low-rank approximations of the controllability and observability Gramians may be reconstructed using a snapshot method (similar to the snapshot method in POD) and by Rowley [80] who suggested an algorithm which recovers the balanced modes without the explicit computation of the low-rank Gramians. Using this technique, referred to as Balanced Proper Orthogonal Decomposition (BPOD), feedback control in various flow configurations has recently been achieved: boundary-layer flow (Bagheri et al. [8]), transitional channel flow (Ilak et al. [48] and Ilak [47]) and unstable flow over a flat plate at large angles of attack (Ahuja & Rowley [1]). It should be mentioned that the reduced-order model obtained by projecting the system onto BPOD modes is similar to the one obtained using the ERA as shown in Ma et al. [65]. This result establishes a link between projection methods and identification methods, and thus brings models based on BPOD closer to experimental implementations.

2 Summary of the articles

2.1 Article 1

In this article we study the stabilization of a globally unstable flow using feedback control based on reduced-order models (ROMs). The test case considered is the incompressible flow over a two-dimensional square cavity (figure 2.1) at $Re = 7500$ (based on the inflow velocity and the height of the cavity). At this Reynolds number, the cavity exhibits self-sustained perturba-

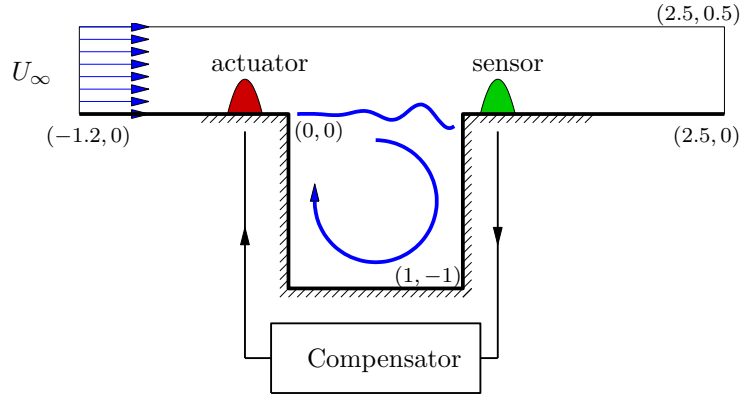


FIGURE 2.1 – Sketch of flow over an open cavity.

tions [84]. A control strategy based on a blowing/suction (vertical velocity) actuator located at the upstream edge of the cavity and a shear-stress sensor located at the downstream edge of the cavity is chosen to suppress these perturbations. Since we assume small amplitude perturbations, we model the flow using the Navier-Stokes equations linearized about the unstable base flow at $Re = 7500$ computed using a Newton method. The linearized Navier-Stokes equations with the actuator (implemented using a lifting procedure) are discretized on a finite-element mesh :

$$\mathbf{Q} \frac{d\mathbf{X}}{dt} = \mathbf{A}\mathbf{X} + \mathbf{Q}\mathbf{C}c, \quad (2.1a)$$

$$m = \mathbf{M}\mathbf{X}. \quad (2.1b)$$

\mathbf{X} is the state vector (longitudinal velocity, transversal velocity and pressure), the matrices \mathbf{Q} , \mathbf{A} , \mathbf{C} and \mathbf{M} are respectively the weight matrix arising from the discretization, the linearized Navier-Stokes operator, the control matrix and the measurement matrix; c and m are respectively the control law and the measurement.

To obtain the stability characteristics of the flow, a global stability analysis is performed by solving the generalized eigenvalue problem $\mathbf{A}\mathbf{X} = \lambda\mathbf{Q}\mathbf{X}$ with $\lambda = \sigma + i\omega$. Four unstable modes (positive growth rate σ) are found (see spectrum in figure 2.2). The aim of this paper is to stabilize these unstable modes using Linear Quadratic Gaussian compensators based on ROMs obtained by Petrov-Galerkin projections.

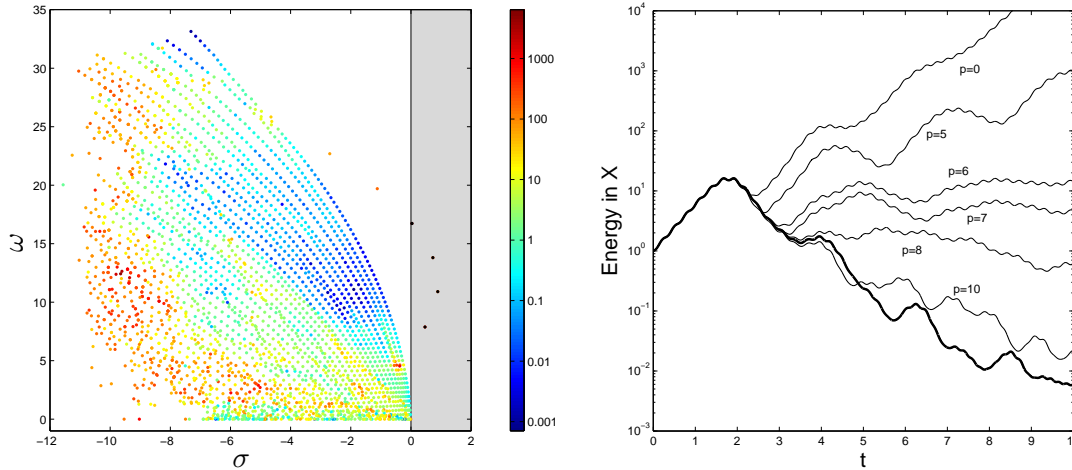


FIGURE 2.2 – left : global spectrum of the cavity flow at $Re = 7500$, σ is the damping rate and ω the frequency. Right : energy of the perturbations in the compensated system for ROMs based on the unstable global modes and p BPOD modes (thin curves) and "best control strategy" (thick curve).

By decomposing the system into its unstable and stable subspaces, it is shown that all the unstable global modes have to be included in the ROM. However, compensators based only on the unstable global modes are found to be incapable of stabilizing the flow. The reason is that while controlling the unstable subspace, the actuator also creates structures in the stable subspace. Since the estimator is designed only with unstable modes, it restricts the complete measurement (structures from both the unstable and stable subspaces) to the unstable modes and converges to a wrong estimate of these modes. This, in turn, results in an inadequate control law and in the instability of the compensated system. Thus, the stable subspace has to be also modeled, in particular, the input-output behavior of the stable subspace of the original system has to be captured [9]. To this end, projection bases consisting of global modes, BPOD modes or POD modes are successively considered. The global modes are computed according to the global stability analysis and the POD and BPOD modes are computed using a snapshot method [80].

In order to assess the ability of these bases to capture the input-output behavior of the original system we start by comparing the transfer function between the actuator and the sensor of the full system and the transfer function predicted by the ROMs. The error between them is evaluated using the \mathcal{H}_∞ norm. It is shown that the global modes are not capable of reconstructing the initial transfer function, even using a very large number of modes. In addition, when very damped global modes are added to the ROM, the discrepancy between the ROM and the full model increases drastically. To further examine this surprising feature we have derived a criterion to select the stable global modes which contribute the most to the transfer function. This criterion is given by $\Gamma_i = |C_i| |M_i| / |\sigma_i|$ where C_i is the control coefficient of the mode i , M_i its measurement coefficient and σ_i its growth rate. It preferably selects modes which are highly controllable and observable and less damped. These modes are colored by hot colors in figure 2.2(a) and are very damped modes. This has been further investigated and linked to the norm of the adjoint global modes which also increases drastically for very damped modes. This feature is related to the convective non-normality of the linearized Navier-Stokes operator which, in particular, locates the very damped direct modes close to the outflow boundary and their respective adjoint modes close to the inflow boundary. Therefore, in order to respect the bi-orthogonality condition, i.e. the scalar product between a direct global mode and its corresponding adjoint mode is one, the norm of the

adjoint modes increases tremendously. On the contrary, ROMs based on BPOD modes are shown to accurately approximate the full transfer function with very few modes but are sensitive to numerical issues and may be unstable. ROMs based on POD modes are always stable but require a higher number of modes to achieve similar performances as ROMs based on BPOD modes.

In the second part of this article, compensators based on these ROMs are computed and their performance in stabilizing a Linearized Direct Numerical Simulation (LDNS) is assessed. More precisely, the so-called control gain \hat{K} and Kalman gain \hat{L} ($\hat{\cdot}$ refers to quantities in the ROM) are computed according to the LQG control theory by solving two Riccati equations in the small gain limit. The full compensated system (see figure 1.5) is composed of the state-space system eq.(2.2) and of the controller defined by $c = \hat{K}\hat{X}$ and the estimator defined by $\dot{\hat{Y}} = \hat{A}\hat{Y} + \hat{C}c - \hat{L}(m - \hat{M}\hat{Y})$. The integration in time of this augmented system corresponds to the compensated system.

We found that the performance of the ROMs is highly correlated to their ability to capture the input-output behavior of the original system. In particular, when global modes are considered as a reduction basis the compensated system is always unstable. This instability gets stronger when very damped modes are added to the ROM. On the contrary, ROMs based on BPOD modes stabilize the system with a reduced number of modes (see figure 2.2(right)). ROMs based on POD modes benefit from their inherent stability, but need more modes to achieve comparable results as ROMs based on BPOD modes. Considering a stability analysis of the full compensated system, we suggested a computationally efficient method to assess the stabilization of the compensated system for a large number of ROMs (see figure 2.3).

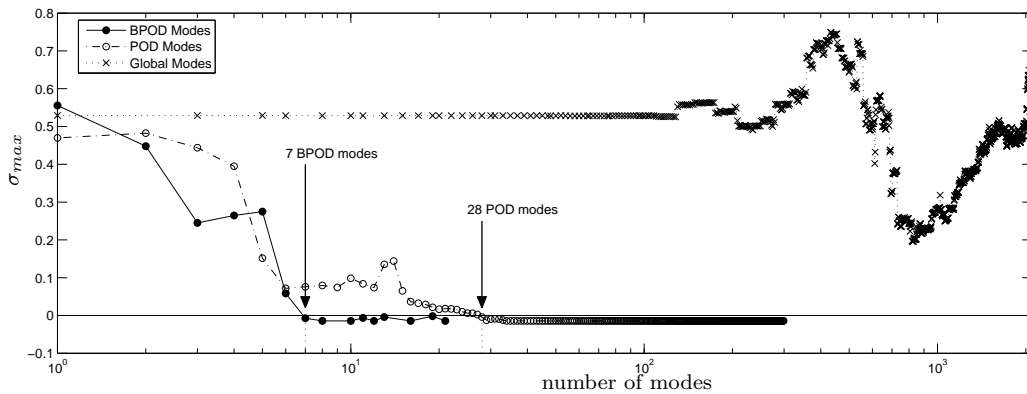


FIGURE 2.3 – Growth rate σ_{max} of the least stable eigenmode of the full compensated system.

Finally, we observed that ROMs based on BPOD or POD modes converge to a particular solution referred to as the "best control strategy" (thick dark curve in figure 2.2(right)) when the number of modes included in the ROM increases. It is shown that the "best control strategy" actually corresponds to the (artificial) case where the measurement m provided to the estimator is replaced by its projection onto the ROM. This proves that the input-output behavior is the correct quantity to be captured by the ROM in order to obtain optimal performance. We conclude that the inability of ROMs based on global modes to approximate this quantity is the reason of their failure to stabilize the flow.

2.2 Article 2

This article is concerned with the feedback control of a globally unstable flow based on a Reduced Order Model (ROM) obtained by a Petrov-Galerkin projection onto global modes. It is motivated by the diverging conclusions available in the literature concerning the ability of such models to successfully stabilize unstable systems. More precisely, the separated flow over a shallow cavity and a bump have been stabilized close to criticality ([4], [33]) but the flow over the square cavity described in §2.1 could not be controlled ([11]). The first goal of this article is to explain these diverging results. The second goal is to improve the open-loop evaluation of ROMs when their performance in capturing the input-output behavior of the original system is assessed. We will particularly focus on improved evaluation norms.

The configuration considered in this article is the incompressible flow over the two-dimensional square cavity studied in §2.1. The differences with the previous study are : an evaluation of the control efficiency from the critical Reynolds number $Re_c = 4140$ ([84]) to $Re = 7500$ and the replacement of the blowing/suction actuator by a body force on the vertical velocity. For different Reynolds numbers, a global stability analysis is conducted to compute the eigenvalues $\lambda = \sigma + i\omega$ such that their growth rate σ satisfies $\sigma > -4$. Reduced-order models are then obtained for each Reynolds number using a Petrov-Galerkin projection. These models may be written in state-space form as :

$$\frac{d\hat{X}}{dt} = \hat{A}\hat{X} + \hat{B}u, \quad (2.2)$$

$$m = \hat{C}\hat{X}. \quad (2.3)$$

\hat{X} is composed of the amplitude coefficients corresponding to each global mode, the matrices \hat{A} , \hat{B} and \hat{C} are respectively the linearized Navier-Stokes operator, the control matrix and the measurement matrix ; u and m are respectively the control law and the measurement.

To control an unstable flow, the instability must be accurately captured by the ROM, therefore all the unstable modes are included in the ROM ([11]). However, contrary to POD and BPOD bases which are respectively ordered by energy content or input-output importance, the choice of which stable global modes to include in the ROM is still open. We have considered four different ranking criteria referred to as the growth rate, the criterion Γ , the criterion $\tilde{\Gamma}$ and the "quasi-optimal" ranking. The growth rate ranking ([4] and [11]) selects the least damped modes. The criterion Γ ranks the modes by decreasing values of Γ where $\Gamma_i = |\mathbf{B}_i| |\mathbf{C}_i| / |\sigma_i|$. This criterion selects modes which are highly controllable, highly observable and weakly damped. The criterion $\tilde{\Gamma}$ works similarly but $\tilde{\Gamma}$ is defined by $\tilde{\Gamma}_i = |\tilde{\mathbf{B}}_i| |\mathbf{C}_i| / |\sigma_i|$ where the control coefficient $\tilde{\mathbf{B}}_i$ arises from an orthogonal projection which has the effect of minimizing the error between the original and the projected actuator ([33]). Finally, the "quasi-optimal" ranking criterion consists in selecting iteratively the modes which, when included in the ROM, enable the largest decrease of the compensated growth rate. This criterion is only considered as a demonstration tool but gives valuable information about an optimal selection of global modes. As an example of the ranking process, the modes preferably selected by the criterion Γ are displayed by hot colors on figure 2.4(left).

The properties of the ROMs based on these different ranking methods are illustrated with a detailed study at $Re = 7500$. The ability to capture the input-output behavior of the stable part of the high-dimensional simulation is tested by comparing the transfer function H of the original system and the transfer function \hat{H} of the ROMs for each ranking criteria. The error between them is first evaluated using the traditional \mathcal{H}_2 (see figure 2.4(right) and corresponding legend in figure 2.5) and \mathcal{H}_∞ norms. The lowest error (but still relatively high) is achieved using the "quasi-optimal ranking" with $\mathcal{O}(100)$ modes. The criterion Γ behaves better than the growth rate, and the ROMs based on the criterion $\tilde{\Gamma}$ display high errors.

Then, the stabilization of the system is evaluated for each ranking criterion using the method described in §2.1. The growth rate of the least stable eigenvalue of the full compensated system

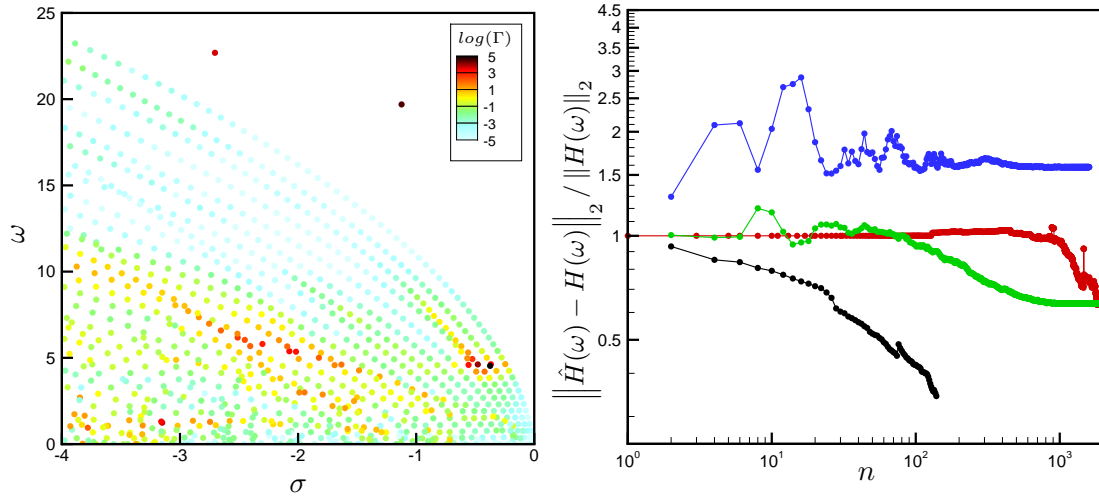


FIGURE 2.4 – left : global spectrum colored by criterion Γ . Right : relative \mathcal{H}_2 norm of the error between the full system and the ROM versus the number n of stable global modes included in the ROM (see legend on figure 2.5(left)).

is shown in figure 2.5(left). The flow is only stabilized ($\sigma_{max} < 0$) using the ”quasi-optimal”

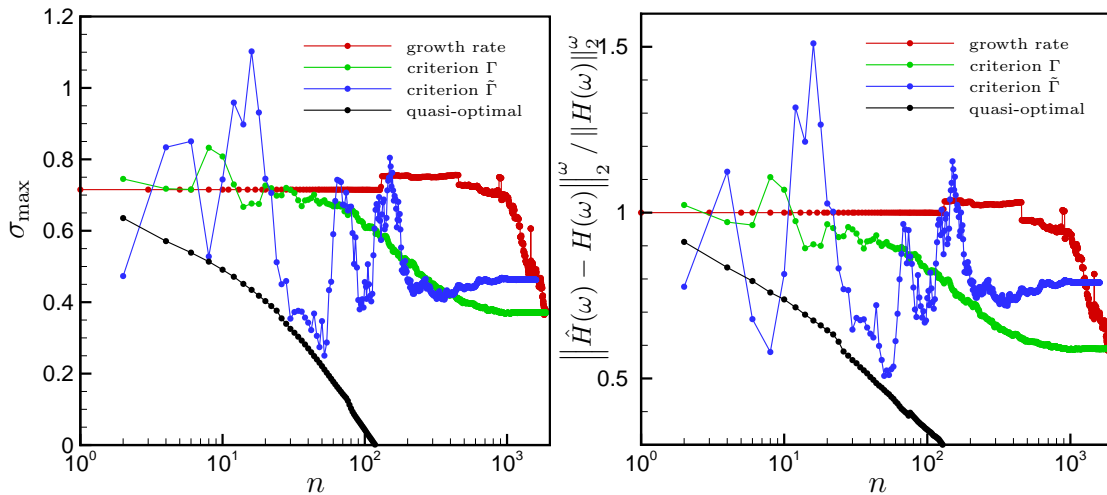


FIGURE 2.5 – left : growth rate σ_{max} of the least stable mode of the compensated system versus the number n of stable global modes included in the ROM. Right : relative frequency-restricted \mathcal{H}_2 norm of the error between the full system and the ROM versus the number n of stable global modes included in the ROM.

ranking. When other criteria are considered, the instability is generally reduced but often insufficiently to stabilize the flow. In particular, ROMs based on the criterion $\tilde{\Gamma}$ are surprisingly efficient (see $20 < n < 50$) although the same models behaved poorly during the open-loop analysis (see figure 2.4(right)). This shows that there is not a good correlation between the open-loop properties measured with the \mathcal{H}_2 and \mathcal{H}_∞ error norms and the closed-loop performance evaluated with σ_{max} and may indicate that the \mathcal{H}_2 and \mathcal{H}_∞ error norms are not optimal in characterizing the ROMs’ ability to control unsteady flows. By closely studying the transfer functions related to the different ranking criteria and correlating these observations to the stability properties of the compensated systems, it appeared that the transfer functions of the ROMs only need to approximate the transfer function of the full system in the frequency range defined by the unstable modes. Following this idea, we have defined a frequency-restricted \mathcal{H}_2

norm as :

$$\|H\|_2^\omega = \left(\int_{10}^{17} |H(\omega)|^2 d\omega \right)^{1/2}. \quad (2.4)$$

The error between the transfer function of the original system and the transfer function of the ROM is evaluated using this norm and shown in figure 2.4(right). In this case, the plot displays similar behavior as observed for the stability of the compensated system which proves the relevance of a frequency-restricted evaluation of the ROMs.

The end of this article is devoted to the study of the stabilization of the flow from $Re = 4140$ to $Re = 7500$. Only considering the unstable modes in the ROM, it is shown that the flow can be stabilized from $Re_c = 4140$ to $Re \approx 5200$ (see figure 2.6(left)). This proves that even if

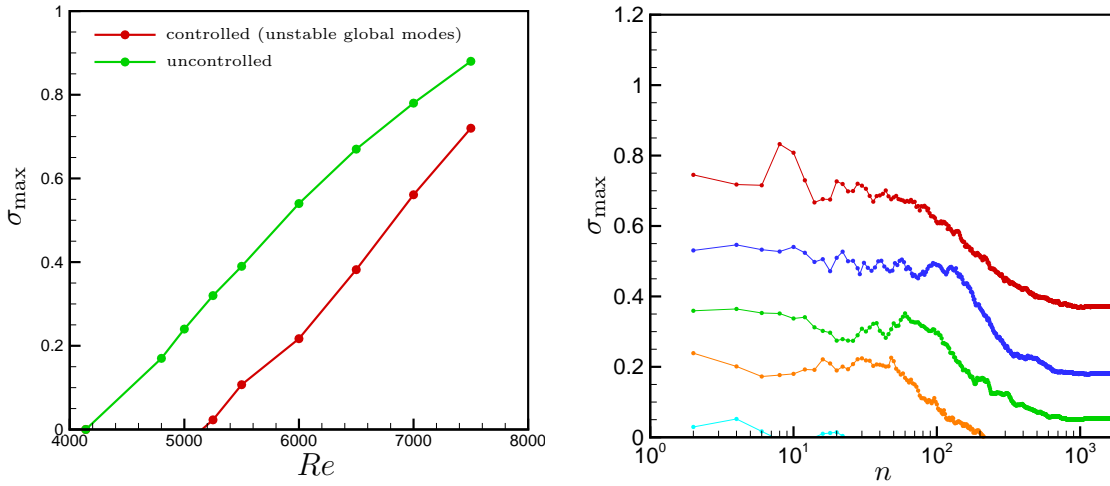


FIGURE 2.6 – left : growth rate σ_{max} of the least stable mode of the compensated system versus the Reynolds number. The ROM is only composed of unstable global modes. Right : growth rate σ_{max} of the least stable mode of the compensated system versus the number of stable global modes included in the ROM. The modes are ranked according to the criterion Γ . The different curves correspond from top to bottom to $Re=7500$, $Re=7000$, $Re=6500$, $Re=6000$ and $Re=5500$.

the ROM does not approximate the input-output dynamics correctly, the inherent robustness (stability margin) of the LQG compensator may be sufficient. When stable modes are added to the ROMs we found that the flow can be stabilized at even higher Re numbers. This has been investigated by computing the growth rate of the least stable mode of the compensated system for each ranking criterion and each Reynolds number. This quantity is shown in figure 2.6(right) for the criterion Γ . Each curve corresponds to a Reynolds number, as the Reynolds number increases the curves rise, showing the limit of stabilizability using this approach. To conclude, it may be stated that LQG compensators designed with a ROM based on global modes may stabilize unstable flows close to criticality due the inherent robustness of the compensator. This explains the successful results available in the literature. However, if the Reynolds number is further increased these ROMs are no longer appropriate to stabilize the flow.

2.3 Article 3

In this article, the feedback-control of a noise-amplifier flow is attempted using an LQG compensator based on a reduced-order model. We study the incompressible flow over a two-dimensional rounded backward-facing step (see figure 2.7). The Reynolds number based on the step height and the inflow velocity is $Re = 600$. For this Reynolds number the flow is globally stable and exhibits a noise-amplifier behavior which is triggered in our simulation by a noise source (body force on the vertical velocity B_1 in figure 2.7). To control these perturbations, an

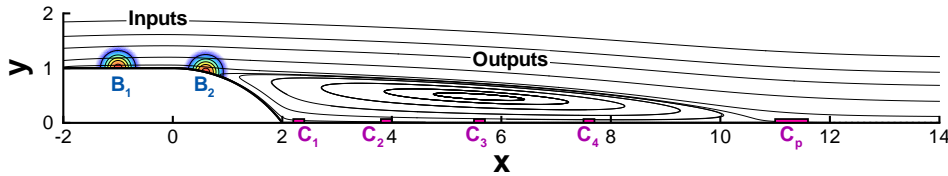


FIGURE 2.7 – Sketch of the geometry.

LQG control strategy is considered where the actuator B_2 is a body force on the vertical velocity and the sensor is a shear-stress measurement at the wall which will be chosen between C_1 , C_2 , C_3 and C_4 . Finally, a shear-stress measurement referred to as C_p in figure 2.7 is considered as the quantity to be minimized. In order to study the linear evolution of the perturbations, we consider the linearized Navier-Stokes equations which are discretized on a finite-element mesh. The final system may be written :

$$\mathbf{Q} \frac{d\mathbf{X}}{dt} = \mathbf{A}\mathbf{X} + \mathbf{Q}\mathbf{B}_1 w + \mathbf{Q}\mathbf{B}_2 u, \quad m = \mathbf{C}\mathbf{X} \quad (2.5)$$

\mathbf{X} is the state vector (longitudinal velocity, transversal velocity and pressure), the matrices \mathbf{Q} , \mathbf{A} , \mathbf{B}_1 , \mathbf{B}_2 and \mathbf{C} are respectively the weight matrix arising from the discretization, the linearized Navier-Stokes operator, the noise matrix, the control matrix, the measurement matrix; u , m and w are respectively the control law, the measurement and a random noise of variance W^2 . Finally, the LQG compensator is designed using a ROM based on 150 POD modes computed with a frequency-based snapshot method ([28]). The equation governing the ROM is :

$$\frac{d\hat{\mathbf{X}}}{dt} = \hat{\mathbf{A}}\hat{\mathbf{X}} + \hat{\mathbf{B}}_1 w + \hat{\mathbf{B}}_2 u, \quad m = \hat{\mathbf{C}}_i \hat{\mathbf{X}}. \quad (2.6)$$

The superscript $\hat{\cdot}$ refers to quantities of the ROM, the notations are similar to eq.(2.5).

Feedback control of globally stable flows has already been achieved, usually focusing on the reduced-order modeling techniques. In this article the main motivation is to give physical insight into the control's action on the flow. For that reason, the ROM considered is quite basic (although more advanced methods would have resulted in a smaller ROM). With the objective to get closer to experimental implementation, we have addressed four practical questions about LQG compensators in quasi-independent sections : how does the sensor location influence the estimation process, which quantity to minimize in the cost functional, what are the effects of shortcomings in the ROM on the performance of the controller and how well does a linear compensator stabilize a non-linear system.

The first part of this article is devoted to the estimation process, in particular to the placement of the sensor (the controller is turned off). It is shown that the estimation parameter in the Riccati equation corresponds to the noise-to-signal ratio of the sensor. Choosing a high value for this parameter simulates the case where the noise is large compared to the signal received by the sensor : the estimator is not capable of estimating the flow. On the contrary for lower values of this parameter, the signal is not corrupted by noise and the estimation is efficient. Since the system exhibits a convective instability, the perturbation is amplified during

its convection. It is therefore important to place the sensor downstream to reduce the noise-to-signal ratio which permits a better estimation. However, by studying the estimation of an impulse of noise, it is shown that an estimated state can only be computed if the perturbation is detected by the sensor. This is illustrated in figure 2.8 where the error of the estimation $\hat{\mathbf{Z}}$ (difference between the real state and the estimated state) is displayed for estimators based on $\hat{\mathbf{C}}_1$, $\hat{\mathbf{C}}_2$, $\hat{\mathbf{C}}_3$ and $\hat{\mathbf{C}}_4$ with respect to time. The error decreases only when the perturbation

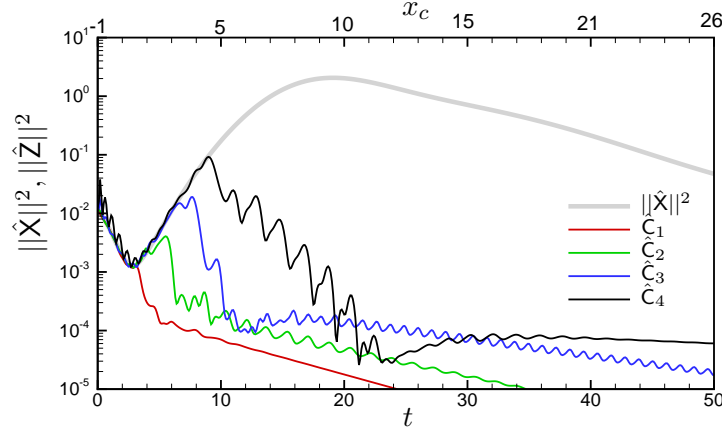


FIGURE 2.8 – Energy of the error vector $\|\hat{\mathbf{Z}}\|^2$ versus time color coded by the sensor considered, energy of the (uncontrolled) state $\|\hat{\mathbf{X}}\|^2$ (in gray).

reaches the sensor. The placement of the estimator must be chosen by considering a balance between the speed of estimation (location upstream) and a sufficiently low noise-to-signal ratio (location downstream).

In the second part of the article, the controller is turned on and the attention is given to the cost functional to be minimized. When the controller is designed to reduce the perturbations measured by sensor \mathbf{C}_p (as would be the case for ROMs obtained by system identification), we observe that, in the large gain limit, the total kinetic energy is increased (although the control objective is minimized). This has been further investigated and attributed to an extreme sensitivity of the compensator when designed close to the large gain limits which creates strong control actions at high frequencies. It is shown that this behavior can be suppressed by targeting the kinetic energy in the complete domain in the cost functional (which is not possible with ROMs obtained by system identification).

The third part of the article deals with the possibility of controlling a linear system, in our case the linearized Navier-Stokes equations, with a compensator designed using a slightly different model, in our case the ROM. This question is important since the loss of information arising from the order reduction implies that the original system and the ROM are inevitably different. It is found that the compensated system becomes unstable when the control parameter l and the estimation parameter G/W are chosen in the large gain limit. When the plant deviation increases, the unstable region grows and the range of usable parameters l and G/W is reduced such that the optimal control performances are not available anymore. The region of instability in the $(l, G/W)$ plane is displayed in figure 2.9. Considering a particular plant, we have designed a "perfect" compensator which has been used to control a modified version of the plant. The difference *err* between the original plant and the modified plant is evaluated using the relative \mathcal{H}_2 error. The different contour lines, separating unstable regions from stable regions, correspond to different values of *err*. We see that the unstable region grows as the difference between the original plant and the modified plant (*err*) increases. In addition, closed-loop control of the linearized Direct Numerical Simulation (DNS) have been performed for various values of l and W/G . The red square symbols (resp. green square symbols) denote unstable compensated simulations (resp. stable compensated simulations). Since the error between the

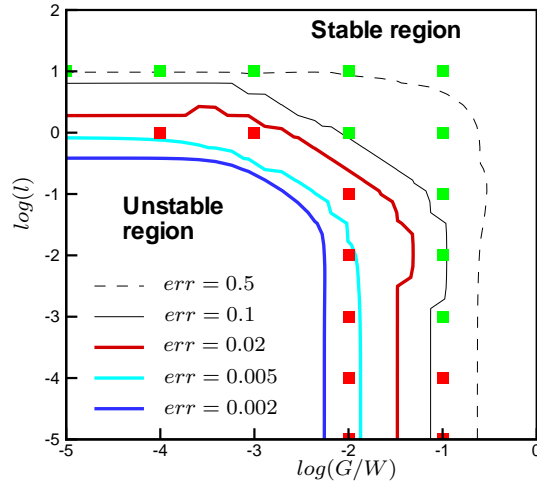


FIGURE 2.9 – Regions defining the unstable and stable compensated systems for different values of the error between the plant and the reduced-order model based on which the compensator is designed. The red squares (resp. green squares) represent the unstable (resp. stable) compensated LDNS.

original ROM (used for the compensator design) and the linearized DNS is $err = 0.02$, the previous results may be confirmed. Finally, one may remember that the more the ROM is different from the plant to be controlled, the larger the mismatch between the ROM and the compensated system, and the usable range of parameters l and G/W may be restricted.

The last part is devoted to the control of a non-linear DNS using a linear compensator. The forcing term is chosen to be a random noise and its variance is modified to simulate a quasi-linear, a weakly non-linear and a strongly non-linear development of the perturbations. We have found that when the perturbations are sufficiently weak to be comparable to the linear case the control is very efficient. If the perturbation is close to the linear solution before reaching the sensor used for estimation and becomes non-linear after the sensor, a rather good control effort is observed. When non-linear effects are visible upstream of the sensor used for estimation, the control is less efficient. The strongly non-linear simulation is illustrated in figure 2.10 where the kinetic energy of the perturbations as a function of time is displayed. The thick curves correspond to the non-linear simulations and the dashed curves to linear simulations. The random sequence is identical and non-linear effects are clearly visible. Finally for even stronger non-linearities, the compensated system may diverge. It is however interesting that the compensator has a positive action on the flow for a wide range of perturbation amplitudes.

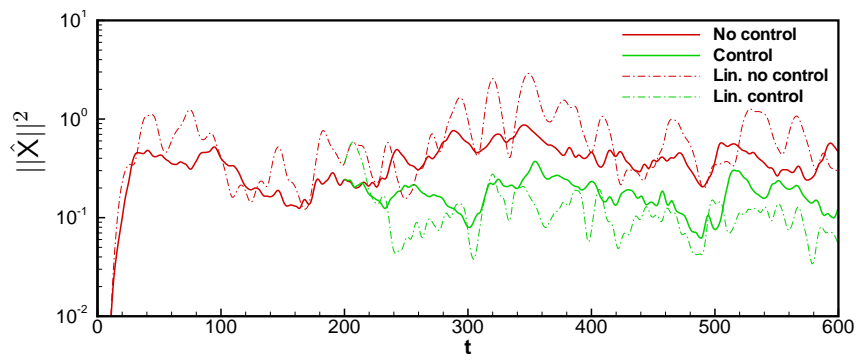


FIGURE 2.10 – Energy of the perturbations versus time. Thick curves : strongly non-linear simulations, dashed curves : linear simulations (same random sequence).

3 Conclusions and future work

This thesis is a contribution to model reduction and feedback control of low Reynolds number flows. Our focus has been on the stabilization of small amplitude perturbations which develop linearly on laminar base flows. Both categories of unsteady flow behavior have been considered : oscillator and noise-amplifier flows. To control these perturbations a Linear Quadratic Gaussian (LQG) control has been employed. The main advantages of this method are a rigorous mathematical description and the availability of theoretical results such as the existence of a stabilizing solution at any control cost for oscillator flows using a linear quadratic regulator (of course, under additional assumptions) or the reflection of the unstable eigenvalues into the stable half plane in the small gain limit. In addition, the optimal nature of this control strategy is appealing since it gives the best performance achievable (with respect to a particular cost functional). However, this method has also severe drawbacks, in particular, the necessity to solve two Riccati equations. Since these equations are not computationally tractable for common two- or three-dimensional discretizations. The compensator has to be designed using a reduced-order model (ROM) of the flow. In this thesis, we have concentrated on ROMs obtained by Petrov-Galerkin projection of the discretized equations onto a reduced set of modes. The three most popular projection bases, namely the global modes, the Proper Orthogonal Decomposition (POD) modes and the Balanced Proper Orthogonal Decomposition (BPOD) modes have been evaluated for their ability to produce a successful compensator.

3.1 Summary of the results

We start by reviewing the results obtained with ROMs based on global modes to control a globally unstable cavity flow. The starting point has been the computation of a large spectrum with more than 5000 eigenmodes. This spectrum has first been analyzed in detail : presentation of the spatial structure of the stable and unstable modes and location of the modes with respect to their energy distribution. In particular, we have observed modes located on the shear-layer which display vortical structures similar to Kelvin-Helmholtz vortices, modes located inside the cavity which represent the dynamics inside the cavity and modes pinned against the outflow boundary. The physical relevance of these latter modes is not obvious and this behavior has been linked to the convective non-normality of the flow over the cavity. Finally, the effect of increasing the Reynolds number was investigated for Reynolds numbers ranging from the critical Reynolds number (where the first pair of global modes becomes unstable) to higher Reynolds numbers (four pairs of unstable modes). It was observed that an unstable branch composed of modes located on the shear-layer emerges from the spectrum and moves into the unstable subspace. On the contrary the other branches, which are composed of cavity modes, move towards the unstable subspace without crossing the critical line.

Then, ROMs have been computed using a Petrov-Galerkin projection onto these global modes. While unstable modes are always included in the ROMs, various ranking criteria have been considered for selecting the stable modes to be included in the ROMs. By studying the stable part of this model in an open-loop configuration, we noticed that these ROMs were not able to accurately capture the input-output dynamics between the actuator and the sensor, no matter the ranking method considered or the number of stable modes included in the ROM.

In particular, it was observed that the inclusion of very damped modes in the ROM adversely influences the ROM. To explain this behavior we have derived a criterion which selects the modes which most significantly contribute to the input-output behavior of the model. These modes were found to be very damped modes. Further investigations showed that the non-normality of the global mode basis was responsible for this behavior. These results suggest that computing more global modes may only decrease the quality of the ROM. Finally, the ability to stabilize a linearized direct numerical simulation has been assessed from the critical Reynolds number $Re_c = 4140$ to $Re = 7500$ (Reynolds number based on the depth of the cavity and the inflow velocity). We found that if the instability is weak, i.e. the Reynolds number is sufficiently close to criticality ($Re < 5200$), the flow may be stabilized using only unstable global modes, although the input-output behavior of the original system is not correctly captured. This was attributed to the inherent robustness of the LQG compensators. When relevant stable global modes are included in the model, for example selected according to our input-output ranking criterion, the stabilization of the flow was obtained for even higher Reynolds numbers ($Re < 6500$). However, as the Reynolds number is further increased, these ROMs did not provide sufficiently robust controllers to stabilize the flow.

ROMs based on POD and BPOD modes have also been considered to model the stable part of the flow for designing LQG compensators to stabilize the globally unstable flow over a cavity. These modes are computed using snapshot methods. In this case, the unstable global modes are also included in the ROM to model the unstable subspace. Similarly to global modes, the ability of these models to capture the input-output dynamics between the actuator and the sensor of the original has been evaluated in an open-loop setting. It appeared that BPOD modes approximate very accurately the input-output behavior with very few modes (1% error with only 10 modes). Similar performances may be obtained using POD modes using a higher number of modes (1% error requires 100 modes). This result is expected since POD modes are by construction only optimal in extracting the energy content of the structures generated by the actuator. BPOD modes are, on the contrary, optimal in capturing the structures created by the actuator *and* measured by the sensor, which is exactly the definition of the input-output dynamics. In order to emphasize this point, a comparison of POD and BPOD bases has been conducted, which proved the higher observability of the BPOD modes. Even though ROMs based on POD and BPOD modes should theoretically be stable, which was not always the case for models based on BPOD. As a result, ROMs based on POD modes seem more robust.

LQG compensators based on the unstable global modes (to model the unstable subspace) and POD or BPOD modes have been computed and used to stabilize the unstable cavity flow at $Re = 7500$ (where compensators only based on global modes failed). Similarly to their open-loop performances, ROMs based on BPOD stabilized the flow with only 7 modes (provided the ROM is stable) and POD stabilized the flow when more than 27 modes are considered. In addition, we noticed that both models converge to an optimal solution referred to as the "best control strategy" when the order of the system increases. We found that this solution corresponds to the (artificial) case where the measurement fed to the estimator is previously modified such that the part which is not captured by the model is removed. In other words, this proves that the optimal solution is obtained when the ROM captures "exactly" the input-output behavior of the original system.

The control of noise amplifier flows is rather different from the control of oscillator flows even though the control strategy is similar. In addition, studies concerned with the stabilization of globally stable flows using ROMs based on POD or BPOD modes are already available in the literature. For this reason, our study is designed to complement previous studies as far as practical implementation of such control techniques in experiments is concerned. In this view, the behavior of the estimator is first considered without control, in particular the position of the sensor is assessed. Since the perturbation is amplified during its convection, a sensor located too far upstream may not differentiate the perturbation signal from the inherent noise, resulting in

a bad estimation. Even though the sensor needs to be placed sufficiently upstream such that the detected perturbation is still controllable, i.e. in the control area of the actuator. In other words, the placement of the sensor is a subtle balance between the speed of estimation and the noise-to-signal ratio of the sensor. By studying the compensated system, we have observed that, as the cost functional minimized by the controller targets the measurement's energy at a particular location of the system, the compensator can become unstable (when designed close to the large gain limit) and generates large energetic structures at other locations of the flow. It is shown that this behavior can be suppressed by minimizing the kinetic energy in the complete domain in the cost functional. When the compensator designed using a ROM is used to control a linearized Direct Numerical Simulation (DNS), the discrepancy between the ROM and the linearized DNS may alter the control's efficiency. It is shown that this discrepancy may actually lead to an unstable compensated system; in this case, the region of instability is proportional to the error between the ROM and the linearized DNS. Finally, linear compensators have been considered for the control of non-linear simulations subject to random forcing. It is shown that as the amplitude of the forcing term increases, the non-linear effects are more visible and the compensator's action is less efficient. As the non-linearities become too strong, the compensated system may even become unstable and converge.

3.2 Future work

Even if considerable care has been taken to remain close to physical experiments, a direct implementation of the control techniques developed in this thesis in an experimental setting would be premature.

So far, the application of optimal control to fluid dynamics has deliberately been considered for idealized configurations in order to master the design process, to understand the physical mechanisms at play and to optimize the control schemes. Along this line, theoretical tools such as adjoint simulations (for the computation of BPOD modes) have been adopted. Given a direct operator, the associated adjoint operator is a mathematical concept which can easily be obtained theoretically and numerically, but which does not have an experimental counterpart. This implies that BPOD modes, unlike POD modes, cannot be obtained from experimental data. A recent suggestion to dispense with adjoints during the model reduction process has recently been reported in [65] where it has been shown that the same ROM obtained by Galerkin projection onto BPOD modes may be obtained using only data from the direct simulation. The algorithm considered in [65] belongs to the class of system identification methods. As suggested below, ROMs obtained by system identification may be more easily applied in practical applications.

Projection methods are generally difficult to handle since they require the computation of a projection basis which often requires the solution of large eigenvalue problems. Whatever the approach considered (computational or experimental), the ROM represents the dynamics of the data on which it has been designed. If the purpose of the ROM is to accurately capture various flow situations, the required amount of data for the ROM design will increase drastically. For that reason, projection techniques may only accurately represent one or a few particular flow situations; in other words, they are particularly suited to control engineering systems with a unique or very few operating regimes. To probe the off-design performance of a ROM obtained by a projection technique, we have used our best compensator for the cavity flow, designed at $Re = 7500$, to control linearized simulations at lower and higher Reynolds numbers. These simulations could only be stabilized in the neighborhood of the design conditions. These preliminary tests demonstrate that a rather accurate ROM is required for a successful control application.

Considering the flow over an airplane, the conditions at take-off and landing are entirely different from cruise conditions. In this case, it is unlikely that ROMs based on projection techniques will be able to cope with such different flow situations.

We believe that for a wide range of operating conditions only a ROM which can be adjusted in real time can be expected to succeed. ROMs designed with system identification techniques offer this possibility. One could imagine a control scheme composed of two separate components. The first component is the same compensator as studied in this work and described in figure 1.5; the second component takes as input the measurement and control law and computes (in real time) an updated ROM. As soon as the estimated state from the ROM used in the compensator deviates too strongly from the real state, the ROM is updated in the compensator (along with updated control and Kalman gains). This idea may be related to the "trust-region" concept considered in [15]. If the model is updated repeatedly, it is even conceivable to construct a simple linear model to reproduce the non-linear dynamics of the flow.

In our approach, we have designed a linear compensator to control a linear flow (the Navier-Stokes equations linearized about a particular base flow). This is certainly justifiable. When this compensator is used to control the non-linear development of the perturbations, under best conditions the performance of the compensator is reduced, under worst conditions the compensated system becomes unstable. Preliminary tests of closed-loop control of a non-linear cavity flow simulation at $Re = 7500$ with the linear compensator which stabilizes the linear flow have always resulted in an unstable system as soon as (and sometimes before) non-linear effects were observable. Even though the obvious solution is to convert to non-linear ROMs along with non-linear control and estimation techniques (generalized Kalman filter, for example), a first attempt and convenient way to bypass the difficulties arising from a non-linear control technique is to adhere to a linear representation of the non-linear dynamics. Note that this model is different from the linear model which simulates the linear dynamics of the flow. As mentioned before, such models can be computed easily by system identification. Since a linear ROM is unlikely to represent the changes of the non-linear dynamics with respect to a parameter change (Reynolds number for example), a real-time adjustment of the ROM may be necessary. If this simple solution of treating the non-linear case does not succeed, non-linear control techniques may become inevitable.

In order to apply flow control techniques to "real" situations, the robustness of the compensator is a major issue. Similar to the investigation of the plant deviation from the ROM, studies about shortcomings in the modeling of the actuator, the sensor and the noise should be undertaken. These studies can simply be carried out by artificially perturbing the control law, the measurement, the noise function and the location of the actuator, sensor and noise. If the LQG compensator is not robust with respect to changes in these parameters, it will be necessary to consider more robust control techniques such as the \mathcal{H}_∞ control or the Transfer Loop Recovery (LTR). Finally, using these techniques, it should be possible to incorporate in numerical simulations some practical informations taken from experiments : for example, turbulence levels, noise-to-signal ratios of sensors, and time delays from the data acquisition and processing. A low-cost investigation of important parameters such as the location of the sensors and actuators may be achieved and directly transferred to experiments.

To conclude this outlook towards "applied research" directions, we would like to mention that a promising way to control low-frequency unsteadiness at high Reynolds numbers is to consider the Unsteady Reynolds-Average Navier-Stokes (URANS) equations.

Finally, a more theoretical direction, where the control's action is taken into account in the design of the ROM, deserves further investigations. Following the idea that the control triggers only a selected range of frequencies (i.e., the idea underlying the frequency-restricted \mathcal{H}_2 norm), the POD and BPOD modes may be computed to capture, respectively, the energy and the input-output dynamics corresponding to this frequency range. This may be obtained by defining the Gramians in frequency-space ([28]) and restricting the frequency range of the resulting integral. An attractive feature of this formulation is the possibility to capture both the unstable and stable parts of the flow. If the snapshots are computed in the time domain, it can be shown that frequency-restricted snapshots may be computed by using a simulation

where the control law is the inverse Fourier-transform of a gate function (or rectangle function) defined over the frequencies of interest. Based on these snapshots, the remaining computation of the modes is similar to the classical snapshot method. Preliminary results using such frequency-restricted ROMs exhibit significant improvements over standard ROMs.

References

- [1] AHUJA, S., AND ROWLEY, C. W. Feedback control of unstable steady states of flow past a flat plate using reduced-order estimators. *J. Fluid Mech.* 645 (2007), 447–478.
- [2] AIDER, J.-L. Contrôle d'écoulement décollé et aérodynamique automobile. *Mémoire d'habilitation à diriger des recherches* (2008).
- [3] ÅKERVIK, E., EHRENSTEIN, U., GALLAIRE, F., AND HENNINGSON, D. S. Global two-dimensional stability measures of the flat plate boundary-layer flow. *Eur. J. Mech. B/Fluids* 27 (2008), 501–513.
- [4] ÅKERVIK, E., HÖPFFNER, J., EHRENSTEIN, U., AND HENNINGSON, D. S. Optimal growth, model reduction and control in a separated boundary-layer flow using global modes. *J. Fluid Mech.* 579 (2007), 305–314.
- [5] ALIZARD, F., AND ROBINET, J.-C. Modeling of optimal perturbations in flat plate boundary layer using global modes : benefits and limits. *Theor. Comput. Fluid Dyn. in press* (2010).
- [6] ANTOULAS, A. C. *Approximation of Large-Scale Dynamical Systems*. SIAM Publishing, 2005.
- [7] AUBRY, N., HOLMES, P., LUMLEY, J., AND STONE, E. The dynamics of coherent structures in the wall region of a turbulent boundary layer. *J. Fluid Mech.* 192 (1988), 115–174.
- [8] BAGHERI, S., BRANDT, L., AND HENNINGSON, D. S. Input-output analysis, model reduction and control of the flat-plate boundary layer. *J. Fluid Mech.* 620 (2009), 263–298.
- [9] BAGHERI, S., HÖPFFNER, J., SCHMID, P. J., AND HENNINGSON, D. S. Input-output analysis and control design applied to a linear model of spatially developing flows. *Appl. Mech. Rev.* 62 (2009), 020803.
- [10] BAGHERI, S., SCHLATTER, P., SCHMID, P. J., AND HENNINGSON, D. S. Global stability of a jet in crossflow. *J. Fluid Mech.* 624 (2009), 33–4.
- [11] BARBAGALLO, A., SIPP, D., AND SCHMID, P. J. Closed-loop control of an open cavity flow using reduced-order models. *J. Fluid Mech.* 641 (2009), 1–50.
- [12] BARKLEY, D., GOMES, M. G., AND HENDERSON, R. D. Three-dimensional instability in flow over a backward-facing step. *J. Fluid Mech.* 473 (2002), 167–190.
- [13] BASLEY, J., PASTUR, L. R., LUSSEYRAN, F., FAURE, T. M., AND DELPRAT, N. Experimental investigation of global structures in an incompressible cavity flow using time-resolved piv. *Exp. Fluids* (2010).
- [14] BEAUDOIN, J.-F., CADOT, O., AIDER, J.-L., AND WESFREID, J. E. Three-dimensional stationary flow over a backward-facing step. *Eur. J. Mech. B/Fluids* 23 (2003), 147–155.
- [15] BERGMANN, M., AND CORDIER, L. Optimal control of the cylinder wake in the laminar regime by trust-region methods and pod reduced-order models. *J. Comp. Phys.* 227 (2008), 7813–7840.
- [16] BERGMANN, M., CORDIER, L., AND BRANCHER, J.-P. Optimal rotary control of the cylinder wake using POD reduced-order model. *Phys. Fluids* 17 (2005), 305–314.

- [17] BEWLEY, T. R. Flow control : new challenges for a new renaissance. *Progr. Aerosp. Sci.* 37 (2001), 21–58.
- [18] BEWLEY, T. R., AND LIU, S. Optimal and robust control and estimation of linear paths to transition. *J. Fluid Mech.* 365 (1998), 305–349.
- [19] BLACKBURN, H. M., BARKLEY, D., AND SHERWIN, S. J. Convective instability and transient growth in flow over a backward-facing step. *J. Fluid Mech.* 603 (2008), 271–304.
- [20] BRES, G. A., AND COLONIUS, T. Three-dimensional instabilities in compressible flow over open cavities. *J. Fluid Mech.* 599 (2008), 309–339.
- [21] BURL, J. B. *Linear optimal control. \mathcal{H}_2 and \mathcal{H}_∞ methods*. Addison-Wesley, 1999.
- [22] CHEN, K. K., AND ROWLEY, C. W. H_2 optimal actuator and sensor placement in the linearised complex ginzburg-landau system. *subm. to J. Fluid Mech.* (2010).
- [23] CHEVALIER, M., HÖPFFNER, J., ÅKERVIK, E., AND HENNINGSON, D. Linear feedback control and estimation applied to instabilities in spatially developing boundary layers. *J. Fluid Mech.* 588 (2007), 163–187.
- [24] CHOI, H., JEON, W.-P., AND KIM, J. Control of flow over a bluff body. *Ann. Rev. Fluid Mech.* 40 (2008), 113–139.
- [25] CHOMAZ, J.-M. Global stabilities in spatially developing flows : non-normality and non-linearity. *Ann. Rev. Fluid Mech.* 37 (2005), 357–392.
- [26] COSSU, C., AND CHOMAZ, J. M. Global measures of local convective instabilities. *Phys. Rev. Lett.* 78 (1997), 4387–4390.
- [27] CROUCH, J., GARBARUK, A., AND MAGIDOV, D. Predicting the onset of flow unsteadiness based on global instability. *J. Comp. Phys.* 224 (2007), 924–940.
- [28] DERGHAM, G., SIPP, D., ROBINET, J., AND BARBAGALLO, A. Model reduction for fluids using frequential snapshots. *subm. to Phys. Fluids* (2010).
- [29] DURIEZ, T. Application des générateurs de vortex au contrôle d’écoulements décollés (vortex generator application to separated flows control). *PhD Thesis* (2009).
- [30] EHRENSTEIN, U., AND GALLAIRE, F. On two-dimensional temporal modes in spatially evolving open flows : the flat plate boundary layer. *J. Fluid Mech.* 536 (2005), 209–218.
- [31] EHRENSTEIN, U., AND GALLAIRE, F. Optimal perturbations and low-frequency oscillations in a separated boundary-layer flow. *AIAA paper 2008-4232, 5th AIAA Theoretical Fluid Mechanics Conference* (2008).
- [32] EHRENSTEIN, U., AND GALLAIRE, F. Two-dimensional global low-frequency oscillations in a separating boundary-layer flow. *J. Fluid Mech.* 614 (2008), 315–327.
- [33] EHRENSTEIN, U., PASSAGGIA, P.-Y., AND GALLAIRE, F. Control of a separated boundary layer : reduced-order modeling using global modes revisited. *Theor. Comput. Fluid Dyn. in press* (2010).
- [34] FARRELL, B. F., AND IOANNOU, P. J. Accurate low-dimensional approximation of the linear dynamics of fluid flow. *Journal of the Atmospheric Sciences* 58 (2001), 2771–2789.
- [35] FAURE, T. M., ADRIANOS, P., LUSSEYRAN, F., AND PASTUR, L. Visualizations of the flow inside an open cavity at medium-range reynolds numbers. *Exp. Fluids* 42 (2007), 169–184.
- [36] GALLAIRE, F., MARQUILLIE, M., AND EHRENSTEIN, U. Three-dimensional transverse instabilities in detached boundary layers. *J. Fluid Mech.* 571 (2007), 221–233.
- [37] GALLETTI, B., BOTTARO, A., BRUNEAU, C., AND IOLLO, A. Accurate model reduction of transient and forced wakes. *Eur. J. Mech. B* 26 (2007), 354–366.
- [38] GALLETTI, B., BRUNEAU, C., ZANNETTI, L., AND IOLLO, A. Low-order modelling of laminar flow regimes past a confined square cylinder. *J. Fluid Mech.* 503 (2004), 161–170.

- [39] GARDARIN, B. Contrôle par générateur de vortex d'un écoulement turbulent décollé. *PhD Thesis* (2009).
- [40] GHARIB, M., AND ROSHKO, A. The effect of flow oscillations on cavity drag. *J. Fluid Mech.* 177 (1987), 501–530.
- [41] GIANNETTI, F., AND LUCHINI, P. Structural sensitivity of the first instability of the cylinder wake. *J. Fluid Mech.* 581 (2007), 167–197.
- [42] GREENBLATT, D., AND WYGNANSKI, I. The control of separation by periodic excitation. *Progr. Aerosp. Sci.* 36 (2000), 487–545.
- [43] HÖGBERG, M., BEWLEY, T., AND HENNINGSON, D. Linear feedback control and estimation of transition in plane channel flow. *J. Fluid Mech.* 481 (2003), 149–175.
- [44] HÖGBERG, M., AND HENNINGSON, D. Linear optimal control applied to instabilities in spatially developing boundary layers. *J. Fluid Mech.* 470 (2002), 151–179.
- [45] HUANG, S.-C., AND KIM, J. Control and system identification of a separated flow. *Phys. Fluids* 20 (2008), 101509.
- [46] HUERRE, P., AND ROSSI, M. Hydrodynamic instabilities in open flows. In *Hydrodynamics and Nonlinear Instabilities*. Cambridge University Press, Cambridge, 1998, pp. 81–294.
- [47] ILAK, M. Model reduction and feedback control of transitional channel flow. *PhD Thesis* (2009).
- [48] ILAK, M., AND ROWLEY, C. Modeling of transitional channel flow using balanced proper orthogonal decomposition. *Phys. Fluids* 20 (2008), 034103.
- [49] ILLINGWORTH, S. J. Feedback control of oscillations in combustion and cavity flows. *PhD Thesis* (2009).
- [50] ILLY, H., JACQUIN, L., AND GEFFROY, P. Observations on the passive control of flow oscillations over a cavity in a transonic regime by means of a spanwise cylinder. *4th AIAA Flow Control Conference 2008-3774* (2008).
- [51] JACKSON, C. P. A finite-element study of the onset of vortex shedding in flow past variously shaped bodies. *J. Fluid Mech.* 182 (1987), 23–45.
- [52] JACQUIN, L., MOLTON, P., DECK, S., MAURY, B., AND SOULEVANT, D. Experimental study of shock oscillation over a transonic supercritical profile. *AIAA J.* 47 (2009), 1985–1994.
- [53] JOSHI, S., SPEYER, J., AND KIM, J. A systems theory approach to the feedback stabilization of infinitesimal and finite-amplitude disturbances in plane Poiseuille flow. *J. Fluid Mech.* 332 (1997), 157–184.
- [54] JOSLIN, R. D. Aircraft laminar flow control. *Ann. Rev. Fluid Mech.* 30 (1998), 1–29.
- [55] KIM, J., AND BEWLEY, T. A linear systems approach to flow control. *Ann. Rev. Fluid Mech.* 39 (2007), 383–417.
- [56] LAUGA, E., AND BEWLEY, T. Modern control of linear global instability in a cylinder wake model. *Int. J. Heat and Fluid Flow* 23 (2002), 671–677.
- [57] LAUGA, E., AND BEWLEY, T. The decay of stabilizability with Reynolds number in a linear model of spatially developing flows. *Proc. R. Soc. Lond. A* 459 (2003), 2077–2095.
- [58] LAUGA, E., AND BEWLEY, T. Performance of a linear robust control strategy on a nonlinear model of spatially developing flows. *J. Fluid Mech.* 512 (2004), 343–374.
- [59] LEE, C., KIM, J., AND CHOI, H. Suboptimal control of turbulent channel flow for drag reduction. *J. Fluid Mech.* 358 (1998), 245–258.
- [60] LIM, J., AND KIM, J. A singular value analysis of boundary layer control. *Phys. Fluids* 16, 6 (2004), 1980–1988.
- [61] LJUNG, L. *System identification*. 2nd ed. Prentice Hall, 1999.

- [62] LUCHTENBURG, D. M., GÜNTHER, B., NOACK, B. R., KING, R., AND TADMOR, G. A generalized mean-field model of the natural and high-frequency actuated flow around a high-lift configuration. *J. Fluid Mech.* 623 (2009), 283–316.
- [63] LUMLEY, J. L. *Stochastic Tools in Turbulence*. Academic Press, 1970.
- [64] MA, X., AND KARNIADAKIS, G. E. A low-dimensional model for simulating three-dimensional cylinder flow. *J. Fluid Mech.* 458 (2002), 181–190.
- [65] MA, Z., AHUJA, S., AND ROWLEY, C. W. Reduced-order models for control of fluids using the eigensystem realization algorithm. *Theor. Comput. Fluid Dyn.* 611 (2010), 205–214.
- [66] MACK, C. J., AND SCHMID, P. J. Global stability of swept flow around a parabolic body : features of the global spectrum. *J. Fluid Mech.* in press (2011).
- [67] MACK, C. J., SCHMID, P. J., AND SESTERHENN, J. L. Global stability of swept flow around a parabolic body : connecting attachment-line and crossflow modes. *J. Fluid Mech.* 611 (2008), 205–214.
- [68] MARQUET, O., SIPP, D., CHOMAZ, J.-M., AND JACQUIN, L. Amplifier and resonator dynamics of a low-Reynolds number recirculation bubble in a global framework. *J. Fluid Mech.* 605 (2008), 429–443.
- [69] MARQUET, O., SIPP, D., AND JACQUIN, L. Sensitivity analysis and passive control of cylinder flow. *J. Fluid Mech.* 615 (2008), 221–252.
- [70] MIN, C., AND CHOI, H. Suboptimal feedback control of vortex shedding at low reynolds numbers. *J. Fluid Mech.* 401 (1999), 123–156.
- [71] MOORE, B. Principal component analysis in linear systems : controllability, observability, and model reduction. *IEEE Trans. Autom. Contr.* 26 (1981), 17–32.
- [72] NOACK, B., AFANASIEV, K., MORZYNSKI, M., TADMOR, G., AND THIELE, F. A hierarchy of low-dimensional models for the transient and post-transient cylinder wake. *J. Fluid Mech.* 497 (2003), 335–363.
- [73] NOACK, B., AND ECKELMANN, H. A global stability analysis of the steady and periodic cylinder wake. *J. Fluid Mech.* 270 (1994), 297–330.
- [74] NOACK, B., PAPAS, P., AND MONKEWITZ, P. A. The need for a pressure-term representation in empirical galerkin models of incompressible shear flows. *J. Fluid Mech.* 523 (2005), 339–365.
- [75] PERRY, A., AND LIM, T. Coherent structures in coflowing jets and wakes. *J. Fluid Mech.* 88 (1978), 243–256.
- [76] PODVIN, B., AND LUMLEY, J. A low-dimensional approach for the minimal flow unit. *J. Fluid Mech.* 362 (1998), 121–155.
- [77] PUJALS, G., DEPARDON, S., AND COSSU, C. Drag reduction of a 3d bluff body using coherent streamwise streaks. *Exp. Fluids* 49 (2010), 1085–1094.
- [78] ROCKWELL, D., AND NAUDASCHER, E. Review - self-sustaining oscillations of flow past cavities. *Trans. ASME I : J. Fluid Engng* 100 (1978), 152–165.
- [79] ROSSITER, J. Wind-tunnel experiments on the flow over rectangular cavities at subsonic and transonic speeds. Tech. rep., Aeronautical Research Council Reports and Memorandum num 3438, 1964.
- [80] ROWLEY, C. Model reduction for fluids using balanced proper orthogonal decomposition. *Int. J. Bifurc. Chaos* 15 (2005), 997–1013.
- [81] ROWLEY, C., AND WILLIAMS, D. Dynamics and control of high-Reynolds number flow over open cavities. *Ann. Rev. Fluid Mech.* 38 (2006), 251–276.

-
- [82] ROWLEY, C. W., WILLIAMS, D. R., COLONIUS, T., MURRAY, R. M., AND MACMYNOWSKI, D. G. Linear models for control of cavity flow oscillations. *J. Fluid Mech.* 547 (2006), 317–330.
- [83] SAMIMY, M., DEBIASI, M., CARABALLO, E., SERRANI, A., YUAN, X., LITTLE, J., AND MYATT, J. Feedback control of subsonic cavity flows using reduced-order models. *J. Fluid Mech.* 579 (2007), 315–346.
- [84] SIPP, D., AND LEBEDEV, A. Global stability of base and mean flows : a general approach and its applications to cylinder and open cavity flows. *J. Fluid Mech.* 593 (2007), 333–358.
- [85] SIPP, D., MARQUET, O., MELIGA, P., AND BARBAGALLO, A. Dynamics and control of global instabilities in open flows : a linearized approach. *Appl. Mech. Rev.* 63 (2010), 030801–1–030801–26.
- [86] SIRISUP, S., AND KARNIADAKIS, G. E. A spectral viscosity method for correcting the long-term behavior of pod models. *J. Comp. Phys.* 194 (2004), 92–116.
- [87] SIROVICH, L. Turbulence and the dynamics of coherent structures. *Quart. Appl. Math.* 45 (1987), 561–590.
- [88] STRYKOWSKI, P. J., AND SREENIVASAN, K. R. On the formation and suppression of vortex "shedding" at low reynolds numbers. *J. Fluid Mech.* 218 (1990), 71–107.
- [89] THEOFILIS, V. Advances in global linear instability analysis of nonparallel and three-dimensional flows. *Prog. Aerosp. Sci.* 39 (2000), 249–315.
- [90] WELLER, J., CAMARRI, S., AND IOLLO, A. Feedback control by low-order modelling of the laminar flow past a bluff body. *J. Fluid Mech.* 634 (2009), 405–418.
- [91] WELLER, J., LOMBARDI, E., AND IOLLO, A. Robust model identification of actuated vortex wakes. *Physica D* 238 (2009), 416–427.
- [92] WILLCOX, K., AND PERAIRE, J. Balanced model reduction via proper orthogonal decomposition. *AIAA J.* 40 (2002), 2323–2330.
- [93] ZHOU, K., SALOMON, G., AND WU, E. *Robust and Optimal Control*. Prentice Hall, New Jersey, 2002.

Deuxième partie

Articles

4 Article 1

Closed-loop control of an open cavity flow using reduced-order models

Closed-loop control of an open cavity flow using reduced-order models

ALEXANDRE BARBAGALLO^{1,2},
DENIS SIPP¹ AND PETER J. SCHMID^{2†}

¹ONERA-DAFE, 8 rue des Vertugadins, 92190 Meudon, France

²Laboratoire d'Hydrodynamique (LadHyX), CNRS-Ecole Polytechnique, 91128 Palaiseau, France

(Received 30 October 2008; revised 23 July 2009; accepted 24 July 2009; first published online
30 November 2009)

The control of separated fluid flow by reduced-order models is studied using the two-dimensional incompressible flow over an open square cavity at Reynolds numbers where instabilities are present. Actuation and measurement locations are taken on the upstream and downstream edge of the cavity. A bi-orthogonal projection is introduced to arrive at reduced-order models for the compensated problem. Global modes, proper orthogonal decomposition (POD) modes and balanced modes are used as expansion bases for the model reduction. The open-loop behaviour of the full and the reduced systems is analysed by comparing the respective transfer functions. This analysis shows that global modes are inadequate to sufficiently represent the input–output behaviour whereas POD and balanced modes are capable of properly approximating the exact transfer function. Balanced modes are far more efficient in this process, but POD modes show superior robustness. The performance of the closed-loop system corroborates this finding: while reduced-order models based on POD are able to render the compensated system stable, balanced modes accomplish the same with far fewer degrees of freedom.

Key words: flow control, instability

1. Introduction

Regions of separated fluid flow are a common feature of a great majority of realistic configurations. High-Reynolds-number flow about blunt bodies, airfoils during moderate and high angles of attack, curved engine inlets or engine nozzles or any occurrence of shock-boundary layer interactions are only a few examples where adverse pressure gradients or adverse geometries cause the flow to detach from the wall. Finite regions of separated flow commonly exhibit Kelvin–Helmholtz type instabilities that manifest themselves in an unsteady flow behaviour in the wake of the separation bubble. This behaviour, in turn, negatively affects the mean flow as well as the perturbation dynamics further downstream as it imprints a specific frequency on the subsequent flow. It is thus of great fundamental and technological interest to describe the dynamics of separated flows and design means to suppress its formation or – if separation is inevitable or prohibitively costly – to weaken its unsteadiness.

Because of its inherent complexity and marked sensitivity to specific flow and geometric conditions, results on the dynamics of separated flows are challenging to

† Email address for correspondence: peter@ladhyx.polytechnique.fr

generalize. For this reason, one particular prototypical configuration that captures the dominant features of separated flows has received a great deal of attention and has acted as a proxy for a wide range of more complicated situations: the flow over an open cavity. Even though the majority of these studies has concentrated on the compressible flow over a cavity, in particular the generation of acoustic waves (e.g. Cattafesta *et al.* 2003; Rowley & Williams 2006; Bres & Colonius 2008; Cattafesta *et al.* 2008), we will focus on the incompressible flow over a square cavity. This type of flow exhibits a recirculating component (confined geometrically to the cavity) as well as a strong shear layer that forms at the top of the cavity and, for sufficiently high Reynolds number, becomes unstable and settles into a characteristic periodic motion (see Sipp & Lebedev 2007). Experimental investigations on an equivalent three-dimensional configuration have been carried by Faure *et al.* (2007) emphasizing the three-dimensional development of the flow. An analysis of the dynamic behaviour for an open-cavity flow by traditional means is complicated by the complex geometry and, consequently, the lack of an easily available base flow profile. Rather, a global approach, both for the base flow and the perturbation dynamics, has to be employed in order to assess and quantify the stability characteristics of this type of flow.

The stability analysis of flows with more than one inhomogeneous coordinate direction has been first pursued by Zebib (1987) and Jackson (1987) who studied the stability characteristics of flow past a cylinder and other blunt bodies. These early studies were soon followed by investigations into the perturbation dynamics in cylinder wakes (e.g. Noack & Eckelmann 1994; Zielinska & Wesfreid 1995) using similar means. Since then, the concept of global stability analysis has made significant progress and gained in popularity due to the advent of iterative eigenvalue routines (such as the Arnoldi method; see Lehoucq & Scott 1997; Lehoucq, Sorensen & Yang 1998) that, coupled with flow solvers, provide efficient techniques to extract relevant stability information from simulations of the flow under consideration. This coupling of iterative methods with numerical simulations allows the quantitative description of the disturbance behaviour of any flow that can be simulated with a sufficient degree of fidelity. Among the many stability studies of separated flows we mention Ding & Kawahara (1999) who studied flow in the wake of a cylinder, Barkley, Gomes & Henderson (2002) who analysed flow over a backward-facing step and Ehrenstein & Gallaire (2005, 2008) who treated the separated flow over a smooth bump as a global stability problem. Even the stability of more application-oriented geometries has recently been treated from a global perspective (e.g. Crouch, Garbaruk & Magidov 2007 analysing the onset of transonic shock-buffeting; see Theofilis 2000 for a review of global stability analysis in aeronautical applications). In each case, the extracted global spectrum then represents the inherent dynamic behaviour of the fluid system (given by growth rates, phase velocities, transient growth potential, receptivity behaviour and their dependence on the governing parameters). Even the extraction of non-modal behaviour, such as optimal transient growth, has been accomplished by direct numerical simulations (DNS) feeding flow-field data into a direct-adjoint optimization algorithm (see Blackburn, Barkley & Sherwin 2008 for an application to the flow over a backward-facing step, and Marquet *et al.* 2008 for flow in a curved channel). This type of analysis produces unprecedented stability information about complex flows and forms an important and imperative first step in the more challenging undertaking of manipulating the flow into a more desirable state or into a more acceptable dynamic behaviour.

Over the past years the control of fluid flow has come to prominence as a new and promising subject that combines our understanding of the dynamics of a fluid system with techniques to manipulate it (Bewley 2001; Kim 2003; Kim & Bewley 2007).

Remarkable progress has been made on generic configurations including full-state information control of turbulent channel flow (Moin & Bewley 1994; Joshi, Speyer & Kim 1997), partial-state information control of transitional channel flow (Högberg, Bewley & Henningson 2003), estimation in wall-bounded shear flows (Høpfner *et al.* 2005) and control of spatially growing boundary layers (Chevalier *et al.* 2007). The techniques applied in these situations have greatly relied on a mathematical framework established in control theory as described in standard references (e.g. Burl 1999; Zhou, Salomon & Wu 2002), but additional complications had to be overcome when adapting them to fluid flows. Under even slightly more realistic circumstances, however, severe limitations due to the sheer size of the involved matrix equations have been encountered. It has thus been quickly realized that the application of approximate and iterative algorithms (as reviewed, for example, in Bai 2002 and Freund 2003), as well as the *a priori* reduction of the number of degrees of freedom (see e.g. Antoulas, Sorensen & Gugercin 2001), are crucial techniques when attempting the control design for even moderately complex flows. Mathematically, model reduction can be described as a projection method based on a hierarchical (generally) bi-orthogonal expansion basis, and these techniques are now commonly applied to reduce a linear (or nonlinear) system. It is important to realize, however, that the choice of these fluid structures must be tailored to the application in mind; ignoring this fact can yield to suboptimal results at best, to ineffective control strategies at worst.

Global modes, i.e. the eigenvectors of the global stability problem, are often considered as the representation of the system's linear dynamics. The expression of this dynamics by a linear combination of global modes, hierarchically ordered by their decay rate, can yield a reduced model that accurately describes the inherent linear dynamics of the full system. As soon as forcing (representing either an external disturbance environment or control input) is applied or measurements are extracted from the system, the global mode expansion may no longer be appropriate for capturing the modified dynamics. This behaviour has been observed by Lauga & Bewley (2003, 2004) where the fluid system has been replaced by the complex Ginzburg–Landau (cGL) equation and global modes have been used to reduce the system. The loss of stabilizability using global modes has then been linked to the domain of support of the adjoint global modes. An expansion of a larger-scale fluid system into global modes has been taken by Åkervik *et al.* (2007) for flow over a shallow cavity and by Ehrenstein & Gallaire (2008) for flow over a smooth bump. A reduced-order controller has then been designed to stabilize the globally unstable flow (see also the review by Henningson & Åkervik 2008). In a similar effort, Ehrenstein & Gallaire (2008) could stabilize a globally unstable flow using a reduced-order model based on global modes after they projected the control effort onto the basis of the reduced model. We will outline and investigate the steps involved in these control designs and, in particular, assess the effectiveness of this choice of basis in accomplishing a globally stable compensated system.

Proper orthogonal decomposition (POD) modes are popular in describing fluid dynamical systems by a reduced set of equations. This popularity stems from the simple manner of extracting them from numerical simulations, their orthogonality properties and their interpretation as energy-ranked coherent structures of the flow (see e.g. Lumley 1970; Sirovich 1987; Berkooz, Holmes & Lumley 1993). POD is used in a variety of ways to analyse and describe complex fluid systems. Following their original objectives, POD modes describe a flow field in terms of coherent structures ranked by their inherent energy content. As such, POD is a pattern recognition tool that detects the most energetic fluid elements in a generally turbulent flow configuration. This type of flow analysis has been pursued by a great many researchers

(see Berkooz *et al.* 1993; Podvin *et al.* 2006, among others) for numerically as well as experimentally generated data. It has quickly been recognized that the extracted POD modes are suitable for a low-order approximation of the flow behaviour. The argument that by using a POD-basis for the reduction of the full Navier–Stokes equations via a Galerkin expansion the vast majority of the system’s energy can be captured has spawned a substantial body of literature on low-dimensional models for complex flow dynamics (see e.g. Noack *et al.* 2003; Buffoni, Camarri & Iollo 2006; Galletti *et al.* 2007 and others). More recently, these low-dimensional models have been incorporated into flow control strategies (see Delville, Cordier & Bonnet 1998; Tadmor *et al.* 2004; Bergman, Cordier & Brancher 2006 for flow around a cylinder, or Samimy *et al.* 2007 for flow over an open cavity). It is commonly known that POD modes optimally express the driven dynamics of a fluid system; in mathematical terms, an expansion in POD modes that have been constructed from an impulse released from the control location produces optimal controllability of the reduced system. The application of POD modes to partial-state information control problems (where observability is equally important) may often lead to unsatisfactory results. Adjoint POD modes, on the other hand, produce optimal observability of the reduced model, but usually at the expense of controllability, which makes them less suited for control problems.

It has long been recognized that in order to reduce control problems to a desired size, both controllability, i.e. the ability of the applied forcing to reach flow states, and observability, i.e. the ability of flow states to register at the sensor locations, are equally important. An expansion basis that balances these two concepts would be particularly suited to express the flow of information from the actuator via the linear system to the sensor and thus yield a reduced model that could be subjected to optimal control design. These balanced modes have been introduced more than two decades ago (Moore 1981) and have been applied to small and moderately sized problems; even extensions to unstable systems (Zhou, Salomon & Wu 1999) and nonlinear control problems (Scherpen 1993; Lall, Marsden & Glavaski 2002) have been developed. The necessity to solve matrix Lyapunov and Sylvester equations, however, has precluded them from being applied to large-scale control problems. A recent development (see Rowley 2005 and earlier work by Willcox & Peraire 2002), combining computational methodology from POD modes with a balancing procedure, has overcome this difficulty and has brought the model reduction of large-scale control problems within reach of current computational technology. Since this breakthrough model reduction based on balanced POD modes has become a readily applied technique for the analysis of generic wall-bounded shear flows such as channel (Ilak & Rowley 2006; Ahuja & Rowley 2008; Ilak & Rowley 2008) and boundary layer flow (Bagheri, Brandt & Henningson 2009a) as well as of model equations (Bagheri *et al.* 2009b) mimicking fluid behaviour.

The article proceeds along the following outline. After introducing the flow configuration and details of the discretization and solution algorithm, a partitioning strategy into unstable and stable subspaces and a general bi-orthogonal projection method will be presented which allow the assessment of various commonly used expansion bases for the reduction of the full input–output behaviour to that of a system with significantly fewer degrees of freedom. Global modes will then be extracted from the flow via a shift-invert Arnoldi technique and used as a first expansion basis. Their effectiveness in representing the input–output behaviour, illustrated by the transfer function, will be critically evaluated and analysed. Expansion bases consisting of proper orthogonal modes as well as balanced modes will also be formed and evaluated using the same measure. By closing the control loop, the

various expansion bases will then be examined as to their ability to control the unstable flow and yield a stable compensated system. A summary and discussion of the major findings, and details of derivations in form of an appendix, will conclude this article. The main contributions of this work comprise the application of the lifting procedure for flow in a complex geometry, the partitioning of the linearized flow behaviour into stable and unstable dynamics, a demonstration of the importance of modelling the dynamics in the stable subspace, the introduction of quantitative performance measures for the latter modelling effort and the performance assessment of closed-loop control schemes based on reduced-order models.

2. Configuration and mathematical background

2.1. Configuration

The two-dimensional configuration we consider in this article is sketched in figure 1(a). It consists of a uniform flow of velocity U_∞ over a square cavity of depth D . The precise configuration with its geometric and numerical details is fully described in Sipp & Lebedev (2007). The characteristic quantities of this configuration, i.e. U_∞ , D , as well as the dynamic viscosity ν , are used as reference scales for non-dimensionalizing the governing two-dimensional incompressible Navier–Stokes equations. This results in the Reynolds number, defined as $Re = U_\infty D / \nu$. In the following, we choose $Re = 7500$ so as to have an unstable configuration; the critical Reynolds number of $Re = 4140$ has been determined in Sipp & Lebedev (2007).

Before proceeding with the linear stability analysis and linear control design for this flow a base flow to linearize about has to be determined. This is accomplished by setting the unsteady terms of the two-dimensional Navier–Stokes equations to zero and solving the resulting nonlinear equations by a Newton–Raphson method. The base flow $\mathbf{u}_0 = (u_0, v_0)$ displaying a shear layer above the cavity and a dominant cavity vortex is shown in figure 1(b), visualized by contours of the streamwise velocity and velocity vectors. Note that the boundary layer starts developing at $x = -0.4$ (the origin of our coordinate system coincides with the top left corner of the square cavity). The displacement thickness at the upstream edge of the cavity is $\delta_1 \approx 0.012$, leading to a Reynolds number based on the displacement thickness of $Re_{\delta_1} = U_\infty \delta_1 / \nu \approx 90$. This choice of parameters rules out instabilities related to the boundary layer dynamics.

2.2. Governing equations in state–space form

After a base flow given by the streamwise and normal velocities $\mathbf{u}_0 = (u_0, v_0)$ has been determined, the linearized governing equations can be written in the form of an initial-value problem according to

$$\mathcal{Q} \frac{\partial \mathcal{X}_T}{\partial t} = \mathcal{A} \mathcal{X}_T \quad (2.1)$$

with

$$\mathcal{X}_T = \begin{pmatrix} \mathbf{u}_T \\ p_T \end{pmatrix}, \quad (2.2a)$$

$$\mathcal{Q} = \begin{pmatrix} \mathcal{I} & 0 \\ 0 & 0 \end{pmatrix}, \quad (2.2b)$$

$$\mathcal{A} = \begin{pmatrix} -\nabla() \cdot \mathbf{u}_0 - \nabla \mathbf{u}_0 \cdot () + Re^{-1} \Delta & -\nabla \\ \nabla^* & 0 \end{pmatrix} \quad (2.2c)$$

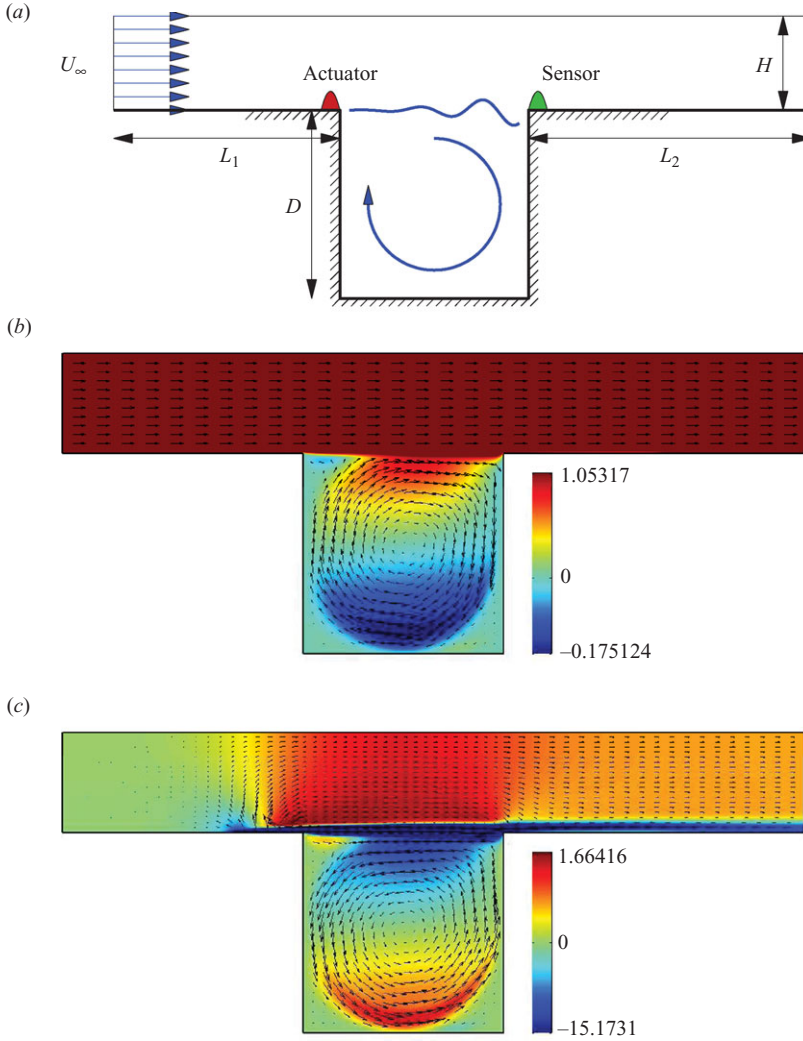


FIGURE 1. (a) Sketch of the geometry for flow over a square cavity. (b) Base flow, visualized by streamwise velocity contours and velocity vectors, for a Reynolds number of $Re = 7500$. (c) Inhomogeneous solution \mathbf{C} with a unit force at the actuator location, visualized by streamwise velocity contours and velocity vectors.

with $\mathbf{u}_T = (u_T, v_T)$ as the perturbation velocity vector, p_T as the perturbation pressure and $\nabla, \nabla^*, \Delta = \nabla^* \nabla$ denoting the Cartesian gradient, divergence and Laplacian operator, respectively. The superscript $*$ stands for the complex conjugate transpose. The fluid enters the domain from the left of the domain (see figure 1a) where a uniform streamwise velocity ($u_T = 1, v_T = 0$) is prescribed. On the top of the domain a symmetry boundary condition ($\partial_y u_T = 0, v_T = 0$) is used. A no-slip ($u_T = 0, v_T = 0$) condition is implemented starting at the location $(x = -0.4, y = 0)$ while a symmetry condition (no stress) is used for $(-1.2 < x < -0.4, y = 0)$ and $(1.75 < x < 2.50, y = 0)$; this will generate a boundary layer of moderate thickness at the upstream edge of the cavity. Finally, a standard outflow condition is prescribed on the right of the domain. More details can be found in Sipp & Lebedev (2007).

In view of treating a flow control problem, we decide on a blowing/suction strategy over a localized section $\partial\Omega_C$ of the wall. Mathematically, this translates into a modified boundary condition of the form $\mathbf{u}_w = \rho(t)\mathbf{u}_G$ where \mathbf{u}_G describes the velocity profile of the injected or extracted flow, while $\rho(t)$ determines its magnitude and temporal behaviour. This boundary condition renders the control problem inhomogeneous, but a transformation, referred to as lifting, will allow us to formulate the control problem as a driven homogeneous problem which has both mathematical and numerical advantages. We take the state vector $\mathcal{X}_T(t)$ as the sum of two parts: a solution \mathcal{X} of the homogeneous problem (i.e. with no control applied, $\rho(t)=0$) and a solution \mathcal{C} of the steady but inhomogeneous problem (i.e. with the specific constant control $\rho(t)=1$ applied). We then express the state vector in the form $\mathcal{X}_T(t) = \rho(t)\mathcal{C} + \mathcal{X}(t)$ and, upon substitution into the governing equation (2.1), obtain

$$\mathcal{L}\frac{\partial\mathcal{X}}{\partial t} = \mathcal{A}\mathcal{X} + \mathcal{L}\mathcal{C}c, \quad (2.3)$$

where $c = -d\rho/dt$.

For the actuator we assume a localized region near the upstream edge of the cavity (see figure 1a) and impose a parabolic normal velocity field over its streamwise extent ($-7/20 \leq x \leq 0, y=0$). The profile is given as

$$u_T(x, y=0, t) = 0, \quad (2.4)$$

$$v_T(x, y=0, t) = -\frac{x(1600x + 560)}{147}\rho(t) \quad (2.5)$$

with the scalings chosen such that ($u_T=0, v_T=\rho$) at the centre of the actuator's support. The associated control function \mathcal{C} stemming from the above-mentioned lifting procedure is shown in figure 1(c), visualized by contours of the streamwise velocity as well as velocity vectors.

What remains in the formulation of the complete control problem is the specification of a measured quantity which yields information about the flow for the design of an estimator. As the measured quantity we take the wall-normal shear stress evaluated at and integrated over a localized region $\partial\Omega_M$ of the wall (the sensor location). We obtain

$$m = \mathcal{M}\mathcal{X} = \int_{\partial\Omega_M} \mathbf{t} \cdot \nabla \mathbf{u} \cdot \mathbf{n}|_w ds = \int_{x=1}^{x=1.1} \left. \frac{\partial u}{\partial y} \right|_{y=0} dx, \quad (2.6)$$

where \mathbf{n} is the inward unit normal on $\partial\Omega_M$ and \mathbf{t} denotes the associated unit tangential vector. The sensor is located near the downstream edge of the cavity, on the segment ($1 \leq x \leq 1.1, y=0$). Note that $m(t) = m_T(t) - \rho(t)m_C$ where $m_T(t)$ and m_C are the measures related to $\mathcal{X}_T(t)$ and \mathcal{C} .

Finally, an energy based inner product of the form

$$\langle \mathcal{Y}, \mathcal{X} \rangle \equiv \iint_{\Omega} \mathcal{Y} \cdot \mathcal{L}\mathcal{X} d\Omega \quad (2.7)$$

will be used for projections.

This concludes the formulation of the continuous flow control problem in state-space form. We then proceed to discretize the problem. To this end, we mesh the domain by an unstructured finite-element grid to properly resolve near-wall and high-shear features and employ (P_2, P_2, P_1) finite elements, in conjunction with a weak formulation of the above equations, to arrive at a discretized form of the governing

equations (2.3). We obtain

$$\mathbf{Q} \frac{d\mathbf{X}}{dt} = \mathbf{A}\mathbf{X} + \mathbf{Q}\mathbf{C}c, \quad (2.8a)$$

$$m = \mathbf{M}\mathbf{X}, \quad (2.8b)$$

$$\mathbf{X}_T(t) = \rho(t)\mathbf{C} + \mathbf{X}(t), \quad (2.8c)$$

$$\langle \mathbf{Y}, \mathbf{X} \rangle = \mathbf{Y}^* \mathbf{Q}\mathbf{X} \quad (2.9)$$

with

$$\mathbf{A}\mathbf{C} = 0, \quad (2.10a)$$

$$\mathbf{C} = \mathbf{C}_G \quad \text{on } \partial\Omega_C. \quad (2.10b)$$

Again, the superscript $*$ represents the complex conjugate transpose. Assuming n degrees of freedom for the state vector \mathbf{X} which includes the two velocity components and the pressure, the above matrices are of the following size: $\mathbf{Q}, \mathbf{A} \in \mathbb{R}^{n \times n}$, $\mathbf{C} \in \mathbb{R}^{n \times 1}$, $\mathbf{M} \in \mathbb{R}^{1 \times n}$ and $c, m \in \mathbb{R}$. A typical discretization yields about 900 000 degrees of freedom stemming from about 200 000 triangles.

3. Perturbation dynamics and global mode analysis

The discretized system of equations (2.8) allows the computation of the temporal global spectrum and the associated global modes via the common assumption of an exponential time-dependence, i.e. $\mathbf{X}(x, y, t) = \tilde{\mathbf{X}}(x, y)e^{zt}$. We consequently obtain a generalized eigenvalue problem for $\lambda \in \mathbb{C}$ and $\tilde{\mathbf{X}}$ of the form

$$\lambda \mathbf{Q}\tilde{\mathbf{X}} = \mathbf{A}\tilde{\mathbf{X}}, \quad (3.1)$$

which has to be solved by iterative numerical techniques.

3.1. Numerical method

The solution of this eigenvalue problem by the direct QZ-algorithm is rather costly due to the size of the matrices \mathbf{Q} and \mathbf{A} . Instead, we apply an iterative Krylov subspace technique, more precisely, the shift-invert Arnoldi algorithm, to extract information about the global spectrum and the corresponding global modes. The inversion is performed using a multifrontal sparse LU solver (MUMPS, see Amestoy *et al.* 2001).

Computations of global modes for flows in complex geometries are generally challenging and care must be exercised to avoid spurious or insufficiently converged eigenvalues and to still extract all relevant global modes. In our case, for each specified shift location 100 eigenvalues have been computed in its neighbourhood, after which the shift is moved to sweep over a sufficiently large part of the complex plane. For each choice of shift location both the direct and the adjoint eigenvalue problem has been solved, and particular care has been exercised to take into account each computed mode only once.

3.2. Direct global modes

The eigenvalues $\lambda = \sigma + i\omega$ of the open cavity flow at $Re = 7500$ are displayed in figure 2(a). The horizontal and vertical axes correspond, respectively, to the amplification rate σ and the frequency ω . The figure is symmetric with respect to $\omega = 0$, and eigenvalues in the half-plane $\sigma > 0$ represent unstable eigenmodes. In our computations the plane $\omega \geq 0$ contains 2630 eigenvalues with a total of 5166 eigenvalues in the entire plane.

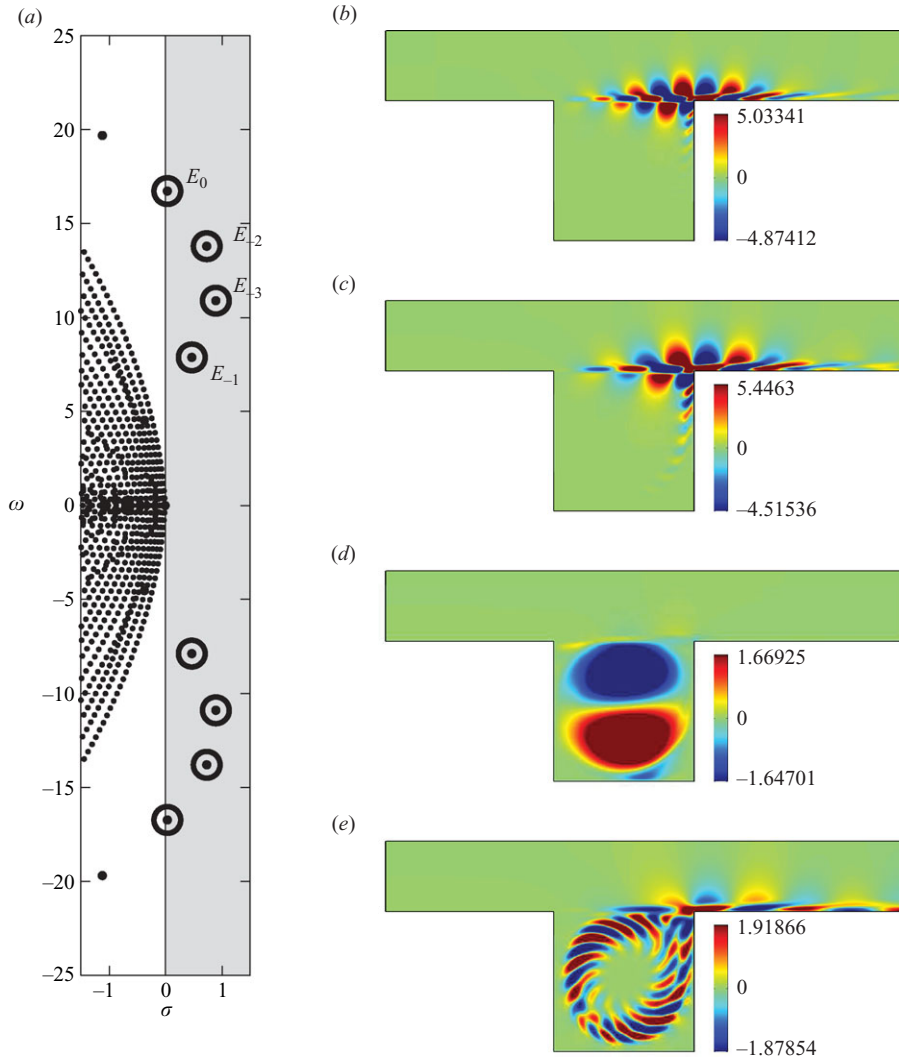


FIGURE 2. (a) Part of the global spectrum for flow over a square cavity at $Re = 7500$, showing four unstable global modes (marked by circles and labelled E_{-3} , E_{-2} , E_{-1} , E_0) and their symmetric counterparts. (b–e) Direct global modes corresponding to E_{-3} (b), E_{-1} (c), E_1 (d) and E_2 (e). The global modes are visualized by their streamwise velocity component.

We observe that there are four unstable global modes in the half-plane $\omega \geq 0$, which yields a total of eight unstable global modes in the complete plane. The four unstable global modes in the upper half-plane are denoted by E_{-3} , E_{-2} , E_{-1} , E_0 . The amplification rate and frequency of these modes are listed in table 1, and the global modes corresponding to the eigenvalues E_{-3} and E_{-1} are displayed in figure 2(b,c). In each subplot we have represented the global structure by the horizontal u -velocity component. In figure 2(b) we observe that the most unstable global mode is composed of a series of counter-rotating vortices located atop the shear layer separating the outer and inner cavity flow. The eigenvector increases in amplitude as one moves downstream along the shear-layer and is most pronounced at the downstream edge of the cavity. Figure 2(c) represents similar results for the modal structure associated

Number	σ	ω	\hat{M}_i	$\text{Re}(\hat{\mathbf{C}}_i)$	$\text{Im}(\hat{\mathbf{C}}_i)$	Γ_i
E_{-3}	0.890	10.9	99.1	-1.65	0.764	
E_{-2}	0.729	13.8	84.2	-2.32	0.160	
E_{-1}	0.466	7.88	113.7	-1.14	1.97	
E_0	0.0324	16.73	73.1	-2.84	-0.155	
E_1	-0.00811	0	1.32	0.605	0	98
E_2	-0.373	4.54	37.6	-6.48	9.32	1142
E_3	-0.716	0.203	10.7	-3.81	9.21	148
E_4	-1.12	19.7	64.1	-2.99	-0.499	173
E_5	-2.70	22.7	50.7	-3.27	-1.84	71
E_6	-5.01	2.71	0.0100	$0.740 \cdot 10^5$	$3.71 \cdot 10^5$	758
E_7	-6.22	17.4	0.0104	$-3.13 \cdot 10^2$	$2.54 \cdot 10^2$	0.67
E_8	-9.65	12.4	$6.47 \cdot 10^{-6}$	$0.592 \cdot 10^9$	$-8.15 \cdot 10^9$	5477

TABLE 1. List of selected global eigenvalues together with variables quantifying their contribution in representing the flow's input–output behaviour (see text for an explanation).

with E_{-1} . We observe that the number of counter-rotating vortices is lower than for E_{-3} which agrees with the fact that E_{-1} has a lower eigenfrequency than E_{-3} .

Owing to the abundance of stable global modes, we will focus on two specific eigenvalues numbered E_1 and E_2 that are listed in table 1 together with various characteristic data. The least stable eigenmode among the damped eigenmodes (denoted in the spectrum by E_1) is depicted in figure 2(d) and consists of a weakly damped large-scale vortical structure located inside the cavity. Figure 2(e) focuses on the global mode corresponding to E_2 which is damped and oscillatory. It is characterized by features both inside the cavity and outside. Inside the cavity, it displays small-scale perturbations convected by the rigidly rotating base-flow. Outside, this structure connects to vortical elements in the base shear-layer that propagate downstream past the cavity.

In anticipation of further computations, the global modes will be gathered into a matrix \mathbf{E} , which is the solution of the generalized eigenproblem

$$\mathbf{A}\mathbf{E} = \mathbf{Q}\mathbf{E}\mathbf{\Lambda}, \quad (3.2)$$

where $\mathbf{\Lambda}$ is a diagonal matrix of dimension $n \times n$ containing the n eigenvalues. Hence, each column j of \mathbf{E} is an eigenvector corresponding to $\mathbf{\Lambda}_{jj}$. Since \mathbf{A} is a real matrix, the eigenvalues are real or appear as complex conjugate pairs. The ordering and grouping of the eigenvalues and eigenvectors in $\mathbf{\Lambda}$ and \mathbf{E} respect this fact, e.g. $\mathbf{\Lambda}_{11} = 0.890 + 10.9i$, $\mathbf{\Lambda}_{22} = 0.890 - 10.9i$, $\mathbf{\Lambda}_{99} = -0.00811$, etc. Furthermore, the eigenvectors are normalized such that their energy $\mathbf{E}_j^* \mathbf{Q} \mathbf{E}_j$ is one and their phase $\mathbf{M} \mathbf{E}_j$ is real and positive.

3.3. Physical explanation of disturbance dynamics

A DNS of the linearized Navier–Stokes equations (2.8a), based on a second-order accurate time marching scheme, has been used to gain further insight into the physics of these unstable global modes. The results of the simulation using the most unstable global mode E_{-3} as an initial condition along with $c(t) = 0$ are displayed in figure 3 where we show a spatio-temporal diagram of the pressure $p(x, y = 0, t)$ in the (x, t) plane.

Starting with an unstable initial condition the pressure increases exponentially. On the shear layer we observe vortical structures associated with low and high

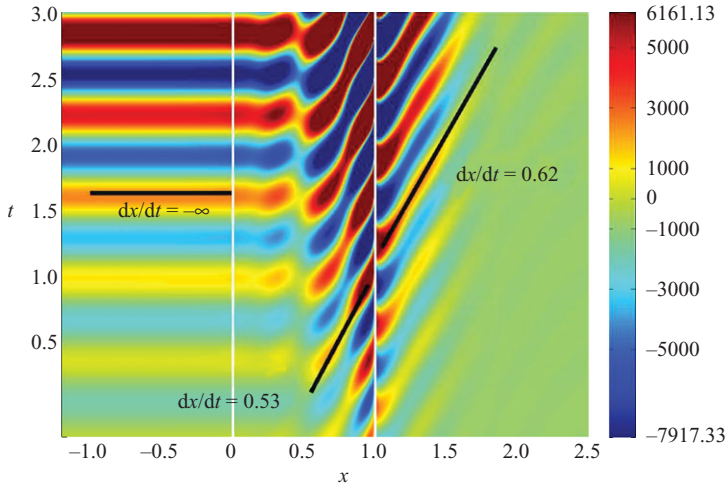


FIGURE 3. Spatio-temporal x - t diagram of pressure $p(x, y=0, t)$ contours with no control applied. The initial condition corresponds to the most unstable global mode. The two vertical white lines indicate the cavity walls. See also movie I in the online version of the paper.

pressure zones that are convected at the speed $dx/dt = 0.53$, i.e. approximately half the free-stream base-flow speed. Once the vortical structures have left the cavity zone, they accelerate and reach a convective speed of $dx/dt = 0.62$, which falls within the range of the free-stream and the low speeds that are present in the boundary layer. The cavity flow is globally unstable based on a classical feedback loop: the vortical structures are convected downstream in the shear layer at a speed of 0.53; during this phase they grow due to a Kelvin–Helmholtz instability (an inflection point is present in the base-flow velocity profile $u_0(x = \text{const}, y)$ near $y = 0$). These vortical structures subsequently impact the downstream cavity edge and generate an infinitely fast pressure wave ($dx/dt = -\infty$) which travels upstream, excites the shear layer near the upstream edge of the cavity and regenerates perturbations that grow again due to a Kelvin–Helmholtz instability (see also Åkervik *et al.* 2007).

The general objective is then to stabilize the flow using a closed-loop control. Mathematically this corresponds to moving the unstable eigenvalue of \mathbf{A} into the stable half-plane. We first, however, have to introduce reduced-order models on which our control design will depend.

4. Model reduction

Flows in complex geometries are characterized by a large number of degrees of freedom and standard (direct) techniques for computing stability characteristics or control schemes can no longer be applied. Instead, a projection onto relevant fluid structures, known as model reduction, has to be employed to reduce the size of the full problem to a more manageable number of degrees of freedom. For this reason, the model reduction techniques and algorithms play an increasingly central role as we attempt to control progressively complex flows. The choice of relevant fluid structures onto which our full system is projected is not obvious; a significant part of this paper is devoted to this important question.

4.1. Bi-orthogonal projection

We will develop a mathematical framework that allows the model reduction of any system in state–space form using a general bi-orthogonal projection basis. This framework then allows the evaluation and analysis of various reduction techniques, e.g. based on global modes, optimally controllable (POD) modes or balanced proper orthogonal decomposition (BPOD) modes.

We start by introducing a general basis given by \mathbf{V} and its dual equivalent \mathbf{W} that satisfy the bi-orthogonality relation based on \mathbf{Q} of the form

$$\mathbf{W}^* \mathbf{Q} \mathbf{V} = \mathbf{I}, \quad (4.1)$$

where $\mathbf{V}, \mathbf{W} \in \mathbb{C}^{n \times q}$ and \mathbf{I} stands for the $q \times q$ identity matrix. The parameter q denotes the dimensionality of the projection basis. The discretized state vector \mathbf{X} is then expressed as a linear combination of the columns of the chosen expansion basis \mathbf{V} according to

$$\mathbf{X} = \mathbf{V} \hat{\mathbf{X}}, \quad (4.2a)$$

$$\hat{\mathbf{X}} = \mathbf{W}^* \mathbf{Q} \mathbf{X}, \quad (4.2b)$$

and the coefficients of this linear combination are contained in the vector $\hat{\mathbf{X}} \in \mathbb{C}^{q \times 1}$ which can be determined by invoking the bi-orthogonality condition. A straightforward Petrov–Galerkin projection then yields the reduced system

$$\frac{d\hat{\mathbf{X}}}{dt} = \hat{\mathbf{A}} \hat{\mathbf{X}} + \hat{\mathbf{C}} c, \quad (4.3a)$$

$$m = \hat{\mathbf{M}} \hat{\mathbf{X}} \quad (4.3b)$$

with the reduced system, control and measurement matrices given as

$$\hat{\mathbf{A}} = \mathbf{W}^* \mathbf{A} \mathbf{V}, \quad (4.4a)$$

$$\hat{\mathbf{C}} = \mathbf{W}^* \mathbf{Q} \mathbf{C}, \quad (4.4b)$$

$$\hat{\mathbf{M}} = \mathbf{M} \mathbf{V}. \quad (4.4c)$$

Depending on the bases used for the model reduction, the above system should be able to represent critical features of the full system and capture the dynamics relevant to a successful control design.

4.2. Basis consisting of global modes

The basis \mathbf{E} consisting of n eigenvectors is non-orthogonal with respect to the scalar product based on \mathbf{Q} . This fact is a consequence of the non-normality of the system matrix \mathbf{A} , and the source of this non-normality lies in the convective terms of the linearized Navier–Stokes operator. Consequently, a second set of vectors – the dual basis \mathbf{F} in the general framework – has to be determined to complete the bi-orthogonal projection. This basis may be obtained by solving for the eigenvalues and eigenvectors of the Hermitian of the linearized Navier–Stokes matrix, i.e.

$$\mathbf{A}^* \mathbf{F} = \mathbf{Q} \mathbf{F} \mathbf{A}^*. \quad (4.5)$$

The above eigenvalue problem produces eigenvalues that are complex conjugate to the eigenvalues of the previous problem. Hence, under the same ordering and grouping each column j of the $n \times n$ matrix \mathbf{F} is associated with the j th column of \mathbf{E} and the eigenvalue Λ_{jj} . It can easily be verified that the two bases \mathbf{E} and \mathbf{F} are bi-orthogonal and that \mathbf{F} may be normalized such that

$$\mathbf{F}^* \mathbf{Q} \mathbf{E} = \mathbf{I}. \quad (4.6)$$

Although the adjoint system is characterized by a spectrum that is complex conjugate to the direct spectrum, the corresponding adjoint eigenvectors differ significantly from their direct counterparts, owing to the non-normal nature of the underlying linearized Navier–Stokes equations. The adjoint global modes (not shown) are similar to their direct counterparts when considering reversing the base flow direction; the amplitude increases in magnitude as one moves upstream along the shear-layer and is largest at the upstream edge of the cavity. These observations confirm the non-normality of the linearized Navier–Stokes operator as the direct global mode is convected downstream whereas its adjoint equivalent propagates upstream.

4.3. Stable subspace based on BPOD or POD basis

The present paper treats a globally unstable flow. As we have seen, eight unstable global modes exist for our parameter settings. A partition of the full dynamics into two subspaces, one containing the unstable dynamics (based on the unstable global modes) and another describing the stable dynamics is required for the subsequent analysis. Since the dynamics within the unstable and stable subspaces are decoupled, they can be modelled separately.

Because of their ability to model the inherent instability (see §3) and because of their low dimensionality, the unstable global modes can be used directly to represent the dynamics in the unstable subspace (see Ahuja & Rowley 2008). This procedure leads to an ‘exact’ model for this subspace in the sense that no modelling assumptions have to be invoked. For the stable subspace, on the other hand, a variety of choices are available.

We proceed by partitioning the eigenvectors \mathbf{E} according to $\mathbf{E} = (\mathbf{E}_u \mathbf{E}_s)$ where \mathbf{E}_u (resp. \mathbf{E}_s) of dimension $n \times 8$ (resp. $n \times (n-8)$) contains the eight unstable modes (resp. remaining stable modes). Similarly, \mathbf{F} is decomposed as $\mathbf{F} = (\mathbf{F}_u \mathbf{F}_s)$ and satisfies the bi-orthogonality relation $\mathbf{F}_u^* \mathbf{Q} \mathbf{E}_u = \mathbf{I}$. Finally, the eigenvalue matrix $\mathbf{\Lambda}$ is split according to

$$\mathbf{\Lambda} = \begin{pmatrix} \mathbf{\Lambda}_u & 0 \\ 0 & \mathbf{\Lambda}_s \end{pmatrix},$$

where the dimension of $\mathbf{\Lambda}_u$ and $\mathbf{\Lambda}_s$ is 8×8 and $(n-8) \times (n-8)$, respectively. In what follows, the subscripts $_u$ will refer to quantities of the unstable subspace while the subscript $_s$ will refer to quantities that are defined in the stable subspace.

We proceed by forming the projection matrices \mathbf{P}_u onto the unstable and \mathbf{P}_s onto the stable subspace as $\mathbf{P}_u = \mathbf{E}_u \mathbf{F}_u^* \mathbf{Q}$ and $\mathbf{P}_s = \mathbf{I} - \mathbf{E}_u \mathbf{F}_u^* \mathbf{Q}$. In the case the unstable subspace is modelled by the unstable global modes, a general projection basis can be written as $\mathbf{V} = (\mathbf{E}_u \mathbf{V}_s)$ and $\mathbf{W} = (\mathbf{F}_u \mathbf{W}_s)$ where \mathbf{V}_s is defined as a basis belonging to the null-space of \mathbf{P}_u , and the relations $\mathbf{W}_s^* \mathbf{Q} \mathbf{E}_u = 0$ and $\mathbf{W}_s^* \mathbf{Q} \mathbf{V}_s = \mathbf{I}$ can be easily verified.

The matrices (defined in (4.4)) appearing in the reduced-order model can now be rewritten as

$$\hat{\mathbf{A}} = \begin{pmatrix} \mathbf{\Lambda}_u & 0 \\ 0 & \hat{\mathbf{A}}_s \end{pmatrix}, \quad \hat{\mathbf{C}} = \begin{pmatrix} \hat{\mathbf{C}}_u \\ \hat{\mathbf{C}}_s \end{pmatrix}, \quad \hat{\mathbf{M}} = (\hat{\mathbf{M}}_u \hat{\mathbf{M}}_s) \quad (4.7)$$

where $\hat{\mathbf{A}}_s = \mathbf{W}_s^* \mathbf{A} \mathbf{V}_s$ is, in general, a dense matrix, and the control and measurement submatrices are respectively given as $\hat{\mathbf{C}}_u = \mathbf{F}_u^* \mathbf{Q} \mathbf{C}$, $\hat{\mathbf{C}}_s = \mathbf{W}_s^* \mathbf{Q} \mathbf{C}$, $\hat{\mathbf{M}}_u = \mathbf{M} \mathbf{E}_u$ and $\hat{\mathbf{M}}_s = \mathbf{M} \mathbf{V}_s$.

The stable subspace is usually high dimensional, and the main effort in reducing the system’s dimension is expended reducing the dynamics in the stable subspace.

Anticipating the results of §6, we assert that the modelling of the stable subspace is essential when it comes to effective closed-loop control design. The stable subspace contains substantial physical information about the overall dynamics, and we will show that extracting the relevant dynamical features from this subspace is pivotal for the success of any control strategy.

In control theory, it has long been recognized (see Zhou *et al.* 2002 and Antoulas 2005) that the transfer of information from the actuator to the sensor – the input–output behaviour – is the critical quantity that has to be carefully taken into consideration. Recent studies of Bagheri *et al.* (2009b) and Bagheri *et al.* (2009a) support this statement within a fluid mechanics framework. This statement then provides the motivation for the following section where the ability of various bases to reproduce the input–output behaviour of the stable subspace will be critically assessed and quantified. Various bases consisting of stable global modes, POD modes and BPOD modes will be successively considered and evaluated. At this point, we would like to point out that a reduced model $\hat{\mathbf{A}}_s$ of the stable subspace dynamics based on a Petrov–Galerkin projection does not necessarily have to result in a stable reduced system. Since the stability of the reduced-order models is critical to the success of closed-loop control, particular attention will be given to this property and its preservation through the model reduction process.

5. Open-loop behaviour

5.1. Input–output behaviour

In closed-loop mode the actuator manipulates the flow in order to reduce the perturbation growth and suppress the instability. Its action is, however, not limited to the unstable perturbations, but also triggers some stable states which are subsequently detected by the sensor. As we will see in the next section, this triggering process can constitute a source of failure for the controller. It is therefore important to understand and model these stable structures which are both excited by the actuator and observed by the sensor; in other words, we have to concern ourselves with the input–output behaviour of the stable subspace.

In this section our goal is to quantify the accuracy of various reduced models in capturing the input–output behaviour of the stable subspace. During this study we will thus consider the equations governing only the stable dynamics, i.e.

$$\mathbf{Q} \frac{d\mathbf{X}}{dt} = \mathbf{A}_s \mathbf{X} + \mathbf{Q} \mathbf{C}_s c, \quad (5.1a)$$

$$m = \mathbf{M} \mathbf{X}, \quad (5.1b)$$

where $\mathbf{A}_s = \mathbf{A} \mathbf{P}_s$ and $\mathbf{C}_s = \mathbf{P}_s \mathbf{C}$. The above set of equations represents the system governed by (2.8) but projected onto the stable subspace.

By definition, the input–output behaviour links the effect of the actuator on the flow to the information extracted by the sensor. It can be described by the impulse response or, equivalently, by the transfer function. The impulse response, i.e. the reaction of the system to a Dirac function for the control law $c(t) = \delta(t)$, produces the measurement $m(t) = \mathbf{M} \mathbf{X}(t)$ where \mathbf{X} is the solution of the initial-value problem

$$\begin{aligned} \mathbf{Q} \frac{d\mathbf{X}}{dt} &= \mathbf{A}_s \mathbf{X}, \\ \mathbf{X}(t=0) &= \mathbf{C}_s. \end{aligned}$$

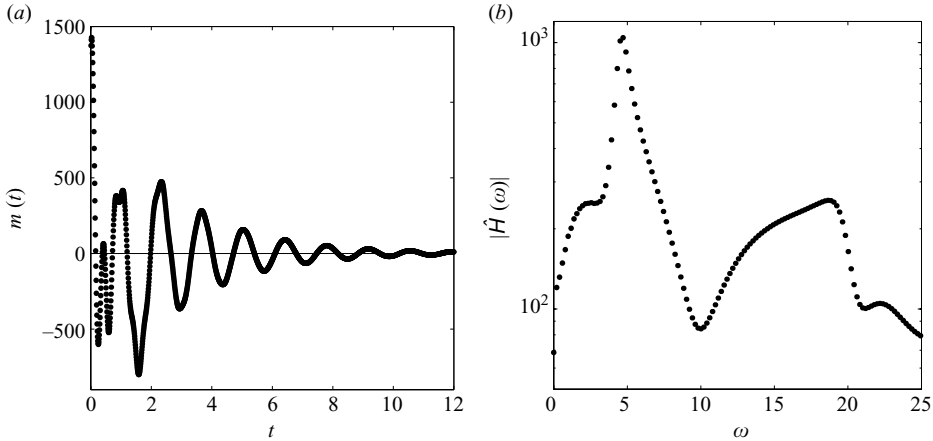


FIGURE 4. Impulse response (a) as a function of time and transfer function (b) as a function of frequency for the stable part of the flow over an open cavity at $Re = 7500$.

In figure 4(a), this impulse response is displayed. In the corresponding simulation, 2.8(a) is integrated in time using a second-order accurate scheme, the initial condition is the control matrix \mathbf{C} and the control law $c(t) = 0$. After each time step the solution is projected, using the matrix \mathbf{P}_s , onto the stable subspace before the computation is advanced in time. Strictly speaking, only the initial condition would have to be projected; however, to avoid the amplification of numerical errors due to components in the unstable subspace, the above projection technique is employed at every time step. A first crucial observation is an immediate effect of the actuation at the sensor location, even though the sensor is far from the actuator location. After a rapid decay and a transient response, the signal settles into a periodic pattern which eventually decays exponentially.

Since all frequencies are excited by an initial impulse, a convenient and alternative way of expressing the input–output behaviour of a linear system is to switch to the frequency domain. The amplitude of the transfer function, which is defined as the Fourier transform of the impulse response, is displayed in figure 4(b). This graph represents the amplitude part of a standard-type gain-phase plot (e.g. a Bode plot); Since we use an impulse function on a causal system with $m = 0$ for all times $t < 0$, the transfer function is simply given by $H(\omega) = \int_0^\infty e^{-i\omega t} m(t) dt$. We recover a preferred frequency around $\omega = 4.6$ which corresponds to the periodic signal observed in figure 4(a).

In the following sections, we will use various bases to produce reduced models for the stable subspace dynamics; in particular, we are interested in the dimensionality of a particular basis to approximate the full transfer function to a prescribed degree of accuracy. The discrepancy between reduced and full transfer function will be quantified using the \mathcal{H}_∞ norm defined as

$$\|\mathbf{G}(\omega)\|_\infty = \sup_\omega |\mathbf{G}(\omega)|. \quad (5.2)$$

The choice of this norm has been motivated by the availability of theoretical bounds, as will be shown later. Nevertheless, the \mathcal{H}_2 norm has also been computed for each of the following cases, and the results were found in qualitative agreement with the \mathcal{H}_∞ norm. The computation of the transfer function for the reduced model is obtained

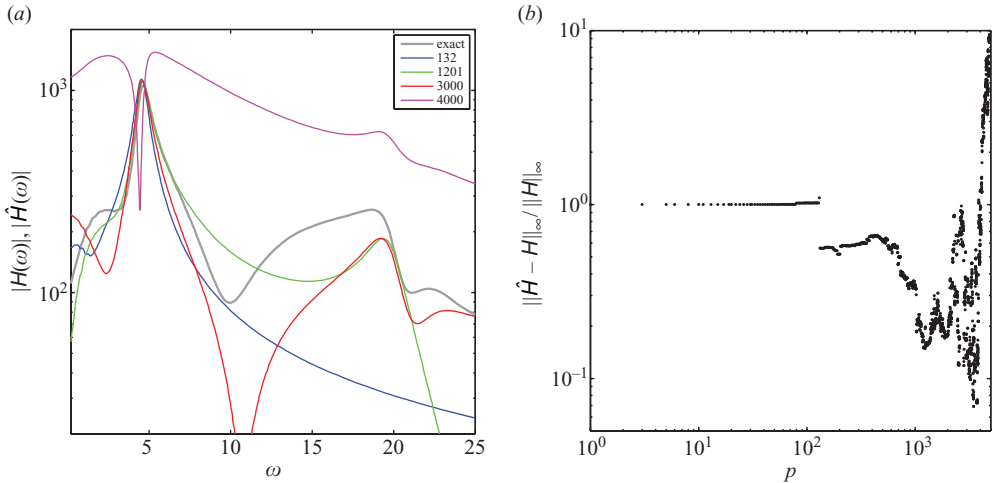


FIGURE 5. (a) Comparison of transfer function of the reduced-order model to the exact transfer function for a projection basis consisting of $p = 132, 1201, 3000, 4000$ stable global modes. (b) Relative \mathcal{H}_∞ -error norm as a function of the number p of included stable global modes.

using the equivalent denotation $\hat{H}(\omega) = \hat{\mathbf{M}}_s(i\omega\hat{\mathbf{I}} - \hat{\mathbf{A}}_s)^{-1}\hat{\mathbf{C}}_s$, where the quantities with $\hat{}$ refer to the reduced matrices.

5.2. Reduced-order modelling using global modes

5.2.1. Transfer function and error norm

We start by considering stable global modes as a basis for computing a reduced-order model; in particular, a stable subspace consisting of p stable global modes, ranked by decaying amplification rate (see Åkervik *et al.* 2007 and Ehrenstein & Gallaire 2008), are taken. The transfer functions corresponding to reduced models based on $p = 132, 1201, 3000$ and 4000 global modes are displayed in figure 5(a) and compared to the transfer function of the full system. It is evident that none of the reduced models is able to approximate the exact transfer function to a satisfactory degree of accuracy. Moreover, although the curves based on $p = 132, p = 1201$ and $p = 3000$ accurately capture the peak around $\omega = 5$, the reduced-order model based on $p = 4000$ modes fails entirely, and it appears that taking additional stable modes does not necessarily improve the quality of the reduced-order model. This is also visible in figure 5(b) where the \mathcal{H}_∞ -error $\|\hat{H} - H\|_\infty / \|H\|_\infty$ is plotted versus the number of stable eigenmodes accounted for in the reduced-order model. For reduced models including up to 100 modes, the error remains at order one. After the 132th mode (E_2 in table 1) has been included in the basis, the error decreases abruptly, thus indicating that this mode is important to represent the correct input–output behaviour. As more global modes are added, the \mathcal{H}_∞ -error decreases again, starts to oscillate and finally increases substantially. On the whole, the quality of the reduced-order model is never satisfactory and generally becomes worse as additional modes are included. Nevertheless, the inclusion of a few particular modes results in a significantly drop in the error norm; these modes warrant some further investigation as to their contribution to the input–output behaviour of the system. Specifically, a criterion will be derived in the next section that facilitates the ranking of stable global modes according to their importance in representing the transfer function.

5.2.2. Criterion to select stable global modes

The erratic convergence behaviour of the transfer function of a reduced-order system based on global modes to the transfer function of the full system portends the fact that the choice of which stable global modes to include in the reduced-order model of the estimator is far from trivial. Nevertheless, a theoretical criterion that guides this choice can be derived (see also Bagheri *et al.* 2009b). To this end, let us first recall the equations that govern the dynamics of the reduced-order model:

$$\frac{d\hat{\mathbf{X}}}{dt} = \hat{\mathbf{A}}\hat{\mathbf{X}} + \hat{\mathbf{C}}c, \quad (5.3)$$

$$\hat{m} = \hat{\mathbf{M}}\hat{\mathbf{X}}. \quad (5.4)$$

For simplicity and without loss of generality, we consider a particular control law in the form

$$c(t) = \cos(\omega t), \quad (5.5)$$

where ω is a given (real) frequency. We then determine the forced response of the dynamical system expressed in terms of the measurement and omitting the initial transient response. We obtain

$$\hat{m} = \frac{1}{2}\hat{\mathbf{M}}\left(i\omega\hat{\mathbf{I}} - \hat{\mathbf{A}}\right)^{-1}\hat{\mathbf{C}}\exp(i\omega t) + \frac{1}{2}\hat{\mathbf{M}}\left(-i\omega\hat{\mathbf{I}} - \hat{\mathbf{A}}\right)^{-1}\hat{\mathbf{C}}\exp(-i\omega t) \quad (5.6)$$

from which we may extract the contribution of the i th global mode as

$$\hat{m}_i = \frac{1}{2}\frac{\hat{\mathbf{M}}_i\hat{\mathbf{C}}_i}{i\omega - \hat{\mathbf{A}}_i}\exp(i\omega t) + \frac{1}{2}\frac{\hat{\mathbf{M}}_i\hat{\mathbf{C}}_i}{-i\omega - \hat{\mathbf{A}}_i}\exp(-i\omega t). \quad (5.7)$$

If the i th eigenvalue has a non-zero imaginary part, we get $\hat{\mathbf{M}}_{i+1} = \hat{\mathbf{M}}_i^*$, $\hat{\mathbf{C}}_{i+1} = \hat{\mathbf{C}}_i^*$ and $\mathbf{A}_{i+1} = \mathbf{A}_i^*$. It then follows that $\hat{m}_{i+1} = \hat{m}_i^*$ and further

$$m_i + m_{i+1} = \left| \frac{\hat{\mathbf{M}}_i\hat{\mathbf{C}}_i}{i\omega - \hat{\mathbf{A}}_i} \right| \cos(\omega t + \psi) + \left| \frac{\hat{\mathbf{M}}_i\hat{\mathbf{C}}_i}{-i\omega - \hat{\mathbf{A}}_i} \right| \cos(-\omega t + \xi).$$

The forced response is the sum of waves of frequency ω . Maximizing over all forcing frequencies ω , we can see that the contribution of the i th eigenmode is proportional to the quantity (see also Antoulas 2005, p. 282 and Bagheri *et al.* 2009b):

$$\Gamma_i = \frac{\left| \hat{\mathbf{M}}_i \right| \left| \hat{\mathbf{C}}_i \right|}{\left| \text{Re}(\hat{\mathbf{A}}_i) \right|}. \quad (5.8)$$

This criterion takes into account three different physical variables to quantify if a stable global mode should or should not be retained in the reduced-order model basis of the estimator: (a) the measurement coefficient $\hat{\mathbf{M}}_i$, which is closely related to the observability of the respective global mode, (b) the control coefficient $\hat{\mathbf{C}}_i$, a measure of controllability of the associated global mode and (c) the decay rate $|\text{Re}(\mathbf{A}_i)|$ of the global mode. In short, the criterion based on Γ_i selects global modes that are observable, controllable and weakly damped. It is noteworthy that Lee *et al.* (2001) used a similar technique for a reduced model by selecting modes that are equally controllable and observable.

This analysis should validate, in some sense, the choice of least stable global modes as adopted by Åkervik *et al.* (2007). Indeed, if the measurement and control coefficients of all global modes were bounded (an assumption that will be proven wrong below),

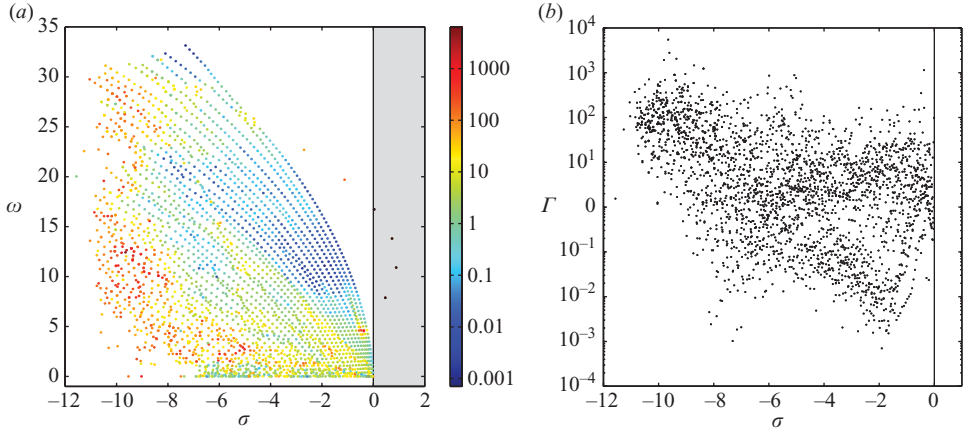


FIGURE 6. (a) Global spectrum of flow over an open square cavity at $Re = 7500$ colour-coded by Γ_i , a measure of each global mode's contribution to the input–output relation (see (5.8) and text for explanation). (b) Criterion Γ_i versus the each mode's amplification rate.

then Γ_i would decay as $1/|\text{Re}(\mathbf{A}_i)|$ as we move to larger decay rates $|\text{Re}(\mathbf{A}_i)|$. This would then justify neglecting highly damped global modes in the reduced-order basis of the estimator. But the choice of included global modes, made purely on their decay rate, does not yield satisfactory results since the notion of controllability and observability of the global modes has not been taken into account.

For our present case of open flow over a square cavity, we observe that Γ_i does not decrease with the decay rate $|\text{Re}(\hat{\mathbf{A}}_i)|$ of the global modes. In figure 6(a), which shows the global spectrum in the (σ, ω) plane, the colouring of the eigenvalues corresponds to Γ_i . The eigenvalues that appear in warm (cold) colours display high (low) values of Γ ; a logarithmic colour map has been used here and Γ_i is meaningful only for damped eigenmodes. We observe that some of the highest values of Γ appear for strongly damped eigenmodes; moreover, the number of eigenmodes with high values of Γ appears to increase as the damping increases since nearly all yellow- and red-coloured eigenvalues appear on the left side of the figure. In figure 6(b), the same information is plotted in a different form: the horizontal axis represents the amplification rate σ of each eigenvalue while the vertical axis represents its value of Γ (on a logarithmic scale). It is clear that Γ does not decrease for highly damped eigenvalues and that more and more eigenvalues with high Γ appear as the damping rate $-\sigma$ increases. Since no theoretical argument can be made for an eventual decrease of Γ as the damping rate increases, we conclude that the damping rate is a poor and inappropriate measure for the judicious inclusion of global modes into the reduced-order model or for the truncation of the expansion basis. We also want to remind ourselves that numerical difficulties stemming from the non-normal nature of the problem prevented us from computing converged global modes beyond the damping rates shown in the above figures. Furthermore, reduced-order models with more than about 100 degrees of freedom quickly become untractable and impractical for closed-loop control efforts.

The divergence of Γ with the damping rate $-\sigma$ warrants a more thorough investigation. We recall from the definition of Γ given in (5.8) that it consists of the product of the control coefficient $\hat{\mathbf{C}}_i$ and the measurement coefficient $\hat{\mathbf{M}}_i$, divided by the damping rate. In figures 7(a) and 7(b) we present, for all converged

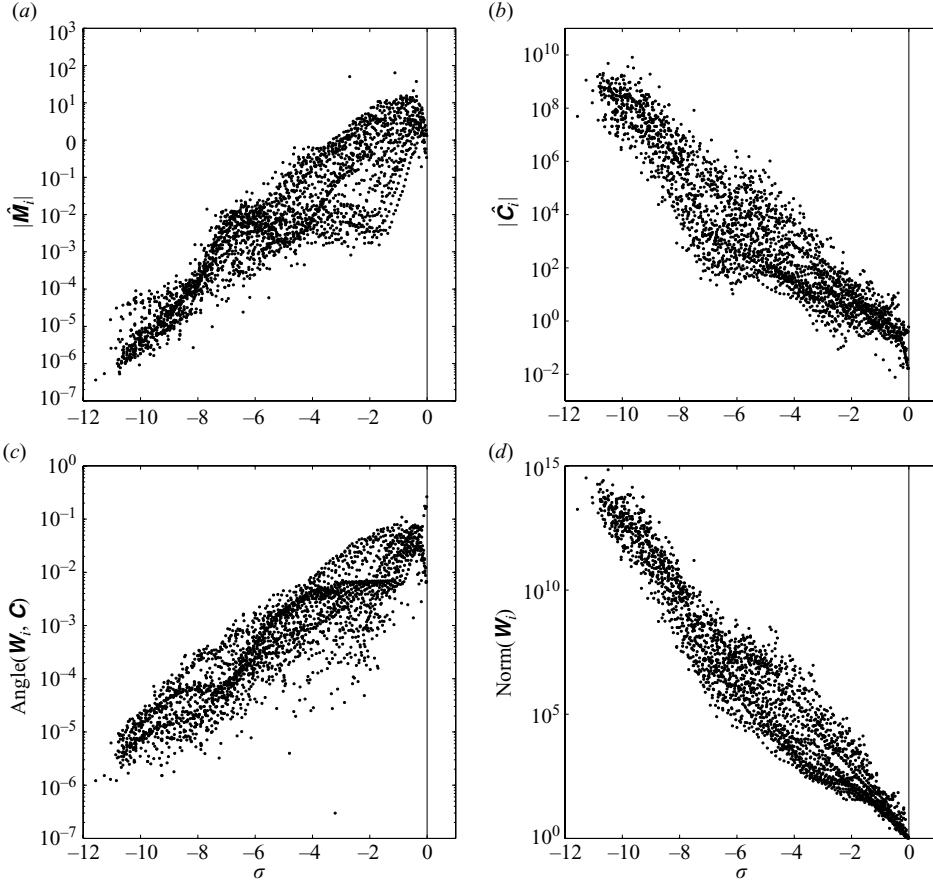


FIGURE 7. Breakup of criterion Γ_i into its individual components. (a) Measurement coefficient \hat{M}_i versus the amplification rate, and (b) control coefficient \hat{C}_i versus the amplification rate. The control coefficient \hat{C}_i is further factored according to (5.9) into (c) the angle between adjoint global mode \mathbf{W}_i and control function \mathbf{C} , and (d) the norm of the adjoint mode \mathbf{W}_i which are displayed versus the amplification rate of the corresponding global mode.

eigenvalues, the modulus of the measurement coefficient and the control coefficient as a function of the amplification rate. Figure 7(a) reveals that modes with higher damping rates have a lower observability. This tendency alone would suggest that based on observability we would be justified in excluding global modes with higher damping. An opposite trend can be observed when controllability is considered: in this case, controllability increases with increasing damping rates. The disadvantageous behaviour of the composite coefficient Γ can thus be traced back to the controllability coefficient defined as $\hat{C}_i = \mathbf{W}_i^* \mathbf{Q} \mathbf{C}$. We note that

$$|\hat{C}_i| = \sqrt{\mathbf{C}^* \mathbf{Q} \mathbf{C}} \underbrace{\frac{|\mathbf{W}_i^* \mathbf{Q} \mathbf{C}|}{\sqrt{\mathbf{W}_i^* \mathbf{Q} \mathbf{W}_i} \sqrt{\mathbf{C}^* \mathbf{Q} \mathbf{C}}}}_{\text{angle}(\mathbf{W}_i, \mathbf{C})} \underbrace{\sqrt{\mathbf{W}_i^* \mathbf{Q} \mathbf{W}_i}}_{\text{norm}(\mathbf{W}_i)}. \quad (5.9)$$

The second term on the right-hand side of the above expression describes the angle between the adjoint global mode \mathbf{W}_i and the control function \mathbf{C} while the last

term on the right-hand side denotes the norm of the adjoint mode \mathbf{W}_i , which may be interpreted as a measure of non-normality of the global mode \mathbf{V}_i . These two quantities have been plotted versus the amplification rate σ of each global mode in figures 7(c) and 7(d), respectively. These two figures show that the non-normality (figure 7d), rather than the angle term (figure 7c), is responsible for the overall lack of convergence of Γ with respect to the damping rate $-\sigma$. This non-normality of the damped global mode basis is linked to physical properties of the base flow. Non-normality has also been identified by Lauga & Bewley (2003) as the reason for loss of stabilizability in their study of the controlled linear Ginzburg–Landau model.

To summarize this section, global modes have been used as a projection basis to capture the input–output behaviour of the stable subspace. Selecting global modes according to either their damping rate or their contribution to the input–output behaviour produced disappointing results as no satisfactory agreement between the reduced and the full transfer function could be obtained. For this reason, other expansion bases to construct a reduced-order model have to be considered.

5.3. Reduced-order modelling using BPOD modes

A powerful technique, commonly applied in control theory and known as balanced truncation, allows us to reduce the stable part of the linear system while optimally preserving its input–output behaviour. The key idea is to compute, rank and select modes that are equally observable and controllable.

We will see in §5.3.2 that the computational effort to compute these balanced modes is rather high for systems of moderate size and quickly becomes unaffordable for systems of large size and realistic complexity. Instead, we will compute an approximation of the balanced modes by an algorithm referred to as balanced proper orthogonal decomposition (BPOD) which remains tractable even for very large systems (see Rowley 2005).

Before dealing with balanced truncation, we will first introduce and analyse the concept of controllability and observability Gramians which will lay the foundation and provide the necessary background for the derivation and application of the exact and approximate balancing transformation. We rewrite (5.1) in the classical state–space formulation (see §A.1 of appendix):

$$\frac{d\mathbf{X}_1}{dt} = \mathbf{A}_1\mathbf{X}_1 + \mathbf{C}_1c, \quad (5.10a)$$

$$m = \mathbf{M}_1\mathbf{X}_1, \quad (5.10b)$$

which governs the dynamics of the velocity field \mathbf{X}_1 . In what follows, the subscript $_1$ will refer to quantities that consist of the velocity components only. We note that the scalar product restricted to the velocity field is written accordingly as $\mathbf{X}_1^*\mathbf{Q}_1\mathbf{X}_1$.

5.3.1. Controllability and observability Gramians

A specific state is deemed controllable if there exists a control law $c(t)$ which is able to modify the flow from any state towards this specific state. For controllable states, the notion of controllability then quantifies how easy (or difficult) the state can be reached from any state. Mathematically this is expressed in terms of the controllability Gramian \mathbf{G}_C defined as

$$\mathbf{G}_C = \int_0^\infty e^{\mathbf{A}_1 t} \mathbf{C}_1 \mathbf{C}_1^* e^{\mathbf{A}_1^* t} dt, \quad (5.11)$$

which is a convergent integral as $t \rightarrow \infty$ since \mathbf{A}_1 is stable. The expression $\mathbf{X}_1^* \mathbf{G}_C^{-1} \mathbf{X}_1$ can be interpreted as the minimum control energy expended over an infinite time horizon, i.e. $\int_0^\infty c(t)^2 dt$, to drive the system from the initial zero state to the state \mathbf{X}_1 (see more details in §A.2 of appendix). Using the snapshot technique introduced by Rowley (2005) the controllability Gramian may be factored as

$$\mathbf{G}_C = \mathbf{T}_1 \mathbf{T}_1^*, \quad (5.12)$$

where \mathbf{T}_1 stands for the matrix containing n_d rescaled snapshots arising from a DNS initialized by the control matrix \mathbf{C} at $t=0$ (see §A.2). Note that this is the same simulation as the impulse response presented in §5.1.

As controllability quantifies the amount of effort it takes to manipulate a particular flow state, observability measures how easy (or difficult) a given flow state can be detected by the sensors. At the sensor location almost unobservable flow states leave hardly any footprint behind and are thus nearly ‘invisible’ to our measurement efforts. The mathematical quantity that enables measuring the observability of a given flow state is the observability Gramian which is defined as

$$\mathbf{G}_O = \int_0^\infty e^{\mathbf{A}_1^* t} \mathbf{M}_1^* \mathbf{M}_1 e^{\mathbf{A}_1 t} dt. \quad (5.13)$$

The expression $\mathbf{X}_1^* \mathbf{G}_O \mathbf{X}_1$ represents the maximum energy $\int_0^\infty m^2(t) dt$ produced by observing the output of the initial state \mathbf{X}_1 (more details are given in §A.3). Again following Rowley (2005) the observability Gramian may be factored according to

$$\mathbf{G}_O = \mathbf{Q}_1 \mathbf{U}_1 \mathbf{U}_1^* \mathbf{Q}_1, \quad (5.14)$$

where \mathbf{U}_1 denotes the matrix containing n_a snapshots arising from the simulation of the adjoint problem initialized by the measurement matrix \mathbf{M} at $t=0$ (see §A.3). It should be mentioned at this stage that the above-described technique requires the knowledge of the adjoint state. For experimental applications, this approach may thus become inapplicable. However, recent attempts to determine balanced modes without having to resort to adjoint information have been reported by Or & Speyer (2008) and Ma, Ahuja & Rowley (2009).

5.3.2. Balancing transformation using the snapshot method

Since both controllability and observability are important when choosing a reduction basis that preserves the input–output relation, a technique has to be applied that extracts flow fields with equal emphasis on either property. This technique is referred to as balancing. Mathematically, it is equivalent to finding a transformation basis in which the Gramians \mathbf{G}_C and \mathbf{G}_O appear diagonal and equal (see Zhou *et al.* 2002). This basis, denoted by \mathbf{J} , and its associated adjoint basis, denoted by \mathbf{K} , satisfy the bi-orthogonality relation

$$\mathbf{K}^* \mathbf{Q} \mathbf{J} = \mathbf{I}, \quad (5.15)$$

where \mathbf{Q} takes into account the finite-element discretization by adding a weight matrix to the standard inner product. The established procedure of finding the balancing transformation consists of computing the Gramians (see §A.2 and §A.3) followed by an eigenvalue decomposition of one of the following products

$$\mathbf{G}_C \mathbf{G}_O \mathbf{J}_1 = \mathbf{J}_1 \boldsymbol{\Sigma}^2, \quad (5.16a)$$

$$\mathbf{G}_O \mathbf{G}_C (\mathbf{Q}_1 \mathbf{K}_1) = (\mathbf{Q}_1 \mathbf{K}_1) \boldsymbol{\Sigma}^2. \quad (5.16b)$$

These eigenvalue problems yield the same eigenvalues, since the transpose of the matrix $\mathbf{G}_C \mathbf{G}_O$ is simply $\mathbf{G}_O \mathbf{G}_C$. The diagonal matrix Σ contains the *Hankel singular values*. By definition, the Hankel singular values are the non-zero singular values of the *Hankel operator* associated with our linear system.

Solving the Lyapunov equations and the eigenvalue problem for the balancing transformation, however, is computationally not feasible. It has been shown (Rowley 2005) that a good approximation of this transformation can be obtained while entirely avoiding the explicit computation of the Gramians. The associated technique relies on the decomposition of the Gramians in the form of (5.12) and (5.14).

A singular value decomposition (SVD) of the matrix product $\mathbf{U}_1^* \mathbf{Q}_1 \mathbf{T}_1 = \mathbf{U}^* \mathbf{Q} \mathbf{T}$, which is of dimension $n_a \times n_d$, results in

$$\mathbf{U}_1^* \mathbf{Q}_1 \mathbf{T}_1 = \mathbf{U}' \Sigma \mathbf{T}'^*, \quad (5.17a)$$

$$\mathbf{U}'^* \mathbf{U}' = \mathbf{I}, \quad (5.17b)$$

$$\mathbf{T}'^* \mathbf{T}' = \mathbf{I}, \quad (5.17c)$$

where \mathbf{T}' , \mathbf{U}' and Σ are of dimension $n_d \times n_d$, $n_a \times n_a$ and $n_a \times n_d$, respectively. In a final step, the bi-orthogonal balancing bases given by \mathbf{J} and \mathbf{K} in (5.16) are found as

$$\mathbf{J} = \mathbf{T} \mathbf{T}' \Sigma^{-1/2}, \quad (5.18a)$$

$$\mathbf{K} = \mathbf{U} \mathbf{U}' \Sigma^{-1/2}. \quad (5.18b)$$

It is easily confirmed that the bi-orthogonality condition $\mathbf{K}^* \mathbf{Q} \mathbf{J} = \mathbf{I}$ is satisfied. We verify that

$$(\mathbf{Q}_1 \mathbf{K}_1)^* \mathbf{G}_C (\mathbf{Q}_1 \mathbf{K}_1) = \Sigma, \quad (5.19a)$$

$$\mathbf{J}_1^* \mathbf{G}_O \mathbf{J}_1 = \Sigma. \quad (5.19b)$$

In Rowley (2005) it is shown that this implies that the columns of \mathbf{J}_1 form the first columns of the balancing transformation and the columns of $\mathbf{Q}_1 \mathbf{K}_1$ constitute the first columns of the inverse transformation.

We conclude this section by emphasizing the fact that our initial condition (\mathbf{M}) for the adjoint simulation to obtain the approximate observability Gramian is different from the one used by Rowley (2005) where the so-called *output-projection technique* has been applied. This technique relies on first defining the entire state vector as the output of the linear system. This in turn would call for one simulation for each degree of freedom, a requirement that of course cannot be met. To nevertheless capture the entire state in an optimal way, a projection onto POD modes is applied. The initial conditions for the adjoint simulations are taken as these POD modes. As a result, the input–output behaviour captured by their BPOD modes is between the actuator (input) and the dynamics described by the POD modes. This technique may yield a good estimation of the interaction of the actuator with the most energetic structures.

If an estimate of the flow state using the measurement matrix \mathbf{M} is needed, an increased number of POD modes may be necessary to reconstruct an accurate measurement signal, since POD modes, by design, are not particularly efficient in capturing information near the sensor. For instance, in Rowley *et al.* (2008) 20 POD modes were needed which implies an equal number of adjoint simulations, a rather costly requirement.

In our case, the output of our system is solely the measurement signal from the sensor. The flow states which are observable from this sensor are given as the result of an adjoint simulation. For this reason, only one adjoint simulation (with the measurement matrix as the initial condition) is necessary. The apparent drawback,

namely that our reduced model may not accurately capture the dynamics in the rest of the domain but merely describe the states excited by the actuator and detected by the sensor, is inconsequential since our primary objective is to control the flow over the cavity by a reduced-order model that is as low-dimensional as possible, and for this objective the input–output behaviour is the only quantity of importance.

5.3.3. Results

Both the direct and adjoint simulations are integrated up to $T = 16$ using a second-order accurate scheme with a fixed time step of $\Delta t = 2 \times 10^{-4}$ in order to produce and gather the snapshots. The direct simulation is identical to the one for extracting the impulse response (see §5.1) and illustrates the effect of the control on the stable part of the flow. The adjoint simulation (defined in (A 17)) is initialized with the matrix \mathbf{M} which represents a unit measurement signal. As was the case for the direct simulation, a projection onto the stable subspace is necessary which was accomplished in an analogous manner. The adjoint simulation then gives us information on which flow structures will be most detectable by the sensor.

Balanced modes forming the basis for the balancing transformation are computed from a sequence of snapshots that are equispaced at an interval of $80\Delta t = 1.6 \times 10^{-2}$. With this parameter setting we produce $n_d = n_a = 1001$ snapshots for each the direct and adjoint simulation.

In figure 8(a) the singular values (SV) Σ_{ii} from the singular value decomposition of $\mathbf{U}_1^* \mathbf{Q}_1 \mathbf{T}_1$ (see (5.17)) are shown. These singular or Hankel values provide a measure of how controllable (and observable) the corresponding balanced modes are. This information can then be used to decide on a truncation point and thus on the size of the reduced-order model. Significant drops in the Hankel values are commonly used to justify truncation of the balancing basis.

In figure 8 the balanced modes corresponding to the first, second, ninth and thirteenth singular value are displayed. The first two modes show a similar structure: vortices are present on the shear-layer, and the effect of actuation is clearly visible. The pairwise occurrence of balanced modes with the displayed spatial structure is linked to the representation of travelling structures by the superposition of these modes. Both modes show an increased amplitude near the actuator (at the upstream edge of the cavity). The ninth balanced mode is located mainly inside the cavity with a structure reminiscent of the least stable global mode (see figure 2d). The 13th BPOD mode again shows structures inside the cavity as well as in the boundary layer. Near the point of actuation a small but noticeable amplitude is present.

5.3.4. Transfer function and error norm

Next, we consider reduced-order models $(\hat{\mathbf{A}}_s, \hat{\mathbf{C}}_s, \hat{\mathbf{M}}_s)$ based on p BPOD modes where the modes are ranked by decreasing Hankel values. The transfer function corresponding to reduced-order models based on $p = 2, 6, 8$ and 10 modes are compared to the exact transfer function in figure 9(a). Contrary to the reduced-order models based on global modes, the exact transfer function is very well approximated even for a moderate number p of modes. When only two balanced modes are considered, the main peak is already well-captured. Figure 9(a) is meant to convey the convergence behaviour of reduced-order transfer functions towards the exact one for a particular number p of BPOD modes. As the number of modes further increases, the approximate transfer function converges rapidly to the exact one. For $p = 13$ modes (not shown in figure 9(a)), the curves for the approximate and exact transfer function coincide to plotting accuracy; the dynamics of the stable subspace

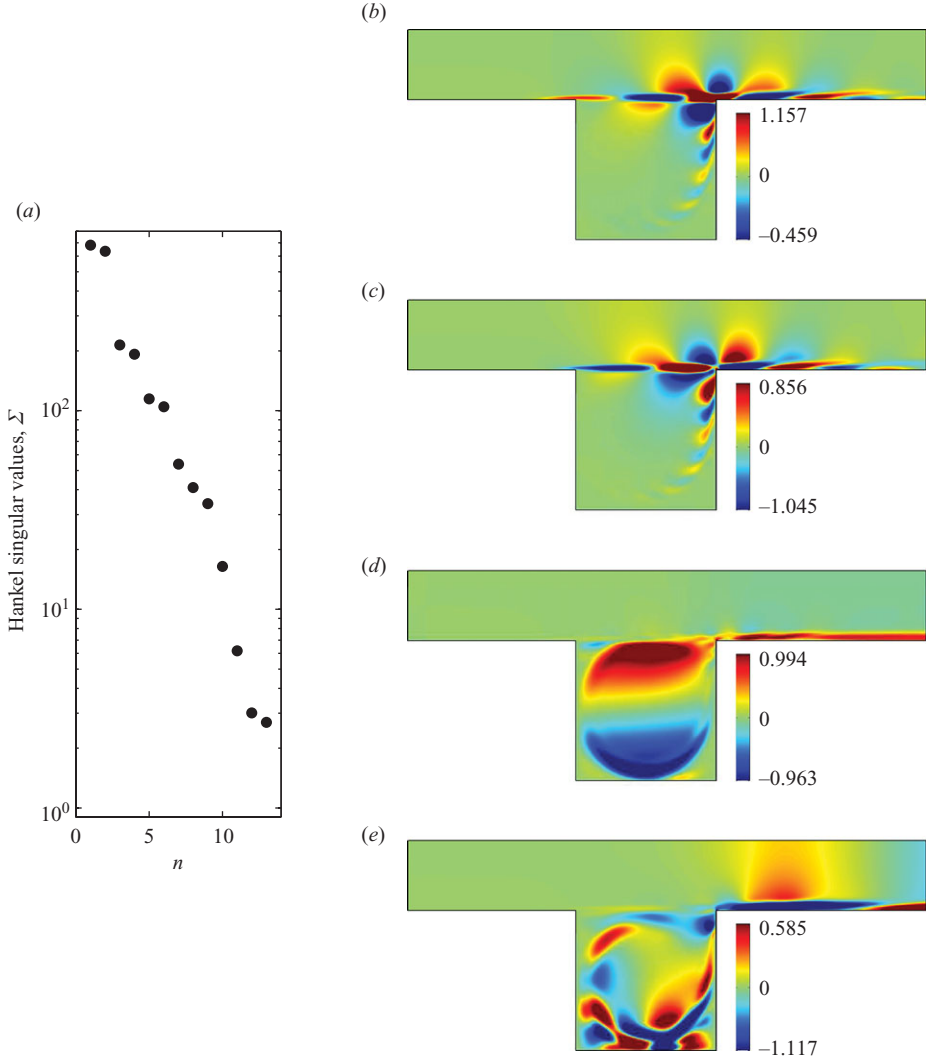


FIGURE 8. (a) Hankel singular values for flow over a square cavity for $Re = 7500$. (b–e) Balanced proper orthogonal decomposition (BPOD) modes. (b) First, (c) second, (d) ninth and (e) thirteenth mode, visualized by the streamwise velocity.

and its projection onto 13 BPOD modes produces virtually the same input–output behaviour.

Bounds on the discrepancy between the approximate and exact transfer function are readily available for balanced truncation. An upper bound for the infinity norm (maximum error) of the transfer function error is given by twice the sum of the neglected Hankel values (see Antoulas 2005). We have

$$\|\hat{H} - H\|_{\infty} \leq 2 \sum_{j=r+1}^{n_1} \Sigma_{jj}, \quad (5.20)$$

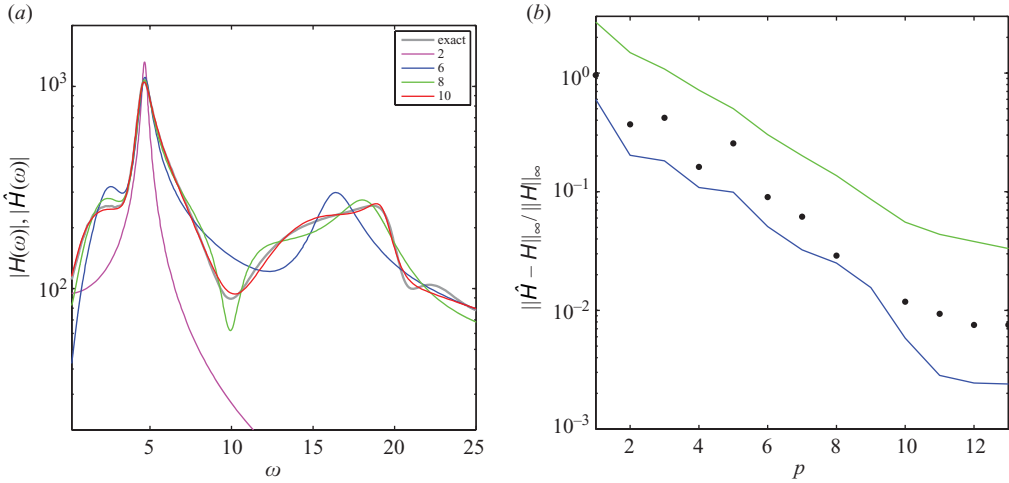


FIGURE 9. (a) Comparison of transfer function of the reduced-order model to the exact transfer function for a projection basis consisting of $p=2, 6, 8, 10$ balanced modes. (b) Relative \mathcal{H}_∞ -error norm as a function of the number p of included balanced modes, together with an upper (green line) and lower bound (blue line) on the error.

where H and n_1 are the transfer function and dimension of the full system, respectively, whereas \hat{H} and r are the equivalent quantities for the reduced-order model. Comparisons made in Rowley (2005), Ilak & Rowley (2008) and Bagheri *et al.* (2009b) suggest that the error committed by approximating the true Gramians by a series of discrete-time snapshots is very close to balanced truncation. A lower bound on the maximum error also exists for any reduced-order model. It can be stated as

$$\|\hat{H} - H\|_\infty > \Sigma_{r+1}. \quad (5.21)$$

In figure 9(b), the \mathcal{H}_∞ error is displayed together with the two error bounds discussed above. For all cases, as required, the error falls between the upper and lower bounds for balanced truncation.

5.3.5. The eigenvalues of the reduced-order model based on BPOD modes

The ability of reduced-order models based on BPOD modes to capture the input–output behaviour, as demonstrated above by comparing the approximate and exact transfer function, raises the question of which parts of the full global spectrum contribute to this input–output relation. In answering this question we will establish a link between balanced truncation and the criterion (5.8), introduced in § 5.2.2, that quantifies the contribution of selected global modes to the input–output behaviour.

In figure 10 the eigenvalues of the reduced-order system matrix $\hat{\mathbf{A}}_{p,p}$ based on $p=13$ BPOD modes are superimposed on the full global spectrum of the cavity which is, in addition, colour-coded by the criterion Γ_i (same as figure 6). As the selection criterion Γ_i is only valid for the stable global modes, we will restrict ourselves to the stable part of the spectrum.

We first notice that the eigenvalues of the BPOD-reduced system are bounded by the global spectrum. This is expected since the BPOD modes approximate the subspace spanned by the stable global modes. Furthermore, varying the order of the BPOD-reduced model does not have any influence on certain eigenvalues of the reduced-order model (not shown here). These eigenvalues, labelled M_1, M_2 , and

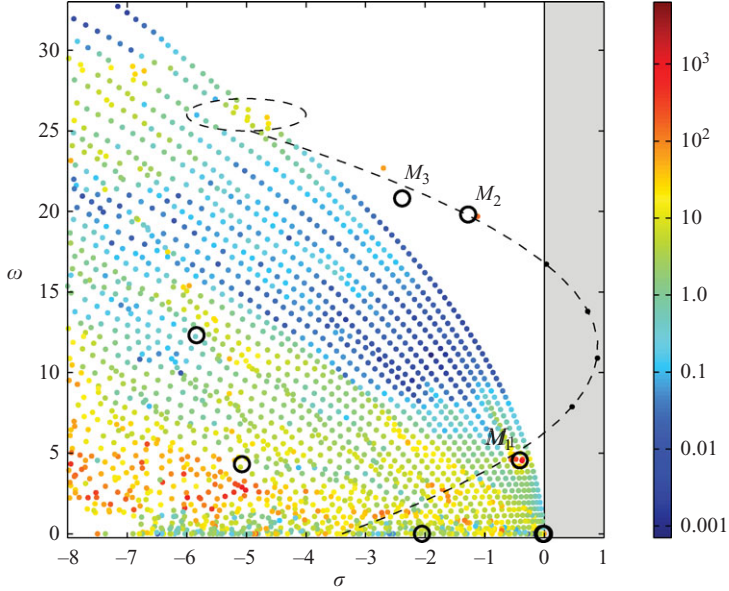


FIGURE 10. Eigenvalues of the reduced matrix $\hat{\mathbf{A}}_{\tilde{p}, \tilde{p}}$ superimposed on the global spectrum of the cavity. Eight unstable global modes and 13 BPOD modes have been included in the reduced model. The global spectrum is coloured according to the criterion Γ_i .

M_3 in figure 10, rapidly converge towards stable global modes with a high value of the selection criterion Γ_i . We believe that this feature underlines the fact that these selected individual modes are rather important in describing the input–output behaviour. This stands as a validation of both the introduced selection criterion for global modes and the extraction of BPOD modes.

In particular, M_1 converges towards the 132th least stable global mode which has a rather high value of Γ_i (see E_2 in table 1). This mode, displayed in figure 2(e), has an oscillatory frequency of $\omega = 4.54$ and is responsible for capturing the peak in the transfer function (see figure 4b). The importance of this mode in terms of its contribution to the input–output relation is also visible in figure 5(b) where a significant drop in the error norm $\|\hat{H} - H\|_\infty / \|H\|_\infty$ occurs as soon as this particular global mode is included in the reduced-order model.

Note that M_1 , M_2 and M_3 appear to belong to the same branch as the one comprising the unstable modes. This tendency should not come as a surprise as this branch is composed of shear-layer modes whose shape provides a link between the upstream edge of the cavity (where the actuator is located) and the downstream edge (where the sensor has been placed) through the shear-layer which acts as an amplifier. In a similar manner, the remaining modes in the BPOD spectrum account for more general structures that play an important role in the overall input–output relation.

5.4. Reduced-order modelling using POD modes

Coherent structures based on the POD are often used in deriving reduced-order models, and large body of literature exists which demonstrates their use in describing the essential dynamics of uncontrolled and controlled fluid systems by a set of equations with a significantly reduced number of degrees of freedom. For the sake of completeness, we will also consider POD modes as a basis for low dimensionally describing the input–output behaviour of our cavity problem.

5.4.1. Presentation of POD modes

The classical snapshot method (see Sirovich 1987) is applied to compute POD modes for the stable subspace of our flow. This technique relies on the snapshots \mathbf{T} collected during the impulse response simulation (see § 5.1, identical to the dataset used for the BPOD computation).

The bi-orthogonal basis of the stable subspace is given by $\mathbf{V}_s = \mathbf{R}$ and $\mathbf{W}_s = \mathbf{S}$ with

$$\mathbf{G}_C \mathbf{Q}_1 \mathbf{R}_1 = \mathbf{R}_1 \boldsymbol{\Sigma}_{POD}^2. \quad (5.22)$$

Since $\mathbf{G}_C = \mathbf{T}_1 \mathbf{T}_1^*$, we obtain

$$\mathbf{T}_1^* \mathbf{Q}_1 \mathbf{T}_1 = \mathbf{T}' \boldsymbol{\Sigma}_{POD}^2 \mathbf{T}^*, \quad (5.23a)$$

$$\mathbf{T}^* \mathbf{T}' = \mathbf{I}, \quad (5.23b)$$

$$\mathbf{R} = \mathbf{T} \mathbf{T}' \boldsymbol{\Sigma}_{POD}^{-1}. \quad (5.23c)$$

The adjoint POD modes are not equal to the direct POD modes due to the existence of an unstable subspace. The adjoint basis has to satisfy $\mathbf{S}^* \mathbf{Q} \mathbf{E}_u = 0$ which leads to $\mathbf{S} = (\mathbf{P}_s \mathbf{R})$.

For our configuration, i.e. flow over an open square cavity at $Re = 7500$, the singular values $\boldsymbol{\Sigma}_{POD}^2$ are depicted in figure 11(a). The plot shows the energy content of the coherent structures identified by the POD analysis, with a steady decay over four orders of magnitude for the first 50 POD modes. The corresponding modes are displayed, again by their streamwise velocity, in figure 11. Even though differences between these modes and the BPOD modes are clearly noticeable, the modes show finite amplitudes at the actuator and sensor location, thus anticipating their ability to represent the flow's input–output behaviour, even though this representation may not be accomplished as efficiently as by BPOD modes.

We would like to emphasize that these POD modes are not general; rather, they strongly depend on the chosen initial condition reflected in the control matrix \mathbf{C} . The extracted modes are optimal in representing the energetic structures triggered by the control. In other words, they can be regarded as the most controllable modes and, as a consequence, are an appropriate approximation basis for full-state information control. However, since no information about their measurement is taken into account in the construction of POD modes, we will show that BPOD-based models outperform POD-based models with respect to capturing the open-loop behaviour.

5.4.2. Transfer function and error norm

We then consider reduced-order models based on p POD modes ranked by decreasing singular values. The transfer functions using a selected number of $p = 10, 28$ and 50 modes are displayed in figure 12(a). Similar to BPOD modes, the reduced-order model correctly approximates the exact transfer function provided that a sufficient number of POD modes are included. Contrary to BPOD modes, the number of modes required for a satisfactory approximation is substantially higher. Using 10 modes, the main peak is overestimated, and the transfer function displays large errors across the entire frequency spectrum. The transfer function of a model based on 28 POD modes shows oscillatory behaviour visible throughout the entire frequency domain, but the general behaviour is rather well predicted. As the number of modes is further increased, the approximate transfer functions match more closely the exact one.

The \mathcal{H}_∞ -error norm is displayed in figure 12(b). For very small-order models, the error increases, but, as more modes are added, the error decreases to reach values

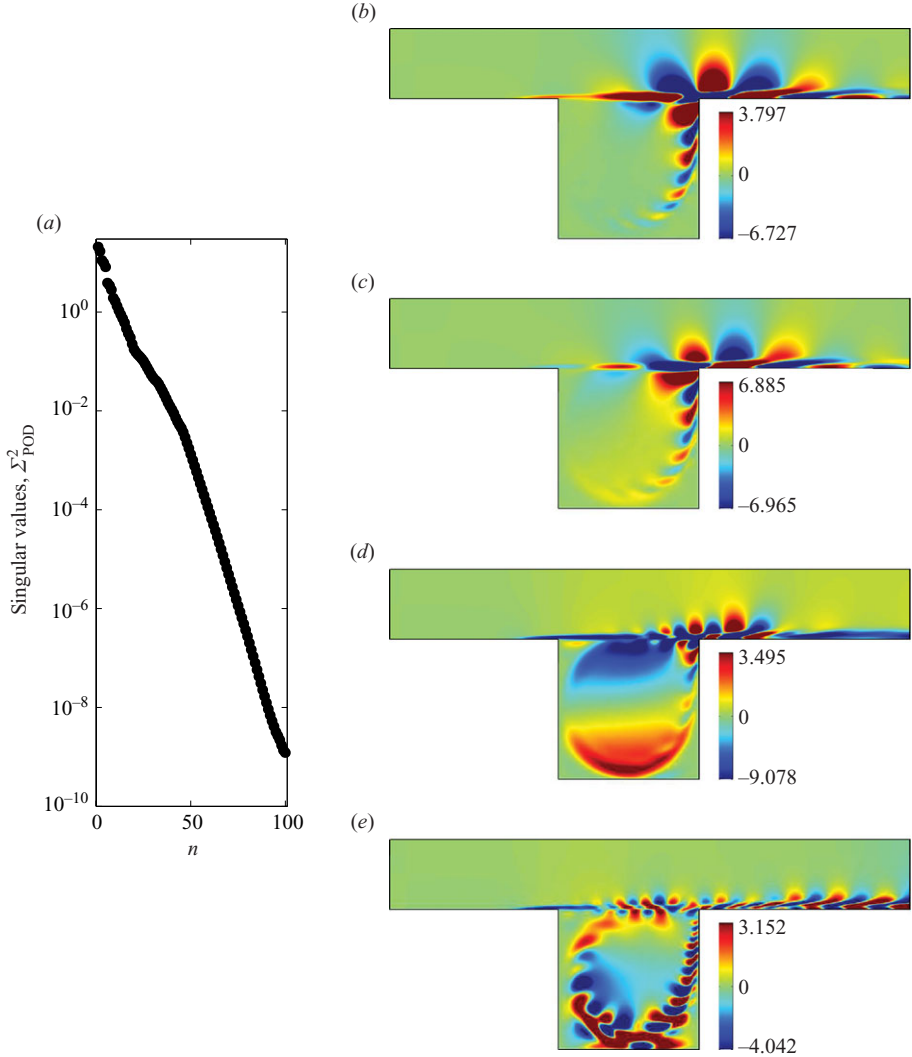


FIGURE 11. (a) Singular values for POD modes. (b–e) POD modes for flow over an open square cavity at Reynolds number $Re = 7500$. The (b) first, (c) second, (d) third and (e) twenty-eighth POD modes are visualized by their streamwise velocity component.

similar to those observed for using BPOD modes. We stress again that, for a given \mathcal{H}_∞ -error, the number of required POD modes is significantly higher than the number of required BPOD modes.

We observe that the reduced-order dynamics for the stable subspace spanned by the POD modes has always been stable no matter the number p of POD modes. The same was not the case for the BPOD bases (see figure 9 where the reduced model based on nine BPOD modes was found unstable). Both POD- and BPOD-based reduced-order systems should be stable, independent of the number p of included modes. In reality, however, the BPOD basis, though far more efficient, is also far more sensitive to numerical issues. POD modes are constructed using only information from the actuator whereas BPOD modes incorporate additional information from the

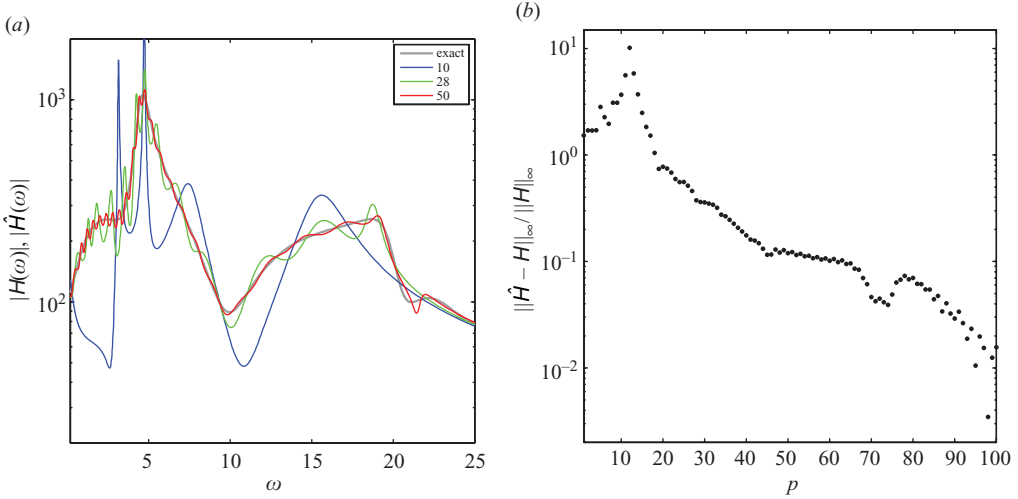


FIGURE 12. (a) Comparison of transfer function of the reduced-order model to the exact transfer function for a projection basis consisting of $p = 10, 28, 50$ POD modes. (b) Relative \mathcal{H}_∞ -error norm as a function of the number p of included POD modes.

measurements. In the following section, we will present a comparison of BPOD and POD bases in terms of their observability.

5.5. Comparison of BPOD and POD bases in terms of observability and controllability

Controllability and observability have been identified as the critical quantities to measure the capability of a specific basis to accurately represent the input–output behaviour of a linear system. It seems reasonable then to analyse the POD and BPOD bases as to these two important criteria. To accomplish this we need to introduce a measure of observability for a given bi-orthogonal basis (\mathbf{V}, \mathbf{W}) that satisfies $\mathbf{W}^* \mathbf{Q} \mathbf{V} = \mathbf{I}$.

First, we recall that the direct BPOD basis, denoted by \mathbf{J}_1 , is a solution of the following eigenvalue problem

$$\mathbf{G}_C \mathbf{G}_O \mathbf{J}_1 = \mathbf{J}_1 \boldsymbol{\Sigma}^2, \quad (5.24)$$

where the controllability Gramian \mathbf{G}_C can be decomposed according to $\mathbf{G}_C = \mathbf{T}_1 \mathbf{T}_1^*$, and \mathbf{T}_1 represents a matrix whose columns contain the direct snapshots $\mathbf{X}_1(t)$ defined by (A 12). As shown by Rowley (2005), this result can be interpreted within a POD framework, since the direct BPOD basis coincides with the POD basis when the observability Gramian is used as a weight matrix in the scalar product, i.e. $\langle \mathbf{Y}, \mathbf{X} \rangle_{\mathbf{G}_O} = \mathbf{Y}^* \mathbf{G}_O \mathbf{X}$. This means that the first i BPOD modes \mathbf{J}_{1i} form an orthogonal basis with respect to an observability-based scalar product and that this basis maximizes observability of the direct snapshots $\mathbf{X}_1(t)$. In addition, one may show that for the i th BPOD structure \mathbf{J}_{1i} , we obtain

$$\int_0^\infty |\langle \mathbf{X}_1(t), \mathbf{J}_{1i} \rangle_{\mathbf{G}_O}|^2 dt = \boldsymbol{\Sigma}_i^2. \quad (5.25)$$

Hence, the square of the i th Hankel singular value, $\boldsymbol{\Sigma}_i^2$, is equivalent to the observability of the i th BPOD mode, and consequently $\boldsymbol{\Sigma}_1^2 + \boldsymbol{\Sigma}_2^2 + \dots + \boldsymbol{\Sigma}_i^2$ is the observability of a basis consisting of the first i BPOD structures.

We are now in a position to define the observability of a given bi-orthogonal basis (\mathbf{V}, \mathbf{W}) . The snapshots \mathbf{X}_1 are first projected onto the subspace spanned by \mathbf{V} using the

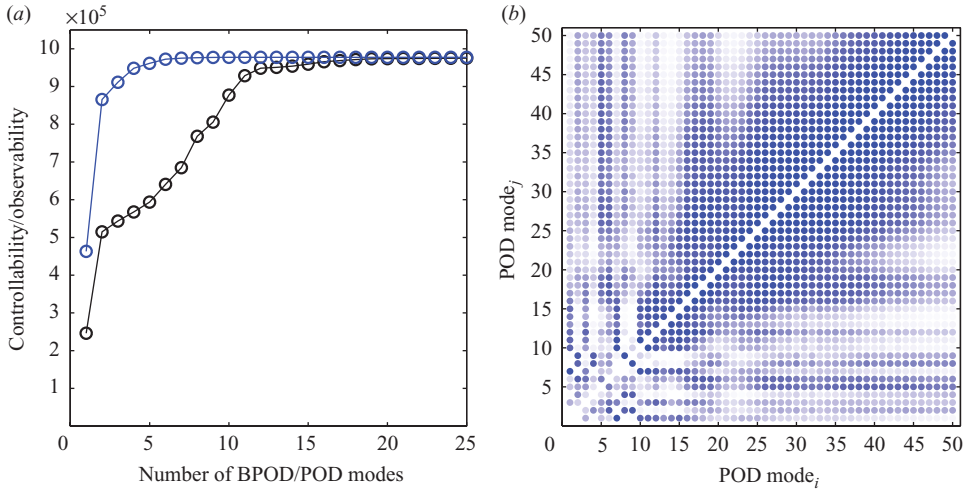


FIGURE 13. (a) Controllability/observability of a BPOD (blue) and POD (black) projection basis. (b) Observability measure of a POD basis according to criterion (5.27).

dual basis \mathbf{W} . This yields projected snapshots $\tilde{\mathbf{X}}_1$ and, hence, a projected controllability Gramian $\tilde{\mathbf{G}}_C = \tilde{\mathbf{T}}_1 \tilde{\mathbf{T}}_1^*$. We proceed by using the true observability measure given by the observability Gramian $\mathbf{G}_O = \mathbf{Q}_1 \mathbf{U}_1 \mathbf{U}_1^* \mathbf{Q}_1$ and subsequently compute the eigenvalues of the large-scale system $\tilde{\mathbf{G}}_C \mathbf{G}_O$. For this, we perform a singular value decomposition of the expression $\mathbf{U}_1^* \mathbf{Q}_1 \tilde{\mathbf{T}}_1$. The sum of the first i eigenvalues $\tilde{\Sigma}_i^2$ (the remaining eigenvalues are zero since the projection onto an i dimensional basis results in a controllability Gramian $\tilde{\mathbf{G}}_C$ of rank i) quantifies the observability of the basis (\mathbf{V}, \mathbf{W}) .

This procedure, applied to a BPOD basis of size i , yields the results shown in figure 13(a) by the blue symbols. This curve is simply the sum of the squared Hankel singular values of the original input–output system. We see that the observability of a basis consisting of i BPOD modes quickly rises to reach a plateau for $i \geq 7$. For the bi-orthogonal POD bases introduced in § 5.4, the results are displayed in the same figure by the black symbols. The observability of these POD-bases increases markedly slower and reaches the plateau, defined by the BPOD bases, only after a minimum of 20 POD modes are considered.

Incidentally, the controllability of a given bi-orthogonal basis (\mathbf{V}, \mathbf{W}) can be defined and analysed in an analogous way. In fact, the adjoint BPOD basis, denoted by \mathbf{K}_1 , is the solution of the eigenvalue problem

$$\mathbf{G}_O \mathbf{G}_C (\mathbf{Q}_1 \mathbf{K}_1) = (\mathbf{Q}_1 \mathbf{K}_1) \Sigma^2, \quad (5.26)$$

where the observability Gramian \mathbf{G}_O can be decomposed according to $\mathbf{G}_O = \mathbf{Q}_1 \mathbf{U}_1 \mathbf{U}_1^* \mathbf{Q}_1$, and \mathbf{U}_1 represents a matrix whose columns contain the adjoint snapshots $\mathbf{Y}_1(t)$ defined by (A 19). As before, an interpretation using a POD framework also holds in this case: the adjoint BPOD basis $\mathbf{Q}_1 \mathbf{K}_1$ corresponds to the POD basis associated with the adjoint snapshots $\mathbf{Y}_1(t)$ and a scalar product based on the controllability Gramian, i.e. $\langle \mathbf{Y}, \mathbf{X} \rangle_{\mathbf{G}_C} = \mathbf{Y}^* \mathbf{G}_C \mathbf{X}$. The adjoint basis is thus orthogonal with respect to a controllability-based scalar product and maximizes controllability of the adjoint snapshots $\mathbf{Y}_1(t)$.

We then propose to define the controllability of a given bi-orthogonal basis as follows. The adjoint snapshots \mathbf{Y}_1 are projected onto the subspace spanned by the dual

basis \mathbf{W} using the primal basis \mathbf{V} . This yields projected snapshots $\tilde{\mathbf{Y}}_1$ and a projected observability Gramian $\tilde{\mathbf{G}}_O = \mathbf{Q}_1 \tilde{\mathbf{U}}_1 \tilde{\mathbf{U}}_1^* \mathbf{Q}_1$. Using the true controllability measure given by the controllability Gramian $\mathbf{G}_C = \mathbf{T}_1 \mathbf{T}_1^*$, we compute the eigenvalues of the large-scale system $\tilde{\mathbf{G}}_O \mathbf{G}_C$. In other words, we perform a singular value decomposition of the expression $\tilde{\mathbf{U}}_1^* \mathbf{Q}_1 \mathbf{T}_1$. The sum of the first i eigenvalues $\tilde{\Sigma}_i^2$ constitutes the controllability of the basis. The results are given in figure 13, showing values identical to those obtained for the observability analysis.

An alternative way to compare the POD and the BPOD basis is to evaluate the non-orthogonality of the POD basis with respect to the observability based scalar product. We recall that the POD basis is orthogonal with respect to the energy-based scalar product while the direct BPOD basis is orthogonal with respect to the observability based scalar product. To compare the two measures, i.e. the energy and the observability measures, we may, for example, evaluate directly the non-orthogonality of the POD basis with respect to the scalar product based on the observability Gramian. Hence, we compute for two POD modes, \mathbf{R}_{1i} and \mathbf{R}_{1j} , the quantity

$$\left| \frac{\mathbf{R}_{1i}^* \mathbf{G}_O \mathbf{R}_{1j}}{\sqrt{\mathbf{R}_{1i}^* \mathbf{G}_O \mathbf{R}_{1i}} \sqrt{\mathbf{R}_{1j}^* \mathbf{G}_O \mathbf{R}_{1j}}} - \delta_{ij} \right|, \quad (5.27)$$

which would be zero if the energy measure based on \mathbf{Q}_1 were equal to the observability measure based on \mathbf{G}_O . Each off-diagonal coefficient of this matrix lies within the interval $[0, 1]$, and the diagonal coefficients are identically zero by construction. If an off-diagonal term is close to zero, the two corresponding POD modes are nearly orthogonal with respect to the observability-based scalar product (in addition to being orthogonal with respect to the energy-based inner product). If, on the other hand, an off-diagonal term is close to one, the two corresponding POD modes are nearly collinear with respect to the observability criterion, even though they are orthogonal with respect to the energy-based inner product.

In figure 13(b) we visualize the matrix defined above for the first 50 POD modes. We observe significant off-diagonal coefficients (indicated by dark blue symbols representing values close to one) which further supports our previous findings and provides additional evidence that POD bases are inferior to BPOD bases when the full-scale input–output behaviour of a fluid system has to be approximated in a lower-dimensional yet efficient manner.

6. Closed-loop control

Among the various bases that have been considered in the previous section, global modes were unsuitable to represent the input–output behaviour while BPOD modes and (to a lesser degree) POD modes were capable of reproducing the transfer function of the full system. In this section we further expound on these findings by considering the complete problem of designing feedback control strategies to stabilize the globally unstable cavity flow. This step constitutes an important step in the performance analysis of reduced-order controllers, since the \mathcal{H}_∞ -error in approximating the exact transfer function gives a first indication of the suitability and effectiveness of the chosen expansion basis but does not allow definite conclusions about the performance of the closed-loop system.

The linearized Navier–Stokes equations (defined in (2.8)) represent the plant to be controlled. For the computation of the control law and the design of the estimator,

a reduced-order model based on (4.3) and (4.7) will be used. This model consists of an unstable subspace which is represented by the unstable global modes and a stable subspace which is modelled by either global modes, BPOD modes or POD modes. After a brief explanation of the LQG framework, the performance of the closed-loop control applied to the linearized numerical simulation will be studied for each of the above bases. In this effort the stability of the compensated system will emerge as a relevant quantity and will be linked to the open-loop behaviour of the model reduction bases.

6.1. The LQG framework

A description that is particularly suited for many fluid dynamical application is based on the LQG framework (Zhou *et al.* 2002). In this formulation, one describes the controlled system by a linear (L) model, a quadratic (Q) cost functional, and an external Gaussian (G) stochastic noise source.

The design of an LQG system consists of two principal steps: the design of a full-state information controller, and the design of an estimator. The estimator's role is to reconstruct, in the best possible manner, the reduced state vector \hat{X} based only on the discrepancy of the measurements from the plant and the estimator. The role of the controller is the forcing of the linear system such that a specified cost objective is reached. The input for this control stems from the estimator. The above-mentioned two principal steps can be taken independent from each other due to the well-known separation principle of control theory (Zhou *et al.* 2002; Kim & Bewley 2007).

We start by designing the full-state information controller and assume a linear relation between the reduced state vector \hat{X} and the control c ,

$$c = \hat{K}\hat{X}. \quad (6.1)$$

The control gain \hat{K} can be determined from a variational principle that minimizes the cost functional $\hat{X}^* \hat{T} \hat{X} + \ell^2 c^2$ subject to the constraint of \hat{X} and c satisfying the governing equations. The user-specified parameter ℓ^2 determines the cost of the control effort. \hat{T} is a Hermitian matrix describing the cost functional. Usually \hat{T} represents the kinetic disturbance energy according to $\hat{T} = \mathbf{V}^* \mathbf{Q} \mathbf{V}$ but it may also be chosen as the square of the measurement signal $\hat{T} = \mathbf{V}^* \mathbf{M}^* \mathbf{M} \mathbf{V}$.

The resulting optimal control gain \hat{K} can be expressed as $\hat{K} = -\hat{\mathbf{C}}\hat{\mathbf{K}}'$ where $\hat{\mathbf{K}}'$ satisfies the algebraic matrix Riccati equation

$$\hat{\mathbf{A}}^* \hat{\mathbf{K}}' + \hat{\mathbf{K}}' \hat{\mathbf{A}} - \hat{\mathbf{K}}' \hat{\mathbf{C}} \hat{\mathbf{C}}^* \hat{\mathbf{K}}' + \frac{\hat{\mathbf{T}}}{\ell^2} = 0. \quad (6.2)$$

With the relation between c and \hat{X} established we can close the loop on the reduced model and formulate the reduced-order closed-loop system as

$$\frac{d\hat{X}}{dt} = (\hat{\mathbf{A}} + \hat{\mathbf{C}}\hat{\mathbf{K}})\hat{X}, \quad (6.3)$$

where $\hat{\mathbf{A}} + \hat{\mathbf{C}}\hat{\mathbf{K}}$ is a stable evolution operator contrary to $\hat{\mathbf{A}}$ which is unstable.

The second step, the design of the estimator, commences with the formulation of the estimator system which will govern the approximation \hat{Y} to the exact reduced state

vector $\hat{\mathbf{X}}$. We have

$$\frac{d\hat{\mathbf{Y}}}{dt} = \hat{\mathbf{A}}\hat{\mathbf{Y}} + \hat{\mathbf{C}}c - \hat{\mathbf{L}}(m - \hat{\mathbf{M}}\hat{\mathbf{Y}}), \quad (6.4)$$

where $c = \hat{\mathbf{K}}\hat{\mathbf{Y}}$ implements the previously defined control term. An additional control term of the form $\hat{\mathbf{L}}(m - \hat{\mathbf{M}}\hat{\mathbf{Y}})$ appears which exerts a forcing on the estimator given by the difference between the measurement m and the measurement $\hat{\mathbf{M}}\hat{\mathbf{Y}}$ of the estimated system. The matrix $\hat{\mathbf{L}}$, referred to as the Kalman gain, determines the manner in which this measurement difference is applied.

Analogous to the control gain $\hat{\mathbf{K}}$, the Kalman gain $\hat{\mathbf{L}}$ can be computed by invoking a variational problem which aims at minimizing the state estimation error while observing the governing equations (6.4). The Kalman gain is then given as $\hat{\mathbf{L}} = -\hat{\mathbf{L}}'\hat{\mathbf{M}}^*$ where $\hat{\mathbf{L}}'$ satisfies the algebraic Riccati equation

$$\hat{\mathbf{A}}\hat{\mathbf{L}}' + \hat{\mathbf{L}}'\hat{\mathbf{A}}^* - \hat{\mathbf{L}}'\hat{\mathbf{M}}^*\hat{\mathbf{M}}\hat{\mathbf{L}}' + \frac{W^2}{G^2}\hat{\mathbf{N}}\hat{\mathbf{N}}^* = 0. \quad (6.5)$$

Here, $\hat{\mathbf{N}}$ and W^2 characterize, respectively, the correlation and the variance of the plant noise while G^2 denotes the variance of the measurement noise.

In a final step, the controlled system and the estimator are combined to form a compensated system. This system is given by the set of equations

$$\frac{d}{dt} \begin{pmatrix} \hat{\mathbf{X}} \\ \hat{\mathbf{Y}} \end{pmatrix} = \begin{pmatrix} \hat{\mathbf{A}} & \hat{\mathbf{C}}\hat{\mathbf{K}} \\ -\hat{\mathbf{L}}\hat{\mathbf{M}} & \hat{\mathbf{A}} + \hat{\mathbf{C}}\hat{\mathbf{K}} + \hat{\mathbf{L}}\hat{\mathbf{M}} \end{pmatrix} \begin{pmatrix} \hat{\mathbf{X}} \\ \hat{\mathbf{Y}} \end{pmatrix}, \quad (6.6a)$$

$$\begin{pmatrix} \hat{\mathbf{X}} \\ \hat{\mathbf{Y}} \end{pmatrix} \Big|_{t=0} = \begin{pmatrix} \mathbf{W}^*\mathbf{Q}\mathbf{X}(0) \\ 0 \end{pmatrix}. \quad (6.6b)$$

We would like to point out that the full-state information controller $\hat{\mathbf{C}}\hat{\mathbf{K}}\hat{\mathbf{X}}$ in (6.3) has been replaced by the controller $\hat{\mathbf{C}}\hat{\mathbf{K}}\hat{\mathbf{Y}}$ using the estimated rather than the exact reduced state vector. In the above system, only the measurements of the full system are used, making this type of control design more promising for a realistic implementation.

An equally convenient and instructive formulation consists of replacing the estimated reduced state vector $\hat{\mathbf{Y}}$ by the state estimation error $\hat{\mathbf{Z}} = \hat{\mathbf{X}} - \hat{\mathbf{Y}}$ (Kim & Bewley 2007). A straightforward manipulation results in

$$\frac{d}{dt} \begin{pmatrix} \hat{\mathbf{X}} \\ \hat{\mathbf{Z}} \end{pmatrix} = \begin{pmatrix} \hat{\mathbf{A}} + \hat{\mathbf{C}}\hat{\mathbf{K}} & -\hat{\mathbf{C}}\hat{\mathbf{K}} \\ 0 & \hat{\mathbf{A}} + \hat{\mathbf{L}}\hat{\mathbf{M}} \end{pmatrix} \begin{pmatrix} \hat{\mathbf{X}} \\ \hat{\mathbf{Z}} \end{pmatrix}, \quad (6.7a)$$

$$\begin{pmatrix} \hat{\mathbf{X}} \\ \hat{\mathbf{Z}} \end{pmatrix} \Big|_{t=0} = \begin{pmatrix} \mathbf{W}^*\mathbf{Q}\mathbf{X}(0) \\ \mathbf{W}^*\mathbf{Q}\mathbf{X}(0) \end{pmatrix}, \quad (6.7b)$$

which demonstrates that due to the block-triangular shape of the composite system matrix in (6.7a), the controller design and estimator design decouple, illustrating the separation principle of control theory. For this reason, the control $\hat{\mathbf{K}}$, determined under the assumption of full-state information, does not have to be recomputed when used with an estimated rather than an exact reduced state vector. The LQG framework insures that $\hat{\mathbf{A}} + \hat{\mathbf{C}}\hat{\mathbf{K}}$ and $\hat{\mathbf{A}} + \hat{\mathbf{L}}\hat{\mathbf{M}}$ are stable while the reduced system $\hat{\mathbf{A}}$ is unstable (Burl 1999).

Note that we use an augmented system in this study where the flow-state includes both the reduced dynamics \hat{X} and the magnitude of the blowing/suction $\rho(t)$:

$$\frac{d}{dt} \begin{pmatrix} \hat{X} \\ \rho \end{pmatrix} = \begin{pmatrix} \hat{A} & 0 \\ 0 & 0 \end{pmatrix} \begin{pmatrix} \hat{X} \\ \rho \end{pmatrix} + \begin{pmatrix} \hat{C} \\ -1 \end{pmatrix} c, \quad (6.8a)$$

$$m = \begin{pmatrix} \hat{M} & 0 \end{pmatrix} \begin{pmatrix} \hat{X} \\ \rho \end{pmatrix}. \quad (6.8b)$$

This step enables us to penalize both the magnitude $\rho(t)$ of blowing/suction and its derivative $c(t) = -d\rho/dt$. Hence, it allows the control effort – and not only its first time-derivative – to be zero at infinite time. For the sake of simplicity, the derivations to follow will tacitly assume this arrangement.

6.2. Small-gain limit

An interesting limit arises in the above equations as the cost of control and the ratio between measurement noise and plant noise tends to infinity, i.e. $\ell^2 \rightarrow \infty$ and $G^2/W^2 \rightarrow \infty$. In this case, any exerted control and estimation effort concentrates on suppressing and estimating the unstable modes of the uncontrolled system.

In this small-gain limit the control and Kalman gains take on the respective special form (see Burl 1999):

$$\hat{K} = (\hat{K}_u \ 0), \quad \hat{K}_u = -\hat{C}_u \hat{K}'_u, \quad (6.9a)$$

$$\hat{L} = \begin{pmatrix} \hat{L}_u \\ 0 \end{pmatrix}, \quad \hat{L}_u = -\hat{L}'_u \hat{M}_u^* \quad (6.9b)$$

with

$$\hat{A}_u^* \hat{K}'_u + \hat{K}'_u \hat{A}_u - \hat{K}'_u \hat{C}_u^* \hat{C}_u \hat{K}'_u = 0, \quad (6.10a)$$

$$\hat{A}_u \hat{L}'_u + \hat{L}'_u \hat{A}_u^* - \hat{L}'_u \hat{M}_u^* \hat{M}_u \hat{L}'_u = 0. \quad (6.10b)$$

Hence the control and Kalman gains reduce in the small gain limit to the gains pertaining only to the unstable modes. The Riccati equations to be solved are therefore of very low dimension. Note that an analytical formulation for the gains in the small-gain limit has been derived in Lauga & Bewley (2003). In addition, it can be shown that the unstable eigenvalues of the uncontrolled system are reflected about the imaginary axis (see Burl 1999) when control is applied. In this case the matrix \hat{T} related to the cost functional and the matrix \hat{N} characterizing the plant noise are no longer significant here and, therefore, do not need to be defined.

To insure small amplitudes in the gains \hat{K} , the location of the actuator is chosen such that $\hat{C} = W^* Q C$ is sufficiently large for the unstable global modes. Higher values of $W^* Q C$ will be attained if the actuator location coincides with regions of high amplitudes of the adjoint modes. The adjoint modes thus indicate the location where the corresponding global modes can be easily excited. This actuator placement procedure ensures reasonable controllability of the unstable global modes, a prerequisite for an effective control design. The values of $\hat{C}_i = W_i^* Q C$ for the global modes $E_{-3}, E_{-2}, \dots, E_8$ are given in table 1. Also, to ensure small amplitudes in the Kalman gain \hat{L} , the sensor location is chosen such that $\hat{M} = M V$ is sufficiently large for the unstable global modes. Under this condition, the unstable global modes are reasonably observable. The values of $\hat{M}_i = M E_i$ for the unstable global modes are given in table 1.

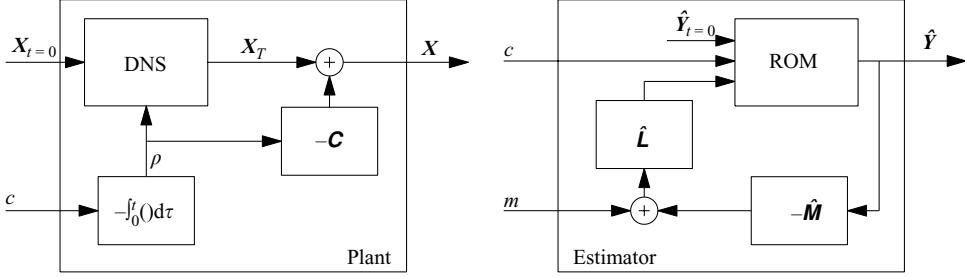


FIGURE 14. Block diagrams for the DNS module (plant) based on (2.8) and the estimator module based on a reduced-order model (ROM) described by (6.4).

The special form of the control and Kalman gain allows the partitioning of the compensated system in matrix form into stable (subscript s) and unstable (subscript u) components as follows:

$$\frac{d}{dt} \begin{pmatrix} \hat{X}_s \\ \hat{X}_u \\ \hat{Z}_u \\ \hat{Z}_s \end{pmatrix} = \begin{pmatrix} \hat{A}_s & \hat{C}_s \hat{K}_u & -\hat{C}_s \hat{K}_u & 0 \\ 0 & \hat{A}_u + \hat{C}_u \hat{K}_u & -\hat{C}_u \hat{K}_u & 0 \\ 0 & 0 & \hat{A}_u + \hat{L}_u \hat{M}_u & \hat{L}_u \hat{M}_s \\ \hline 0 & 0 & 0 & \hat{A}_s \end{pmatrix} \begin{pmatrix} \hat{X}_s \\ \hat{X}_u \\ \hat{Z}_u \\ \hat{Z}_s \end{pmatrix}. \quad (6.11)$$

Thus, provided the reduced models for the plant \hat{X} and for the estimator \hat{Y} are the same, the eigenvalues of the compensated system are those of \hat{A}_s , $\hat{A}_u + \hat{C}_u \hat{K}_u$ and $\hat{A}_u + \hat{L}_u \hat{M}_u$. The performance, usually assimilated as the least stable eigenvalue (long-term smallest decay rate), can then be predicted theoretically.

If the plant \hat{X} is based on the complete set of global modes, the equation acting on \hat{X} in (6.11) is equivalent to the full DNS. If, in addition, the estimated state \hat{Y} is also based on the complete set of global modes, we obtain the ‘best control strategy’ which will be presented in §6.3.3. In this case, we know that in the small-gain limit the spectrum of this compensated system is composed of the stable modes of the uncontrolled simulation (coloured eigenvalues in figure 10) and the reflection of the unstable modes into the stable half-plane. The small-gain limit will be invoked in what follows.

6.3. Analysis of the performance of the compensated system using DNS

For clarity and throughout this investigation, we will present the various control configurations in block-diagram form which will help the reader to evaluate and appreciate the many options and approximations in the design and operation of control strategies. Two main blocks, the plant and the estimator, are principal components of any subsequent control scheme. They are displayed in figure 14. The plant module takes as input the initial condition and the control c and produces a time sequence of state vectors X . Internally, this is accomplished by integrating the control variable c to obtain ρ and by subtracting the solution C of the inhomogeneous problem (with unit forcing at the control location). The internal structure of the DNS module implements the lifting procedure. The estimator module has the task of providing an approximate state vector based on the external measurements m and the internally generated measurements. The Kalman gain \hat{L} is given by (6.9b) and (6.10b). The estimator is driven by a control law c which is the same as the control law that controls the plant.

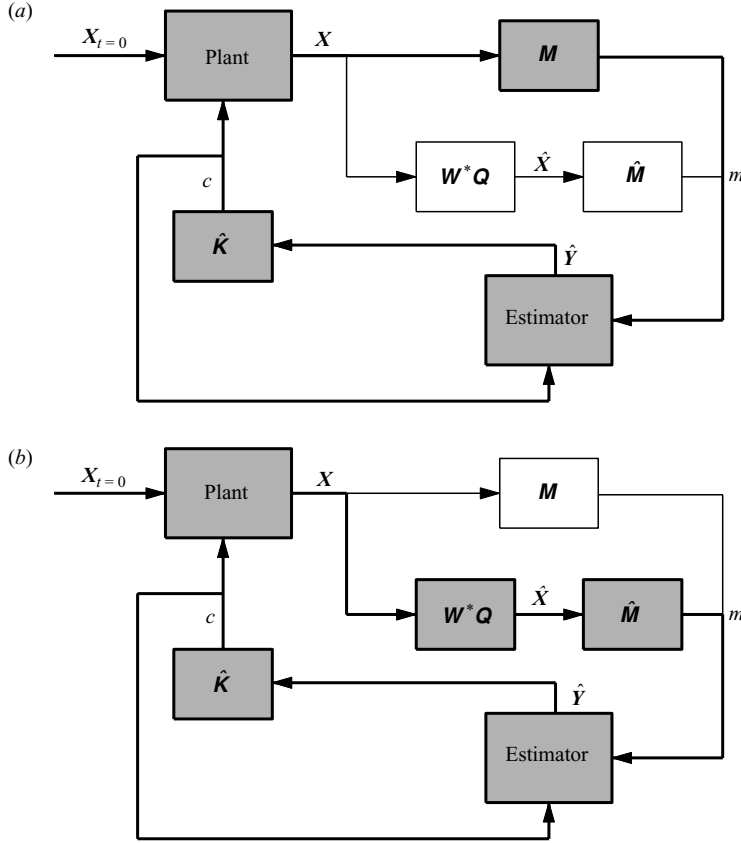


FIGURE 15. Block diagrams demonstrating (a) partial-state information control and (b) ‘best control strategy’. Only the shaded blocks and the thick lines are active in each diagram. The details of the plant and estimator blocks are given in figure 14.

We now turn our attention to the case of control with partial-state information. A schematic of this set-up in form of a block diagram is given in figure 15(a). Once the estimator and controller are defined, the procedure for partial-state information control progresses as follows. The DNS of the flow over a cavity produces a flow field $X(t)$. The sensor, located at the downstream edge of the cavity, extracts from this flow field a skin friction signal via $m(t) = MX(t)$, which constitutes the only flow information available to the compensator. The signal $m(t)$ is subsequently fed into the estimator which in turn yields an estimate $\hat{Y}(t)$ of the flow field. In a final step, the controller converts the estimated flow field $\hat{Y}(t)$ into a control law $c(t)$ according to $c(t) = \hat{K}\hat{Y}(t)$ which governs the blowing/suction strength at the upstream edge of the cavity in the numerical simulation, thus completing the feedback cycle. \hat{K} is given by (6.9a) and (6.10a).

6.3.1. Performance of a reduced-order model based on BPOD modes

We start by assessing the performance of reduced-order model-based estimators where the eight unstable global modes and a series of p BPOD modes are taken into account. In figure 16(a) we plot the energy X^*QX as a function of time for various partial-state control simulations. Each curve represents a different number p of BPOD modes included in the reduced-order model. The uppermost thin line

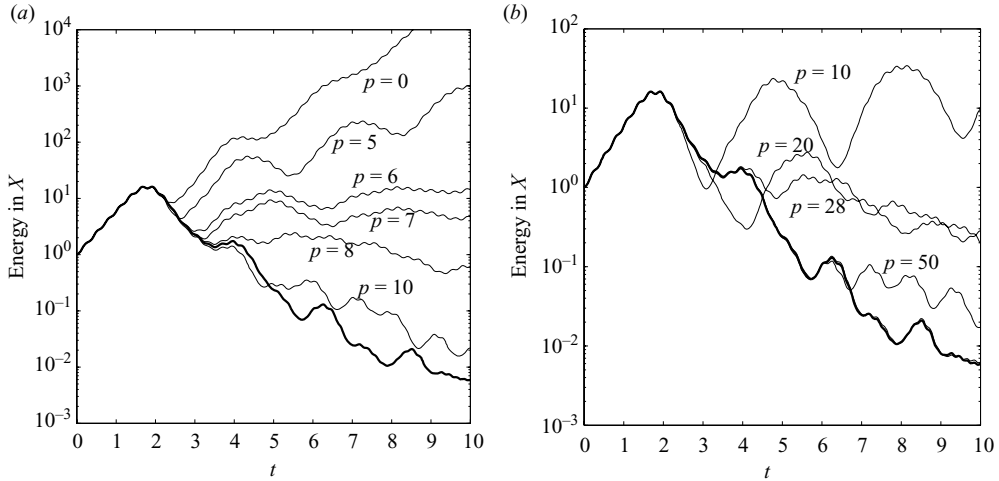


FIGURE 16. Performance of partial-state controller measured as the perturbation kinetic energy versus time for different reduced-order models. (a) The number of included BPOD modes (in addition to the unstable global modes) is denoted by p . (b) The number of included POD modes (in addition to the unstable global modes) is denoted by p .

corresponds to an estimator based on a reduced-order model with the eight unstable global modes and no BPOD modes ($p=0$).

The energy diverges which indicates that this specific reduced-order model (based on unstable global modes only) is not able to provide an accurate estimate of the flow field. Thus, in order to suppress a global instability, modelling only the unstable subspace is not sufficient; rather, a representation of the stable subspace has to be included in the reduced-order model. In view of the results on the reduction of the stable subspace (see § 5), it may come as a surprise that using a few stable modes (for instance only two stable modes are considered in Åkervik *et al.* 2007) will provide sufficient information about the stable subspace to result in a successful control effort. A similar divergent behaviour can be observed for the two next-lower thin lines which correspond to reduced-order models based on five and six BPOD modes, respectively. The divergence though is less severe which we take as an indication that the performance of the estimator improves as the number of included BPOD modes increases. A breakeven point is reached for $p=7$, when the partial-state control manages to keep the energy bounded; for $p=8$ the energy starts to decrease. The sequence of curves depicted in figure 16(a) and labelled by $p=0, 5, 6, \dots$ converge towards a curve (thick solid line) which corresponds to the best control achievable using partial-state control (see § 6.3.3).

6.3.2. Performance of a reduced-order model based on POD modes

We continue our evaluation of reduction bases by studying reduced-order models based on the eight unstable global modes and a series of p POD modes. The kinetic energy of the perturbations is displayed in figure 16(b). A similar behaviour as for the BPOD modes is recovered: when only a few modes are considered in the reduced-order model, the flow cannot be successfully stabilized whereas the energy behaviour converges to the ‘best control strategy’ curve (thick solid line) when more POD modes are added. This behaviour corroborates the results obtained from our analysis of the open-loop response. We however emphasize the fact that the order of the stable

reduced model using POD modes is higher than the one based on BPOD modes which is again in complete agreement with the results of our open-loop analysis.

6.3.3. Convergence towards the ‘best control strategy’

Using reduced-order models based on BPOD and POD modes, we have seen that while the order of the model is increased, the input–output behaviour is better captured and the energy curves converge to a particular curve, the ‘best control strategy’. In this section, we will show that this optimum solution may be obtained through a full-state control strategy, which only involves the unstable global modes in the reduced-order model.

We first emphasize the fact that the estimators and the controllers are based on a reduced model. In particular, we recall the equation governing the approximation of the reduced state (defined in (6.4))

$$\frac{d\hat{Y}}{dt} = \hat{A}\hat{Y} + \hat{C}c - \hat{L}(m - \hat{M}\hat{Y})$$

in which the quantity $(m - \hat{M}\hat{Y})$ is minimized. It is then clear that the relevant quantity to be fed into the estimator is not m which corresponds to the measurement of the whole flow, but a *reduced measure* \hat{m} which corresponds to the measurement arising from the modes comprised in the reduced model, i.e. $\hat{m} = \hat{M}\hat{X}$. This is done in the ‘best control strategy’, illustrated in form of a block diagram in figure 15(b). At first sight it seems similar to the above partial-state information control set-up; but closer inspection shows that the measurement signal to be provided to the estimator is the projected measurement $\hat{m}(t)$ rather than the true measurement $m(t)$. Note that this control strategy requires knowledge of the full flow field and is thus closer to a full-state than to a partial-state information control strategy. It is only considered here as an analysis tool. It is important to note that within the best control strategy the same result (same control law, same simulation) is obtained regardless of the number p of included vectors in the stable subspace. In particular, the best control strategy may be determined with $p = 0$, i.e. with only eight unstable global modes in the reduced-order model of the estimator.

Applying this control strategy, we obtain the thick black lines in figures 16(a) and 16(b). The partial-state simulations in these figures therefore converge towards this curve as the performance of reduced-order models is increased. The energy first increases exponentially up to $t \approx 2$, after which we observe a drastic decrease. More insight into the control’s physics can be gained by looking at the evolution of the pressure field taken along the line $y = 0$. This is shown in the form of an (x, t) plane in figure 17. We notice that the pressure signal first increases, reaching its maximum at time $t \approx 2$. During this initial phase, the vortices, which are low-pressure areas, are convected downstream at the local speed of the base flow. They finally impact the downstream cavity edge and generate an infinitely fast pressure wave which subsequently excites the shear layer at the upstream edge of the cavity. After $t \approx 2$, the pressure signal decreases continuously, and the pressure feedback between the downstream and upstream cavity edge diminishes significantly. Within the linear framework the actuator now generates vortical structures that annihilate the uncontrolled flow field (i.e. the unstable global mode). At the end, the impact of vortical structures on the downstream edge of the cavity is substantially suppressed which in effect eliminates any pressure feedback. From a physical point of view then, the control acts to break the closed pressure feedback-loop that is responsible for the global instability of the uncontrolled flow.

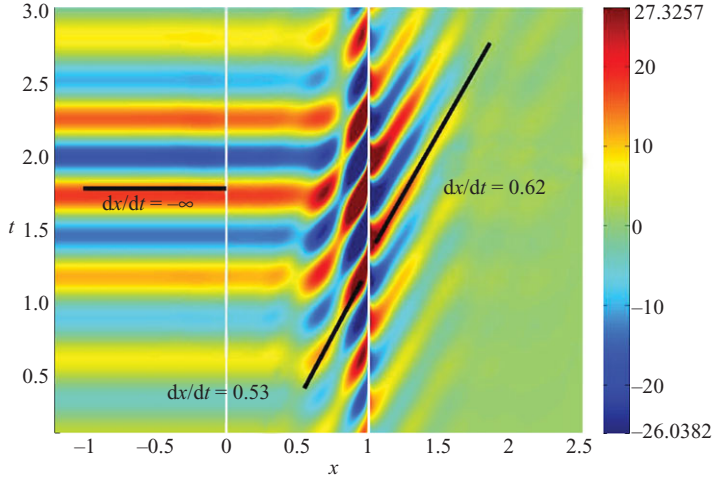


FIGURE 17. Spatio-temporal x - t diagram of pressure $p(x, y=0, t)$ contours with “best control strategy” applied. The initial condition consists of the most unstable global mode. The two vertical white lines indicate the cavity walls. See also movie II in the online version of the paper.

It is interesting to see that even when the ‘best control strategy’ is considered, a certain amount of transient growth is still observed. It is a consequence of the time it takes to estimate the flow state as well as the convective time for the control to be felt. Roughly speaking, the estimator produces a good approximation of the flow field only for $t > 1$, and therefore the control law $c(t)$ which is fed back to the numerical simulation via the controller is only effective for $t > 1$. Vortical structures are then created at the leading edge of the cavity and need approximately $t \approx 1$ to act on the most energetic perturbations located at the trailing edge of the cavity. Thus, the total time before a decrease of perturbation energy due to partial-state measurement control can be expected to be $t \approx 2$.

From these results we conclude that the compensator works optimally if the estimator is provided with the projected measurement $\hat{m}(t)$. To highlight the difference between the full measurement m and the projected (or reduced) measurement \hat{m} we plot the two quantities versus time for the best control strategy with $p=0$ (only eight unstable global modes are used in the reduced-order model) in figure 18(a). We notice that the true measurement $m(t)$ (green line) is significantly different from the projected measurement $\hat{m}(t)$ (black dashed line), particularly in the range $0 < t < 3$. This fact explains the failure of partial-state control with only unstable global modes contained in the reduced-order model. Note also that for $0 < t < 1.7$ the full measurement m is equal to the measurement given by the uncontrolled case (red line). Since the reduced-order model in this case is only based on the unstable global modes, this shows that the stable subspace is excited in a manner that keeps the complete measurement unchanged (see Barbagallo *et al.* 2008).

In addition, this demonstrates that, if the full measurement is to be fed into the estimator (as for partial-state control), the stable subspace needs to be modelled such that the full measurement can be satisfactorily approximated by the reduced-order model. In figure 18(b), it is shown that for partial-state simulations based on a reduced-order model with 13 BPOD modes, the full measurement (green solid line) and the projected measurement \hat{m} (dashed line) agree. When this agreement does not exist, the following arguments furnish an explanation for the failure of the

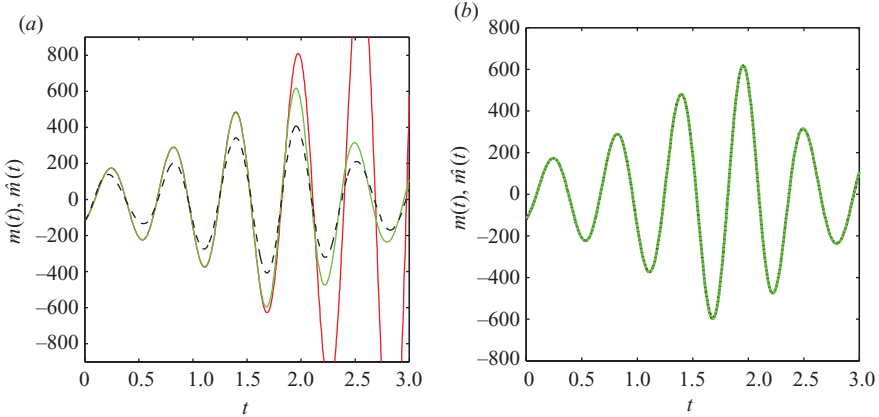


FIGURE 18. Measurement as a function of time using a reduced model based on the unstable global modes with “best control strategy” (a) and using a reduced model based on unstable global modes and 13 BPOD modes with partial-state control (b). Comparison of the true measurement signal (green solid line) with the measurement signal obtained from projecting onto a reduced basis consisting of the unstable global modes and 13 balanced POD modes (black dashed line). Red solid line: full measurement of uncontrolled simulation.

compensator to stabilize the flow: the actuator acts on the modes of the reduced-order model in order to suppress the instabilities but, by doing so, also excites flow states outside the range of the reduced-order model. These states are in turn detected by the sensor and cause a discrepancy between m and \hat{m} which, as demonstrated above, results in an unstable system.

As reported by Ehrenstein & Gallaire (2008), if the control action is restricted to the space spanned by the modes of the reduced-order model, the additional structures (outside the range of the reduced-order model) alluded to above do not arise, and the compensator will be effective in rendering the system stable.

6.3.4. Performance of a reduced model based on global modes

For our flow configuration it has been demonstrated (see §5.2) that an expansion in global modes did not succeed in approximating the exact transfer function to a sufficient degree of accuracy; and it is natural to assume that this shortcoming will also have consequence for the performance of a reduced-order controller based on global modes. Nevertheless, this plan of action has been followed by Åkervik *et al.* (2007) and Ehrenstein & Gallaire (2008) where least stable eigenmodes have been added to augment the expansion basis of the reduced-order model. The same strategy has also been attempted in our case with reduced-order models including up to a few thousand global modes. Alas, a stabilization of the flow could not be obtained, which indicates that the expansion of the stable subspace by the least stable modes does not always yield satisfactory results. This is in agreement with the open-loop behaviour of reduced-order models based on stable global modes which has been found inadequate to approximate the transfer function of the stable subspace.

6.4. Analysis of the performance of the compensated system using stability analysis

The stability of the compensated system has been already alluded to earlier as a desired and necessary property of a successful control design. In this section, we introduce an alternative way of studying the stability of the compensated system by taking advantage of the fact that the input–output behaviour of the numerical

simulation (DNS) can be accurately captured by a low-order system including eight unstable global modes (which model the unstable subspace) and 13 BPOD modes for the stable subspace. This special configuration was chosen since it corresponds to the lowest \mathcal{H}_∞ -error norm (see figure 9). The resulting proxy system will be particularly advantageous, as far as computational efforts are concerned, for our continued investigation and analysis of the stability of the compensated problem using various reduced-order models.

In what follows, we assume that the partial-state simulation is governed by the following system of equations (see (6.6))

$$\frac{d}{dt} \begin{pmatrix} \hat{X}_{\tilde{n},1} \\ \hat{Y}_{\tilde{p},1} \end{pmatrix} = \begin{pmatrix} \hat{A}_{\tilde{n},\tilde{n}} & \hat{C}_{\tilde{n},1} \hat{K}_{1,\tilde{p}} \\ -\hat{L}_{\tilde{p},1} \hat{M}_{1,\tilde{n}} & \hat{A}_{\tilde{p},\tilde{p}} + \hat{C}_{\tilde{p},1} \hat{K}_{1,\tilde{p}} + \hat{L}_{\tilde{p},1} \hat{M}_{1,\tilde{p}} \end{pmatrix} \begin{pmatrix} \hat{X}_{\tilde{n},1} \\ \hat{Y}_{\tilde{p},1} \end{pmatrix}, \quad (6.12a)$$

$$\begin{pmatrix} \hat{X}_{\tilde{n},1} \\ \hat{Y}_{\tilde{p},1} \end{pmatrix} \Big|_{t=0} = \begin{pmatrix} \mathbf{W}^* \mathbf{Q} X(0) \\ 0 \end{pmatrix}, \quad (6.12b)$$

where $\tilde{n} = 13 + 8$ and $\tilde{p} = p + 8$ correspond to the total size of the plant and the estimator. The true measurement is obtained through $m(t) = \hat{M}_{1,\tilde{n}} \hat{X}_{\tilde{n},1}$. We thus have $\hat{A}_{\tilde{n},\tilde{n}}$, $\hat{C}_{\tilde{n},1}$, $\hat{M}_{1,\tilde{n}}$ which remain unchanged since they represent the dynamics of the DNS. On the other hand, $\hat{A}_{\tilde{p},\tilde{p}}$, $\hat{C}_{\tilde{p},1}$, $\hat{M}_{1,\tilde{p}}$ stand for the reduced matrices in the \tilde{p} dimensional reduced basis. In short, the plant is a reduced-order model based on eight unstable global modes and 13 BPOD modes whereas the estimator is based on eight unstable global modes and p stable modes (considering successively BPOD modes, POD modes and stable global modes). The eigenvalues of the coupled matrix which appears in (6.12) may be analysed for different values of p , indicating whether the compensated problem is stable or unstable.

6.4.1. Stability of a reduced-order model based on BPOD modes

In figure 19 we depict the spectrum of the coupled matrix for two cases, taking $p=0$ and $p=13$. In the former case ($p=0$) we obtain five unstable eigenvalues in the half-plane given by $\omega \geq 0$ (the plot is symmetric with respect to $\omega=0$) which leads to the conclusion that the system with an estimator based solely on the unstable global modes is strongly unstable. As the number p of BPOD modes increases, the eigenvalues move towards the stable half-plane. The limiting case is reached for $p=13$ when we retrieve the stable spectrum of the reduced model based on 13 BPOD modes (displayed with black circles in figure 10) plus the four double eigenvalues that result from the reflection of the four unstable global modes about the neutral stability line (four for the estimator and four for the controller).

An interesting feature worth pointing out concerns the non-uniform sensitivity of the eigenvalue location to the quality of the estimator. For example, the eigenvalue located at $(\sigma, \omega) \approx (-0.0324, 16.73)$ is only weakly affected by a decreasing number p of included BPOD modes, whereas the eigenvalue located at $(\sigma, \omega) \approx (-0.890, 10.9)$ for $p=13$ protrudes far into the unstable half-plane as p is reduced. This underlines the fact that robustness of a closed-loop system cannot simply be defined by its least damped eigenvalue.

In figure 20 the amplification rate σ_{max} of the most unstable eigenvalue of the coupled system as a function of the number of considered modes p is shown. For $p=0$ (not shown in figure 20), we find that $\sigma_{max} = 0.53$ which shows again that a partial-state simulation with a reduced-order model including only the eight unstable global modes is strongly unstable. It is interesting to note that as soon as the control is active

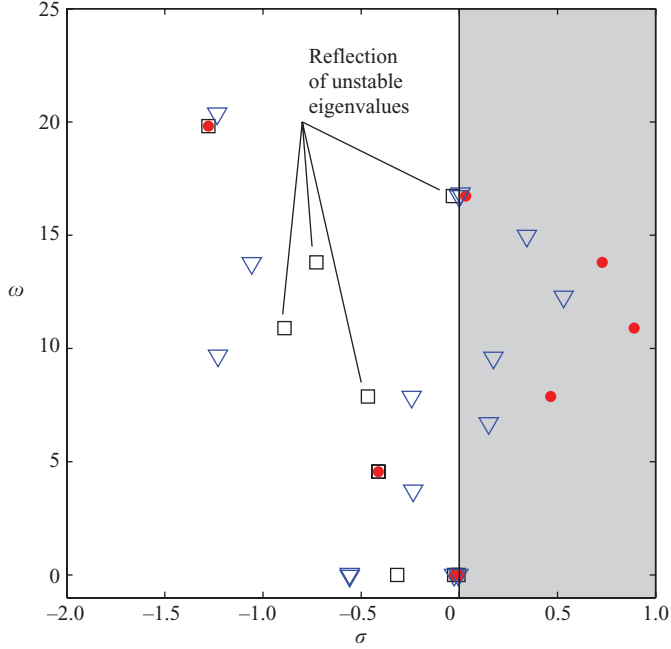


FIGURE 19. Global spectrum of the compensated system for $p=0$ (triangles) and $p=13$ (squares). Red dots correspond to the uncontrolled plant, i.e. eigenvalues of $\hat{\mathbf{A}}_{\bar{n},\bar{n}}$.

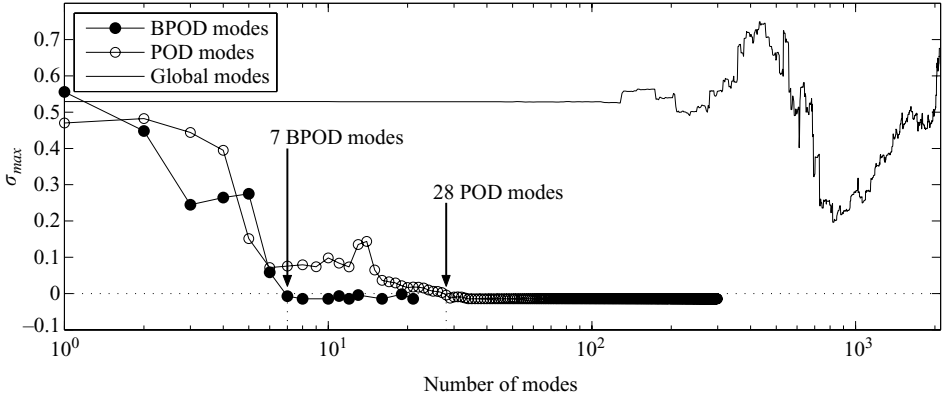


FIGURE 20. Least stable eigenvalue of the compensated system versus the number of included stable modes for BPOD modes (full symbols), POD modes (open circles) and global modes (solid line).

(after $t = 2$) the slope of the energy corresponding to this case (see figure 16) is equal to $2\sigma_{max}$. For $p = 13$ BPOD modes, the amplification rate is $\sigma_{max} = -0.0144$ which is in agreement with the spectra presented in figure 19. Moreover, the partial-state control based on BPOD modes remains unstable up to $p = 6$ suggesting a minimum of seven BPOD modes to stabilize closed-loop simulations. For values of $p \geq 7$, the simulations remain stable, and the amplification rate of the least stable eigenmode converges towards $\sigma_{max} = -0.0144$, a value which is close to the amplification rate $\sigma = -0.00811$ of the least stable eigenmode of the full system.

6.4.2. Stability of a reduced-order model based on POD modes

We now turn our attention to partial-state control systems with estimators that use reduced-order models based on the eight unstable global modes and p POD modes. The procedure is analogous to the one described in §6.4.1 in that, for each number p of POD modes incorporated into the reduced-order model, we compute the eigenvalues of the coupled system (6.12). Results are shown in figure 20 (open circles) where we can see that a POD basis yields an effective estimator once at least 28 POD modes are included in the reduced-order model of the estimator. This is deduced from the fact that the amplification rate σ_{max} of the most unstable eigenvalue of (6.12) is positive for $0 \leq p \leq 27$ and negative for $p \geq 28$. Based on these results we conclude that the POD basis is suboptimal compared to the BPOD basis. Indeed, only seven BPOD modes are needed to arrive at a successful partial-state control system using a reduced-order model, whereas 28 POD modes are necessary to accomplish the same goal.

6.4.3. Stability of a reduced-order model based on global modes

The results of this analysis are given by the solid-line curve in figure 20. For the case $p=0$, i.e. if the reduced-order model includes only the eight unstable global modes, the partial-state control simulation is unstable, and the amplification rate σ_{max} is equal to 0.53, as previously shown. If we then add to the estimator p least stable global modes, the coupled system becomes more unstable (for $p=400$, the amplification rate rises up to $\sigma_{max}=0.75$). This behaviour is followed by a drastic decrease in the amplification rate down to a level of $\sigma_{max} \approx 0.2$ which is obtained using 750 least stable eigenmodes. This result demonstrates that adding more global modes to the estimator improves the coupled system since σ_{max} decreased; at no point, though, do we reach a stable coupled system with $\sigma_{max} < 0$. As a matter of fact, by including even more stable global modes in the reduced-order model of the estimator the performance of the coupled system deteriorates yet again, as is evident by the increasing amplification rate σ_{max} .

7. Summary and conclusions

The incompressible flow over an open square cavity has been studied as a representative example of separated flows. At sufficiently high Reynolds numbers the shear layer atop the cavity exhibits a global instability. It is of general interest to devise effective control strategies to suppress this instability by feeding back measurement signals (taken downstream of the cavity) to actuators which manipulate the flow upstream of the cavity. The design of these control schemes quickly becomes computationally unfeasible due to the complexity of the problem and the resulting size of the matrix equations for the control and estimation gains. A model reduction has to be performed to bring back the construction of a compensated system into the realm of direct design methods. The basis underlying this reduction is a component that is pivotal to the success of the computed control scheme. A general bi-orthogonal projection framework has been developed that allows the analysis of different reduction bases.

The use of global modes for model reduction (see Ehrenstein & Gallaire 2005, 2008; Åkervik *et al.* 2007; Henningson & Åkervik 2008) is common despite the fact that this type of basis may be insufficient and inefficient in representing the input–output behaviour of the compensated system. Even though in Åkervik *et al.* (2007) the studied flow configuration resulted in a stable compensated system based on global

modes, our configuration provides a counter example which suggests that reduced-order modelling based on global modes cannot be generalized to more complex geometry and/or flow physics. In our case, this has been demonstrated by the lack of convergence of reduced transfer functions (based on global mode expansions) towards the exact one. The difficulties of expressing the transfer characteristics between sensor and actuator stems from the non-normality of the linearized Navier–Stokes equations. As a consequence, global modes with a substantial decay rate can still contribute to the input–output behaviour, while weakly damped global modes may not. In other words, the decay rate of global modes is a poor criterion for the inclusion of global modes in a projection basis or in the truncation of the projection basis. Rather, a criterion that accounts for the controllability and observability of each global mode, in addition to its decay rate, is more accurate in assessing which global mode contributes to what extent to the input–output behaviour.

The choice of a more appropriate expansion basis has to address the issues of controllability and observability which is essential in accurately representing the relation between actuator input and sensor output. Balanced modes are designed to accomplish this task by paying equal emphasis to controllability and observability and are thus ideally suited for the low-dimensional representation of the input–output behaviour. Despite this property, their practical computation from numerical simulation poses challenges that take significant effort to overcome. These challenges are mainly related to stability issues of the reduced system which, in turn, is related to the slow convergence of the approximate Gramians towards their exact solution when fluid motion on a slow time scale (such as for modes that have a significant component inside the cavity) is present and needs to be resolved. In this case, excessively long sequences of snapshots are necessary which puts strain on computational resources and memory requirements.

POD modes are often used as a technique to arrive at a reduced-order model. They overemphasize controllability at the expense of observability, but are still capable of expressing the input–output behaviour albeit not as efficiently as balanced modes. Their advantage, however, lies in the simplicity of computing them: a simple snapshot method suffices. In our case, reduced-order models based on POD modes, even though higher-dimensional than models based on BPOD modes, showed improved robustness when used in the design of reduced-order controllers. The approximation of the open-loop transfer function by POD modes shows adequate convergence towards the exact transfer function, even though, compared to balanced modes, many more POD modes are necessary to achieve the same level of accuracy, as measured in the \mathcal{H}_∞ -norm.

In summary, both BPOD and POD modes are suitable choices for reducing the input–output relation of a control problem to a manageable size, where a choice has to be made between (i) an expansion in as few modes as possible, in which case BPOD modes prevail, and (ii) a somewhat more robust computational procedure to determine a larger reduced-order model, in which case POD modes appear to be a reasonable choice.

One should keep in mind, though, that flow over an open cavity – with the sensor located in the wake of the actuator – is particularly amenable to a reduced-order controller based on POD modes since the flow structures identified by the POD reflect the convective transport between the control and measurement device and thus are able to represent the input–output behaviour of the compensated system. For more challenging configurations, where this convective link between actuator and sensor is not given, the discrepancy between POD and BPOD modes may be drastically

higher, and balanced modes may markedly surpass POD modes in their ability and efficiency in rendering the flow stable by reduced-order control schemes.

We like to thank Olivier Marquet and François Gallaire for helpful discussions and comments during the course of this work. The third author gratefully acknowledges financial support from the ‘chaires d’excellence’ programme of the Agence Nationale de la Recherche (ANR). The staff at the Café Daguerre is thanked for indulging our many animated discussions and work sessions.

Appendix. Reduced-order models based on balanced proper orthogonal decomposition

A.1. Projected equations

In this section, we will show that the system of equations (5.1) which governs the dynamics of the stable subspace can be written in the classical state–space form (defined in (5.10)).

Equation (5.1) can be cast in the form

$$\begin{pmatrix} \mathbf{Q}_1 & 0 \\ 0 & 0 \end{pmatrix} \frac{d}{dt} \begin{pmatrix} \mathbf{X}_1 \\ \mathbf{X}_2 \end{pmatrix} = \begin{pmatrix} \mathbf{A}_{s1} & \mathbf{A}_{s2}^* \\ \mathbf{A}_{s2} & 0 \end{pmatrix} \begin{pmatrix} \mathbf{X}_1 \\ \mathbf{X}_2 \end{pmatrix} + \begin{pmatrix} \mathbf{Q}_1 & 0 \\ 0 & 0 \end{pmatrix} \begin{pmatrix} \mathbf{C}_{s1} \\ \mathbf{C}_{s2} \end{pmatrix} c, \quad (\text{A } 1a)$$

$$m = (\mathbf{M}_1 \quad 0) \begin{pmatrix} \mathbf{X}_1 \\ \mathbf{X}_2 \end{pmatrix}, \quad (\text{A } 1b)$$

where \mathbf{X}_1 denotes the velocity fields and \mathbf{X}_2 stands for the corresponding pressure field. In what follows, the subscript $_1$ applied to a vector field will denote the part of the state vector composed of the velocity field only. For the design of control and model reduction schemes we need to reformulate the above equations into standard state–space form. To this end we multiply the momentum equation by $\mathbf{A}_{s2}\mathbf{Q}_1^{-1}$, which yields – assuming that $\mathbf{A}_{s2}\dot{\mathbf{X}}_1=0$ – an expression for the pressure in terms of the velocity field

$$\mathbf{X}_2 = -(\mathbf{A}_{s2}\mathbf{Q}_1^{-1}\mathbf{A}_{s2}^*)^{-1} [(\mathbf{A}_{s2}\mathbf{Q}_1^{-1}\mathbf{A}_{s1})\mathbf{X}_1 + \mathbf{A}_{s2}\mathbf{C}_{s1}]. \quad (\text{A } 2)$$

This relation can be used to eliminate the explicit divergence constraint and allows us to write the governing linearized equations in the desired form

$$\frac{d\mathbf{X}_1}{dt} = \mathbf{P}_1\mathbf{A}_{s1}\mathbf{X}_1 + \mathbf{P}_1\mathbf{Q}_1\mathbf{C}_{s1}c, \quad (\text{A } 3a)$$

$$m = \mathbf{M}_1\mathbf{X}_1, \quad (\text{A } 3b)$$

where

$$\mathbf{P}_1\mathbf{Q}_1 = \mathbf{I} - \mathbf{Q}_1^{-1}\mathbf{A}_{s2}^*(\mathbf{A}_{s2}\mathbf{Q}_1^{-1}\mathbf{A}_{s2}^*)^{-1}\mathbf{A}_{s2} \quad (\text{A } 4)$$

is the projection matrix onto the divergence-free space. This projector is reminiscent of the steps taken by a projection method to correct a preliminary divergent velocity field towards a solenoidal one. Starting from the right of the above expression, we take the divergence (\mathbf{A}_{s2}) of the velocity field, then solve a Poisson equation ($(\mathbf{A}_{s2}\mathbf{Q}_1^{-1}\mathbf{A}_{s2}^*)^{-1}$) for the corrective pressure, and finally take the gradient of the pressure ($\mathbf{Q}_1^{-1}\mathbf{A}_{s2}^*$) and subtract this component from the preliminary velocity field. This procedure then renders the velocity field divergence free. In short, if \mathbf{X}_1 is a non-divergence-free velocity field, then $\mathbf{P}_1\mathbf{Q}_1\mathbf{X}_1$ is the projection of \mathbf{X}_1 onto the divergence-free subspace; if \mathbf{X}_1 is already divergence free, we have $\mathbf{P}_1\mathbf{Q}_1\mathbf{X}_1 = \mathbf{X}_1$. It is important to point out

that the projector $\mathbf{P}_1 \mathbf{Q}_1$ is also used to properly adjust an initial condition which does not satisfy $\mathbf{u} \cdot \mathbf{n} = 0$ along some boundaries like solid walls. It is equally noteworthy that \mathbf{P}_1 is a Hermitian operator, so that we can take advantage of the relation $\mathbf{P}_1^* = \mathbf{P}_1$.

Defining $\mathbf{A}_1 = \mathbf{P}_1 \mathbf{A}_{s1}$ and $\mathbf{C}_1 = \mathbf{P}_1 \mathbf{Q}_1 \mathbf{C}_{s1}$, we recover (5.10).

A.2. Controllability Gramian

We consider the controllability Gramian \mathbf{G}_C defined, for our system, as

$$\mathbf{G}_C = \int_0^\infty e^{\mathbf{A}_1 t} \mathbf{C}_1 \mathbf{C}_1^* e^{\mathbf{A}_1^* t} dt. \quad (\text{A } 5)$$

Let us consider a fully controllable system, which means that all divergence-free states \mathbf{X}_1 may be reached by a control law $c(t)$. Furthermore, let \mathbf{X}_1 be a divergence-free field. We will demonstrate that the minimum energy $\int_0^\infty c^*(t)c(t) dt$ to reach \mathbf{X}_1 is equal to $\mathbf{X}_1^* \mathbf{G}_C^{-1} \mathbf{X}_1$. We know that there exists a unique vector $\boldsymbol{\xi}$ such that $\mathbf{X}_1 = \mathbf{G}_C \boldsymbol{\xi}$ is satisfied and note that $\boldsymbol{\xi} = \mathbf{G}_C^{-1} \mathbf{X}_1$, even though the matrix \mathbf{G}_C may be degenerate. After considering the control law $c(t) = \mathbf{C}_1^* e^{\mathbf{A}_1^* t} \boldsymbol{\xi}$, it may easily be verified that this control law yields \mathbf{X}_1 as $t \rightarrow \infty$

$$\int_0^\infty e^{\mathbf{A}_1 t} \mathbf{C}_1 c(t) dt = \mathbf{X}_1. \quad (\text{A } 6)$$

One may furthermore show that this specific $c(t)$ yields the minimum energy to reach \mathbf{X}_1 . This minimum energy reads

$$\int_0^\infty c^*(t)c(t) dt = \boldsymbol{\xi}^* \int_0^\infty e^{\mathbf{A}_1 t} \mathbf{C}_1 \mathbf{C}_1^* e^{\mathbf{A}_1^* t} dt \boldsymbol{\xi}, \quad (\text{A } 7a)$$

$$= \boldsymbol{\xi}^* \mathbf{G}_C \boldsymbol{\xi}, \quad (\text{A } 7b)$$

$$= \mathbf{X}_1^* \mathbf{G}_C^{-1} \mathbf{X}_1, \quad (\text{A } 7c)$$

which verifies our proposition above.

The controllability Gramian \mathbf{G}_C can be computed by solving a matrix Lyapunov equation (see Antoulas 2005); its actual solution by standard numerical techniques, however, quickly becomes prohibitively demanding on computational resources and algorithms. Instead, the Gramian can be approximated by a discrete integration in time according to

$$\mathbf{G}_C = \int_0^\infty \mathbf{X}_1(t) \mathbf{X}_1^*(t) dt, \quad (\text{A } 8a)$$

$$\approx \sum_{i \geq 0} \mathbf{X}_1(t_i) \mathbf{X}_1^*(t_i) \delta_i \quad (\text{A } 8b)$$

with $\mathbf{X}_1(t) = e^{\mathbf{A}_1 t} \mathbf{C}_1$ and δ_i denoting appropriate quadrature coefficients. The flow fields $\mathbf{X}_1(t_i)$ at discrete instances t_i can be obtained by the integration in time of the linear system

$$\dot{\mathbf{X}}_1 = \mathbf{A}_1 \mathbf{X}_1, \quad (\text{A } 9a)$$

$$\mathbf{X}_1(0) = \mathbf{C}_1 \quad (\text{A } 9b)$$

or

$$\begin{pmatrix} \mathbf{Q}_1 & 0 \\ 0 & 0 \end{pmatrix} \frac{d}{dt} \begin{pmatrix} \mathbf{X}_1 \\ \mathbf{X}_2 \end{pmatrix} = \begin{pmatrix} \mathbf{A}_{s1} & \mathbf{A}_{s2}^* \\ \mathbf{A}_{s2} & 0 \end{pmatrix} \begin{pmatrix} \mathbf{X}_1 \\ \mathbf{X}_2 \end{pmatrix}, \quad \mathbf{X}_1(0) = \mathbf{P}_1 \mathbf{Q}_1 \mathbf{C}_1. \quad (\text{A } 10)$$

This system, corresponding to the direct problem (cf (5.1)), can straightforwardly be solved by our linearized DNS programme. As a result, the controllability Gramian

may therefore be written as

$$\mathbf{G}_C = \mathbf{T}_1 \mathbf{T}_1^*, \quad (\text{A } 11)$$

where

$$\mathbf{T} = [\mathbf{X}(0\Delta t)\sqrt{\delta_0} \quad \mathbf{X}(1\Delta t)\sqrt{\delta_1} \quad \dots]. \quad (\text{A } 12)$$

Although we use an equidistant spacing between the snapshots, a non-equidistant spacing between them is conceivable to increase the accuracy of the integration in time or to account for localized features that require higher temporal resolution. The dimension of \mathbf{T} is $n \times n_d$ where n and n_d denote the number of degrees of freedom in \mathbf{X} and the number of direct snapshots, respectively. Note that \mathbf{T}_1 which represents the velocity components of \mathbf{T} is of dimension $n_1 \times n_d$ with n_1 as the number of degrees of freedom of the velocity field. The quadrature coefficients δ_i correspond to the fourth-order Simpson method.

The above demonstration shows that the controllability Gramian \mathbf{G}_C can be thought of as the spatial correlation matrix for the evolution of an impulsive forcing at the actuator location (the initial condition is $\mathbf{PQ}_1\mathbf{C}_1$). We further conclude that the eigenvectors of $\mathbf{G}_C\mathbf{Q}_1$ are the commonly used POD modes for our particular initial condition. These POD modes represent flow structures that are easily triggered by control input since they require rather small amounts of control energy to be excited.

A.3. Observability Gramian

The observability Gramian is defined as

$$\mathbf{G}_O = \int_0^\infty e^{\mathbf{A}_1^* t} \mathbf{M}_1^* \mathbf{M}_1 e^{\mathbf{A}_1 t} dt. \quad (\text{A } 13)$$

With \mathbf{X}_1 denoting a divergence-free flow field, we will show that the measurement energy is equal to $\int_0^\infty m^*(t)m(t) dt = \mathbf{X}_1^* \mathbf{G}_O \mathbf{X}_1$. The response of the sensor to our initial state \mathbf{X}_1 is simply given by $m(t) = \mathbf{M}e^{\mathbf{A}_1 t} \mathbf{X}_1$, and the following expression

$$\int_0^\infty m^*(t)m(t) dt = \int_0^\infty \mathbf{X}_1^* e^{\mathbf{A}_1^* t} \mathbf{M}_1^* \mathbf{M}_1 e^{\mathbf{A}_1 t} \mathbf{X}_1 dt, \quad (\text{A } 14a)$$

$$= \mathbf{X}_1^* \mathbf{G}_O \mathbf{X}_1 \quad (\text{A } 14b)$$

corroborates our statement above.

Analogous to the previous section, the observability Gramian \mathbf{G}_O can only be meaningfully defined for stable linear systems and can then be determined as the solution of a matrix Lyapunov equation. For the same reason as above, however, the solution based on a Lyapunov equation becomes excessively expensive, thus prompting us to compute an approximation of the observability Gramian based on a discrete integration in time. \mathbf{G}_O can be rewritten as

$$\mathbf{G}_O = \int_0^\infty \mathbf{Q}_1 \mathbf{P}_1 e^{\mathbf{A}_{s1}^* P_1 t} \mathbf{M}_1^* \mathbf{M}_1 e^{P_1 \mathbf{A}_{s1} t} \mathbf{P}_1 \mathbf{Q}_1 dt, \quad (\text{A } 15a)$$

$$= \mathbf{Q}_1 \left(\int_0^\infty e^{P_1 \mathbf{A}_{s1}^* t} \mathbf{P}_1 \mathbf{Q}_1 (\mathbf{Q}_1^{-1} \mathbf{M}_1^*) \mathbf{M}_1 \mathbf{Q}_1^{-1} \mathbf{Q}_1 \mathbf{P}_1 e^{\mathbf{A}_{s1} P_1 t} dt \right) \mathbf{Q}_1, \quad (\text{A } 15b)$$

$$= \mathbf{Q}_1 \left(\int_0^\infty \mathbf{Y}_1(t) \mathbf{Y}_1^*(t) dt \right) \mathbf{Q}_1, \quad (\text{A } 15c)$$

$$\approx \mathbf{Q}_1 \left(\sum_{i \geq 0} \mathbf{Y}_1(t_i) \mathbf{Y}_1^*(t_i) \delta_i \right) \mathbf{Q}_1, \quad (\text{A } 15d)$$

where $\mathbf{Y}_1(t) = e^{\mathbf{P}_1 \mathbf{A}_{s1}^* t} \mathbf{P}_1 \mathbf{Q}_1 (\mathbf{Q}_1^{-1} \mathbf{M}_1^*)$ and δ_i denotes, as before, the quadrature coefficients for the evaluation of the time integral. The flow fields $\mathbf{Y}_1(t)$ can be obtained by integration in time of the adjoint system defined as

$$\frac{d\mathbf{Y}_1}{dt} = \mathbf{P}_1 \mathbf{A}_{s1}^* \mathbf{Y}_1, \quad (\text{A } 16a)$$

$$\mathbf{Y}_1(0) = \mathbf{P}_1 \mathbf{Q}_1 (\mathbf{Q}_1^{-1} \mathbf{M}_1^*) \quad (\text{A } 16b)$$

or

$$\begin{pmatrix} \mathbf{Q}_1 & 0 \\ 0 & 0 \end{pmatrix} \frac{d}{dt} \begin{pmatrix} \mathbf{Y}_1 \\ \mathbf{Y}_2 \end{pmatrix} = \begin{pmatrix} \mathbf{A}_{s1}^* & \mathbf{A}_{s2}^* \\ \mathbf{A}_{s2} & 0 \end{pmatrix} \begin{pmatrix} \mathbf{Y}_1 \\ \mathbf{Y}_2 \end{pmatrix}, \quad \mathbf{Y}_1(0) = \mathbf{P}_1 \mathbf{Q}_1 (\mathbf{Q}_1^{-1} \mathbf{M}_1^*). \quad (\text{A } 17)$$

This adjoint initial-value problem is solved by our adjoint linearized numerical simulation code, i.e. (5.1) in which \mathbf{A} is replaced by its transpose conjugate \mathbf{A}^* .

As a result, the observability Gramian may therefore be rewritten as

$$\mathbf{G}_O = \mathbf{Q}_1 \mathbf{U}_1 \mathbf{U}_1^* \mathbf{Q}_1, \quad (\text{A } 18)$$

where

$$\mathbf{U} = [\mathbf{Y}(0\Delta t)\sqrt{\delta_0} \quad \mathbf{Y}(1\Delta t)\sqrt{\delta_1} \dots]. \quad (\text{A } 19)$$

The dimension of \mathbf{U} is $n \times n_a$ where n_a stands for the number of adjoint snapshots. The quadrature coefficients δ_i correspond again to the fourth-order Simpson method.

REFERENCES

- AHUJA, S. & ROWLEY, C. W. 2008 Low-dimensional models for feedback stabilization of unstable steady states. *AIAA Paper 2008-553*.
- ÅKERVIK, E., HEPFFNER, J., EHRENSTEIN, U. & HENNINGSON, D. S. 2007 Optimal growth, model reduction and control in a separated boundary-layer flow using global modes. *J. Fluid Mech.* **579**, 305–314.
- AMESTOY, P. R., DUFF, I. S., KOSTER, J. & L'EXCELLENT, J.-Y. 2001 A fully asynchronous multifrontal solver using distributed dynamic scheduling. *SIAM J. Matrix Anal. Appl.* **23** (1), 15–41.
- ANTOULAS, A. C. 2005 *Approximation of Large-Scale Dynamical Systems*. SIAM.
- ANTOULAS, A., SORENSEN, D. & GUGERCIN, S. 2001 A survey of model reduction methods for large-scale systems. *Contemp. Math.* **280**, 193–219.
- BAGHERI, S., BRANDT, L. & HENNINGSON, D. S. 2009a Input–output analysis, model reduction and control of the flat-plate boundary layer. *J. Fluid Mech.* **620**, 263–298.
- BAGHERI, S., HEPFFNER, J., SCHMID, P. J. & HENNINGSON, D. S. 2009b Input–output analysis and control design applied to a linear model of spatially developing flows. *Appl. Mech. Rev.* **62** (2), 020803-1-27.
- BAI, Z. 2002 Krylov subspace techniques for reduced-order modelling of large-scale dynamical systems. *Appl. Numer. Math.* **43**, 9–44.
- BARBAGALLO, A., SIPP, D., JACQUIN, L. & SCHMID, P. J. 2008 Control of an incompressible cavity flow using a reduced model based on global modes. In *Fifth AIAA Theoretical Fluid Mechanics Conference*, Seattle. *AIAA paper 2008-3904*.
- BARKLEY, D., GOMES, M. G. & HENDERSON, R. D. 2002 Three-dimensional instability in flow over a backward-facing step. *J. Fluid Mech.* **473**, 167–190.
- BERGMAN, M., CORDIER, L. & BRANCHER, J.-P. 2006 Optimal rotary control of the cylinder wake using POD reduced-order model. *Phys. Fluids* **17**, 305–314.
- BERKOOZ, G., HOLMES, P. & LUMLEY, J. L. 1993 The proper orthogonal decomposition in the analysis of turbulent flows. *Annu. Rev. Fluid Mech.* **25**, 539–575.
- BEWLEY, T. R. 2001 Flow control: new challenges for a new renaissance. *Prog. Aerosp. Sci.* **37**, 21–58.

- BLACKBURN, H. M., BARKLEY, D. & SHERWIN, S. J. 2008 Convective instability and transient growth in flow over a backward-facing step. *J. Fluid Mech.* **603**, 271–304.
- BRES, G. A. & COLONIUS, T. 2008 Three-dimensional instabilities in compressible flow over open cavities. *J. Fluid Mech.* **599**, 309–339.
- BUFFONI, M., CAMARRI, S. & IOLLO, A. 2006 Low-dimensional modelling of a confined three-dimensional wake flow. *J. Fluid Mech.* **569**, 141–150.
- BURL, J. B. 1999 *Linear Optimal Control. \mathcal{H}_2 and \mathcal{H}_∞ Methods*. Addison-Wesley.
- CATTAFESTA, L. N., SONG, Q., WILLIAMS, D. R., ROWLEY, C. W. & ALVI, F. 2008 Active control of flow-induced cavity oscillations. *Prog. Aerosp. Sci.* **44**, 459–502.
- CATTAFESTA, L. N., WILLIAMS, D. R., ROWLEY, C. W. & ALVI, F. S. 2003 Review of active flow control of flow-induced cavity resonance. *AIAA Paper 2003-3567 33rd AIAA Fluid Dyn. Conf.*, Orlando, FL, June 2003.
- CHEVALIER, M., HÖPFFNER, J., ÅKERVIK, E. & HENNINGSON, D. S. 2007 Linear feedback control and estimation applied to instabilities in spatially developing boundary layers. *J. Fluid Mech.* **588**, 163–187.
- CROUCH, J. D., GARBARUK, A. & MAGIDOV, D. 2007 Predicting the onset of flow unsteadiness based on global instability. *J. Comput. Phys.* **224**, 924–940.
- DELVILLE, J., CORDIER, L. & BONNET, J. P. 1998 Large-scale structure identification and control in turbulent shear flows. In *Flow Control: Fundamentals and Practice* (eds M. Gad-el-Hak, A. Pollard, J.-P. Bonnet) pp. 199–273. Springer.
- DING, Y. & KAWAHARA, M. 1999 Three-dimensional linear stability analysis of incompressible viscous flows using finite element method. *Intl J. Numer. Meth. Fluids* **31**, 451–479.
- EHRENSTEIN, U. & GALLAIRE, F. 2005 On two-dimensional temporal modes in spatially evolving open flows. *J. Fluid Mech.* **536**, 209–218.
- EHRENSTEIN, U. & GALLAIRE, F. 2008 Optimal perturbations and low-frequency oscillations in a separated boundary-layer flow. In *Fifth AIAA Theoretical Fluid Mechanics Conference*, Seattle. *AIAA paper 2008-4232*.
- FAURE, T. M., ADRIANOS, P., LUSSEYRAN, F. & PASTUR, L. 2007 Visualizations of the flow inside an open cavity at medium-range Reynolds numbers. *Exp. Fluids* **42**, 169–184.
- FREUND, R. 2003 Model reduction methods based on Krylov subspaces. *Acta Numer.* **12**, 267–319.
- GALLETTI, B., BOTTARO, A., BRUNEAU, C. H. & IOLLO, A. 2007 Accurate model reduction of transient and forced wakes. *Eur. J. Mech. B* **26**, 354–366.
- HENNINGSON, D. S. & ÅKERVIK, E. 2008 The use of global modes to understand transition and perform flow control. *Phys. Fluids* **20**, 031302.
- HÖPFFNER, J., CHEVALIER, M., BEWLEY, T. R. & HENNINGSON, D. S. 2005 State estimation in wall-bounded flow systems. Part 1. Laminar flows. *J. Fluid Mech.* **534**, 263–294.
- HÖGBERG, M., BEWLEY, T. R. & HENNINGSON, D. S. 2003 Linear feedback control and estimation of transition in plane channel flow. *J. Fluid Mech.* **481**, 149–175.
- ILAK, M. & ROWLEY, C. W. 2006 Reduced-order modelling of channel flow using travelling POD and balanced POD. In *Third AIAA Flow Control Conference*, San Francisco, *AIAA paper 2006-3194*.
- ILAK, M. & ROWLEY, C. W. 2008 Modelling of transitional channel flow using balanced proper orthogonal decomposition. *Phys. Fluids* **20**, 034103.
- JACKSON, C. P. 1987 A finite-element study of the onset of vortex shedding in flow past variously shaped bodies. *J. Fluid Mech.* **182**, 23–45.
- JOSHI, S. S., SPEYER, J. L. & KIM, J. 1997 A systems theory approach to the feedback stabilization of infinitesimal and finite-amplitude disturbances in plane Poiseuille flow. *J. Fluid Mech.* **332**, 157–184.
- KIM, J. 2003 Control of turbulent boundary layers. *Phys. Fluids* **15**, 1093–1105.
- KIM, J. & BEWLEY, T. R. 2007 A linear systems approach to flow control. *Annu. Rev. Fluid Mech.* **39**, 383–417.
- LALL, S., MARSDEN, J. E. & GLAVASKI, S. 2002 A subspace approach to balanced truncation for model reduction of nonlinear control systems. *Intl J. Robust Nonlinear Control* **12**, 519–535.
- LAUGA, E. & BEWLEY, T. R. 2003 The decay of stabilizability with Reynolds number in a linear model of spatially developing flows. *Proc. R. Soc. Lond. A* **459**, 2077–2095.
- LAUGA, E. & BEWLEY, T. R. 2004 Performance of a linear robust control strategy on a nonlinear model of spatially developing flows. *J. Fluid Mech.* **512**, 343–374.

- LEE, K. H., CORTELEZZI, L., KIM, J. & SPEYER, J. 2001 Application of reduced-order controller to turbulent flows for drag reduction. *Phys. Fluids* **13**, 1321–1330.
- LEHOUCQ, R. B. & SCOTT, J. A. 1997 Implicitly restarted Arnoldi methods and subspace iteration. *SIAM J. Matrix Anal. Appl.* **23**, 551–562.
- LEHOUCQ, R. B., SORENSEN, D. C. & YANG, C. 1998 *ARPACK Users Guide: Solution of Large Scale Eigenvalue Problems with Implicitly Restarted Arnoldi methods*. SIAM Publishing.
- LUMLEY, J. L. 1970 *Stochastic Tools in Turbulence*. Academic Press.
- MA, Z., AHUJA, S. & ROWLEY, C. W. Reduced order models for control of fluids using the eigensystem realization algorithm. *Theor. Comput. Fluid Dyn.* (submitted)
- MARQUET, O., SIPP, D., CHOMAZ, J.-M. & JACQUIN, L. 2008 Amplifier and resonator dynamics of a low-Reynolds-number recirculation bubble in a global framework. *J. Fluid Mech.* **605**, 429–443.
- MOIN, P. & BEWLEY, T. R. 1994 Feedback control of turbulence. *Appl. Mech. Rev.* **47** (6), S3–S13.
- MOORE, B. 1981 Principal component analysis in linear systems: controllability, observability, and model reduction. *IEEE Trans. Autom. Control* **26**, 17–32.
- NOACK, B., AFANASIEV, K., MORZYNSKI, M., TADMOR, G. & THIELE, F. 2003 A hierarchy of low-dimensional models for the transient and post-transient cylinder wake. *J. Fluid Mech.* **497**, 335–363.
- NOACK, B. R. & ECKELMANN, H. 1994 A global stability analysis of the steady and periodic cylinder wake. *J. Fluid Mech.* **270**, 297–330.
- OR, A. C. & SPEYER, J. L. 2008 Model reduction of input–output dynamical systems by proper orthogonal decomposition. *J. Guid. Control Dyn.* **31–2**, 322–328.
- PODVIN, B., FRAIGNEAU, Y., LUSSEYRAN, F. & GOUGAT, P. 2006 A reconstruction method for the flow past an open cavity. *ASME J. Fluids Engng* **128**, 531–540.
- ROWLEY, C. W. 2005 Model reduction for fluids using balanced proper orthogonal decomposition. *Intl J. Bifurcation Chaos* **15**, 997–1013.
- ROWLEY, C. W., AHUJA, S., TAIRA, K. & COLONIUS, T. 2008 Closed-loop control of leading edge vorticity on 3d wings: simulations and low-dimensional models. In *Thirty-eighth Fluid Dynamics Conference and Exhibit*, Seattle. *AIAA paper 2008-3981*.
- ROWLEY, C. W. & WILLIAMS, D. R. 2006 Dynamics and control of high-Reynolds-number flow over open cavities. *Annu. Rev. Fluid Mech.* **38**, 251–276.
- SAMIMY, M., DEBIASI, M., CARABALLO, E., SERRANI, A., YUAN, X., LITTLE, J. & MYATT, J. 2007 Feedback control of subsonic cavity flows using reduced-order models. *J. Fluid Mech.* **579**, 315–346.
- SCHERPEN, J. M. 1993 Balancing for nonlinear systems. *Syst. Control Lett.* **21**, 143–153.
- SIPP, D. & LEBEDEV, A. 2007 Global stability of base and mean flows: a general approach and its applications to cylinder and open cavity flows. *J. Fluid Mech.* **593**, 333–358.
- SIROVICH, L. 1987 Turbulence and the dynamics of coherent structures. *Q. Appl. Math.* **45**, 561–590.
- TADMOR, G., NOACK, B., MORZYNSKI, M. & SIEGEL, S. 2004 Low-dimensional models for feedback flow control. Part II. Control design and dynamical estimation. *AIAA Paper 2004-2409*.
- THEOFILIS, V. 2000 Advances in global linear instability analysis of nonparallel and three-dimensional flows. *Prog. Aerosp. Sci.* **39**, 249–315.
- WILCOX, K. & PERAIRE, J. 2002 Balanced model reduction via proper orthogonal decomposition. *AIAA J.* **40**, 2323–2330.
- ZEBIB, A. 1987 Stability of a viscous flow past a circular cylinder. *J. Engng Math.* **21**, 155–165.
- ZHOU, K., SALOMON, G. & WU, E. 1999 Balanced realization and model reduction for unstable systems. *Intl J. Robust Nonlinear Control* **9**, 183–198.
- ZHOU, K., SALOMON, G. & WU, E. 2002 *Robust and Optimal Control*. Prentice Hall.
- ZIELINSKA, J. A. & WESFREID, J. E. 1995 On the spatial structure of global modes in wake flow. *Phys. Fluids* **7** (6), 1418–1424.

5 Article 2

Input-output measures for model reduction and closed-loop control: application to global modes

Input-output measures for model reduction and closed-loop control: application to global modes

By ALEXANDRE BARBAGALLO^{1,2},
DENIS SIPP¹ AND PETER J. SCHMID²

¹ONERA-DAFE, 8 rue des Vertugadins, 92190 Meudon, France

²Laboratoire d'Hydrodynamique (LadHyX), CNRS-Ecole Polytechnique, 91128 Palaiseau, France

(Received 25 August 2010)

Feedback control applications for flows with a large number of degrees of freedom require the reduction of the full flow model to a system with significantly fewer degrees of freedom. This model-reduction process is accomplished by Galerkin projections using a reduction basis composed of modal structures that ideally preserve the input-output behavior between actuators and sensors and ultimately result in a stabilized compensated system. In this study, global modes are critically assessed as to their suitability as a reduction basis, and the globally unstable, two-dimensional flow over an open cavity is used as a test case. Four criteria are introduced to select from the global spectrum the modes that are included in the reduction basis. Based on these criteria, four reduced-order models are tested by computing open-loop (transfer function) and closed-loop (stability) characteristics. Even though weak global instabilities can be suppressed, the concept of reduced-order compensators based on global modes does not demonstrate sufficient robustness to be recommended as a suitable choice for model reduction in feedback control applications. The investigation also reveals a compelling link between frequency-restricted input-output measures of open-loop behavior and closed-loop performance, which suggests the departure from mathematically-motivated \mathcal{H}_∞ -measures for model reduction toward more physically-based norms; a particular frequency-restricted input-output measure is proposed in this study which more accurately predicts the closed-loop behavior of the reduced-order model.

1. Introduction

As active control strategies are increasingly applied to high-dimensional and complex flow configurations arising in industrial and academic settings, model reduction becomes a key technology. The goal of model reduction is the projection of the high-degrees-of-freedom flow dynamics onto a smaller system which is subsequently used in estimating the flow state based on measurement information. There is a considerable amount of choice for the bases of this projection which in the past yielded a wide range of reduction strategies but also varied results. In this article we specifically consider global modes for the reduction basis, develop measures and tools to assess their effectiveness and comment on their suitability for feedback control applications based on reduced-order models.

In our study we will concentrate on a flow configuration that exhibits oscillator behavior in the form of a self-sustained cyclic perturbation dynamics which is rather insensitive to stochastic outside influences. A global stability analysis of this type of flows exhibits

unstable global modes and provides frequencies and growth rates as well as the spatial shapes of the self-sustained structures. In many industrial applications, oscillatory behavior is typical and often a source of acoustic radiation and/or structural excitation which can cause material fatigue or damage. For this reason, passive and active control strategies to weaken or suppress these oscillations are of great interest.

Passive control strategies, such as mean flow modifications, do not add energy to the system and are particularly attractive due to their simplicity of implementation and efficiency (see Strykowski & Sreenivasan 1990; Giannetti & Luchini 2007; Marquet *et al.* 2008). However, while these strategies can successfully extend the parameter range of stable flows, they ultimately may not be able to prevent the onset of instabilities as a critical parameter value is exceeded. In this case, due to their time-independent design, they can no longer influence the unsteady nature of the flow. Active control, on the other hand, adds energy to the system in form of a predesigned actuation (open-loop control) or an actuation using flow information from sensor measurements (closed-loop control). Among the closed-loop control theories, the Linear Quadratic Gaussian (LQG) strategy (see Burl 1999; Zhou *et al.* 2002) has been considered for and successfully applied to the feedback control of unsteady flows (see, e.g., Bewley & Liu 1998; Kim & Bewley 2007; Barbagallo *et al.* 2009; Bagheri *et al.* 2009a; Sipp *et al.* 2010). This method is based on a linear description of the flow behavior and includes an estimator that optimally reconstructs an approximate flow field from sensor measurements. This approximate flow state provides the basis on which an optimal control law is designed. The optimization of the estimation and control leads to two Riccati equations which can only be solved for a rather low number of degrees-of-freedom. It is thus desirable and paramount to reduce the size of the compensator (i.e. the combined estimator and controller) using a procedure known as model reduction. However, since this reduction procedure implies a loss of information, it is of critical importance to retain only the relevant features of the original model in the reduced-order model. The key feature to be conserved is the input-output behavior, i.e. the effect of the actuator on the sensor; its conservation is a sufficient condition for the success of LQG control design based on reduced-order models.

Among the various procedures to obtain a reduced-order model, the Galerkin projection method has been widely used in flow control applications. This method consists in projecting the Navier-Stokes equations (or Linearized Navier-Stokes equations) onto spatial modal structures (Antoulas *et al.* 2001; Antoulas 2005). The choice of these modes is pivotal and changes considerably the properties of the resulting reduced-order model (see Bagheri *et al.* 2009b; Barbagallo *et al.* 2009). A common choice is to use Proper Orthogonal Decomposition (POD) modes as the projection basis. These modes are optimal in describing the most energetic structures of the flow (Lumley 1970; Sirovich 1987; Berkooz *et al.* 1993) but yield reduced-order models which are not optimal for closed-loop control applications since they do not take into account the flow's observability by the sensors. This difficulty is overcome by projecting onto Balanced Proper Orthogonal Decomposition (BPOD) modes which, by construction, give equal emphasis to the controllability and observability of the flow (Moore 1981; Rowley 2005). Closed-loop control with reduced-order compensators based on POD and BPOD modes have been studied on various globally unstable configurations (see Barbagallo *et al.* 2009; Ahuja & Rowley 2010) where stabilization of the flow could be achieved within the limitations of the linear approximation.

Reduced-order models obtained by a Galerkin projection onto global modes have also been considered in previous work in an attempt to control globally unstable flows. The flow over a shallow cavity has been successfully stabilized in Åkervik *et al.* (2007); Henningson & Åkervik (2008) using a reduced-order model merely based on the unstable and

a few stable global modes. A similar model, however, failed at suppressing the instabilities over an open square cavity, no matter the numbers of stable global modes added to the reduced-order model (Barbagallo *et al.* 2009). This failure has been attributed to the ineffectiveness of global modes in capturing the input-output behavior of the original system which could further be linked to the strong non-normality of the global modes yielding, in turn, extreme controllability coefficients. This feature has subsequently been observed by Ehrenstein *et al.* (2010) in a study of the separated flow over a shallow bump. Introducing the so-called *double-projection* (i.e., an orthogonal projection for the actuator combined with a bi-orthogonal projection for the remaining terms in the governing equations) in an attempt to reduce in magnitude the coefficients arising from the projection of the actuator, Ehrenstein *et al.* (2010) were able to stabilize the separated flow.

In face of these diverse and possibly conflicting results, it seems helpful and beneficial to assess and clarify the suitability of global modes as a reduction basis in closed-loop control design for globally unstable flows. This is the primary aim of this article. A secondary, and equally important, objective is the development of appropriate input-output measures that allow the most efficient design of reduced-order models. For example, balanced truncation, one of the most effective techniques for model reduction in feedback control applications, minimizes the \mathcal{H}_∞ -error between the full and reduced transfer function (see, e.g., Antoulas 2005); yet, it may appear too stringent and limiting to focus on the worst-case error over all frequencies and to tacitly neglect the flow response contained in other frequencies. Our present studies suggest frequency-restricted input-output measures that reflect physical attributes of the underlying fluid dynamics which in turn result in more effective reduced-order models.

We will begin with a brief description of the flow configuration (§ 2) together with the mathematical formulation of our problem. After a short outline of closed-loop control and model reduction techniques (§ 3), we will introduce and motivate selection criteria for the inclusion of global modes in a reduced-order model (§ 4). Open-loop transfer functions and stability properties of the compensated system will aid in assessing the effectiveness of the criteria and, more generally, the limitations of reduced-order model based on global modes (§ 5). A representative case ($Re = 7500$) will be treated in detail; key properties of the analysis will then be investigated for a range of Reynolds numbers (§ 6). A summary and concluding remarks will complete this article.

2. Flow configuration and governing equations

The flow configuration chosen to address the suitability of global modes for closed-loop control applications is the two-dimensional incompressible flow over an open square cavity. The geometry and control set-up is shown in figure 1 and is identical to the one studied in Barbagallo *et al.* (2009). The flow enters the domain from the left with a uniform horizontal velocity \mathbf{U}_∞ after which a boundary layer develops. It then detaches at the left side of the cavity and forms a shear layer instability if the critical Reynolds number (based on the incoming velocity and the length/depth D of the cavity) exceeds $Re_c = 4140$ (see Sipp & Lebedev 2007). The shear layer separates the recirculation motion inside the cavity from the external flow. Unstable flows that are characterized by self-sustained oscillatory motion, like the open cavity flow at supercritical Reynolds numbers, are often referred to as oscillators within a global stability framework. In this present study, we will use active feedback control schemes and attempt to stabilize the flow for marginal and supercritical Reynolds numbers ranging from $Re = 4140$ to $Re = 7500$.

The essential mechanism for the development of a global instability is based on a

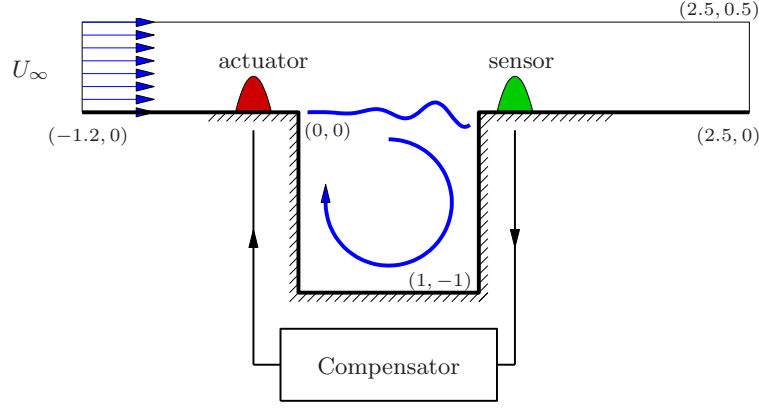


FIGURE 1. Sketch of flow over an open cavity.

combination of the linear amplification of specific infinitesimal perturbations followed by their saturation due to nonlinear effects once finite-amplitudes have been reached. In the present approach we aim at stabilizing the flow in its linear regime, i.e., under conditions when the small perturbation amplitudes justify the use of a linearized model of the flow. This model consists of the Navier-Stokes equations linearized about a base flow $\mathbf{u}_0 = (u_0, v_0)$. This base flow, which represents a solution of the nonlinear Navier-Stokes equations, is unstable to perturbations and thus may be computed using a Newton-Raphson technique. The linearized evolution equations for the perturbation field $\mathbf{u} = (u, v, p)$ are then derived and nondimensionalized using the length of the cavity D and the incoming uniform velocity \mathbf{U}_∞ . They read

$$\frac{\partial \mathbf{u}}{\partial t} + (\mathbf{u} \cdot \nabla) \mathbf{u}_0 + (\mathbf{u}_0 \cdot \nabla) \mathbf{u} = -\nabla p + \frac{1}{Re} \Delta \mathbf{u} \quad (2.1a)$$

$$\nabla \cdot \mathbf{u} = 0 \quad (2.1b)$$

where ∇ (resp. Δ) is the gradient (resp. the Laplacian) operator. The above equations are spatially discretized using finite elements of Taylor-Hood type (P2-P2-P1) implemented in the software Freefem++ (Hecht *et al.* 2005). The discretized system of equations can formally be written in matrix form as

$$\mathbf{Q} \frac{d\mathbf{X}}{dt} = \mathbf{A}\mathbf{X} \quad (2.2)$$

where $\mathbf{X} = (\mathbf{U} \ \mathbf{V} \ \mathbf{P})^T$ is the state vector composed of the streamwise velocity \mathbf{U} , the normal velocity \mathbf{V} and the pressure \mathbf{P} . The matrix \mathbf{A} represents the linearized Navier-Stokes operator while the matrix \mathbf{Q} contains the weights arising from the discretization by finite elements. For our case, the total number of degrees of freedom of the discretized system (i.e., the size of the matrices \mathbf{Q} and \mathbf{A}) is approximately $n = 900,000$. The weight matrix \mathbf{Q} can also be used for defining a discrete scalar product based on a kinetic energy norm according to

$$\|\mathbf{X}\|_2^2 = \langle \mathbf{X}, \mathbf{X} \rangle = \mathbf{X}^* \mathbf{Q} \mathbf{X} \quad (2.3)$$

where $*$ denotes the transpose conjugate operator. The actuation on the flow by the controller is modeled as a Gaussian body force on the vertical velocity. This forcing is spatially localized near the upstream edge of the cavity where it has a distinct effect on the shear layer and, consequently, on the instability mechanism. Approximating a realistic actuator requires its spatial extent to be small compared to the size of the cavity; we

choose

$$v(x, y) = \exp \left[-\frac{(x - x_0)^2 + (y - y_0)^2}{2\sigma^2} \right]$$

with $x_0 = -0.1$, $y_0 = 0.02$ and $\sigma = 0.0849$. These specific values define a Gaussian function of unit amplitude and width 0.2. Using a body force (instead of a lifting procedure) has the advantage of a direct comparison with previous work (Åkervik *et al.* 2007; Ehrenstein *et al.* 2010) and results in a simplified formulation of the control problem compared to a true actuation at the wall (see Barbagallo *et al.* 2009). The full control effort is obtained by multiplying the spatial Gaussian profile by a temporal scalar function $u(t)$ which transforms equation (2.2) into a forced problem

$$\mathbf{Q} \frac{d\mathbf{X}}{dt} = \mathbf{A}\mathbf{X} + \mathbf{Q}\mathbf{B}_2 u \quad (2.4)$$

where \mathbf{B}_2 is a real vector of dimension n arising from the spatial discretization of the actuator using the finite-element bases.

Within a closed-loop (feedback) framework the temporal control law $u(t)$ is to be computed in real time using real-time measurements of the system. In the present work we choose to measure the wall-shear stress at the downstream edge of the cavity, expressed mathematically as

$$m(t) = \int_{x=1}^{x=1.1} \left. \frac{\partial u}{\partial y} \right|_{y=0} dx,$$

which, after finite-element discretization, yields $m = \mathbf{C}\mathbf{X}$ with \mathbf{C} as a real column vector of length n extracting the wall-shear stress from the full state vector \mathbf{X} . This concludes the state-space formulation of the flow control problem given by

$$\mathbf{Q} \frac{d\mathbf{X}}{dt} = \mathbf{A}\mathbf{X} + \mathbf{Q}\mathbf{B}_2 u, \quad (2.5a)$$

$$m = \mathbf{C}\mathbf{X}. \quad (2.5b)$$

In what follows, this system of equations will form the basis for control design and model reduction efforts.

3. Closed-loop control design and model reduction

At Reynolds number above the critical one, instabilities arise that ultimately lead to exponential growth in kinetic perturbation energy within the linear framework. In order to suppress these instabilities we consider an active closed-loop control strategy that exploits real-time flow information from the sensor and manipulates the flow via the actuator such that a user-specified objective (the suppression of instabilities) is achieved with optimal effort.

3.1. Linear Quadratic Gaussian (LQG) control

The design of such a control strategy takes advantage of the widely used Linear Quadratic Gaussian (LQG) theory (Burl 1999; Zhou *et al.* 2002). The underlying principle of this theory is graphically presented in figure 2. In this sketch the plant represents the inherent (uncontrolled) dynamics of the flow, in our case governed by (2.4). The output from the sensor, i.e., the measurement $m(t) = \mathbf{C}\mathbf{X}$, represents the sole information on which the control law will be based. This measurement is then fed into an estimator which recovers an approximate state $\hat{\mathbf{Y}}$ which is subsequently multiplied by the control gain $\hat{\mathbf{K}}$ to produce

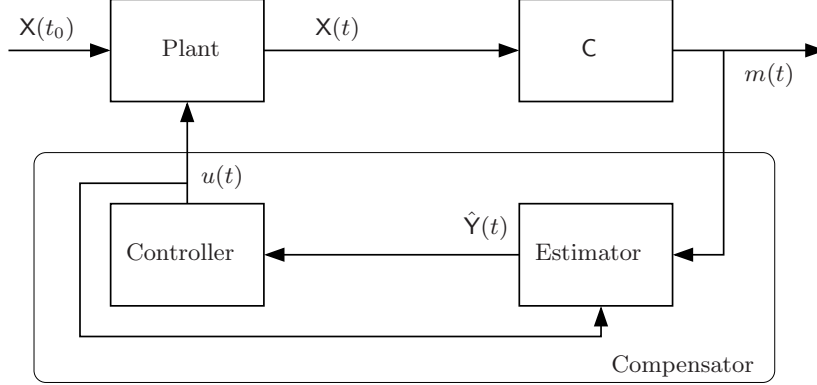


FIGURE 2. Block diagram of feedback control set-up showing the plant, estimator and controller components.

a control signal $u(t)$; this signal is finally fed back into the flow system. The objective of the control is the minimization of a given cost functional, in our case, the kinetic energy of the perturbation. The design of both an estimator — in particular, the Kalman gain \hat{L} which optimally exploits measurement information to recover state information — and a controller requires the solution of algebraic Riccati equations, a matrix equation that can only be solved by direct techniques for a rather limited number of degrees of freedom. For this reason, the feedback loop from measurement $m(t)$ to control $u(t)$ via the estimator and controller has to be based on a substitute system of significantly fewer degrees of freedom, i.e., on a reduced-order model (ROM). With this reduced-order model in place, the Riccati equations for the control gain K and Kalman gain \hat{L} can be solved by standard techniques (e.g., Datta 2003).

3.2. Model reduction basics

The goal of model reduction is to represent pertinent features of the original system (2.5) with a reduced number of states. In its most common form this reduction is accomplished by a Petrov-Galerkin projection of the full system onto an identified basis. The choice of this basis then determines the effectiveness and accuracy of the reduced system. In the present study, we will evaluate the performance of reduced-order models obtained from a projection onto global modes and assess their efficiency when incorporated into a feedback control loop. To this end, we gather a selection of n_r global modes as columns of the $n \times n_r$ matrix V . The details of the selection will be left undetermined at this point, but will be specified later. The state X will then be expressed in this basis as

$$X(t) = V\hat{X}(t). \quad (3.1)$$

where \hat{X} is a column vector of length n_r , denoting the reduced state (the symbol $\hat{\cdot}$ shall be used to indicate reduced variables or matrices). The i^{th} component of \hat{X} represents the dynamics of the corresponding i^{th} global mode $V_{(:,i)}$.

Defining a second basis W that is bi-orthogonal to V according to $W^*QV = I$, the reduced state variable \hat{X} is given by

$$\hat{X} = W^*QX. \quad (3.2)$$

The reduced system in state-space form, obtained by applying the Petrov-Galerkin pro-

Reynolds number Re	5250	5500	6000	6500	7000	7500
number of unstable modes	4	4	6	6	6	8
number of computed stable modes	1324	1391	1511	1636	1764	1875

TABLE 1. Number of unstable and computed stable global modes for flow over an open square cavity at various Reynolds numbers considered in this study.

jection to (2.5), reads

$$\frac{d\tilde{X}}{dt} = \hat{\Lambda}\tilde{X} + \hat{B}_2 u \quad (3.3a)$$

$$m = \hat{C}\tilde{X} \quad (3.3b)$$

where the reduced system, control and measurement matrices are respectively given by

$$\hat{\Lambda} = W^* A V, \quad \hat{B}_2 = W^* Q B_2, \quad \hat{C} = C V. \quad (3.4)$$

The choice of global modes as a reduction basis yields a diagonal reduced system matrix $\hat{\Lambda}$ containing the associated eigenvalues of the selected global modes.

4. Reduced-order models based on global modes

To study the linear stability of non-parallel two- or three-dimensional base flows a global stability analysis is commonly applied. It consists of a decomposition of the perturbation into a complex exponential time dependence and a purely spatial structure, referred to as a global mode:

$$X(t) = \tilde{X} \exp(\lambda t) \quad \text{where} \quad \lambda = \sigma + i\omega. \quad (4.1)$$

The asymptotic temporal behavior of each global mode is then governed by its growth rate σ and frequency ω . Positive growth rates ($\sigma > 0$) indicate global instability.

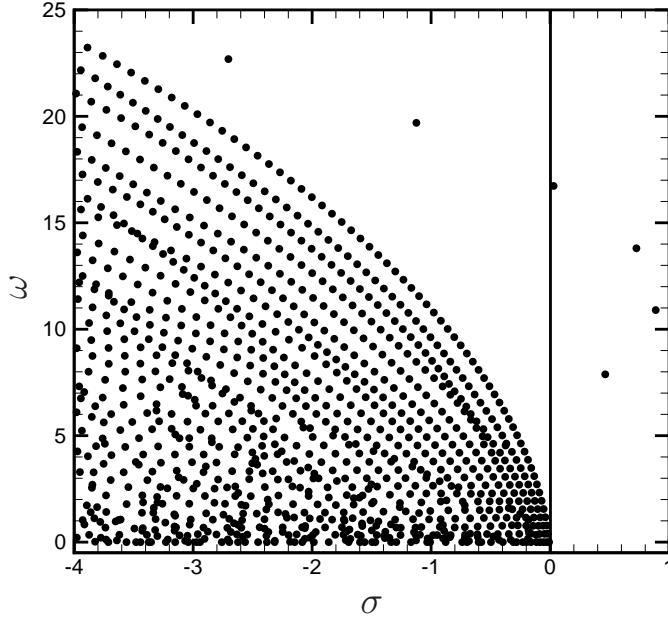
4.1. Direct and adjoint global modes

The assumption (4.1) transforms the initial-value problem (2.2) into a generalized eigenvalue problem for the eigenvalue λ and the global mode \tilde{X} . We have

$$A\tilde{X} = \lambda Q\tilde{X} \quad (4.2)$$

which has to be solved by iterative techniques owing to the size ($\sim 10^6 \times 10^6$) of the matrices A and Q . A shift-invert Arnoldi algorithm (see Lehoucq & Scott 1997) has been used to determine the global spectrum, where we restricted our computations to growth rates above $\sigma = -4$. Details of the numerical procedure can be found in Barbagallo *et al.* (2009). Depending on the Reynolds number Re the number of eigenvalues found in this domain varies from 1328 to 1883 modes (see table 1). For eigensolutions with decay rates lower than $\sigma \approx -4$ first effects of round-off errors are encountered which exacerbate until they entirely inhibit computations of global modes beyond $\sigma < -8$ due to the non-normality of the matrix A . Moreover, the availability of $\mathcal{O}(10^3)$ global modes for a model reduction effort was deemed sufficient for the reduced-order model to still qualify as “reduced”; ideally, much fewer modes should be necessary.

The matrix A is non-normal, resulting in a set of non-orthogonal global modes (Schmid & Henningson 2000). An additional basis W – the set of adjoint global modes – is thus necessary. The adjoint global modes are solutions of the adjoint eigenvalue problem

FIGURE 3. Global spectrum for flow over an open cavity at $Re = 7500$.

$$\mathbf{A}^* \tilde{\mathbf{X}}^+ = \lambda^* \mathbf{Q} \tilde{\mathbf{X}}^+. \quad (4.3)$$

The adjoint global modes are denoted by $\tilde{\mathbf{X}}^+$; the eigenvalues of the adjoint problem are simply the complex conjugate of the direct eigenvalues λ . After proper normalization, the direct and adjoint global modes satisfy the bi-orthogonality relation

$$\langle \tilde{\mathbf{X}}_i^+, \tilde{\mathbf{X}}_j \rangle = \tilde{\mathbf{X}}_i^{+*} \mathbf{Q} \tilde{\mathbf{X}}_j = \delta_{ij} \quad (4.4)$$

with δ_{ij} as the Kronecker symbol.

4.2. Analysis of the spectrum

Since we wish to construct reduced-order models based on global modes, it will be instructive to analyze the properties and characteristics of the eigensolutions of \mathbf{A} . We will focus on the case $Re = 7500$, but would like to stress that equivalent results have been obtained for lower Reynolds numbers. The global spectrum (restricted to the half-plane $\omega \geq 0$ due to symmetry) for $Re = 7500$ is displayed in figure 3. At this parameter setting, we have eight unstable global modes with $\sigma > 0$ (four appear in the ω -half-plane in figure 3). The spatial structure of the most unstable global mode is presented in figure 4, visualized by contours of the streamwise velocity. It is spatially localized and describes a Kelvin-Helmholtz-type instability of the shear-layer across the cavity.

In contrast to the unstable eigenspace, the stable subspace (consisting of modes with $\sigma < 0$) is high-dimensional; see table 1. In addition, while the unstable global modes had a clear physical explanation in terms of observable instabilities, the interpretation of stable modes is far less obvious. More insight can be gained by computing the energy-weighted x -centroid x_c for each global mode defined by

$$x_c = \frac{\iint_{\Omega} x e \, dx \, dy}{\iint_{\Omega} e \, dx \, dy} \quad (4.5)$$

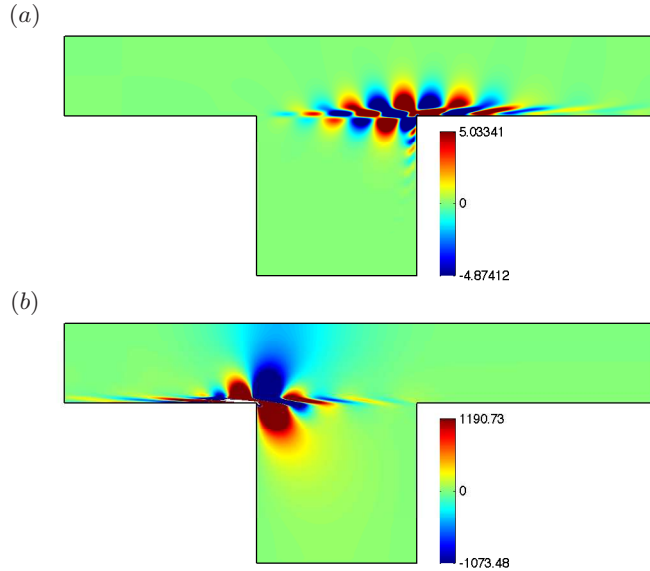


FIGURE 4. Selected direct and adjoint global modes for flow over an open cavity at $Re = 7500$. (a) Most unstable direct global mode, (b) adjoint global mode associated with the most unstable direct global mode in (a). Both modes are visualized by contours of the streamwise velocity component.

with e as the energy of the global mode and Ω denoting our computational domain. By definition, this quantity falls within the interval $-1.2 \leq x_c \leq 2.5$. The global spectrum, colored by the centroid x_c , is shown in figure 5 and indicates the energy-weighted location of global modes within the computational domain.

Two principal groups of global modes can be distinguished: (i) modes located near the cavity with $0 \leq x_c \leq 1$ and (ii) modes located near the outflow boundary of the domain with $x_c \approx 2.5$. Eigenvalues for the former group can be found in the upper right part of the spectrum. These modes describe the stable dynamics of the motion inside the cavity as well as the unstable motion of the shear layer atop the cavity. Eigenvalues for the latter group (with $x_c \approx 2.5$) are mainly located near the left part of the (σ, ω) -plane at higher damping rates; their corresponding global modes are pinned to the right edge of the computational domain. Surprisingly few global modes have their energy-weighted centroid in the interval $1 \leq x_c \leq 2.5$, thus leaving essentially only global modes linked to either the cavity dynamics or the outflow boundary. A similar picture arises for the adjoint global modes: a first group of modes, whose centroid is located inside the cavity, can be distinguished from a second group of highly damped modes, whose centroid coincides with the inlet boundary at $x = -1.2$.

The localization of the global modes near and inside the cavity and at the outflow boundary is even better illustrated by computing the energy density d of a global mode versus the streamwise coordinate. The energy density is defined as the kinetic energy of a mode at a fixed streamwise location integrated over the vertical coordinate, i.e., $d(x) = \int e(x, y) dy$. Results are given in figure 5(c,e). Cavity modes, with significant energy density values in the interval $0 \leq x \leq 1$, rapidly decrease in energy density away from the cavity; they show strong localization within our computational domain. Global modes located at the outlet, on the other hand, show only low to moderate energy densities near the cavity and exponential growth over many decades toward the outflow

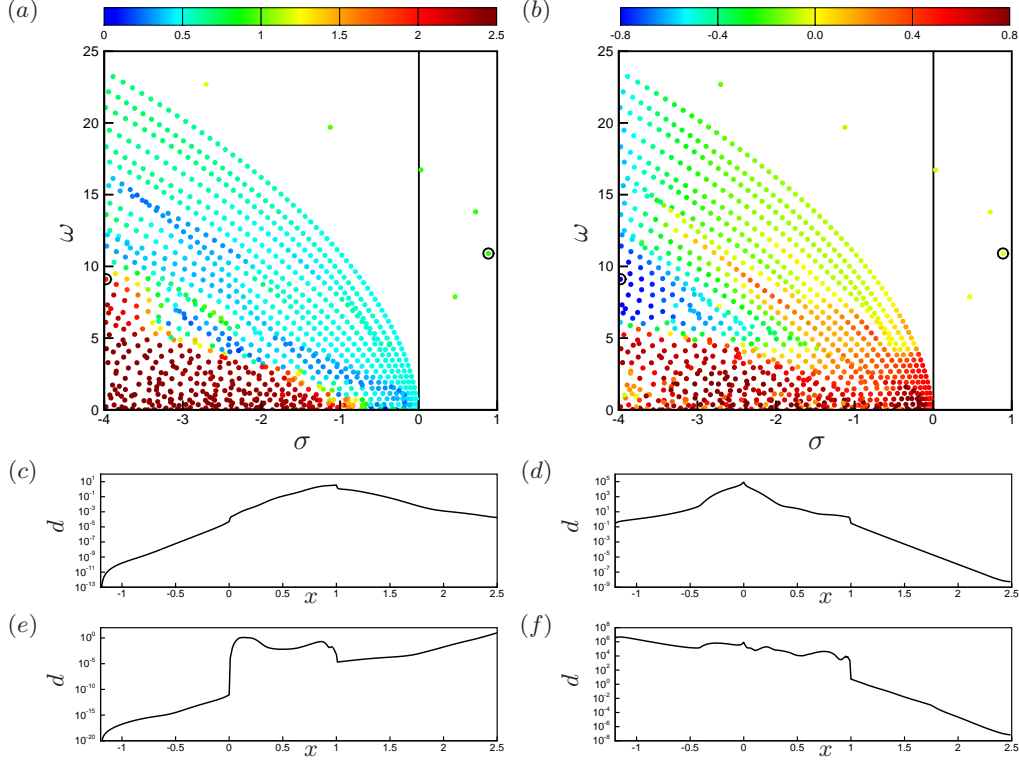


FIGURE 5. (a) Global spectrum color-coded by the x -centroid of associated global modes, (b) global spectrum color-coded by the x -centroid of the associated adjoint global modes. (c,e) Energy density versus the streamwise position for two direct global modes, (c) the least stable direct global mode and (e) a strongly damped ($\sigma \approx -4$) direct global mode; both modes are labeled by symbols in subfigure (a). (d,f) Energy density versus the streamwise position for the two associated adjoint global modes, (d) the least damped adjoint global mode and (f) a strongly damped ($\sigma \approx -4$) adjoint global mode; both modes are labeled by symbols in subfigure (b).

boundary. Similar observations can be made for the corresponding adjoint global modes (figure 5(d,f)): spatially localized adjoint cavity modes coexist with adjoint modes with strong exponential growth toward the inlet boundary.

The above analysis raises the question about the *physical* significance of stable global modes, in particular, in light of the fact that increasing the computational domain will influence the stable global modes and pin them anew against the extended computational boundary. In this sense, the majority of stable global modes are linked to numerical details, in particular, to the discretization and location of outflow boundaries (see Sipp *et al.* 2010, for more details).

4.3. Selection criteria for inclusion in a reduced model

At this point, the global modes and their adjoint counterparts are available for the design of a reduced-order model and a feedback control strategy. It remains to be decided, however, which of the global modes shall be included in the reduction basis \mathbf{V} (and the associated basis \mathbf{W}). We recall that *all unstable* modes have to be included; for the selection of global modes from the stable half-plane a criterion has to be specified. Even though many options exist and a clear choice is far from obvious, we will concentrate on four criteria that have either appeared in previous studies (Åkervik *et al.* 2007; Barba-

gallo *et al.* 2009; Ehrenstein *et al.* 2010) or can be argued for mathematically. In the next sections we will introduce and discuss these criteria and present their advantages, limitations and deficiencies. Arguments will be made and presented for the case of $Re = 7500$; it is important to stress, however, that the results extend qualitatively to lower Reynolds numbers.

4.3.1. Damping rate

The first criterion is based on the damping rate of the global modes and employs the argument that modal structures with large decay rates are dynamically less relevant than modes that are only weakly damped. This criterion has been applied by Åkervik *et al.* (2007) in their study of flow over a shallow cavity. This criterion is particularly convenient from a numerical viewpoint as highly damped global modes are difficult to compute by iterative means — even after applying spectral transformations. An obvious flaw of this criterion is the fact that modes are selected on the basis of their dynamics rather than their controllability, observability or their contribution to the input-output behavior between actuator and sensor. Figure 6(a) displays the stable part of the global spectrum for $Re = 7500$, colored by the growth rate. Using a criterion based on the damping rate, global modes of darker colors are included first in the basis V ; global modes of lighter colors are included last.

4.3.2. Contribution to the input-output behavior

Acknowledging the importance of controllability and observability of each individual global mode, the criterion (see, e.g., Bagheri *et al.* 2009b; Barbagallo *et al.* 2009)

$$\Gamma_i = \frac{|B_i| |C_i|}{|\lambda_i|} \quad (4.6)$$

has been introduced where B_i is the projection of the actuator onto the i^{th} global mode, C_i is the measured component of the i^{th} global mode and λ_i is the decay rate of the i^{th} global mode. This criterion identifies modes that are simultaneously responsive to control efforts, can be measured by the sensor and are only weakly damped.

Figure 6(b) depicts the global spectrum, again for $Re = 7500$, colored by the criterion Γ . Darker colors indicate modes with high values of Γ_i ; these modes would be preferentially included in a reduced-order model based on the Γ -selection criterion. Modes with lighter colors have lower associated values of Γ_i and would tend to be neglected in a reduction basis. The first modes selected according to the criterion are clustered near $\lambda = (\sigma, \omega) \approx (-0.4, 4.5)$, $(-1.1, 19.7)$ and $(-2.7, 22.7)$. Close analysis (see also Barbagallo *et al.* 2009) reveals that the corresponding modes show a spatial structure similar to the unstable global modes, that is, linking actuator and sensor by a chain of vortical elements. More problematic is the fact that a substantial number of modes with high damping rates appear to contribute to the input-output behavior; even modes near our cut-off damping rate of $\sigma = -4$ seem to be important, which suggests that even higher damping rates would have been favored, had they been available.

4.3.3. Orthogonal projection

The third criterion makes use of an additional projection and has been suggested in Ehrenstein *et al.* (2010). It has been shown to improve results obtained by only applying the bi-orthogonal projection introduced earlier. The method combines the bi-orthogonal projection for the unstable subspace with a least-squares projection for the stable supplementary one. The central idea stems from the observation by Ehrenstein *et al.* (2010) that the actuator expressed in the bi-orthogonal projection is spatially rather different

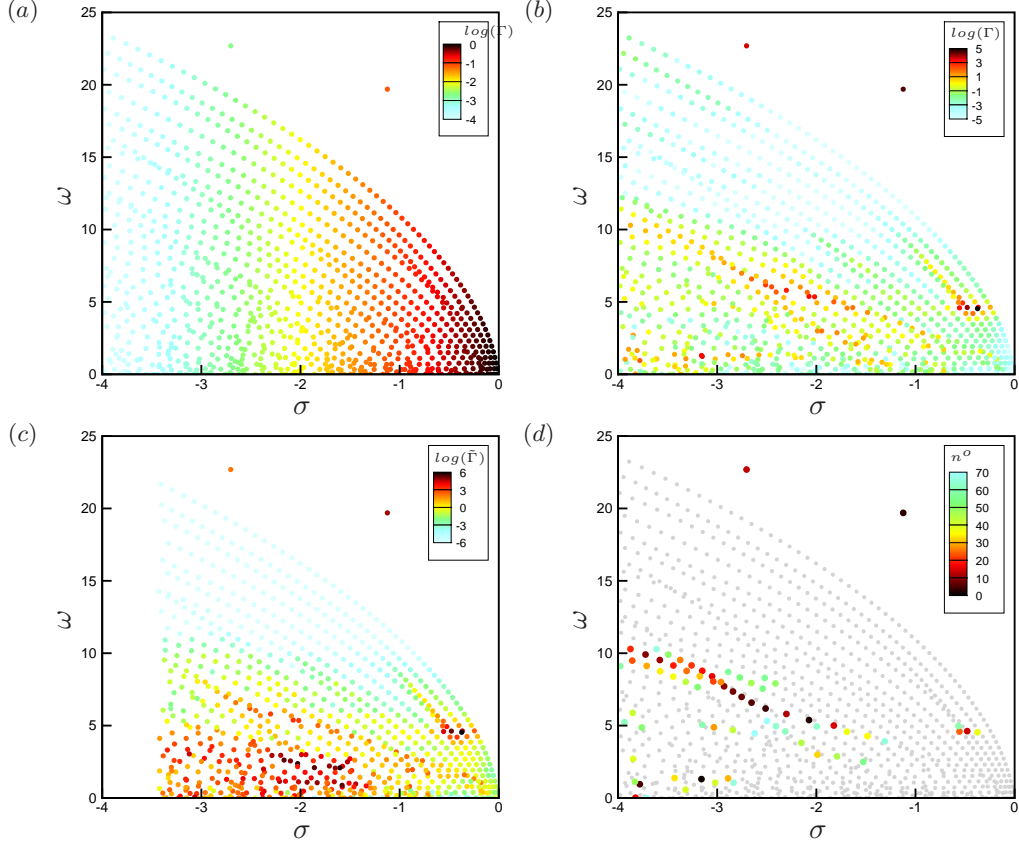


FIGURE 6. Identification of global modes by color-coding according to the four respective criteria (see text): (a) growth rate, (b) contribution to input-output behavior, (c) orthogonal projection, and (d) “quasi-optimal” stability ranking. Only the stable part of the spectrum is displayed; the Reynolds number is $Re = 7500$.

from its original form. For this reason, they suggest a least-squares projection method for the actuator as it minimizes the error between the original and projected actuator. Following this concept, the global modes are ranked using the criterion

$$\tilde{\Gamma}_i = \frac{|\tilde{B}_i| |C_i|}{|\lambda_i|} \quad (4.7)$$

where the coefficient \tilde{B}_i is now based on the least-squares projection.

Figure 6(c) shows the global spectrum ($Re = 7500$) colored by the above criterion $\tilde{\Gamma}$ to indicate a classification of global modes (from darker to lighter colors) for their inclusion in the reduced-order model. A similar general tendency is observed as in figure 6(b): preference of modes that resemble the globally unstable modes and of highly damped, low-frequency modes. In addition, the least-squares projection becomes computationally more sensitive for modes at higher damping rates which allowed us to accurately evaluate the criterion $\tilde{\Gamma}$ only for modes with $\sigma > -3.4$. This marked numerical sensitivity has been observed for all Reynolds numbers considered in this study. It is also worth pointing out that due to the two independent projections (bi-orthogonal and least-squares), the resulting reduced-order model cannot be written as a single projection of the initial

system onto a set of global modes; rather, the coefficients \tilde{B}_i enter the dynamics given by (3.3).

4.3.4. "Quasi-optimal" stability ranking

The fourth criterion is included as a demonstration tool for the ability of reduced models based on global modes to yield a stable compensated system. As will become clearer in the following sections, the fully compensated system, i.e., the plant coupled with a reduced estimator and controller, suffers from instabilities when global modes are used in the reduced-order model. These instabilities render the ROM ineffective and provide quantitative proof of the unsuitability of the chosen reduction basis for closed-loop control applications. The fourth criterion aims at exploring the best possible choice of global modes such that stability of the fully compensated system is approached as swiftly as possible. As such the criterion provides a benchmark for what is possible with a judicious choice of global modes. It is computed iteratively and *a posteriori* as follows. We start with a reduced-order model comprising only the unstable modes and compute the growth rate σ of the compensated system (plant plus reduced-order estimator plus reduced-order controller). Next we search through all available stable global modes and add the one to the reduction basis \mathbf{V} which results in the largest reduction of σ for the augmented compensated system. This procedure is repeated, thus building a sequence of global modes where each added global mode improves the stability of the compensated system more than any of the remaining modes.

We note that for a model with p stable modes, the truly optimal ranking according to stability would be given by the best combination of p modes chosen from the complete set of n stable modes. The number of admissible combinations is $n!/(p!(n-p)!)$ which far exceeds our computational means. For this reason, the "quasi-optimal" sequential algorithm for building a reduction basis has been chosen.

Figure 6(d) illustrates the global spectrum colored by the ordering based on the above criterion. The eigenvalues selected by the "quasi-optimal" stability procedure are reminiscent of some of the eigenvalues chosen by the Γ -criterion (see figure 6(b)). On the other hand, many global modes with high values of Γ are not selected by the stability criterion, a feature that will be discussed in more detail later.

4.4. Final form of the compensator using a reduced-order model based on global modes

We conclude this section by stating the equations governing the compensator. In particular, we emphasize the partitioning of the reduced-order model into an unstable (indicated by subscript u) and stable (indicated subscript s) part. The control gain \hat{K} as well as the Kalman gain \hat{L} have been computed in the small gain limit (see, e.g., Burl 1999) which introduces zero matrices since the estimator and controller only act on the unstable subspace. We have

$$\begin{aligned} \frac{d}{dt} \begin{pmatrix} \hat{Y}_u \\ \hat{Y}_s \end{pmatrix} &= \begin{pmatrix} \hat{\Lambda}_u & 0 \\ 0 & \hat{\Lambda}_s \end{pmatrix} \begin{pmatrix} \hat{Y}_u \\ \hat{Y}_s \end{pmatrix} + \begin{pmatrix} \hat{B}_{2u} \\ \hat{B}_{2s} \end{pmatrix} (\hat{K}_u \quad 0) \begin{pmatrix} \hat{Y}_u \\ \hat{Y}_s \end{pmatrix} \\ &\quad - \begin{pmatrix} \hat{L}_u \\ 0 \end{pmatrix} \left[m - (\hat{C}_u \quad \hat{C}_s) \begin{pmatrix} \hat{Y}_u \\ \hat{Y}_s \end{pmatrix} \right], \end{aligned} \quad (4.8a)$$

$$u = (\hat{K}_u \quad 0) \begin{pmatrix} \hat{Y}_u \\ \hat{Y}_s \end{pmatrix}. \quad (4.8b)$$

The complete compensator is now set up. In the following section we will present open-

loop tests based on the approximation of the full transfer behavior by the reduced model and closed-loop tests based on the stability properties of the compensated system. The four selection criteria will be investigated for the representative case of cavity flow at $Re = 7500$.

5. Performance evaluation of reduced-order models for $Re = 7500$

Two performance measures will be used to assess the performance of the reduced-order models based on global modes. The first measure is concerned with the accurate representation of the input-output behavior of the full system by the reduced model. The approximation error is quantified by the mismatch of the true transfer function and the transfer function of the reduced system, measured in the \mathcal{H}_2 - or \mathcal{H}_∞ -norm. The second measure probes the ability of the reduced model to yield a stable compensated system. In this case, the eigenvalue of the coupled plant-compensator system with the largest growth rate will be used as a performance indicator.

5.1. Open-loop performance evaluation

It is generally acknowledged that a successful control design requires the representation of the correct input-output behavior by the reduced model. Since there is no choice in selecting unstable global modes, only the accuracy of modeling the stable subspace dynamics needs to be addressed. The governing equations for the stable subspace dynamics in state-space form can be written as

$$\mathbf{Q} \frac{d\mathbf{X}}{dt} = \mathbf{A}_s \mathbf{X} + \mathbf{Q} \mathbf{B}_{2s} u \quad (5.1a)$$

$$m = \mathbf{C} \mathbf{X} \quad (5.1b)$$

where \mathbf{B}_{2s} denotes the actuator projected onto the stable subspace. The input-output dynamics is computed numerically by imposing a Dirac impulse $u(t) = \delta(t)$ as the control input and subsequently measuring the signal $m(t)$ at the sensor location. Since, by definition, the subspace system given by \mathbf{A}_s is stable, the signal $m(t)$ will eventually decay as $t \rightarrow \infty$. Transforming this impulse response into the frequency domain according to $\hat{m}(\omega) = \int_0^\infty m(t) \exp(-i\omega t) dt$ (for a causal system), we obtain the transfer function $H(\omega) = \hat{m}(\omega)$ which quantifies the response of the system to a harmonic forcing at a frequency ω . In figure 7 the transfer functions (in the frequency domain) are shown. The transfer function curves correspond to the amplitude part of a Bode diagram and exhibit two (nearly constant) plateaus for $\omega \in [0, 3] \cup [20, 25]$ and $\omega \in [5, 19]$. The latter range approximately corresponds to the frequency range of the unstable modes. We also notice an abrupt drop around $\omega \approx 4$, causing a nearly vanishing response at this frequency and suggesting the presence of nearly unobservable states.

Once the transfer function of the full system has been computed from a Fourier transform of the impulse response, we can juxtapose the transfer functions of the reduced-order models and assess the quality of the approximation as more and more global modes are added to the reduction basis according to one of the four criteria.

In figure 7 the amplitude of the transfer function is displayed for reduced-order models using the selection criteria described in paragraph § 4.3. The transfer functions have been computed using the expression $\hat{H}(\omega) = \hat{\mathbf{C}}(i\omega\mathbf{I} - \hat{\mathbf{A}}_s)^{-1} \hat{\mathbf{B}}_{2s}$. The different reduced-order models are identified by colors (see the figure legends) and correspond to a specific number of included global modes ranked by the respective criterion. The transfer function of the original (full) system is given in black. At a first glance it can be observed that

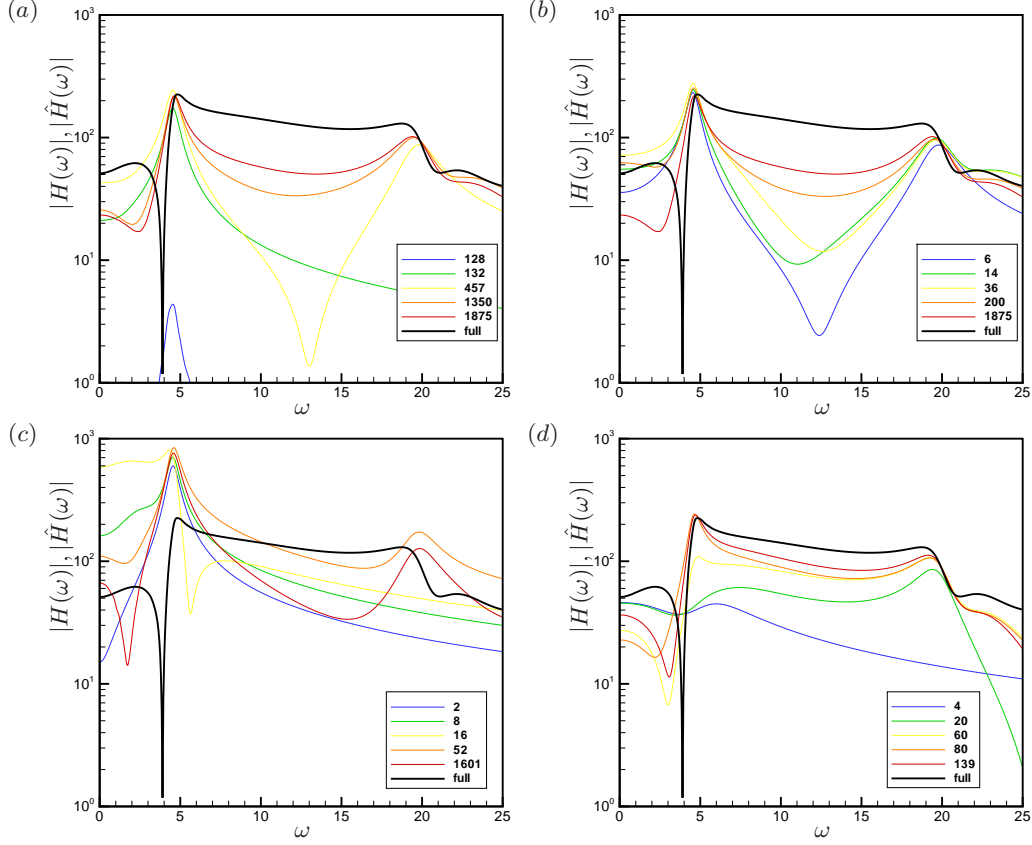


FIGURE 7. Approximation of the modulus of the exact transfer function (in black) as global modes are added to the reduction basis \mathbf{V} according to the four selection criteria; (a) adding modes based on damping rate, (b) adding modes according to their contribution to the input-output behavior, (c) adding modes using orthogonal projections, (d) adding modes based on the "quasi-optimal" stability ranking. The Reynolds number is $Re = 7500$.

– maybe with the exception of the "quasi-optimal" stability criterion – none of the four selection criteria produces satisfactory results even if more than a thousand global modes are included.

To quantify the degree of approximation of the original transfer function we consider the \mathcal{H}_2 - and \mathcal{H}_∞ -norms defined as

$$\|H\|_2 = \left(\int_0^{25} |H(\omega)|^2 d\omega \right)^{1/2}, \quad (5.2a)$$

$$\|H\|_\infty = \sup_{\omega} |H(\omega)|. \quad (5.2b)$$

The \mathcal{H}_2 -norm measures the overall error over a given frequency range, whereas the \mathcal{H}_∞ -norm concentrates on the worst error that occurs in a frequency range. In figure 8 the \mathcal{H}_2 - and \mathcal{H}_∞ -error are displayed and corroborate the findings from the previous plot. In particular, the ranking based on orthogonal projections of the controller shows rather discouraging results.

Figure 7(a) displays the amplitude of the transfer function for reduced-order models of dimension 128, 132, 457, 1350 and 1875 where the modes have been ranked by damping

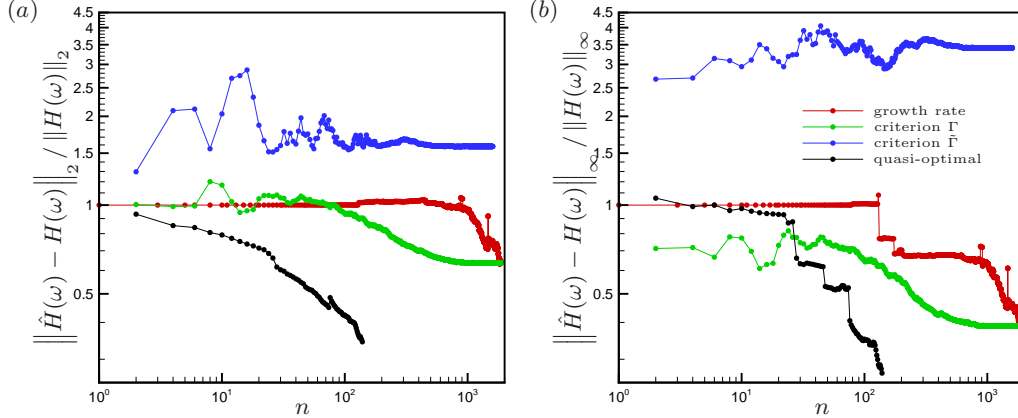


FIGURE 8. Relative approximation error of the full transfer function as global modes are added to the reduction basis V according to the four criteria (see text). (a) Relative error measure in the \mathcal{H}_2 -norm, (b) relative error measured in the \mathcal{H}_∞ -norm. The Reynolds number is $Re = 7500$.

rate (first criterion in § 4.3). As the dimension of the reduced models is increased, the transfer functions of the reduced models approach the transfer function of the original system. This effect is also visible in figure 8 (red curves); in both norms, the error is gradually decreasing. The convergence, however, is rather erratic: for example, the transfer functions of a reduced model of order 128 and of order 132 are entirely different, even though they merely differ by four stable global modes that have been added to the latter model.

In figure 7(b) we see the amplitude of the transfer function for reduced-order models of dimension 6, 14, 36, 200 and 1875; this time, the modes have been ranked by the input-output criterion Γ (see § 4.3). Similarly to the previous case, the transfer functions approach the one of the original system, but better approximations are achieved for smaller numbers of included modes. This validates the relevance of the Γ -criterion in selecting global modes for the reduction basis V . The first few modes are assumed to contribute significantly to the input-output behavior; it may thus seem confusing that the relative errors (green curves in figure 8) do not decrease as the first modes are added. This phenomenon can be explained by the fact that phase information is lost in the definition of the Γ -criterion. For this reason, it seems conceivable that, while the amplitude of the transfer function approaches the one of the full system, the phase between full and reduced system drifts apart. Unless the original transfer function is known *a priori*, it does not seem straightforward to include phase information into the definition of Γ_i .

Figure 7(c) depicts the amplitude of transfer functions for reduced models of dimension 2, 8, 16, 52 and 1601 where the modes have been ranked by the criterion $\tilde{\Gamma}_i$ (see § 4.3). Compared to the transfer functions of figures 7(a) and 7(b) all reduced-order transfer functions exhibit very high amplitude values at low frequencies. This is not surprising since the $\tilde{\Gamma}$ -criterion mainly selects modes associated with low frequencies (see figure 6(c)). A more grave difference to the previous two criteria is the lack of convergence towards the original system as the order of the reduced model is increased (see blue curves in figure 8).

Finally, figure 7(d) shows the amplitude of the transfer function for reduced models of dimension 4, 20, 60, 80 and 139 where the modes have been ranked according to the "quasi-optimal" stability criterion (see § 4.3). As the dimension of the reduced-order model increases, we observe an adequate convergence of the reduced transfer functions to-

ward the original one (in particular, for the frequency interval $\omega \in [5, 20]$). This behavior may indicate that the transfer function does not have to approximate the original transfer function over the entire frequency range — an issue that will be further investigated in paragraph § 5.3.

Overall, we confirm that the relative error norms based on the fourth criterion are markedly lower than the error norms for the previous three criteria. This indicates that a particular ordering of global modes may indeed produce an effective reduced-order model, an *a priori* and definitive selection criterion, however, may be difficult to devise. The study of the open-loop behavior of reduced-order models, expressed by their transfer function, has established that the criterion for selecting global modes that are to be included in a reduced-order model is pivotal. Intuitive concepts, such as growth rate, are often misleading and produce ineffective models; even more sophisticated criteria cannot guarantee robust success over a broad range of flow parameters. The underlying reason for this may lie in the fact that most of the stable global modes carry little physical meaning.

In the following section, the more categorical test of a reduced-order model, namely the stabilization of the full compensated system, will be presented.

5.2. Performance of the closed-loop system

For supercritical Reynolds numbers, the objective of the LQG-control loop, shown in figure 1 and 2, is to suppress the instabilities in the system. To test whether the closed-loop system has succeeded in this effort, the growth rate σ_{\max} of the least stable eigenvalue of the compensated system is the natural quantity to evaluate. If at least one unstable eigenvalue exists, the controlled system is still unstable. If all eigenvalues of the compensated system are stable, the originally unstable system has been stabilized.

The compensated system is constructed by coupling the plant (2.5) to the compensator (4.8). The spectrum of this coupled system then provides information about the success of our closed-loop control design as well as our model reduction efforts. Since the plant contains a very large number of degrees of freedom (in our case, nearly one million), spectral information about the coupled system is challenging to extract. Instead, we will follow Barbagallo *et al.* (2009) and reduce the computational costs by replacing the full plant model (2.5) by a reduced-order model based on unstable global modes and proper orthogonal decomposition (POD) modes for the stable subspace; see the appendix for further details. A sufficient number of POD modes has to be taken into account to accurately represent the plant dynamics and its response behavior. With this substitution, the compensated system can then be written as

$$\frac{d}{dt} \begin{pmatrix} \hat{X}_u^{gm} \\ \hat{X}_s^{pod} \\ \hat{Y}_u^{gm} \\ \hat{Y}_s^{gm} \end{pmatrix} = \hat{A}_c \begin{pmatrix} \hat{X}_u^{gm} \\ \hat{X}_s^{pod} \\ \hat{Y}_u^{gm} \\ \hat{Y}_s^{gm} \end{pmatrix} \quad \text{with} \quad (5.3a)$$

$$\hat{A}_c = \begin{pmatrix} \hat{\Lambda}_u^{gm} & 0 & \hat{B}_{2u}^{gm} \hat{K}_u^{gm} & 0 \\ 0 & \hat{A}_s^{pod} & \hat{B}_{2s}^{pod} \hat{K}_u^{gm} & 0 \\ -\hat{\Gamma}_u^{gm} \hat{C}_u^{gm} & -\hat{\Gamma}_u^{gm} \hat{C}_s^{pod} & \hat{\Lambda}_u^{gm} + \hat{B}_{2u}^{gm} \hat{K}_u^{gm} + \hat{\Gamma}_u^{gm} \hat{C}_u^{gm} & \hat{\Gamma}_u^{gm} \hat{C}_s^{gm} \\ 0 & 0 & \hat{B}_{2s}^{gm} \hat{K}_u^{gm} & \hat{\Lambda}_s^{gm} \end{pmatrix}. \quad (5.3b)$$

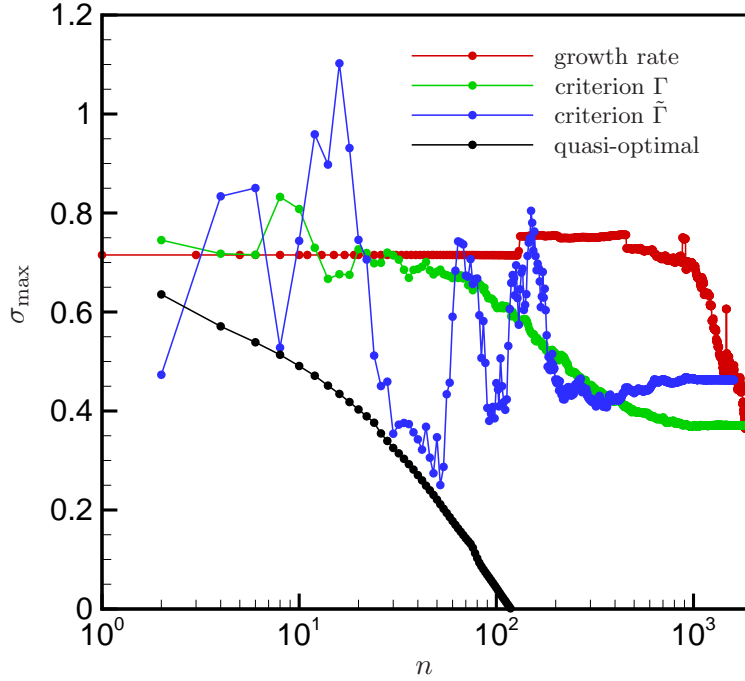


FIGURE 9. Growth rate of least stable eigenvalue of the compensated system as global modes are added to the reduction basis V according to the four criteria (see text). The Reynolds number is $Re = 7500$.

Superscripts gm and pod denote whether the respective matrix has been reduced by global or POD modes; the subscripts $_u$ and $_s$ stand, as before, for the unstable or stable subspace, respectively. The above system then describes the compensated dynamics, and the growth rate of the least stable eigenvalue of the matrix \hat{A}_c indicates failure or success of the reduced-order LQG controller to stabilize the otherwise unstable system. We will now use this technique to evaluate the closed-loop performance of reduced-order models based on selected global modes, again for a representative Reynolds number of $Re = 7500$.

The eigenvalues of the compensated system matrix \hat{A}_c have been determined. Direct methods could be employed since the original system matrix A for the plant has been replaced by a lower-dimensional matrix based on POD modes. The growth rate σ_{\max} of the least stable eigenvalue determines the stability property of the compensated system. Figure 9 displays this growth rate σ_{\max} as a function of the number n of stable global modes included in the reduced-order model. The selection and ranking criteria introduced earlier have been used, and the various stability characteristics for each criteria are color-coded in the figure.

The compensated system can only be stabilized by the "quasi-optimal" ranking procedure (black line). In this case, stabilization of the flow is achieved, once more than 120 stable global modes are used in the reduced-order model. We observe a monotonic decrease of σ_{\max} which is expected since at each n only the global mode that maximally decreases σ_{\max} is added to the reduced-order model.

Models using the growth rate criterion (red line) also show a decrease in σ_{\max} as more stable modes are taken into account. Within the limits of our available modes, however, a stable compensated system could not be attained. An interesting observation is that the red curve in figure 9 is highly correlated to the equivalent curve representing the relative \mathcal{H}_2 -error (red curve in figure 8(a)) which appears to suggest a link between a

better approximation (in the \mathcal{H}_2 -sense) of the open-loop input-output behavior and an improved stability of the closed-loop system.

Similar results are obtained when using a ranking of the stable global modes according to the Γ -criterion (green curve). However, as in the open-loop test, an improvement of the stability properties of the compensated system emerges substantially earlier compared to the ranking based on the growth rate. Nevertheless, within the limit of available global modes, no stabilization could be achieved.

Lastly, the results corresponding to the $\tilde{\Gamma}$ -criterion (using an orthogonal projection for the actuator) are displayed in blue. The behavior of σ_{\max} appears quite erratic for less than $n = 200$ global modes; variations from “close to optimal” (for $n = 2, 8, 20 - 50$) to “worse than uncontrolled” (for $n = 12 - 18$) can be observed. The favorable properties of this projection reported in Ehrenstein *et al.* (2010) could not be recovered for our flow configuration. In addition, the abrupt changes in stability of the flow when only a few modes are added (for example, comparing $n = 8$ and $n = 10$, or $n = 52$ and $n = 60$) cast doubt on the practicality of this criterion.

5.3. A frequency-restricted norm measuring open-loop behavior

The similarities between the curves of σ_{\max} (figure 9), which express the performance of the compensator, and the curves of the relative \mathcal{H}_2 -error (figure 8), which express the accuracy of capturing the input-output behavior of the original system, are striking and warrant a further investigation.

Special attention has to be paid to the choice of norm when evaluating the open-loop characteristics. The \mathcal{H}_∞ -norm is commonly adopted in control and model reduction applications since rigorous error bounds are available for this norm (see, e.g. Antoulas 2005). Our study, however, indicates that the performance of the closed-loop system (figure 9) is much closer linked to the \mathcal{H}_2 -errors (figure 8(a)) than the \mathcal{H}_∞ -errors (figure 8(b)) of the reduced transfer function. This suggests that the overall behavior of the reduced-order model may be more relevant than its worse departure from the exact behavior at a particular frequencies.

Another remarkable observation is that, according to the \mathcal{H}_2 -error of the open-loop behavior, the reduced-order models based on the $\tilde{\Gamma}$ -criterion are expected to perform poorly: the (blue) error curve is far above the curve representing models based on the growth-rate criterion (in red) in figure 8(a). Nevertheless, $\tilde{\Gamma}$ -models stabilize the system noticeably better than models using the growth-rate criterion, as can be seen in figure 9. This apparent inconsistency may give insight into which frequency range of the open-loop transfer function has to be captured sufficiently by the reduced-order model to yield improved stability properties for the closed-loop system. None of the reduced-order models reproduces the full transfer function behavior adequately at low frequencies (see figure 7); the $\tilde{\Gamma}$ -model (subfigure (c)) shows the most irregular behavior. Nevertheless, considering the case $n = 52$ for the $\tilde{\Gamma}$ -criterion, the instability of the full system is reduced convincingly (see figure 9, blue curve) while the transfer function is well-approximated over a frequency range of $\omega \in [10, 20]$ (see figure 7(c), orange line).

This observation is in agreement with the physical understanding of the control dynamics. In an effort to eliminate an unstable mode, the controller generates an opposite structure that destructively interferes with the instability. Since the unstable modes are characterized by well-defined frequencies, the actuator also has to operate at the same frequencies. Doing so, it mainly triggers the stable part of the flow at these frequencies. As a result, the control-oriented reduced-order model must largely capture the full input-output behavior at these frequencies. Frequencies outside this range play a subordinate role in the control law, and the transfer behavior at these frequencies may not have to be

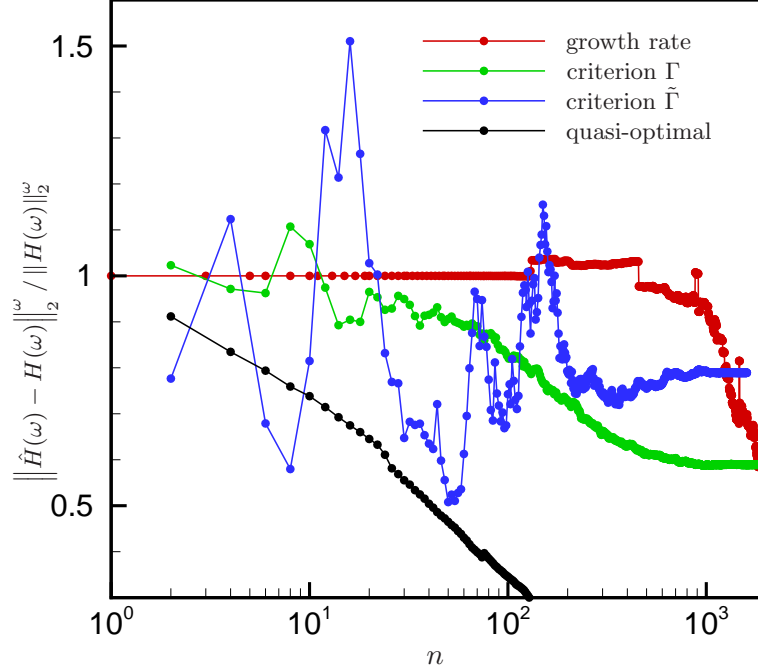


FIGURE 10. Relative approximation error of the reduced-model transfer function as global modes are added to the reduction basis \mathcal{V} according to the four criteria (see text). The relative error is measure in the frequency-restricted norm \mathcal{H}_2^ω . The Reynolds number is $Re = 7500$.

captured as accurately. Based on this argument, we propose to evaluate the reduced-order models using a frequency-restricted \mathcal{H}_2 -norm; the frequency range is chosen to include the frequencies of the unstable modes. We introduce

$$\|H\|_2^\omega = \left(\int_{10}^{17} |H(\omega)|^2 d\omega \right)^{1/2} \quad (5.4)$$

and refer to this norm as the \mathcal{H}_2^ω -norm. The \mathcal{H}_2^ω -error of the reduced transfer functions is plotted in figure 10. First inspection shows that all curves reflect the corresponding performance of the closed-loop system (figure 9). More importantly, the relative positions of the curves are very similar to the results in figure 9 which confirms our supposition that it is of critical importance to capture the behavior of the original system at the frequencies where the control acts.

6. Reynolds number dependence

It is apparent from the previous sections that the performance of reduced-order models based on global modes depends on the details of the instabilities that have to be controlled, which in turn depend on the Reynolds number. The goal of this section is to explore the range of Reynolds numbers for which closed-loop control can be successfully applied with a compensator based on global modes.

6.1. Changes in the spectrum

We start by studying how the stability properties of the uncontrolled flow are modified as the Reynolds number Re is increased. In figure 11 the spectrum (in the $\omega > 0$ half-plane) is displayed for Reynolds numbers from $Re = 4800$ to 7500 . Only the branch containing

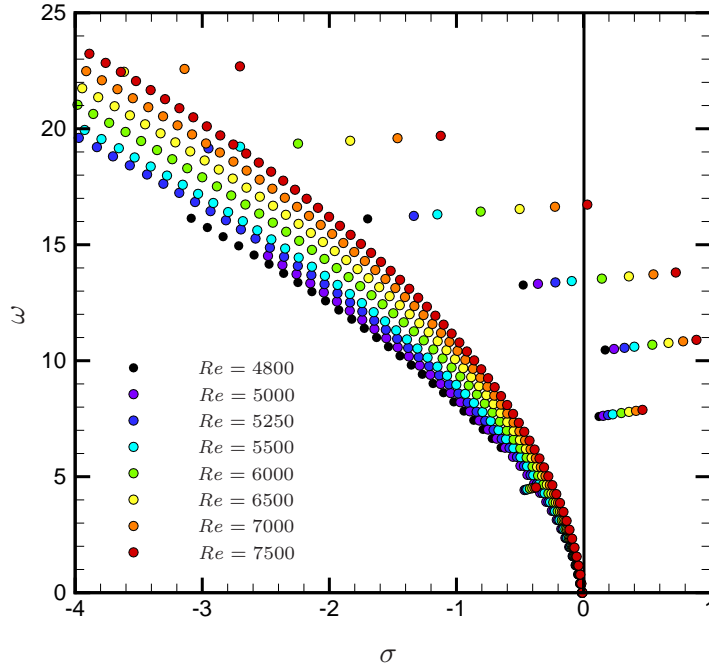


FIGURE 11. Changes in the global spectrum of flow over an open cavity as the Reynolds number is varied from $Re = 4800$ to $Re = 7500$.

the unstable global modes and the least stable of stable branches are shown. The general behavior is a destabilization of the spectrum as the Reynolds number increases. The unstable branch is further displaced into the unstable half-plane and the number of unstable modes increases. The stable eigenvalues move closer towards the unstable half-plane, but ultimately remain stable. This behavior is to be expected from an advection-diffusion problem as the diffusive terms play an increasingly minor role. While the decay rates are affected noticeably, the frequencies and spatial shapes (not shown) seem rather insensitive to Reynolds number variations.

6.2. Changes in the stability of the controlled system

An interesting question concerns the ability of the compensator to stabilize the flow for a range of Reynolds numbers. To this end, a compensator based on global modes of the flow at a given Reynolds number is computed, after which the previously described method will be employed to determine the least stable eigenvalue of the compensated problem – and thus the performance of the reduced-order control problem.

6.2.1. Compensators based only on the unstable global modes

Previously it was argued that the unstable global modes of the flow have to be accounted for in the reduced-order model. The stable subspace, though, is not necessarily required, which prompts the questions (i) whether the flow can be stabilized using only the unstable modes and (ii) if so, up to what Reynolds number such a primitive compensator will be successful. In answer to these questions, figure 12 displays the growth rate of the least stable mode (σ_{\max}) of the closed-loop system where the compensator consists of only the unstable global modes. For Reynolds numbers less than $Re \approx 5250$, the growth rate σ_{\max} is indeed negative which indicates that the flow can be stabilized without accounting for the stable subspace in the reduced-order model. For Reynolds

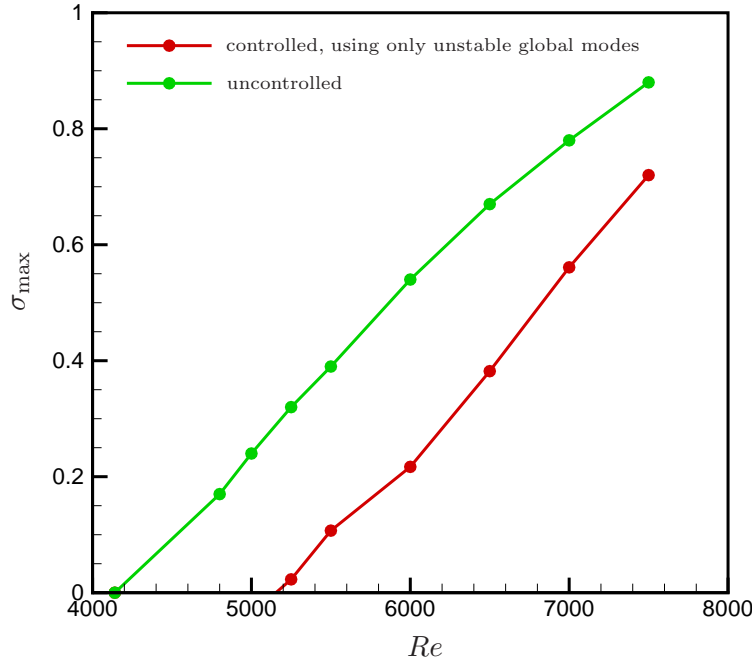


FIGURE 12. Growth rate of the least stable eigenvalue of the (green) uncontrolled and the (red) compensated system using a reduced-order model based on the unstable global modes only.

numbers above $Re \approx 5250$, the instability grows too strong, and reduced-order models based on merely the unstable global modes cease to succeed in stabilizing the flow.

In Barbagallo *et al.* (2009) it has been shown that the flow can be stabilized at $Re = 7500$, if relevant information about the stable subspace, in this case using proper orthogonal decomposition (POD) modes or balanced (BPOD) modes, is incorporated into the reduced-order model. The subsequent paragraph explores the question whether the same can be accomplished by including global modes where Reynolds numbers ranging from $Re = 5250$ to $Re = 7500$ are considered.

6.2.2. Compensators based on the unstable and selected stable global modes

Unstable and stable global modes are added to the reduction basis \mathbf{V} to obtain a reduced-order model of the flow. Stable modes are included according to one of the four ranking criteria defined in § 4.3. In figure 13 the largest growth rate σ_{\max} of the compensated system is displayed. Each subplot represents a specific ranking criterion; the various colors denote different Reynolds numbers.

In figure 13(a), stable global modes are included in the ROM according to their damping rate. Independent of the Reynolds number, the curves display similar behavior. As the first stable modes are included, each curve shows a nearly constant plateau, until approximately $n = 500$ stable global modes have been added; at this point, σ_{\max} decreases as more modes get incorporated into the reduced-order model. If the initial instability is sufficiently weak, as is the case for $Re = 5250$, 5500 and 6000 , the system can eventually be stabilized. However, even with all global modes (up to $\sigma > -4$) included, flow over an open cavity for Reynolds numbers larger than $Re \approx 6500$ can no longer be rendered stable by a compensator based on global modes.

When the global modes are ranked according the Γ -criterion (see figure 13(b)) analogous conclusions can be drawn. However, similar to the case $Re = 7500$ studied in § 5,

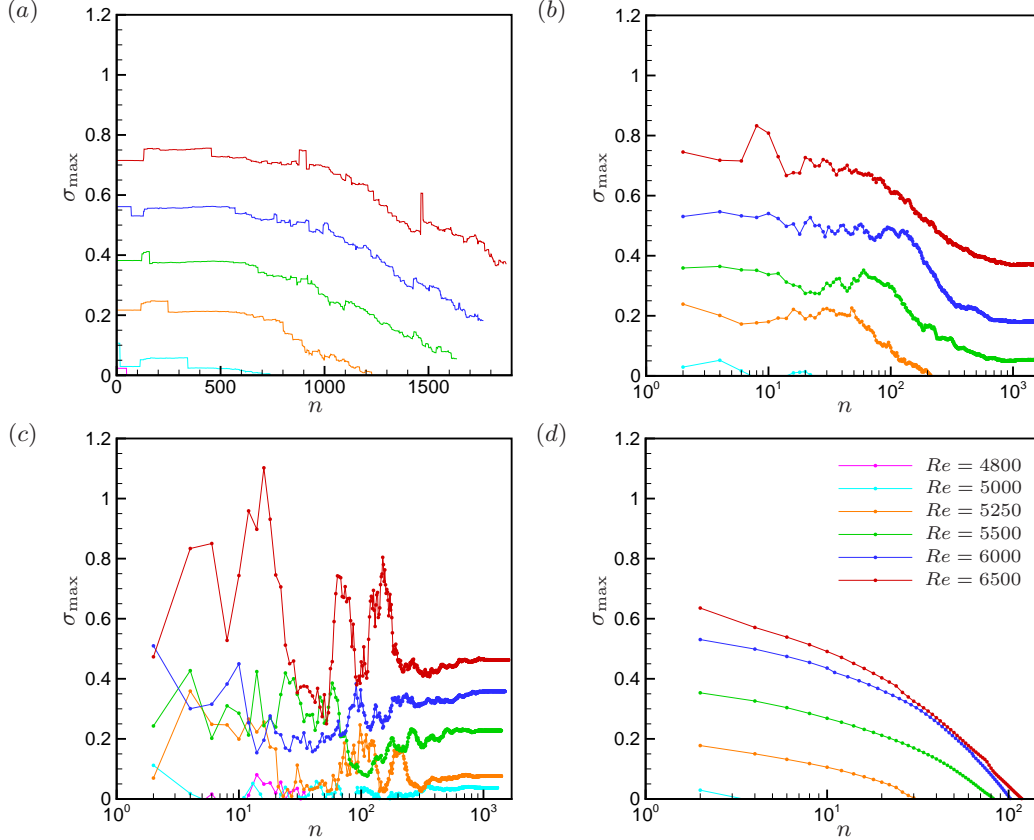


FIGURE 13. Growth rate of the least stable eigenvalue of the compensated system as global modes are added to the reduction basis according to the four selection criteria (see text): (a) growth rate, (b) contribution to the input-output behavior Γ_i , (c) orthogonal projections $\tilde{\Gamma}_i$, and (d) “quasi-optimal” stability ranking. The Reynolds numbers range from $Re = 4800$ to $Re = 6500$. Stabilization of the compensated system is achieved when $\sigma_{\max} < 0$.

the stabilization of the compensated system occurs at a lower number of stable modes. In figure 13(c) we consider stable global modes ranked by the $\tilde{\Gamma}$ -criterion. In this case, the system can only be stabilized for $Re = 5250$. As mentioned previously, the criterion does not yield favorable results for our case, even though it has been successfully applied to other configurations (Ehrenstein *et al.* 2010).

In contrast (and as expected), the system can be eventually stabilized for all considered Reynolds numbers ($5250 \leq Re \leq 7500$) if the “quasi-optimal” ranking is employed (see figure 13(d)).

The above results demonstrate that some unstable flows can be stabilized using reduced-order models based on global modes. Despite that, the number of stable global modes necessary to model the stable subspace dynamics increases dramatically with Reynolds number. The question then arises whether, given an arbitrary (high) Reynolds number, a sufficient number of stable global modes can be computed accurately so that such a reduced-order model can be constructed. In our case, a large but still finite number of global modes could be calculated, before round-off error deteriorated the iterative computations. This phenomenon can be linked to the non-normality of the linearized Navier-Stokes matrix A which makes iterative eigenvalue computations an ill-conditioned (and

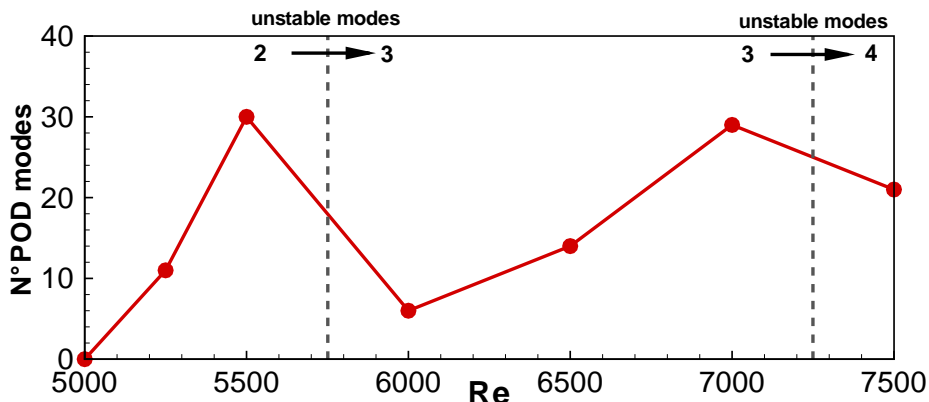


FIGURE 14. Minimum number of proper orthogonal decomposition (POD) modes to stabilize the compensated system consisting of a reduced model based on unstable global modes and POD modes. At critical values of the Reynolds number (indicated by dashed lines) additional global modes become unstable.

ill-fated) undertaking. But as more stable global modes become necessary to stabilize the flow at larger Reynolds numbers, the finite limit of computable modes will at last be reached.

Another relevant question is concerned with the reason for the drastic increase in stable global modes needed to stabilize the flow at higher Reynolds number. A facile and simplistic answer would argue that the stable subspace is generally less damped (see § 6.1) which generates a more complex dynamics and, in turn, a larger number of degrees of freedom. To follow up with this argument, we consider a compensator based on the unstable global modes and POD modes to model the stable subspace. The minimum number of POD modes required to stabilize the flow is shown in figure 14. The flow can be stabilized at each Reynolds number considered using at most thirty POD modes to represent the stable subspace dynamics. Clearly, this behavior runs counter to the claim that the complexity of the stable subspace requires a reduced-order model of high dimensions. We are left with the fact that a few thousand stable global modes need to be computed, ranked and incorporated into a reduced-order model in order to represent a subspace dynamics that can equally well (or better) be described by thirty POD modes; we thus conclude that global modes constitute a poor basis when designing closed-loop control strategies using reduced-order models. Our study suggests that a reduced-order model based on global modes is capable of stabilizing systems that are only weakly unstable (such as the configurations studied by Åkervik *et al.* (2007) and Ehrenstein *et al.* (2010)). If stronger instabilities (such as the one studied in Barbagallo *et al.* (2009)) are encountered, reduced-order models based on global modes will fail and different reduction bases, such as POD modes or balanced modes, have to be explored.

7. Summary and conclusions

Projection-based model reduction techniques leave a great many choices to compute low-dimensional systems from high-dimensional models. In this article, we have investigated the suitability of global modes in closed-loop control applications of oscillator-type flows (in particular, the flow over an open cavity at supercritical Reynolds numbers).

The reduced-order models are composed of unstable global modes, capturing the inherent instability, and selected stable global modes, representing the stable subspace of

the perturbation dynamics. The selection of stable global modes is critical and has been carried out based on four criteria, yielding four different reduced-order models composed of global modes. Using a representative test case ($Re = 7500$) the open-loop behavior of these models has first been assessed, which revealed that the damping rate (criterion 1, Åkervik *et al.* (2007)) is a poor indicator in selecting global modes, while choosing global modes with high controllability and observability but low damping rate (criterion 2, Bagheri *et al.* (2009a); Barbagallo *et al.* (2009)) showed better performance but nonetheless failed since phase information has been disregarded. A selection criterion (criterion 3, Ehrenstein *et al.* (2010)) based on *double-projection* could not demonstrate the same advantages and potential as reported in Ehrenstein *et al.* (2010), but rather showed irregular and unpredictable convergence behavior when applied to our configuration. A fourth criterion, an *a posteriori*-selection rule, has been added both as a benchmark to gauge near-optimal results and as verification that highly damped modes have to be considered to capture the correct input-output behavior. The closed-loop performance of the different models has been characterized by the stability of the compensated system. With the exception of the artificial fourth criterion (“quasi-optimal” stability ranking), all computed system were found unstable for the test case, thus confirming the conclusions drawn from the open-loop study.

An interesting finding of our analysis was the strong evidence that the commonly applied \mathcal{H}_2 - and \mathcal{H}_∞ -measures are *not* optimal to evaluate the open-loop behavior of reduced-order models and their performance in feedback control applications. Since global instabilities occur at discrete frequencies, the compensator responds at these same frequencies. For this reason, it seems sensible that a reduced-order compensator that well captures the perturbation dynamics in the vicinity of these frequencies should perform better — or more efficiently — than a compensator that approximates the transfer function over a wide range of (some dynamically irrelevant) frequencies or puts emphasis on minimizing the largest-magnitude error with no concern at which frequency this maximum error occurs. This reasoning is in contrast to the widely accepted \mathcal{H}_∞ -norm minimization intrinsic in balanced truncation (see Antoulas 2005) and may warrant a re-evaluation of proper input-output measures that favor physically motivated frequency ranges over mathematically inspired optimization. Based on our observations, a frequency-restricted \mathcal{H}_2^ω -norm, which accurately links open-loop and closed-loop performance analysis, has been proposed and defined. Applications and consequences of this definition will be further explored in a future effort.

The limits of stabilizability using reduced-order models based on global modes has been quantified by conducting a parameter study in the Reynolds number ranging from the critical value of $Re_c = 4140$ to $Re = 7500$. For very weak global instabilities ($Re \leq 5250$) only the unstable modes suffice to stabilize the system. Thus, even entirely neglecting the stable subspace dynamics, the LQG compensator successfully suppressed the global instability. This seeming robustness of the compensator, however, does not extend far beyond weak instabilities: already moderate instabilities can no longer be controlled, even if stable global modes are added. The flow cases considered in Åkervik *et al.* (2007) and Ehrenstein *et al.* (2010) are believed to fall into the “weak” category where reduced-order compensators accounting for all unstable and a few stable modes are still able to stabilize the flow.

Nevertheless, accounting for the limitation to control only weak instabilities, recognizing the difficulty of computing a large number of global modes owing to non-normality and acknowledging the lack of a rigorous and effective selection criterion, it must be concluded that global modes do not constitute a suitable choice of reduction basis for closed-loop control applications.

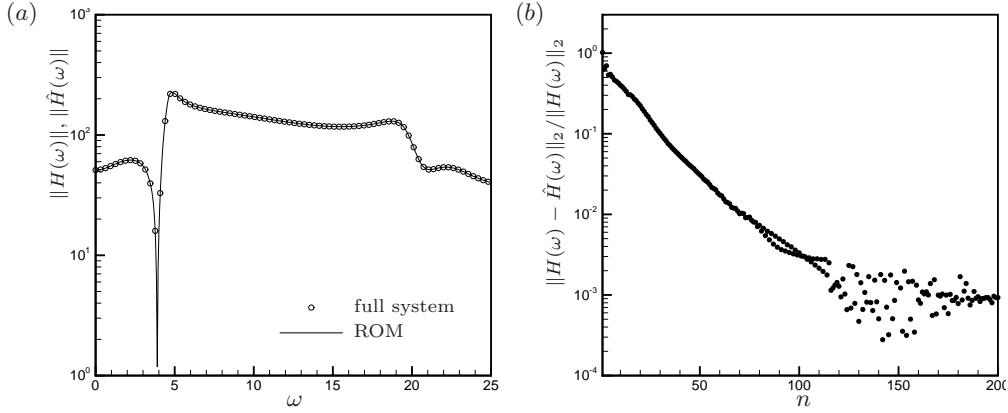


FIGURE 15. (a) Magnitude of the transfer function of the full system (symbols) and the reduced-order mode based on POD modes (solid line). (b) Relative \mathcal{H}_2 -error of the transfer function of the reduced-order plant model based on n POD modes.

Appendix A. Replacing the full system by a reduced-order model

The behavior of an unstable system can be separated into its unstable and stable dynamics which decouple. The system matrix A can be decomposed according to

$$A = \begin{pmatrix} A_u & 0 \\ 0 & A_s \end{pmatrix} \quad (\text{A } 1)$$

where A_u (resp. A_s) denotes the matrix governing the unstable (resp. stable) states (see Barbagallo *et al.* 2009; Ahuja & Rowley 2010). We wish to replace the full system by a reduced model which (i) still captures the unstable dynamics of the original system and (ii) accurately reproduces the input-output behavior, that is, the link between actuator and sensor. The first requirement is satisfied by choosing the unstable global modes for a reduction basis. For the Reynolds numbers considered in this work the dimension of the unstable subspace (dimension of A_u) varies from two to eight. For the second requirement we choose proper orthogonal decomposition (POD) modes to express the stable subspace dynamics. This choice has been shown (see, e.g., Barbagallo *et al.* 2009) to result in an accurate description of the stable input-output behavior with a moderate number of modes. The POD modes are computed for each Reynolds number using a snapshot method (Sirovich 1987). An impulse response is computed based on (5.1) until a dimensionless time of $T = 20$ resulting typically in a decrease of the perturbation energy by three orders of magnitude. Snapshots are extracted from the linearized simulations at equi-spaced time intervals of $\Delta t = 0.02$. The POD modes are then computed from these snapshots and used in a Petrov-Galerkin projection of the system (2.5) resulting in

$$\frac{d\hat{X}}{dt} = \hat{A}_s^{pod} \hat{X} + \hat{B}_{2s}^{pod} u \quad (\text{A } 2a)$$

$$m = \hat{C}^{pod} \hat{X} \quad (\text{A } 2b)$$

where the symbol $\hat{\cdot}$ denotes quantities with reduced dimensions; the superscript pod indicates a reduction based on POD modes.

The transfer function of the reduced-order model is given by $\hat{H}(\omega) = \hat{C}^{pod}(i\omega I - \hat{A}_s^{pod})^{-1} \hat{B}_{2s}^{pod}$ and is displayed for $Re = 7500$ using 150 POD modes in figure 15(a) by a solid line together with the transfer function of the full system (in symbols). Very good agreement is observed which is confirmed by computing the relative error between the

reduced-order and full transfer functions using the \mathcal{H}_2 - and \mathcal{H}_∞ -norm. Results are shown in figure 15(b); both curves decrease rapidly and eventually converge to an acceptable error for about 120 POD modes. Similar results have been obtained at lower Reynolds numbers (not shown here); thus, reduced-order models for the full linearized dynamics based on 150 POD modes will be considered for each Reynolds number. It is important to keep in mind, however, that the reduced-order model does not capture the complete dynamics of the stable subspace but only the part relevant to our study, namely the input-output behavior between actuation and measurement.

In summary, the system given by (2.5) will be replaced by the reduced-order model

$$\frac{d}{dt} \begin{pmatrix} \hat{X}_u^{gm} \\ \hat{X}_s^{pod} \end{pmatrix} = \begin{pmatrix} \hat{\Lambda}_u & 0 \\ 0 & \hat{A}_s^{pod} \end{pmatrix} \begin{pmatrix} \hat{X}_u^{gm} \\ \hat{X}_s^{pod} \end{pmatrix} + \begin{pmatrix} \hat{B}_{2u}^{gm} \\ \hat{B}_{2s}^{pod} \end{pmatrix} u \quad (\text{A } 3a)$$

$$m = \begin{pmatrix} \hat{C}_u^{gm} & \hat{C}_s^{pod} \end{pmatrix} \begin{pmatrix} \hat{X}_u^{gm} \\ \hat{X}_s^{pod} \end{pmatrix} \quad (\text{A } 3b)$$

which is based on unstable global modes for representing the unstable behavior (indicated by the superscript gm) and on POD modes for capturing the input-output dynamics contained in the stable subspace (indicated by the superscript pod).

REFERENCES

- AHUJA, S. & ROWLEY, C. W. 2010 Feedback control of unstable steady states of flow past a flat plate using reduced-order estimators. *J. Fluid Mech.* **645**, 447–478.
- ÅKERVIK, E., HEPFFNER, J., EHRENSTEIN, U. & HENNINGSON, D. S. 2007 Optimal growth, model reduction and control in a separated boundary-layer flow using global modes. *J. Fluid Mech.* **579**, 305–314.
- ANTOULAS, A., SORENSEN, D. & GUGERCIN, S. 2001 A survey of model reduction methods for large-scale systems. *Contemp. Math.* **280**, 193–219.
- ANTOULAS, A. C. 2005 *Approximation of Large-Scale Dynamical Systems*. SIAM Publishing.
- BAGHERI, S., BRANDT, L. & HENNINGSON, D. S. 2009a Input-output analysis, model reduction and control of the flat-plate boundary layer. *J. Fluid Mech.* **620**, 263–298.
- BAGHERI, S., HEPFFNER, J., SCHMID, P. J. & HENNINGSON, D. S. 2009b Input-output analysis and control design applied to a linear model of spatially developing flows. *Appl. Mech. Rev.* **62**(2).
- BARBAGALLO, A., SIPP, D. & SCHMID, P. J. 2009 Closed-loop control of an open cavity flow using reduced-order models. *J. Fluid Mech.* **641**, 1–50.
- BERKOOZ, G., HOLMES, P. & LUMLEY, J. L. 1993 The proper orthogonal decomposition in the analysis of turbulent flows. *Ann. Rev. Fluid Mech.* **25**, 539–575.
- BEWLEY, T. R. & LIU, S. 1998 Optimal and robust control and estimation of linear paths to transition. *J. Fluid Mech.* **365**, 305–349.
- BURL, J. B. 1999 *Linear optimal control. \mathcal{H}_2 and \mathcal{H}_∞ methods*. Addison-Wesley.
- DATTA, B. 2003 *Numerical Methods for Linear Control Systems*. Academic Press.
- EHRENSTEIN, U., PASSAGGIA, P.-Y. & GALLAIRE, F. 2010 Control of a separated boundary layer: Reduced-order modeling using global modes revisited. *Theor. Comp. Fluid Dyn.* pp. DOI 10.1007/s00162-010-0195-5.
- GIANNETTI, F. & LUCHINI, P. 2007 Structural sensitivity of the cylinder wake’s first instability. *J. Fluid Mech.* **581**, 167–197.
- HECHT, F., PIRONNEAU, O., HYARIC, A. LE & OHTSUKA, K. 2005 *Freefem++*, the book. UPMC-LJLL Press.
- HENNINGSON, D.S. & ÅKERVIK, E. 2008 The use of global modes to understand transition and perform flow control. *Phys. Fluids* **20**, 031302.
- KIM, J. & BEWLEY, T.R. 2007 A linear systems approach to flow control. *Ann. Rev. Fluid Mech.* **39**, 383–417.

- LEHOUCQ, R.B. & SCOTT, J.A. 1997 Implicitly restarted Arnoldi methods and subspace iteration. *SIAM J. Matrix Anal. Appl.* **23**, 551–562.
- LUMLEY, J. L. 1970 *Stochastic Tools in Turbulence*. Academic Press.
- MARQUET, O., SIPP, D. & JACQUIN, L. 2008 Sensitivity analysis and passive control of cylinder flow. *J. Fluid Mech.* **615**, 221–252.
- MOORE, B. 1981 Principal component analysis in linear systems: controllability, observability, and model reduction. *IEEE Trans. Autom. Contr.* **26**, 17–32.
- ROWLEY, C.W. 2005 Model reduction for fluids using balanced proper orthogonal decomposition. *Int. J. Bifurc. Chaos* **15**, 997–1013.
- SCHMID, P. J. & HENNINGSON, D. S. 2000 *Stability and Transition in Shear Flows*. Springer Verlag.
- SIPP, D. & LEBEDEV, A. 2007 Global stability of base and mean flows: a general approach and its applications to cylinder and open cavity flows. *J. Fluid Mech.* **593**, 333–358.
- SIPP, D., MARQUET, O., MELIGA, P. & BARBAGALLO, A. 2010 Dynamics and control of global instabilities in open flows: a linearized approach. *Appl. Mech. Rev.* **63**, 030801.
- SIROVICH, L. 1987 Turbulence and the dynamics of coherent structures. *Quart. Appl. Math.* **45**, 561–590.
- STRYKOVSKI, P.J. & SREENIVASAN, K.R. 1990 On the formation and suppression of vortex shedding at low Reynolds numbers. *J. Fluid Mech.* **218**, 71–107.
- ZHOU, K., SALOMON, G. & WU, E. 2002 *Robust and Optimal Control*. Prentice Hall, New Jersey.

6 Article 3

Closed-loop control of amplifier flows

Closed-loop control of amplifier flows

By ALEXANDRE BARBAGALLO^{1,2},
GREGORY DERGHAM³, DENIS SIPP¹,
PETER J. SCHMID²
AND JEAN-CHRISTOPHE ROBINET³

¹ONERA-DAFE, 8 rue des Vertugadins, 92190 Meudon, France

²Laboratoire d'Hydrodynamique (LadHyX), CNRS-Ecole Polytechnique, 91128 Palaiseau, France

³DynFluid Laboratory, Arts et Metiers ParisTech, 151 Bd. de l'Hopital, 75013 Paris, France

(Received 22 October 2010)

Amplifier flows are defined by their tendency to respond strongly to external sources of noise and perturbations. This behavior poses significant challenges to the design of closed-loop control strategies, since the sensitivity of the flow applies not only to physical perturbations but to inaccuracies in the design procedure as well. A comprehensive study of various components of LQG-control design — covering sensor placement, choice and influence of the cost functional, accuracy of the reduced-order model, compensator stability and performance — is conducted on numerical simulations of two-dimensional incompressible flow over a rounded backward-facing step. Robustness of the compensator will be emphasized, and the effect of various environmental factors on its performance and stability will be quantified. The noise-to-signal ratio of the estimation sensor features prominently in this study. The results show that, contrary to oscillator-type flows, amplifier flows require a judicious balance between estimation speed and estimation accuracy and between stability limits and performance requirements. Numerical experiments using impulsive and random noise confirm that the inherent amplification behavior of the flow can be reduced by an order of magnitude, if the above-mentioned constraints are observed. Coupling the linear compensator to nonlinear simulations shows a gradual deterioration in control performance as the amplitude of the noise increases.

1. Introduction

Many industrial fluid devices are afflicted by undesirable flow behavior — such as unsteadiness, separation, instabilities, and transition to turbulence — which limits performance, endanger safe operation or are detrimental to structural components. Flow control is quickly becoming a key technology in engineering design to overcome inherent limitations, to advance into unexplored parameter regimes, to extend safety margins and to ensure operation under optimal conditions. A prototypical and much-studied example is the compressible flow over a cavity which is characterized by instabilities that manifest themselves in a buffeting motion, in induced drag (Gharib & Roshko 1987) and in intense noise emission (see Rossiter 1964). In air intakes of aircraft engines separated flow can act as an amplifier for incoming perturbations causing unsteadiness which in turn results in loss of performance and material fatigue. Transitional and turbulent boundary layers have long attracted attention from the flow control community (see, e.g., Joslin 1998; Saric *et al.* 2003; Kim 2003; Boiko *et al.* 2008; Archambaud *et al.* 2008), mainly due to their ubiquity in vehicle aerodynamics and their central role as the source of skin friction. For all three examples, flow control techniques that effectively eliminate insta-

bilities, efficiently reduce noise amplification or successfully diminish drag are essential in maintaining desired flow conditions.

Control strategies greatly vary in complexity, in expended energy, but also in their ability to achieve prescribed control objective under realistic conditions. Passive control devices, which aim at modifying the mean flow, are popular in many industrial applications due to their simplicity and reliability. For example, vortex generators can be effective in energizing boundary layers and thus preventing or delaying flow separation (see Lin 2002; Choi 2008). Constant blowing or suction at the wall has similar effects, but the considerable amount of required energy to modify the mean flow is generally acknowledged as the principal drawback of passive control devices. An alternative strategy directly targets the perturbation dynamics without altering the mean flow. This active approach has received significant interest in industry and academia, and feedback control methods have been developed and applied to a great many generic flow configurations.

The design procedure of flow control laws critically depends on the nature of the flow to be controlled. Oscillator-type flows which are defined by a global instability resulting in self-sustained oscillatory fluid behavior are more easily controlled, since the flow is dominated by a limited number of structures of well-defined frequencies. Sensitivity to noise is comparatively low, and the estimator and controller can simply reconstruct the flow state from measurements and act upon it according to the control objective. A second type of flow behavior, referred to as noise-amplifiers, is substantially more challenging to control. This type of flow is globally stable but is characterized by a strong propensity to amplify noise and a broadband spectrum of responsive frequencies. This characteristic makes the flow and the control performance highly sensitive not only to physical noise sources and uncertainties, but also to methodological approximations, modeling inaccuracies and truncation errors that inevitably arise during the estimator and control design. The propagation of small perturbations, whether of physical or computational origin, is appropriately tracked and quantified by frequency-based transfer functions which reveal preferred frequencies or confirm the successful reduction of the flow's amplification potential.

Optimal flow control techniques have been widely applied for active control purposes. In particular, the linear quadratic Gaussian (LQG) framework has been adopted for the control of small-amplitude perturbations in oscillator and amplifier flows. Examples of oscillator flows include, among others, the supercritical flow over a shallow or deep cavity (Åkervik *et al.* 2007; Barbagallo *et al.* 2009), the flow over a shallow bump (Ehrenstein *et al.* 2010) and the flow past a flat plate (Ahuja & Rowley 2010). In all cases, stabilization of the flow by feedback control strategies could be accomplished. Amplifier flows are dominated by convective and transient processes, and successful control is defined by a marked reduction of the flow's inherent amplification potential. Control of amplifier flows using LQG techniques has first been attempted for very idealized geometries (see, e.g., Joshi *et al.* 1997; Bewley & Liu 1998), namely, in simple, one-dimensional configurations. For more complex and higher-dimensional flows, direct application of the LQG-framework becomes prohibitively expensive, and reduced-order models have to be introduced for the practical design of the compensator. LQG-based compensators using reduced-order models have been applied by Bagheri *et al.* (2009) to control the amplification of perturbations in a spatially developing boundary layer and by Ilak & Rowley (2008) to control transitional channel flow. In Bagheri & Henningson (2010), strong emphasis has been put on the model reduction technology; in particular, it has been demonstrated that the reduced-order model had to accurately capture the input-output behavior between actuators and sensors to ensure a positive compensator performance (Kim & Bewley 2007). Despite first successful attempts at applying LQG-feedback control to amplifier

flows, many questions remain open about the design and practical implementation of compensators for this type of flow. Owing to the flow's tendency to transiently amplify perturbations, sensitivity becomes the key concept in the design and performance evaluation of compensators: sensitivity to sensor and actuator placement, sensitivity to the accuracy of the reduced-order model, sensitivity to nonlinear effects. Some of these issues have been addressed using an idealized (parallel base flow) model problem in Ilak (2009); a comprehensive analysis of closed-loop control for amplifier flows, however, is missing.

The goal of the present study is an identification of the various environmental and procedural factors and the assessment of their influence on the performance of the compensator for amplifier flows. To this end, we consider the two-dimensional, laminar flow over a rounded backward-facing step. This configuration is characterized by a detachment of the flow close to the step followed by a recirculation zone; even though the flow is globally stable, perturbations are amplified as they are convected along the shear-layer. This flow thus represents a prototypical example of an amplifier flow (see Marquet *et al.* 2008). The present study is structured as follows. After a brief description of the flow configuration, its noise amplification behavior and the basic principles of LQG-control and model reduction (§ 2), we start by considering the estimation problem (§ 3), address sensor placement and estimation speed and establish the noise-to-signal ratio as a critical parameter. In § 4 the controller will be introduced, performance limitations of the compensator will be discussed and the influence of the choice of control objective will be assessed. § 5 will present the application of the LQG-controller to linearized numerical simulations; specifically the sensitivity to model inaccuracies and its relation to stability margins for the compensated system will be treated. Two cases will be considered: the control of an impulse of noise and the control of random forcing. In § 6 we apply linear control to a nonlinear simulation and discuss the validity range of the linear compensator. A summary of results and conclusions are given in § 7.

2. Configuration and mathematical model

2.1. Flow configuration and governing equations

We study the laminar and incompressible flow over a two-dimensional rounded backward-facing step which is sketched in figure 1 together with the geometric measures, the base flow streamlines and the setup of control inputs and sensor outputs. Only a reduced part of the computational domain is shown. The step height h and the inflow velocity U_∞ are chosen as the characteristic length and velocity scales of the problem. The rounded part of the step consists of a circular arc extending from $(x = 0, y = 1)$ to $(x = 2, y = 0)$. The flow enters the computational domain from the left (at $x = -20$) with a constant streamwise velocity. A free-slip condition is imposed on the upstream part of the lower boundary ($-20 \leq x \leq -2, y = 1$) beyond which a laminar boundary layer starts to develop; no-slip conditions are enforced on the remaining lower boundary given by $-2 \leq x \leq 100$. On the top part of the computational domain, at $y = 20$ a symmetry condition is implemented, and a standard outflow condition is prescribed at the outlet ($x = 100$).

The Reynolds number based on the step height and inflow velocity is chosen as $Re = 600$ and held constant throughout our study. For this Reynolds number, the flow separates at $x \approx 0.6$ and reattaches at $x \approx 11$, forming an elongated recirculation bubble. The displacement thickness of the incoming boundary layer at $x = 0$ is equal to $\delta^* \approx 0.082$ which yields a Reynolds number based on the displacement thickness of $Re_{\delta^*} \approx 49.2$. The base flow, a solution of the nonlinear steady Navier Stokes equations, is visualized by streamlines in figure 1.

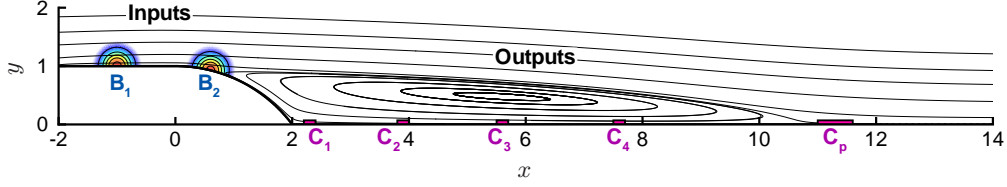


FIGURE 1. Sketch of the geometry for flow over a rounded backward-facing step, showing streamlines of the base flow at $Re = 600$. The upstream, downstream and top boundaries are respectively located at $x = -20$, $x = 100$ and $y = 20$. A typical mesh yields $n \approx 360\,000$ degrees of freedom from about 90 000 triangles. The positions of the input ($B_{1,2}$) and output ($C_{1,2,3,4,p}$) devices are also shown.

Flow over a rounded backward-facing step is a prototypical example for an amplifier flow since small upstream perturbations may be selectively amplified in the shear layer due to a Kelvin-Helmholtz instability (see next section for details). Characteristic unsteadiness arises from low-level noise via a linear amplification mechanism, which subsequently saturates nonlinearly once sufficiently high amplitudes have been reached. It is the goal of this article to devise and assess an active feedback control strategy that decreases the convective amplification of random perturbations. This strategy is designed for and operates within the linear regime which justifies using the Navier-Stokes equations linearized about the base flow as a mathematical model. The governing equations are spatially discretized using finite elements of Taylor-Hood type (P2-P2-P1) and implemented using the FreeFem++ software (see Hecht *et al.* 2005). In matrix form, these read

$$\mathbf{Q} \frac{d\mathbf{X}}{dt} = \mathbf{A}\mathbf{X} \quad (2.1)$$

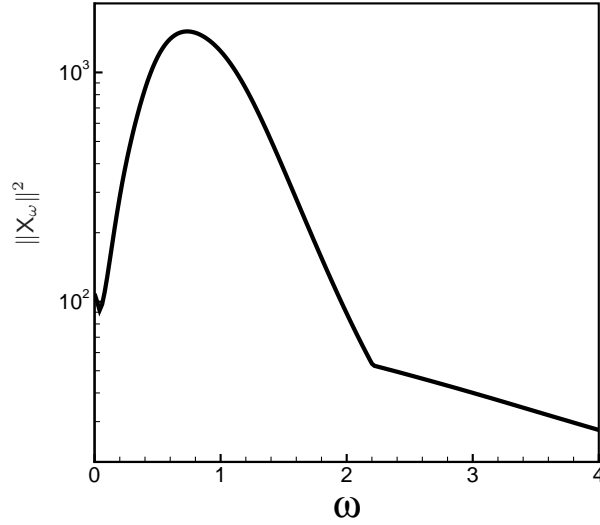
where \mathbf{X} denotes the state vector containing the velocity and pressure fields, \mathbf{A} represents the linearized Navier-Stokes operator and \mathbf{Q} stands for the mass matrix, which simultaneously defines the perturbation kinetic energy according to $\|\mathbf{X}\|^2 = \mathbf{X}^* \mathbf{Q} \mathbf{X}$.

2.2. Noise amplification behavior

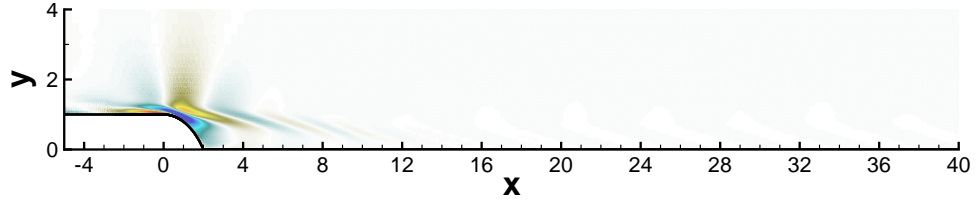
For the chosen Reynolds number of $Re = 600$ the flow is globally stable and the matrix \mathbf{A} does not show any unstable eigenvalues. Yet, sustained unsteadiness may arise from the continuous excitation of the flow by upstream noise. This noise amplifier behavior can be analyzed and quantified in terms of the optimal harmonic forcing and its response in the frequency domain (see Alizard *et al.* 2009; Sipp *et al.* 2010). For a given frequency ω , a periodic forcing of the form $\mathbf{F}_\omega \exp(i\omega t)$ yields a corresponding response $\mathbf{X}_\omega \exp(i\omega t)$ where \mathbf{X}_ω is given by $\mathbf{X}_\omega = (i\omega \mathbf{Q} - \mathbf{A})^{-1} \mathbf{Q} \mathbf{F}_\omega$. The optimal forcing is defined as the forcing \mathbf{F}_ω of unit energy (i.e. $\|\mathbf{F}_\omega\|^2 = 1$) which maximizes the energy of the response. The corresponding response \mathbf{X}_ω is referred to as the optimal response; its energy $\|\mathbf{X}_\omega\|^2$ is the optimal energy gain due to external forcing at a prescribed frequency ω . We will use the subscript ω to indicated quantities defined in the frequency domain.

In figure 2(a), the optimal energy gain is presented as a function of the forcing frequency. The semi-logarithmic graph shows a parabolic curve with the highest response to forcing around a frequency of $\omega = 0.8$. For frequencies above $\omega \approx 2$, the energy gain decays monotonically. In figure 2(b) and (c), the spatial shapes of the optimal forcing and response (real part only) taken at the highest energy gain are visualized by contours of the streamwise component. In accordance with the convective nature of the flow, we observe that the optimal forcing is concentrated upstream near the step while the associated response is located further downstream. Hence, a noise source situated near

(a)



(b)



(c)

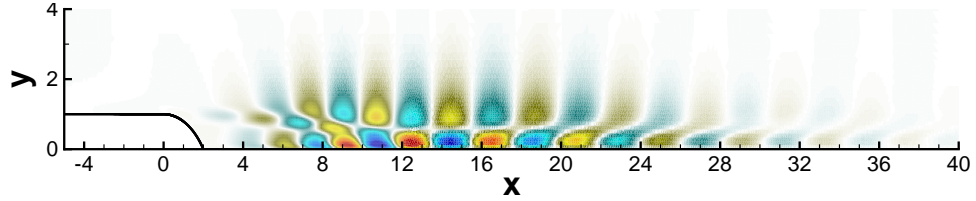


FIGURE 2. (a) Optimal energy response of the linear system to a harmonic forcing of frequency ω . (b) Optimal forcing visualized by contours of the streamwise velocity. (c) Optimal response visualized by contours of the streamwise velocity.

the rounded step can efficiently trigger perturbations whose maximum amplitudes are attained near $x \approx 12$. Based on this result, we model the noise as a Gaussian-shaped momentum forcing located at $(x = -1, y = 1)$ with a width of 0.6 and a thickness of 1. After discretization, this forcing appears in form of the matrix B_1 in the following linear system

$$Q \frac{dX}{dt} = AX + QB_1 w(t) \quad (2.2)$$

with $w(t)$ describing the temporal behavior of the noise. For the sake of simplicity, the noise will be taken as white-in-time with zero mean $\langle w \rangle = 0$ and variance $\langle w^2 \rangle$ denoted by W^2 .

In continuing to set up our flow control problem, an appropriate objective or cost functional has to be specified. To this end, two quantities will be considered. The first quantity consists of the shear stress measured at the wall and is computed following

$m_p = C_p X = \int_{x=11}^{x=11.6} \partial_y u dx$. The placement of this sensor has been motivated by the location of maximum response of the flow to harmonic excitation (see figure 2(c)). The second quantity of interest is the total kinetic perturbation energy contained in the entire domain; it is given by $E = X^* Q X$. The control to be designed will aim at diminishing either m_p or E . It is interesting to note that, under random forcing, the two quantities of interest, m_p and E , display a frequency response strikingly similar to the one given in figure 2(a); the spatial structure of the stochastic response resembles the one given in figure 2(c) (the reader is referred to figure 11 for verification).

2.3. Linear Quadratic Gaussian (LQG) control

A closed-loop control strategy is considered in order to weaken or suppress the amplification of perturbations. In contrast to open-loop control strategies, this method extracts information from the system via measurements which is then processed to apply real-time actuation. This technique allows flow manipulation with rather low expended energy and permits the application and adaptation of control laws to a variety of flow situations, provided the model is representative of and robust to physical and parametric changes. The approach taken in our study is based on a compensator designed within the Linear Quadratic Gaussian (LQG) control framework (see Burl 1999). The actuator through which control efforts are exerted on the flow consists of a body force acting on the vertical momentum component; the location, shape and type of the actuator is summarized in the matrix B_2 (see figure 1). The control law $u(t)$ which describes the temporal behavior of the actuator is based on real-time measurements of the flow from sensors located at various positions along the wall. These sensors extract either shear stress or pressure information. The governing system of equations, including the actuators and sensors, can be cast into the familiar state-space form

$$Q \frac{dX}{dt} = AX + QB_1 w + QB_2 u, \quad (2.3a)$$

$$m = CX. \quad (2.3b)$$

The link between the measurement signal m and the actuation law u is provided by the compensator. Figure 3 presents a sketch of a typical LQG-control setup, including the system to be controlled as well as the two components of the compensator: the estimator and the controller. The module labeled "plant" represents our fluid system whose flow characteristics we wish to modify; it is given mathematically by (2.3a). The plant depends on the initial condition $X(t_0)$, the noise input $w(t)$ and the control law $u(t)$ and provides as an output the state vector X . A measurement signal m can be extracted at all times from the state vector which is then passed to the compensator. In a first step, the estimator will reconstruct an estimated state $\hat{Y}(t)$ from the measurement m which is, in a second step, used by the controller to compute the control law $u(t)$. More details about the design of the estimator and the controller will be given below.

It is important to stress that the placement of the actuator and sensor is critical for the success of closed-loop control. In our case, the actuator is positioned near the separation point (see control input B_2 in figure 1) which corresponds to the location where the optimal forcing structure is most prominent (see figure 2(b)). This placement optimally exploits the sensitivity of the flow to external forcing and suggests that low-amplitude control at this location may exert sufficient influence on the flow behavior to accomplish our control objective. In other words, the chosen actuator location should ensure low control gains. Analogously, the placement of the sensor requires care and thought. Commonly, measurements are taken at locations where the flow feature we wish to suppress is particularly prevalent. Recalling the spatial structure of the most amplified

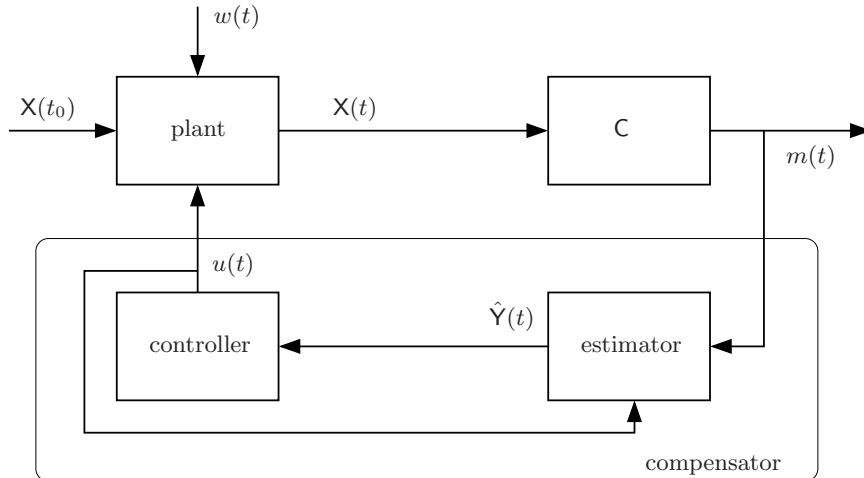


FIGURE 3. Sketch of a typical LQG-control setup.

flow response to optimal forcing (see figure 2(c)), this would suggest a sensor placement downstream of the reattachment point near $x \approx 12$. Nevertheless, we will demonstrate that this particular choice does not yield an efficient and effective closed-loop control, and we will methodically explore the estimator performance based on sensors placed further upstream in the recirculation bubble (see figure 1). In particular, four discrete sensor locations, denoted by $C_{1,2,3,4}$, will be assessed; these are distinct from the performance sensor C_p .

2.4. Reduced-order model based on proper orthogonal decomposition

The design of the estimator and controller involves the numerical solutions of two Riccati equations for the Kalman and control gain, respectively. The numerical effort is proportional to the dimension of the system matrix A , which makes the direct solution of the Riccati equation excessively expensive or even impossible. It is thus necessary and common practice to substitute the full system by an equivalent system of considerably smaller dimensions and to compute the two gains based on this reduced-order model of the flow. A standard technique to arrive at a reduced-order model of the flow uses a Galerkin projection of the governing equations onto proper orthogonal decomposition (POD) modes (see Sirovich 1987). This method proves to be efficient (see Bagheri *et al.* 2009; Bagheri & Henningson 2010; Barbagallo *et al.* 2009) in capturing the main characteristics of the original system required for closed-loop control, namely the dynamics between the inputs (given by B_1 and B_2) and the outputs (given by sensors $C_{1,2,3,4}$ and the control objectives E and C_p). The governing equation for the reduced-order model is similar to (2.3) and is given by

$$\frac{d\hat{X}}{dt} = \hat{A}\hat{X} + \hat{B}_1 w + \hat{B}_2 u \quad (2.4a)$$

$$m = \hat{C}\hat{X} \quad (2.4b)$$

where the superscript $\hat{\cdot}$ indicates reduced quantities. The use of a reduced-order model decreases the dimension of the system from $\mathcal{O}(10^6)$ to ~ 150 degrees of freedom and thus allows the application of standard direct algorithms for LQG-control design. Reduced-order models with even lower dimensions are possible, e.g., by using balanced POD

modes (see Bagheri *et al.* 2009; Barbagallo *et al.* 2009; Ahuja & Rowley 2010) but are beside the point of this study.

3. Estimation and sensor placement

As a first step of the full control design and performance evaluation process, we concentrate on the estimator, in particular its performance with respect to the location of the sensors.

3.1. Presentation of the estimator

In general, the estimator's task is the approximate reconstruction of the full state vector using only limited information from the measurement. This approximate state vector will then be used by the controller to determine a control strategy that accomplishes our objective. The estimated state \hat{Y} is assumed to satisfy a set of equations similar to the one governing the original system (2.4). We have

$$\frac{d\hat{Y}}{dt} = \hat{A}\hat{Y} + \hat{B}_2u(t) - \hat{L}(m - \hat{C}\hat{Y}) \quad (3.1)$$

where the original noise term $\hat{B}_1w(t)$ has been replaced by the forcing term $-\hat{L}(m - \hat{C}\hat{Y})$. The latter term represents the difference between the true measurement signal $m(t) = \hat{C}\hat{X}$ and the estimated measurement signal $\hat{C}\hat{Y}$ and is applied as a forcing term premultiplied by \hat{L} . This term is to drive the estimated state \hat{Y} toward the true state \hat{X} . In the forcing term, the so-called *Kalman gain* \hat{L} can be computed from a constrained optimization problem in which the cost functional is taken as the error between the full and estimated state, i.e., $\hat{Z} = \hat{X} - \hat{Y}$, and is subsequently minimized. The resulting optimality condition yields a Riccati equation, from which the Kalman gain \hat{L} follows (see Burl 1999). Commonly, the energy of the estimation error is formulated in the time domain; it will prove advantageous in our case, though, to recast the energy in the frequency domain. Using Parseval's theorem we obtain

$$\bar{Z} = \int_{-\infty}^{\infty} \|\hat{Z}_\omega\|^2 d\omega \quad (3.2)$$

where \hat{Z}_ω denotes the Fourier-transform of the error \hat{Z} . Two sources of noise — both assumed as white in time — are taken into account in the derivation and solution of the Riccati equation: a plant noise $w(t)$ of variance W^2 driving the dynamics of the original system (2.4) and a measurement noise $g(t)$ with variance G^2 contaminating the measurement $m(t)$. The ratio of the two standard deviations, i.e., G/W , can be taken as a parameter that governs the speed of the estimation process, but can also be interpreted as the noise-to-signal ratio of the sensor. For example, considering a constant standard deviation W of the plant noise, the parameter G/W represents a quality measure of the sensor. Large values of G/W indicate that the measurement noise $g(t)$ is too high to ensure a correct signal; the corresponding Kalman gain \hat{L} tends to zero. Consequently, the forcing term in (3.1) has a negligible effect on the system which, in turn, leads to a poorly performing estimator. This parameter regime is referred to as the small gain limit (SGL). Contrary to the small gain limit, for $G/W \ll 1$ the corruption of the measurement signal by noise is low compared to the stochasticity arising from the system itself; as a consequence, the estimation process becomes highly effective due to the substantial Kalman gains. This parameter regime, referred to as the large gain limit (LGL), comprises the most performing estimators for a given configuration.

By construction, the performance of the estimator crucially depends on details related to the measurement signal, and the type of sensor (in terms of its noise-to-signal ratio) as well as its location have to be chosen judiciously if overall success of the closed-loop control effort is to be expected. In what follows, we will consider four sensors $\hat{C}_{1,2,3,4}$ that are identical in type but placed at four different positions within the recirculation bubble and assess their capability of efficiently estimating the flow state. Special emphasis will also be directed toward the quantitative influence of the noise-to-signal ratio G/W introduced above.

3.2. Performance of the estimator

In this paragraph, we further elaborate on estimating the flow state \hat{X} governed by (2.4). The estimation problem is decoupled from the control problem (see Burl 1999). For this reason, we can set the control law to zero ($u(t) = 0$) without loss of generality and continue our study of the estimation problem without actuation. The system is driven by white noise represented by $w(t)$; but, owing to the linearity of (2.4), the performance of the estimator can equivalently be studied by considering harmonic forcings $w(t) = \exp(i\omega t)$ of a given frequency ω . It is then convenient to reformulate the coupled plant/estimator system in the frequency domain and state the governing equations for the harmonic response as

$$\begin{pmatrix} \hat{X}_\omega \\ \hat{Y}_\omega \end{pmatrix} = \begin{pmatrix} i\omega\hat{I} - \hat{A} & \hat{0} \\ \hat{L}\hat{C} & i\omega\hat{I} - (\hat{A} + \hat{L}\hat{C}) \end{pmatrix}^{-1} \begin{pmatrix} \hat{B}_1 \\ \hat{0} \end{pmatrix}. \quad (3.3)$$

where, as before, the subscript ω indicates variables defined in the frequency domain. The estimation error in frequency space is given as $\hat{Z}_\omega = \hat{X}_\omega - \hat{Y}_\omega$.

In figure 4 the frequency dependence of the estimation error $\|\hat{Z}_\omega\|^2$ is displayed for shear-stress sensors placed at the four above-mentioned locations (see figure 1) and for selected values of the noise-to-signal parameter G/W . For comparison, the norm of the state vector $\|\hat{X}_\omega\|^2$, which is similar to figure 2(a), is included in each subplot as a dashed line. In the small gain limit (red lines), each estimator, as expected, does not succeed in identifying the state, producing an error as large as the norm of the original state. As the parameter G/W decreases though, the estimation process improves due to a less contaminated input from the sensors and the estimation error is reduced — mainly at frequencies where the system reacts strongly to external excitations. As the parameter G/W approaches the large gain limit (blue lines), the various error curves eventually converge to the lowest possible values for each configuration. These curves then define the best attainable performance for each sensor.

This general behavior is observable for each of the four sensors. The final errors in the large gain limit (blue lines), however, are not identical for all sensors: the best performance is achieved by sensor \hat{C}_1 . As the location of the sensor is moved further downstream in the separation bubble (considering successively the sensors \hat{C}_1 , \hat{C}_2 , \hat{C}_3 and \hat{C}_4), the frequencies which are naturally amplified by the system are less well predicted; a failure of correctly estimating the higher frequencies ($\omega > 3$) is also discernible. This suggests that the estimator based on \hat{C}_1 will be more efficient in accurately determining the flow state.

An instructive way of assessing the performance of an estimator over all frequencies is to directly compute the cost functional \bar{Z} (see eq. (3.2)) normalized by the energy of the state. We thus introduce $\sqrt{\bar{Z}/\bar{E}_0}$ with $\bar{E}_0 = \int_{-\infty}^{\infty} \|\hat{X}_\omega\|^2 d\omega$ and $\hat{X}_\omega = (i\omega\hat{I} - \hat{A})^{-1}\hat{B}_1$. When this quantity is close to 1, the estimation process has failed with a 100% estimation error; the smaller the value, the better-performing the estimator. This quantity

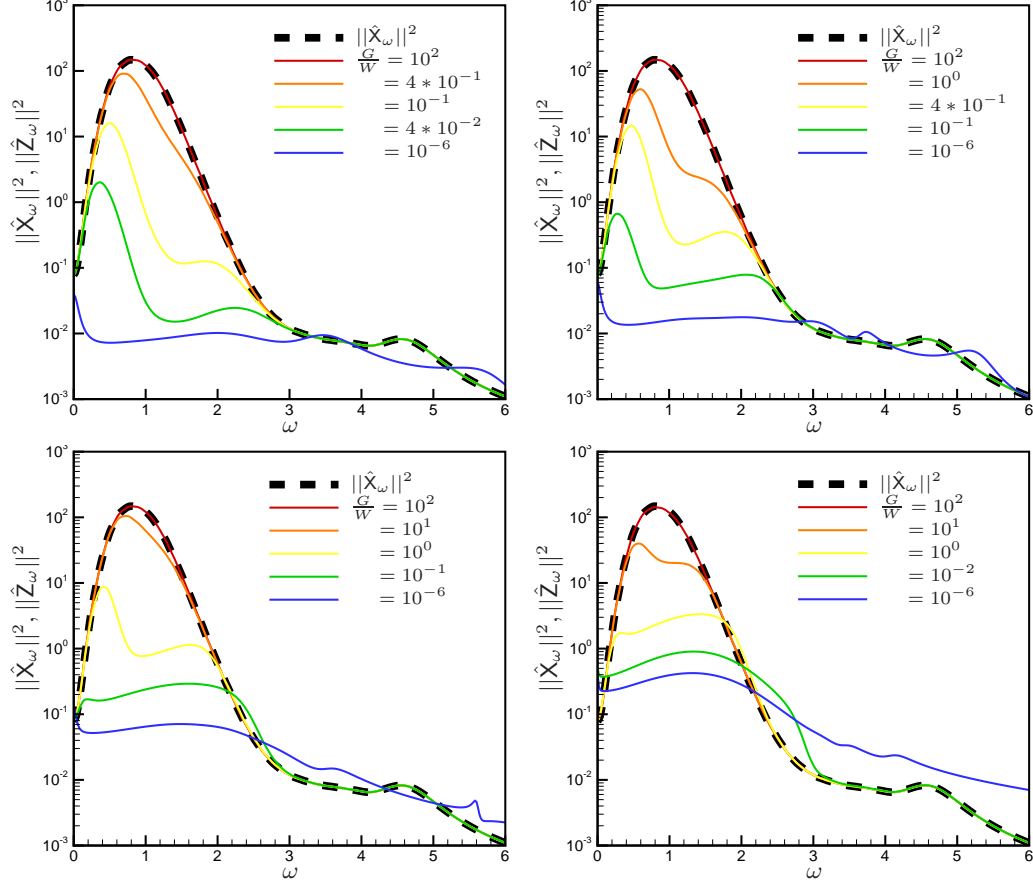


FIGURE 4. Performance of the estimator versus frequency using four different sensors and selected values of the estimation (noise-to-signal) parameter G/W . Top left: sensor \hat{C}_1 , top right: sensor \hat{C}_2 , bottom left: sensor \hat{C}_3 , bottom right: sensor \hat{C}_4 .

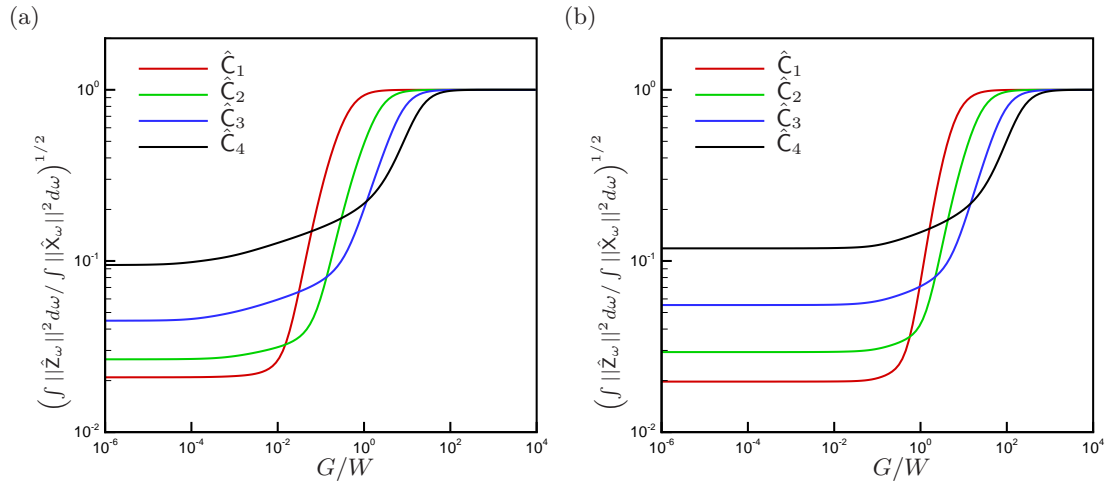


FIGURE 5. Normalized performance of the estimator, integrated over all frequencies, versus the estimation parameter G/W for four different sensor locations; (a) measuring shear-stress, (b) measuring pressure.

is displayed in figure 5(a) versus the estimation parameter G/W for each of the four sensors. The red curve represents the estimator performance based on sensor \hat{C}_1 . For this sensor location and for noise-to-signal ratios above 1, the sensor noise prohibits a correct estimation resulting in an estimation error of 100%. As the noise-to-signal ratio diminishes further, the performance of the estimator progressively increases until it reaches the large gain limit for values of G/W less than approximately 10^{-2} . Below this value of G/W , the estimator performs at its optimum. Similar behavior can be observed for the remaining sensor locations given by \hat{C}_2 , \hat{C}_3 and \hat{C}_4 : the small-gain-limit regime is clearly detectable at high values of G/W . However, the exact values for which the estimator reaches the large gain limit becomes less sharply defined as the sensor location is moved further downstream in the separation bubble. Comparing the performance of estimators based on different sensors, we conclude, in agreement with figure 4, that the performance in the large gain limit is best for the sensor \hat{C}_1 and decreases as the sensor is moved further downstream. It is surprising though that the estimator based on \hat{C}_4 , which performs worst in the large gain limit, shows better performance at high values of the noise-to-signal ratio G/W . For example, if we consider the value $G/W = 10^0$, the estimator based on \hat{C}_4 displays a relative error of 20% while the estimator based on \hat{C}_1 still shows an error of 100%. If a constant noise level of the system-generated signal is assumed ($W = \text{const.}$), this implies that the estimator based on \hat{C}_4 can cope with higher levels of measurement noise than the estimator based on \hat{C}_1 . In practice, this means that less-quality sensors can be used as long as they are placed further downstream; this point will be discussed further in the next section.

To conclude, the estimation errors are rather small ($< 10^{-1}$) for all sensors in the large gain limit. Yet, the estimator based on \hat{C}_1 is most efficient with a performance measure of $2 \cdot 10^{-2}$, while the estimator based on \hat{C}_4 only reaches a value of 10^{-1} in the large gain limit. At first glance, this difference in performance may seem small and insignificant, but it will be shown below (section § 4) that it nonetheless has a strong influence on the efficiency of the compensator. But first, the next section will offer a physical explanation for the observed loss of estimation performance by analyzing the above results in the time domain rather than the frequency domain.

3.3. Interpretation in the time domain

Even though a formulation of the estimation problem in the frequency domain is the proper choice for designing closed-loop control strategies for amplifier flows, it nevertheless remains challenging to attach physical meaning to the frequency-based results; an interpretation of our findings in the time domain seems more intuitive. The main result — the estimator's performance deteriorates as the sensor is gradually moved from the upstream \hat{C}_1 to the downstream \hat{C}_4 position — suggests that the travel time of a perturbation, before it is detected by the sensor, plays a critical role. To validate this proposition, we start by rewriting the estimation performance parameter in the time domain using Parseval's theorem. We obtain $\int_{-\infty}^{\infty} \|\hat{Z}_\omega\|^2 d\omega = (2\pi)^{-1} \int_0^{\infty} \|\hat{Z}\|^2 dt$, with $\hat{Z} = \hat{X} - \hat{Y}$ and \hat{X} and \hat{Y} satisfying the following systems of equations in the time domain:

$$\frac{d}{dt} \begin{pmatrix} \hat{X} \\ \hat{Y} \end{pmatrix} = \begin{pmatrix} \hat{A} & \hat{0} \\ -\hat{L}\hat{C} & \hat{A} + \hat{L}\hat{C} \end{pmatrix} \begin{pmatrix} \hat{X} \\ \hat{Y} \end{pmatrix}, \quad \begin{pmatrix} \hat{X} \\ \hat{Y} \end{pmatrix}_{t=0} = \begin{pmatrix} \hat{B}_1 \\ \hat{0} \end{pmatrix}. \quad (3.4)$$

The above system determines an impulse response triggered by the noise term \hat{B}_1 : the initial condition $\hat{X}_{t=0} = \hat{B}_1$ is advected downstream while being amplified along the shear-layer of the recirculation bubble. The energy $\|\hat{X}\|^2$ of this perturbation is displayed versus

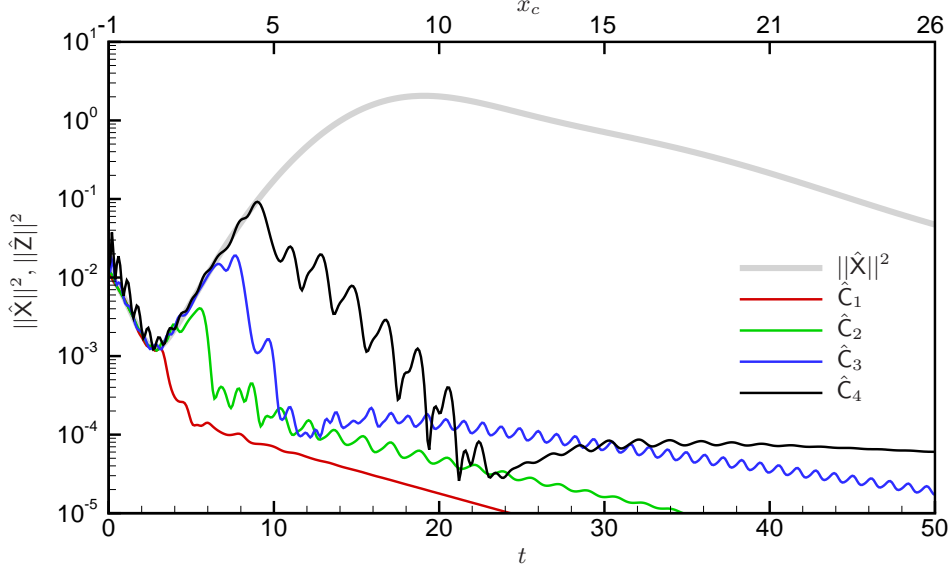


FIGURE 6. Temporal evolution of the energy of the error vector $\|\hat{\mathbf{Z}}\|^2$ for four different sensor locations $\hat{\mathbf{C}}_{1,2,3,4}$, and energy of the (uncontrolled) state $\|\hat{\mathbf{X}}\|^2$ (in gray).

time by a gray thick line in figure 6. In addition to the time axis, a second axis is displayed at the top of the figure where the location of the advected wave packet, evaluated by the energy-weighted x -centroid x_c defined as $x_c(t) = \int x e(x, y, t) dx dy / \int e(x, y, t) dx dy$ with $e(x, y, t) = |u|^2 + |v|^2$ as the pointwise energy at time t , is shown. The initial condition is associated with the non-zero state energy $\|\hat{\mathbf{X}}\|^2 = \|\hat{\mathbf{B}}_1\|^2$ at $t = 0$. The energy then decreases for $0 < t \lesssim 1.5$ as the perturbation traverses the stable region of the flow between the noise location and the separation point. Beyond the separation point of the shear layer, the wave packet enters the convectively unstable region and its energy grows until the perturbation reaches the attachment point. At time $t \approx 19$ the energy reaches a maximum; the corresponding energy-weighted x -centroid x_c is located at $x \approx 9.5$. The perturbation continues through a convectively stable region and the state energy decreases accordingly. During this advective process the estimator tries, in real-time, to reconstruct the actual state from the information provided by one sensor, and the estimation performance parameter is given by the integral in time of the actual estimation error $\hat{\mathbf{Z}}$. In the following analysis, all estimators ($\hat{\mathbf{C}}_1$ to $\hat{\mathbf{C}}_4$) will operate at their respective large gain limit, which ensures the best attainable performance for each estimator.

In figure 6 the thin solid lines display the energy of the estimation error $\|\hat{\mathbf{Z}}\|^2$ as a function of time for all four sensors. The red curve traces the estimation error associated with sensor $\hat{\mathbf{C}}_1$. For short times ($0 < t \lesssim 3$), the estimation error energy is comparable to the state energy, indicating a relative estimation error of 100%. Starting at $t \approx 3$, the error drops abruptly by one order of magnitude before a more gradual decrease sets in for $t \gtrsim 6$. The estimator becomes effective as soon as the error curve clearly detaches from the state energy curve (gray thick solid line); the state is hence well estimated beyond $t \approx 4$ using sensor $\hat{\mathbf{C}}_1$. The estimation error curves (green, blue and black curves) for the remaining sensors $\hat{\mathbf{C}}_{2,3,4}$ display a similar behavior: a relative estimation error of 100% for early times, followed by a pronounced drop after a critical time and finally a gradual decay. The abrupt decline in the estimation error energy, however, occurs considerably

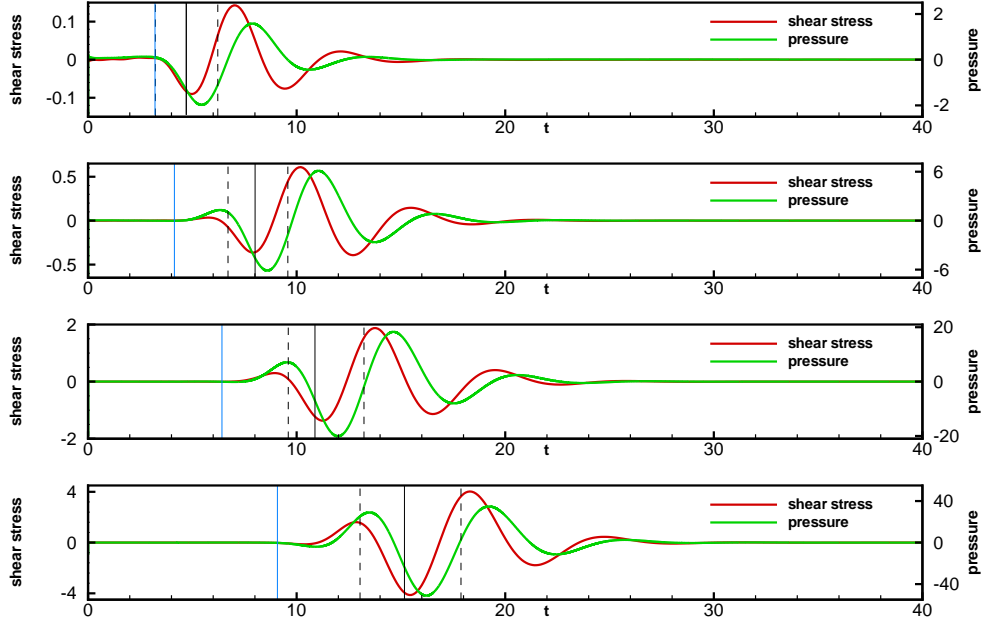


FIGURE 7. Measured impulse response at the four sensor locations, $\hat{C}_{1,2,3,4}$ (top to bottom); shear stress measurement in red, pressure measurements in green. Notice the dual labeling of the vertical axis. The blue vertical lines correspond to the times when $\|\hat{Z}\|^2/\|\hat{X}\|^2 = 0.9$ (see figure 6). The black vertical lines indicate the times when the energy-based x -centroid of the wave packet x_c reaches the sensor; the dash lines give the times when $x_c \pm \sigma$ reaches the sensor, with σ denoting the standard deviation of the wave packet.

later than for sensor \hat{C}_1 , and this delay increases steadily as the sensor location is moved further downstream. Nevertheless, in all cases the estimation error ultimately decreases, and the flow state appears to be well-estimated for large times. We thus conclude that the principal difference between the estimators is the time at which they start to become effective: sensor \hat{C}_1 , located furthest upstream, yields the earliest accurate estimates of the state, followed by \hat{C}_2 , \hat{C}_3 and finally \hat{C}_4 .

More insight is gained by displaying the measurements from the different sensors for the above impulse-response simulation (see figure 7). We will for the moment concentrate on the red curves, showing shear-stress measurements. For sensor \hat{C}_1 (top figure) we observe a quiet phase ($0 < t \lesssim 4$), after which a sinusoidal signal, the footprint of the wave packet traveling downstream in the shear layer above the sensor, is detected. The measurement returns to zero for $t \gtrsim 16$. Similar features can be observed for the other three sensors; however, the time of first detection is delayed and the amplitude of the signal is substantially increased (by nearly forty times between \hat{C}_1 and \hat{C}_4) as we move the sensor location further downstream. The time delay in detecting the wave packet is closely linked to the overall performance of the four estimators: early detection yields better results. The detection times in figure 7 (blue vertical bars) correspond to the critical times in figure 6. After the wave packet has been captured by the sensor, the estimation proceeds rapidly due to the large Kalman gains (large gain limit). If noise is generated at \hat{B}_1 , the \hat{C}_4 -estimator is able to identify the associated response in the region $x > 5$ but is imperceptive for any response in the region $-1 < x < 5$; the regions of the flow domain where disturbances are undetectable by the four sensors are outlined

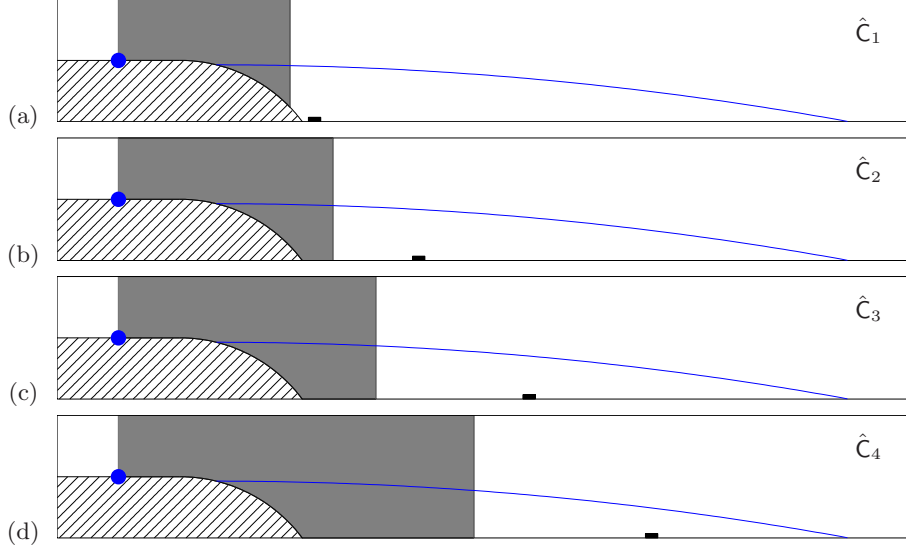


FIGURE 8. Sketch of regions of the flow domain where disturbances cannot be detected by the sensor: (a) for sensor \hat{C}_1 , (b) for sensor \hat{C}_2 , (c) for sensor \hat{C}_3 , and (d) for sensor \hat{C}_4 . The location of \hat{B}_1 is indicated by a blue symbol; the respective sensor location is shown as a black rectangle.

in figure 8. The performance of the estimator is thus less determined by the quality of the reconstructed state — all energy curves in figure 6 tend to zero — than by its reaction time which translates into a spatial range where state responses to noise are detectable. It is this distinction that will have a dramatic impact on the performance of closed-loop control of amplifier systems (see § 4) and will reveal the effectiveness of seemingly performing estimators when incorporated into a compensator.

Larger amplitudes are detected at sensors located further downstream which stems from the amplification of the wave packet due to a convective instability along the shear layer of the separation bubble; the four sensors $\hat{C}_{1,2,3,4}$ capture the wave packet at various stages of this instability. This difference in amplitude also explains some features observed in figure 5. Comparing the curves associated with the different sensors $\hat{C}_{1,2,3,4}$, we notice that the estimation process becomes effective for different values of the noise-to-signal ratio G/W . For example, sensor \hat{C}_1 starts to perform well for $G/W < 1.25$, while sensor \hat{C}_4 only requires $G/W < 52$; which leads us to conclude that higher-quality sensors are required when one plans to place them further upstream where signals are generally weaker.

We continue by assessing the effectiveness of the estimation process by considering the true noise-to-signal ratio G/W' with W' as the actual amplitude of the signal detected by a given sensor. The ratio W'/W may be obtained from figure 7 by finding the maximum amplitude of the signal (the impulse response based on noise) measured by the respective sensor; for example, $W'/W = 0.14$ for sensor \hat{C}_1 and $W'/W = 4$ for sensor \hat{C}_4 . Values for all four sensors are reported in the second column of table 1. We then determine, for all four sensors, critical values of the true noise-to-signal ratio G/W' for the estimation process using $G/W' = (G/W)/(W'/W)$. Figure 5 displays results for sensor \hat{C}_1 showing that estimation becomes effective for $G/W < 1.25$ which corresponds to $G/W' < 8.9$. Analogous results for the other sensors are reported in table 1. It appears that the estimation process for each of the four sensors starts being efficient for values of the true noise-to-signal ratio $G/W' \approx 10$, i.e., when the magnitude (measured by W') of the signal

sensor	W'/W	$G/W _{SGL}$	$G/W _{MGL}$	$G/W' _{SGL}$	$G/W' _{MGL}$
1	0.14	1.25	0.21	8.9	1.5
2	0.31	6.4	1	10.5	1.64
3	1.87	21	3.5	11.2	1.87
4	4	52	7	13	1.75

TABLE 1. Estimation parameters G/W and true noise-to-signal ratios G/W' for the four sensors $\hat{C}_{1,2,3,4}$ in the small gain limit (SGL) and medium gain limit (MGL). The critical values for the small gain limit are based on $\sqrt{\bar{Z}/\bar{E}_0} = 0.95$; the critical values for the medium gain limit are based on $\sqrt{\bar{Z}/\bar{E}_0} = 0.5$.

from the plant is ten times smaller than the noise intrinsic to the sensor (measured by G). If G/W' is of order one (see sixth column of table 1), the estimation process performs significantly better: the estimation performance parameter in figure 5 has reached the mean-value between the small-gain-limit performance (unity for all sensors) and the large-gain-limit performance (e.g., 0.02 for sensor \hat{C}_1). Optimal performance is obtained for true noise-to-signal ratios G/W' of order 10^{-2} .

Besides the location and quality of sensors, the type of signal measured by the sensor is equally important. For this reason, we also consider pressure probes by assuming that both normal and tangential stresses can be measured simultaneously on a small segment of the wall. A quantitative comparison between shear-stress and pressure sensors is made possible by multiplying the measured pressure signal by the Reynolds number since the stress component at the lower horizontal wall reads $-p\mathbf{e}_y + Re^{-1} \partial_y u \mathbf{e}_x$. The location and size of the pressure sensors have been chosen identical to the previous study of shear-stress sensors, and the signals from the impulse responses are plotted (in green) in figure 7 for the four configurations $\hat{C}_{1,2,3,4}$. The general appearance of the signals is similar to the shear-sensor case, the pressure signal, however, is approximately one order of magnitude larger than the corresponding shear-stress signal. This finding is also reflected in the estimation error analysis, shown in figure 5(b): the individual large gain limits are nearly identical to the shear-stress case, the curves corresponding to the pressure signals are shifted by about one decade to higher noise-to-signal ratios G/W . The estimation performance of shear-stress sensors can be matched by pressure probes with G/W one order of magnitude higher; in other words, pressure sensors can be far less effective than shear-stress sensors and still accomplish equivalent results. The little difference in behavior between shear-stress and pressure sensors runs counter to the intuition that pressure perturbations propagate infinitely fast in incompressible flow; our study illustrates that pressure probes do not detect disturbances any earlier than shear-stress sensors.

In summary, two competing mechanisms have been isolated in the estimation process for amplifier flows: (i) for an effective estimator, the sensor has to be located sufficiently upstream to allow a *rapid* identification of the perturbation; (ii) on the other hand, the noise-to-signal ratio G/W has to be sufficiently small to enable an *accurate* estimate, thus favoring or forcing the placement of noisy sensors further downstream where the signal amplitudes are higher. In short, a balance between speed and accuracy of the estimation process has to be struck. Whereas the upstream placement of the sensors runs somewhat counter to the intuitive placement of the sensor near the reattachment-line, it will be shown that, for our prototypical configuration, the speed of estimation appears more

critical for a successful compensator performance than the capture of highly accurate measurements.

4. Closed-loop control based on reduced-order model

After our analysis of the estimator and its performance, we now direct our attention to the complete compensator. After a brief presentation of the controller and its design steps, we investigate the performance of the compensator built on the four sensors $\hat{C}_{1,2,3,4}$. Two objective functionals for the controller will be studied: (i) the square of the measurement based on \hat{C}_p and integrated over time, and (ii) the time-integral of the entire perturbation energy. Within this section, the plant is modeled by the reduced-order model introduced in § 2.

4.1. Presentation of the controller

We will aim at suppressing perturbations in our fluid system by employing an optimal control strategy which will be designed to minimize a predefined cost functional. In mathematical terms, a control law of the form $u(t) = \hat{K}\hat{X}$ will be assumed where the control gain \hat{K} arises from the solution of a Riccati equation (see Burl 1999). Traditionally, the cost functional is related to a quantity measuring the energy of the state, but also takes into account the control effort in terms of its expended energy.

In our study, two measures of the state will be considered in the minimization process: the energy contained in the measurement extracted at location \hat{C}_p (see figure 1) yielding a cost functional of the form

$$J_m = \int_0^\infty \left(\hat{X}^* \hat{C}_p^* \hat{C}_p \hat{X} + l^2 u^2 \right) dt, \quad (4.1)$$

or the perturbation energy contained in the entire domain leading to a cost functional of the form

$$J_e = \int_0^\infty \left(\hat{X}^* \hat{Q} \hat{X} + l^2 u^2 \right) dt. \quad (4.2)$$

The parameter l appears in either choice and is referred to as the cost of control, as it quantifies the user-specified weighting of the control energy compared to the quantity to be minimized. Similar to the estimator, a small-gain-limit (resp. large-gain-limit) parameter regime exists where the controller exerts nearly no action (resp. maximum action) on the flow. Invoking the separation principle (see Burl 1999), the controller design can be carried out independent of the estimator design.

The performance assessment of the compensator will follow the frequency-based framework for amplifier flows outlined in § 2 and § 3. Considering the state-space system (2.4) driven by a harmonic excitation $w(t) = \exp(i\omega t)$ the response of the compensated system reads

$$\begin{pmatrix} \hat{X}_\omega \\ \hat{Y}_\omega \end{pmatrix} = \begin{pmatrix} i\omega \hat{I} - \hat{A} & -\hat{B}_2 \hat{K} \\ \hat{L} \hat{C} & i\omega \hat{I} - (\hat{A} + \hat{B}_2 \hat{K} + \hat{L} \hat{C}) \end{pmatrix}^{-1} \begin{pmatrix} \hat{B}_1 \\ \hat{O} \end{pmatrix}. \quad (4.3)$$

The above equation will form the basis for our performance analysis of the compensated system, where we will focus on the influence of controllers designed with J_m or J_e as well as on the impact of the control cost l and the noise-to-signal ratio G/W .

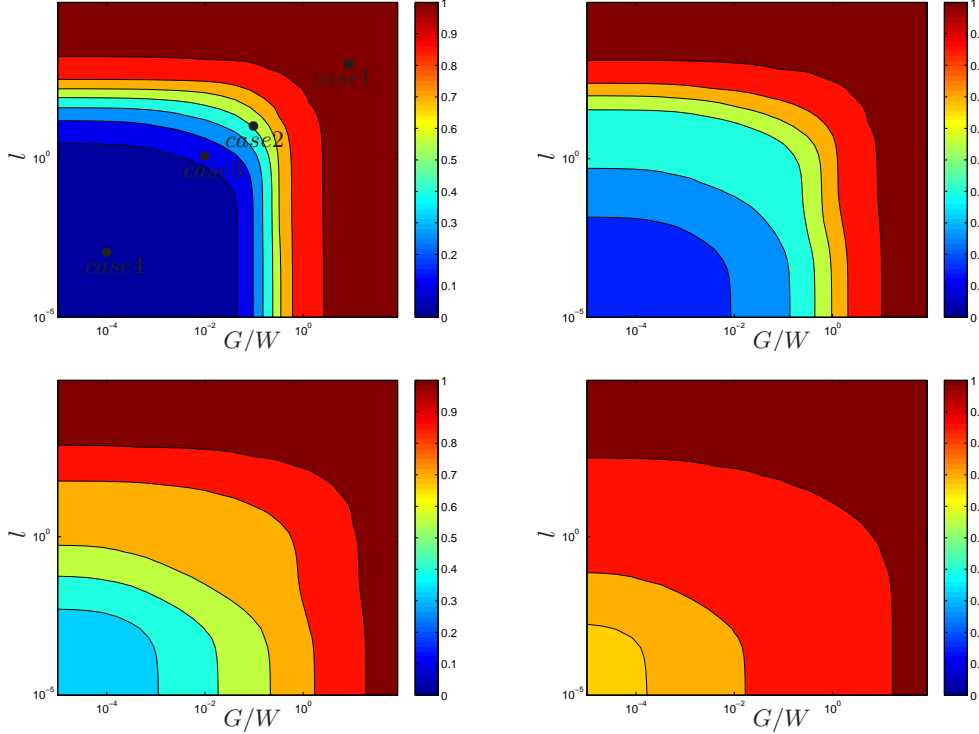


FIGURE 9. Contours of the performance measure P_m based on the measurement energy as a function of noise-to-signal ratio G/W and control cost parameter l . Top left: sensor \hat{C}_1 , top right: sensor \hat{C}_2 , bottom left: sensor \hat{C}_3 , bottom right: sensor \hat{C}_4 .

4.2. Performance of the compensator using a cost functional based on the measurement

We start by considering a compensator whose controller has been designed using the cost functional J_m , i.e., the state is measured by the energy output of the sensor \hat{C}_p and the resulting controller aims at minimizing the measurement $m_p = \hat{C}_p \hat{X}$.

4.2.1. Response in the frequency domain: effect on the perturbation measure m_p

Even though the controller is designed based on the measurement m_p only, the performance of the compensator will be evaluated by considering the reduction of the perturbation measurement m_p as well as the reduction of the perturbation energy in the entire domain. This point has particular implications for experimental control setups where reduced-order models are typically obtained by identification techniques based on input and output data. By construction, such models cannot express or capture state information, and the question arises whether targeting the measurement energy in the cost functional produces commensurate reductions in the entire perturbation energy.

Figure 9 shows the performance of the compensator designed to minimize the measurement where each subplot displays results using a different sensor $\hat{C}_{1,2,3,4}$ for the estimator. The measurement-based performance P_m of the compensator is defined as

$$P_m = \left[\frac{\int_{-\infty}^{+\infty} \hat{X}_\omega^* \hat{C}_p^* \hat{C}_p \hat{X}_\omega d\omega}{\bar{m}_0^2} \right]^{1/2} \quad (4.4)$$

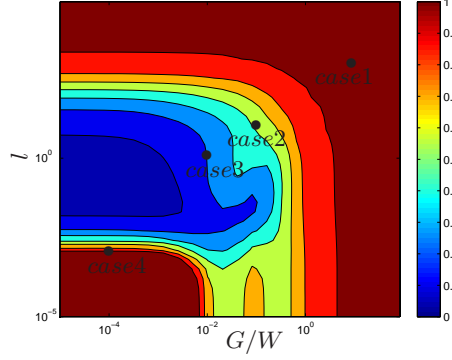


FIGURE 10. Contours of the performance measure P_e based on the global perturbation energy as a function of noise-to-signal ratio G/W and control cost parameter l for sensor \hat{C}_1 .

where \hat{X}_ω is given by (4.3) and \bar{m}_0^2 is the measurement energy related to the uncontrolled case. Each plot shows iso-contours of P_m in the $(G/W, l)$ -plane. Contours with hot colors (red) indicate parameter combinations where the control has been ineffective in reducing the measurement energy; contours with cold colors (blue) point to values of $(G/W, l)$ where the perturbation measure has been reduced successfully. The convergence of the performance P_m towards one (ineffective closed-loop control) is common to all sensor configurations as either the control cost l or the noise-to-signal ratio G/W exceeds a critical value. This parameter regime corresponds to small-gain-limit situations where either the control gain \hat{K} or the Kalman gain \hat{L} approach zero. For small noise-to-signal ratios G/W and small control parameters l (inexpensive control), the estimator provides an accurate approximation of the state which is subsequently multiplied by a non-zero control gain to obtain a positive action on the perturbation. As a result, the performance measure P_m is rather small in this parameter regime since both the estimator and the controller reach their large gain limit and behave at their best. The compensator based on sensor \hat{C}_1 is, by a considerable margin, the most efficient with a performance parameter P_m equal to 0.026 in the large gain limit; this means that only 2.6% of the uncontrolled measurement energy remains after control is applied. As the sensor location for the estimator is moved further downstream though, the performance parameter P_m rises substantially in the large-gain region: 17%, 36% or 71% of the uncontrolled measurement energy could not be removed by the compensator using sensors \hat{C}_2 , \hat{C}_3 or \hat{C}_4 , respectively. This exercise clearly demonstrates that an actuator placed near the edge of the step requires a sensor located in its vicinity, if satisfactory performance of the compensator is to be expected; alternatively, a sensor further downstream (e.g., \hat{C}_4) requires an actuator in its upstream neighborhood, but this layout will produce larger control gains and ultimately less performance compared to the upstream configuration (e.g. \hat{C}_1). In what follows, we will concentrate on sensor \hat{C}_1 and further probe its performance behavior and limitations.

More physical insight into the compensated system can be gained by computing the transfer function between the noise w and the performance measurement m_p . Four cases, labeled accordingly in figure 9(a), are analyzed in detail: case 1 is representative of an ineffective compensator in the small gain limit, both cases 2 and 3 characterize a system with average performance while case 4 corresponds to a compensator operating in the large gain limit. The governing parameters, i.e., the noise-to-signal ratio and control cost,

case	l	G/W	$P_m _{cf:m}$	$P_e _{cf:m}$	$P_m _{cf:e}$	$P_e _{cf:e}$
1	10^3	10^1	1.000	1.000	1.000	1.000
2	10^1	10^{-1}	0.566	0.574	0.784	0.707
3	10^0	10^{-2}	0.135	0.254	0.292	0.157
4	10^{-3}	10^{-4}	0.026	1.084	0.037	0.005

TABLE 2. Performance measures based on measurement energy (subscript m) or global perturbation energy (subscript e). The compensator has been designed using on a cost functional based on measurement energy (subscript $cf:m$) or on global perturbation energy (subscript $cf:e$). Four selected cases, ranging from the small gain limit to the large gain limit, are presented.

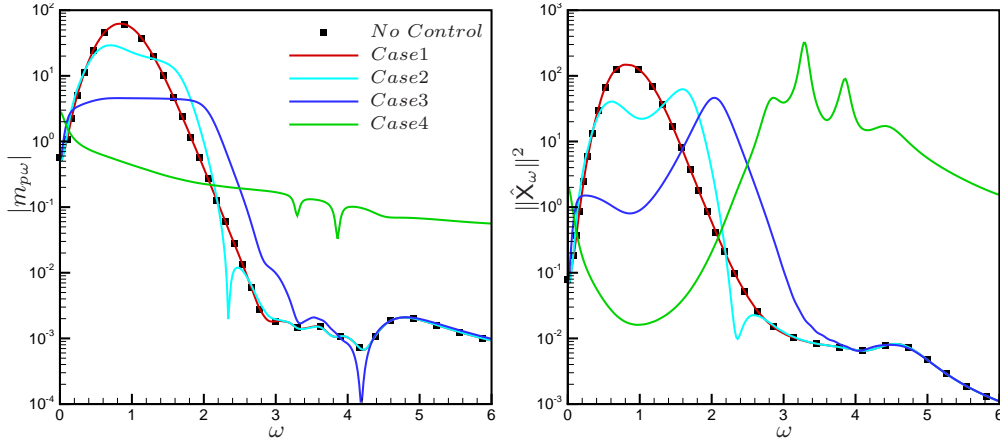


FIGURE 11. (a) Magnitude of the transfer function $|m_{pw}|$ for four different $(G/W, l)$ -parameter settings, as well as the uncontrolled case. (b) Transfer function between noise and global energy for the same four parameter settings.

for these cases are summarized in table 2 (second and third column) together with values of various performance measures.

In figure 11(a) the magnitude of the transfer function from $w(t)$ to $m_p(t)$ for each of the four cases is displayed, and results pertaining to the uncontrolled system are overlaid in black symbols. As expected, the compensator operating in the small gain limit (case 1, shown in red) does not act on the flow and the transfer function is identical to the uncontrolled one. By progressively reducing the noise-to-signal ratio and the control parameter (light blue and dark blue curve), the most amplified frequencies are considerably reduced and the compensator becomes effective over a wider range of frequencies, even though frequencies above $\omega \approx 1.5$ are slightly more amplified compared to the uncontrolled case. This tendency continues until the large gain limit (in green) is reached: the low frequencies ($\omega < 2$) which would be naturally amplified by the uncontrolled system have been successfully suppressed, which explains the very good performance of the compensator with $P_m = 0.026$ (see table 2, fourth column).

The results above confirm the successful manipulation of the inherent amplification behavior (see figure 2(a)) of the uncontrolled flow: the pronounced response to low frequencies has been strongly reduced by the compensator.

4.2.2. Response in the frequency domain: effect on the perturbation energy

While the control gain is still based on the measurement-based cost functional J_m , we now probe the broader impact of the control action on the entire domain by evaluating the global energy performance measure

$$P_e = \frac{\int_{-\infty}^{+\infty} \hat{X}_\omega^* \hat{Q} \hat{X}_\omega d\omega}{\bar{E}_0} \quad (4.5)$$

with \hat{X}_ω from (4.3) and \bar{E}_0 as the energy based on the uncontrolled system. The ratio P_e of the perturbation energy for the compensated case to the perturbation energy for the uncontrolled case is depicted in the $(G/W, l)$ -plane in figure 10. This plot shows similar characteristics than figure 9(a) but also displays important differences. For large values of G/W and l (the small gain limit for estimator and controller) the control action is negligible and no reduction in the perturbation energy is achieved ($P_e = 1$). For moderate estimation and control-cost parameters, the performance parameter P_e decreases, and it appears that a reduction in measurement energy measure P_m brings about a proportional reduction in the overall perturbation energy. However, as the large gain limit is approached (case 4), the value of P_e increases again, even above one, indicating that the perturbation energy of the controlled case exceeds the energy of the uncontrolled case. The measurement energy, however, is efficiently reduced, as by design.

As before, the transfer function between the noise and the energy in the domain $\|\hat{X}_\omega\|^2$ provides more details of the observed behavior (see figure 11(b)). Case 1 (in red) represents the small gain limit, and the transfer function coincides with the one for the uncontrolled flow since no control action is exerted on the flow. As G/W and l are reduced (light blue curve), the dominant, inherently amplified frequencies around $\omega = 1$ are reduced by the compensator but higher frequencies appear near $\omega = 1.8$. Nonetheless, the energy in the entire domain diminishes ($P_e = 0.458$), see values in table 2 (fifth column). This trend continues as the governing parameters are further decreased (dark blue curve). Finally, in the large gain limit (green curve), the dominant frequencies of the uncontrolled system ($\omega \approx 1$) have been reduced by four decades, while the energy in higher frequencies ($\omega > 2$) has been amplified by four orders of magnitude. This amplification outweighs the control effort on the lower frequencies, thereby leading to an increase in the overall energy of the system ($P_e = 1.085$) and a failure of the compensator when measured in the global energy norm (figure 10).

4.2.3. Interpretation in the time-domain

A re-interpretation of the above behavior in the time-domain may shed some light on the underlying physical processes. As before, we consider the impulse response of the compensated system triggered by the noise term according to $w(t) = \delta(t)$. We obtain

$$\frac{d}{dt} \begin{pmatrix} \hat{X} \\ \hat{Y} \end{pmatrix} = \begin{pmatrix} \hat{A} & \hat{B}_2 \hat{K} \\ -\hat{L} \hat{C} & \hat{A} + \hat{B}_2 \hat{K} + \hat{L} \hat{C} \end{pmatrix} \begin{pmatrix} \hat{X} \\ \hat{Y} \end{pmatrix}, \quad \begin{pmatrix} \hat{X} \\ \hat{Y} \end{pmatrix}_{t=0} = \begin{pmatrix} \hat{B}_1 \\ \hat{0} \end{pmatrix}. \quad (4.6)$$

In figure 12(a) the measurement signal $m_p(t)$ is shown for the four cases (as defined in table 2). As expected, in the small gain limit (red curve) the measurement is identical to the measurement extracted from the uncontrolled simulation (black symbols), since no control action is employed in this limit. As the parameters G/W and l are decreased (cases 2 and 3), the measurement signal decreases in amplitude; interestingly, trailing-edge features of the wavepacket are more effectively controlled than leading-edge components (see, e.g., case 2). In the large gain limit (case 4), the measurement signal has been nearly attenuated by control, in accordance with our frequency-based results above. Figure 12(b)

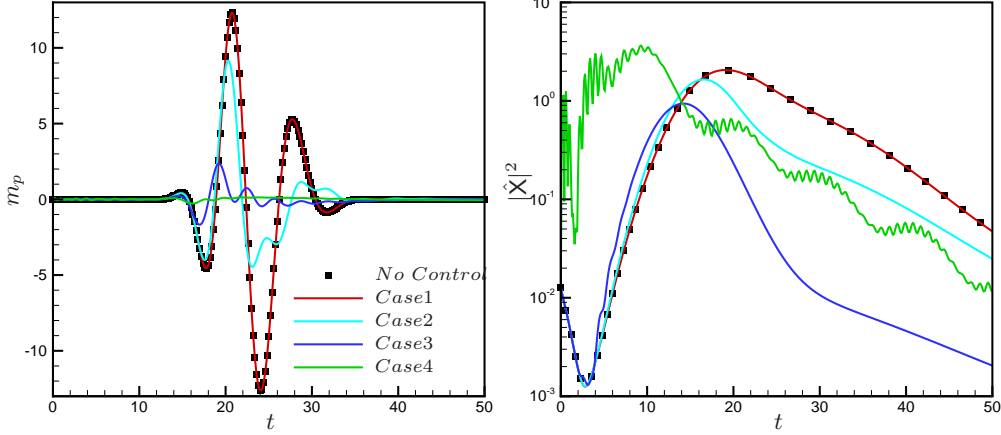


FIGURE 12. (a) Measurement signal at \hat{C}_p for four selected $(G/W, l)$ -parameter settings. (b) Temporal evolution of the global perturbation energy for the same parameters.

shows the temporal evolution of the perturbation energy in the entire domain. Starting with the expected correspondence between small gain results and the uncontrolled case, the curves for smaller values of G/W and l , in light and dark blue, show the addition of energy by the control (at $t \approx 10$ in case 2 and for $5 < t < 12$ in case 3) after which the perturbation energy in the entire domain drops rapidly and remains below the uncontrolled level. The time behavior of case 4 is completely different: a rather large energy amplification is observed for very early times. This result is unexpected in light of the fact that the wavepacket triggered by \hat{B}_1 has not yet reached the sensor location \hat{C}_1 (see figure 7(a)) and the control at early times should be zero. We must thus conclude that the large gain limit produces a highly sensitive estimator which produces large-amplitude output from even minute measurement signals which, in turn, get further amplified by the large control gain into a strong control input $u(t)$.

In summary, the energy of the measurement signal extracted at \hat{C}_p can be significantly reduced by a compensator that operates in or near the large gain limit. The perturbation energy in the entire domain, however, is affected by the increasing sensitivity of the compensator as this limit is approached, and the reduction of global energy by a compensator that has been designed on measurement energy only becomes progressively difficult. A possible remedy would be to base the controller design on a cost functional consisting of several sensors distributed along the lower wall of the recirculation bubble. Alternatively, if a reduced-order model of the flow is available, a direct targeting of the perturbation energy may be more efficient. This latter approach will be pursued next.

4.3. Performance of the compensator using a cost functional based on the energy

Since our reduced-order model is based on POD modes, it accurately captures the energy of the original system. It is therefore possible to base the controller design on the cost functional J_e and to directly target the perturbation energy in the entire domain. This section then repeats the above analysis of the compensated system using J_e -based controllers.

4.3.1. Response in the frequency domain

We start by evaluating the performance of the compensator for different values of G/W and l measured by the response of system (4.3). The two previously introduced performance quantities P_m and P_e are shown in figure 13(a,b) as a function of noise-to-

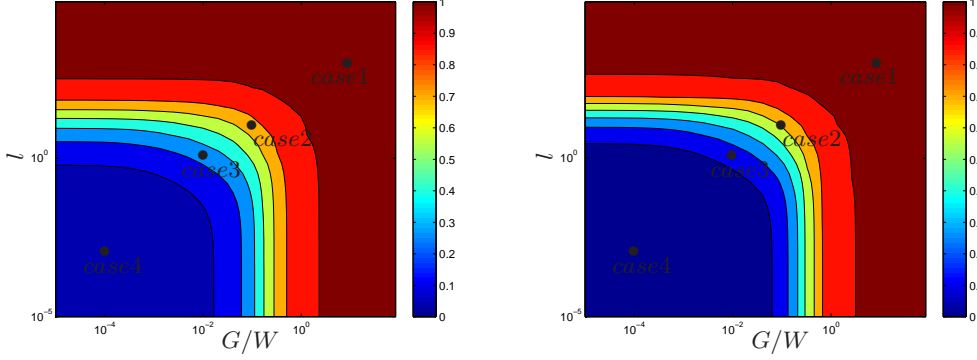


FIGURE 13. (a) Contours of the performance measure P_m based on the measurement energy as a function of noise-to-signal ratio G/W and control cost parameter l for sensor \hat{C}_1 . (b) Contours of the performance measure P_e based on the global perturbation energy as a function of noise-to-signal ratio G/W and control cost parameter l for sensor \hat{C}_1 .

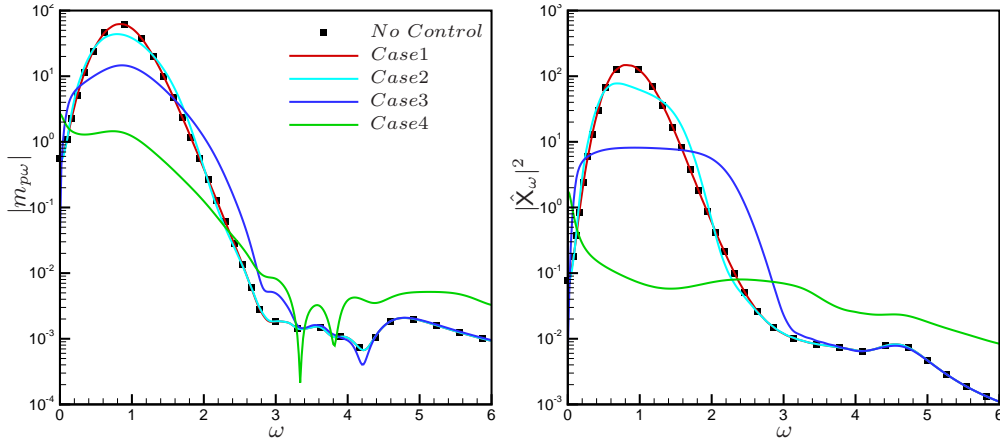


FIGURE 14. (a) Magnitude of the transfer function $|m_{pw}|$ for four different $(G/W, l)$ -parameter settings, as well as the uncontrolled case. (b) Transfer function between noise and global energy for the same four parameter settings.

signal ratio G/W and control-cost parameter l . The results based on the quantity P_m are very similar to earlier findings in figure 9(a): a transition from entirely ineffective to highly effective control as we change from the small gain to the large gain limit. A quantitative comparison can be deduced from table 2 (sixth and seventh columns). In contrast, figure 13(b) displaying the quantity P_e is markedly different from figure 10; in particular, a substantial reduction of the global energy ($P_e = 0.005$) in the large gain limit can be accomplished. The energy-based compensator was thus able to minimize the energy in the entire domain and, with it, the measurement energy extracted from \hat{C}_p .

The transfer functions from the noise $w(t)$ to the measure $m_p(t)$ and from the noise to the perturbation energy for the four cases introduced in § 3 are shown in figure 14. Similarities with the corresponding plots in figure 11 are clearly visible, but the excitation of high frequencies by the control action is entirely absent in figure 11. The energy in the entire domain can be efficiently controlled if it is accounted for in the controller design via the cost functional.

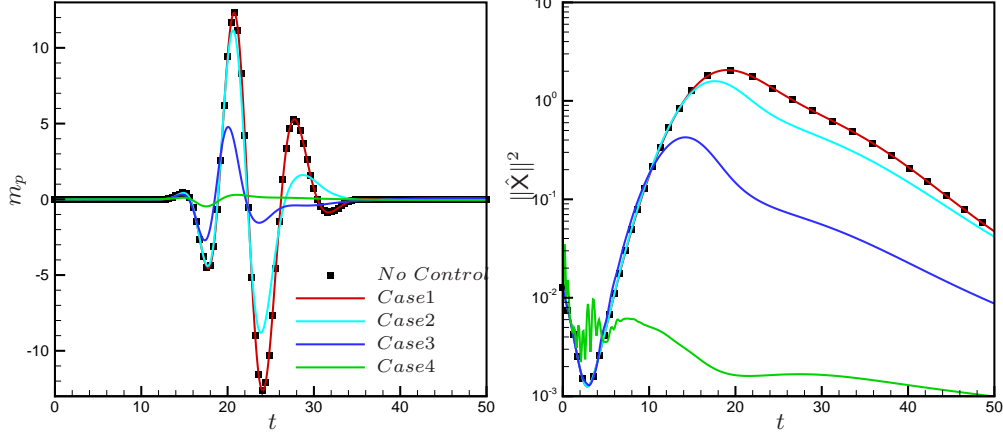


FIGURE 15. (a) Measurement signal at \hat{C}_p for four selected $(G/W, l)$ -parameter settings. (b) Temporal evolution of the global perturbation energy for the same parameters.

4.3.2. Interpretation in the time-domain

The time responses of m_p and $\|\hat{X}\|^2$ for the four cases (figure 15) again support our frequency-based observations. Strong energy gains for short times ($t < 5$) are no longer present in case 4, even though small energy oscillations are still visible as a reminder of the sizable sensitivity of the compensator designed for the large gain limit.

5. Closed-loop control using linearized Navier-Stokes simulations

In general, the design of LQG controllers and estimators for the closed-loop control of high-dimensional fluid systems requires a reduced-order model that accurately captures the input-output (actuator-sensor) dynamics of the full system. Compensators based on accurate reduced-order models are expected to perform well when employed directly on the high-dimensional plant. If discrepancies between the full and reduced-order transfer function prevail, however, a satisfactory performance of the compensator is no longer guaranteed, nor can any bounds on the decline in performance be given. In any model reduction effort, approximation errors are present and can potentially degrade or ruin the compensator's efficacy. The purpose of this section is an assessment of the compensator's sensitivity to deviations of the reduced-order input-output behavior from the one of the full system. To this end, we will again consider the best-performing estimator based on sensor \hat{C}_1 and design a controller based on the cost-functional J_e .

5.1. Effect of the level of accuracy of the reduced-order model on closed-loop control

5.1.1. Modeling the deviation between the plant and the reduced-order model

Throughout our study, the compensator has been designed using a reduced-order model based on the projection of the governing equations onto 150 POD modes; this model will be referred to as ROM_{150} . The same model has also been used to model the plant for the study of the estimator (§3) and the compensator (§4). The question then arises whether the good performance of the compensator based on this model is robust to small changes in the plant. To quantify the robustness or sensitivity we will artificially degrade the reduced-order model of the plant by considering only the first n components of the ROM_{150} -model, denoted by ROM_n . Various levels of truncation may be compared to the earlier model in terms of the dynamics between input variables (noise $w(t)$ and control $u(t)$) and

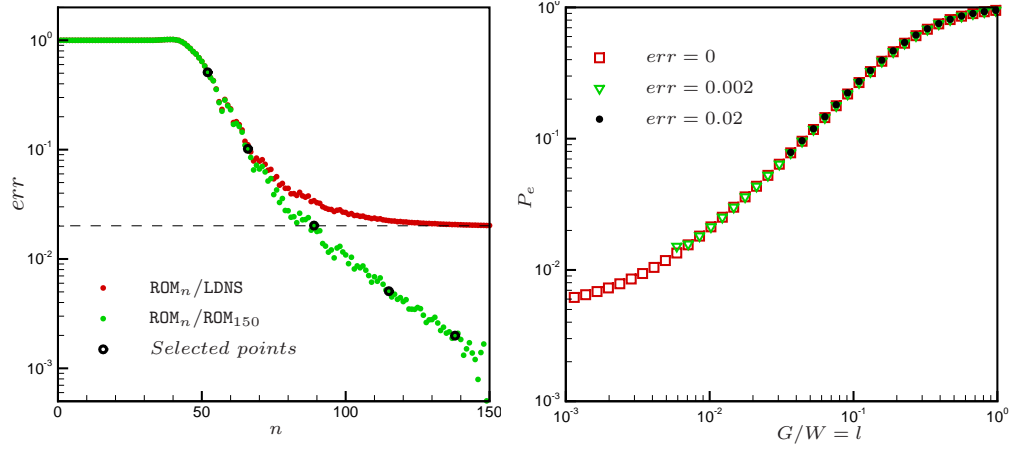


FIGURE 16. (a) Error between the reduced-order model and the linearized direct numerical simulations (LDNS) in red; error between the reduced-order model and the reduced-order model ROM₁₅₀ in green. The black symbols correspond to the error curves shown in figure 17. (b) Comparison of the performance measure P_e obtained by controlling a plant modeled by ROM₁₅₀ ($err = 0$, red squares), ROM₁₃₉ ($err = 0.002$, green triangles) and ROM₈₉ ($err = 0.02$, black dots) with a compensator based on ROM₁₅₀.

output quantities (estimation measure $m_1(t)$ corresponding to sensor \hat{C}_1 , performance measure $m_p(t)$ and performance measure based on the global perturbation energy $E(t)$). We will see that the input-output behavior from control $u(t)$ to estimation $m_1(t)$ is the most critical one. Figure 16 illustrates (in green) the error err between reduced-order models of varying truncation levels, ROM _{n} , and the original model ROM₁₅₀ defined as

$$err = \left[\frac{\int_{-\infty}^{\infty} |\hat{m}_{1\omega} - m_{1\omega}|^2 d\omega}{\int_{-\infty}^{\infty} |m_{1\omega}|^2 d\omega} \right]^{1/2} \quad (5.1)$$

where $m_{1\omega}$ is the frequency-transformed measurement triggered by an impulse on the control B_2 in model ROM₁₅₀, and $\hat{m}_{1\omega}$ stands for the analogous measurement using model ROM _{n} . For severe truncations ($n < 40$), reduced-order models ROM _{n} exhibit an error of 100% which can be linked to the fact that the relation between $u(t)$ and $m_1(t)$ is not well captured by the first forty POD modes. As more POD modes are included, the error decreases steadily towards $\sim 10^{-3}$. This behavior will allow us to study the influence of plant inaccuracies on the compensator performance, with plant errors ranging from 0.1% to 100%.

5.1.2. Effect of the plant deviation on the closed-loop control

When the model, on which the design of the compensator is based, differs from the model of the plant that it is intended to control, the performance of the compensator may be negatively affected or the compensated system may even exhibit an instability. The dynamics of the compensated system is given by

$$\frac{d}{dt} \begin{pmatrix} X \\ \hat{Y} \end{pmatrix} = \begin{pmatrix} A & B_2 \hat{K} \\ -\hat{L}C & \hat{A} + \hat{B}_2 \hat{K} + \hat{L}\hat{C} \end{pmatrix} \begin{pmatrix} X \\ \hat{Y} \end{pmatrix} + \begin{pmatrix} B_1 \\ \hat{0} \end{pmatrix} w(t) \quad (5.2)$$

where the superscript $\hat{\cdot}$ refers to matrices of the ROM₁₅₀-system while matrices without the superscript are associated with the ROM _{n} -model. The performance of the above com-

compensated system crucially depends on the stability of the matrix

$$\begin{pmatrix} \mathbf{A} & \mathbf{B}_2 \hat{\mathbf{K}} \\ -\hat{\mathbf{L}}\mathbf{C} & \hat{\mathbf{A}} + \hat{\mathbf{B}}_2 \hat{\mathbf{K}} + \hat{\mathbf{L}}\hat{\mathbf{C}} \end{pmatrix}. \quad (5.3)$$

If this matrix is unstable, performance of the compensated system is lost. A detailed analysis between system inputs $\{\mathbf{B}_1, \mathbf{B}_2\}$ and system outputs $\{\mathbf{C}_{1,2,3,4}, \mathbf{C}_p, E\}$ involves transfer functions for all combinations; however, only the most dominant ones have to be taken into account. Stability only depends on \mathbf{A} , \mathbf{B}_2 and \mathbf{C} , which describe the input-output dynamics between $u(t)$ and $m_1(t)$, but does not depend on \mathbf{B}_1 and \mathbf{Q} , which is to say, that the input-output dynamics between $w(t)$ and $m_1(t)$, between $w(t)$ and $E(t)$ and between $u(t)$ and $E(t)$ has no influence on the stability of the above matrix. For stable matrices (5.3) the performance parameter may be defined as in § 4, that is,

$$P_e = \frac{\int_{-\infty}^{+\infty} \mathbf{X}_\omega^* \mathbf{Q} \mathbf{X}_\omega d\omega}{E_0} \quad (5.4)$$

with

$$\begin{pmatrix} \mathbf{X}_\omega \\ \hat{\mathbf{Y}}_\omega \end{pmatrix} = \begin{pmatrix} i\omega\mathbf{I} - \mathbf{A} & -\mathbf{B}_2 \hat{\mathbf{K}} \\ \hat{\mathbf{L}}\mathbf{C} & i\omega\mathbf{I} - (\hat{\mathbf{A}} + \hat{\mathbf{B}}_2 \hat{\mathbf{K}} + \hat{\mathbf{L}}\hat{\mathbf{C}}) \end{pmatrix}^{-1} \begin{pmatrix} \mathbf{B}_1 \\ 0 \end{pmatrix} \quad (5.5)$$

and E_0 as the energy of the uncontrolled case, given by $E_0 = \int_{-\infty}^{\infty} \mathbf{X}_\omega^* \mathbf{Q} \mathbf{X}_\omega d\omega$ with $\mathbf{X}_\omega = (i\omega\mathbf{I} - \mathbf{A})^{-1} \mathbf{B}_1$. The performance parameter P_e depends on the quantities \mathbf{A} , \mathbf{B}_1 , \mathbf{B}_2 , \mathbf{C} and \mathbf{Q} , which affect the input-output dynamics $w(t) \rightarrow m_1(t)$, $w(t) \rightarrow E(t)$, $u(t) \rightarrow m_1(t)$ and $u(t) \rightarrow E(t)$. In figure 16(b) we display the performance parameter P_e as a function of $l = G/W$ for a compensator based on ROM₁₅₀ but coupled to plants modeled by ROM₁₅₀ (reference case in red squares), by ROM₁₃₈ (green triangles) and by ROM₈₉ (black dots). In figure 16(a), we see that model ROM₁₃₈ reaches an error of $err = 0.2\%$ whereas model ROM₈₉ attains a larger error of $err = 2\%$; incidentally, values of P_e are only shown for stable compensated systems. For plants whose dynamics is described by ROM₁₃₈ or ROM₈₉, stability of the compensated systems is lost when the parameters $l = G/W$ takes on sufficiently small values. Under stable condition, however, the performance parameter P_e for the two models is identical to the reference case based on ROM₁₅₀. This leads us to conclude that performance of the compensated system is lost via a loss of stability; as long as stability is maintained however, no difference in performance is detected between the models with varying numbers of POD modes. Above a critical value of G/W , where stability of the compensated system can be ensured, the error between the plant and the reduced-order model will influence performance: if the error is sufficiently large, the performance derived from ROM₁₅₀ may not be observed. Hence, it is sufficient to detect instability of the compensated system in order to assess its performance, which furthermore means that only the input-output dynamics from control $u(t)$ to sensor measurement $m_1(t)$ suffices to describe overall robustness. For this reason, we will investigate the stability of matrix (5.3).

Figure 17 displays regions in the $(G/W, l)$ -plane where compensated systems are stable or unstable for different errors err between the plant (modeled by ROM _{n}) and the reduced-order-model (ROM₁₅₀) on which the compensator is based. For five different values of the error err (highlighted by black symbols in figure 16(a)) the neutral curve — separating stable from unstable compensated systems — is shown in the $(G/W, l)$ -plane (see figure 17). Concentrating on the dark blue curve, we argue that if the error between the reduced-order model (on which the compensator is built) and the plant is 0.2%, closing the loop will result in an unstable system if the control cost parameter l and noise-to-signal ratio G/W are chosen from inside the unstable region (lower left corner

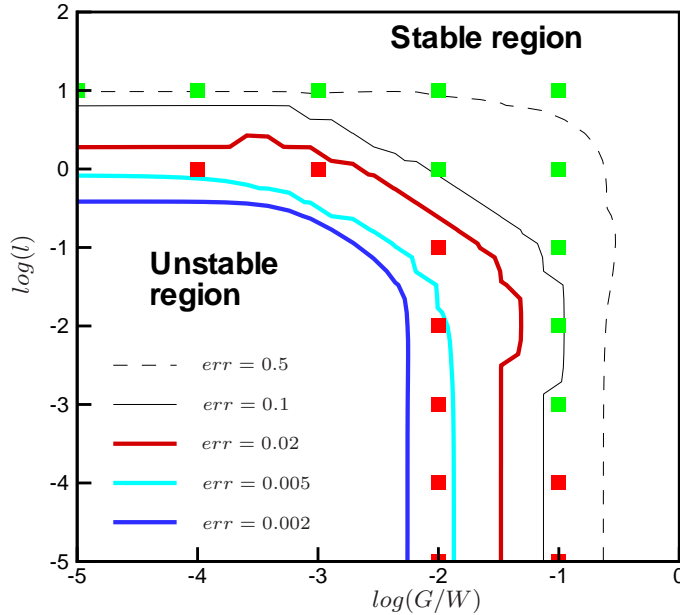


FIGURE 17. Neutral curves defining the unstable and stable compensated systems for different values of the error between the plant and the reduced-order model. The compensator has been designed using model ROM_{150} . The red squares (resp. green squares) represent unstable (resp. stable) results from compensated linearized Navier-Stokes simulations.

of figure 17). Instability hence imposes limitations on the choice of l and G/W and, consequently, on the final performance of the compensator. For less accurate reduced-order models (light-blue, red, black solid, black dashed curve), the region of unstable parameter combinations increases, and eventually the entire large-gain-limit (i.e., optimal compensator performance) region is impeded by an instability of the compensated system. For very accurate models, on the other hand, the entire parameter range in the $(G/W, l)$ -plane is accessible, and compensators at the optimal setting (large gain limit) can be employed.

5.1.3. Validation using a linearized direct numerical simulation

In a further step to investigate the influence of discrepancies between the input-output behavior upon which the compensator has been built and the input-output behavior of the system that is to be controlled, we replace the plant by the linearized direct numerical simulation (LDNS), i.e., the full, unreduced model for flow over a rounded backward-facing step. In many flow control studies, this represents the essential performance test of the compensator.

We again consider in this section the situation where an impulse of noise is controlled. The plant is given by the discretized system of equations (2.3), a second-order scheme is used for the time integration, and the system is triggered, as before, by an impulse imposed on the noise term, i.e., $\mathbf{X}_{t=0} = \mathbf{B}_1$ and $w(t) = 0$; the compensator has been designed based on model ROM_{150} . Various test cases covering a range of control costs l and noise-to-signal ratios G/W have been performed and indicated by square symbols in figure 17. Both stable and unstable configurations have been found. When neither l nor G/W are small (indicated by green symbols in figure 17), the response of the linearized simulation is identical to the response of model ROM_{150} which is in agreement with the results in § 5.1.2. We recall that the stability of the compensated system implies identical

performances for reduced-order models of various levels of truncation. As a consequence, the linearized DNS achieves the same performance as the one displayed in figure 13(b); cases 1, 2 and 3, studied in § 3 and § 4, belong to this category and are thus recovered by the linearized DNS. On the other hand, we also encountered cases in which the linearized direct numerical simulation was rendered unstable by the compensator (indicated by red symbols in figure 17). These cases are concentrated at the large gain limit in the $(G/W, l)$ -plane; case 4, studied in § 3 and § 4, falls into this category.

It is instructive to evaluate the error in the input-output dynamics $u(t) \rightarrow m_1(t)$ between the linearized DNS and the ROM₁₅₀-model. Figure 16(a) displays (in red symbols) the error err between the linearized DNS and reduced-order models of various truncation levels ROM _{n} . For $n < 40$, the reduced-order models fail to accurately represent the control action, resulting in an error of 100%. As the order and accuracy increases, the error between linearized DNS and reduced-order models decreases until it approaches a level of 2% — which can be taken as the error between the linearized DNS and the ROM₁₅₀-model. This value is identical to the error between ROM₈₉ and ROM₁₅₀; we can thus make use of the neutral curve given by the red line in figure 17. The stability observations from our simulations (linearized DNS coupled with a ROM₁₅₀-based compensator) fall correctly on either side of the neutral curve (except for low values of l), i.e., the neutral curve divides stable (green) parameter combinations from unstable (red) ones.

We note in passing that the above study has used the 2-norm for the definition of errors; other choices may yield quantitatively different results. For example, frequency-restricted 2-norms may more accurately reflect the physical properties of the system and result in more precise measures, as was shown in Barbagallo *et al.* (2010) for globally unstable flows. Nevertheless, the qualitative behavior of the compensated system is expected to be insensitive to our choice of error norm.

5.2. Control of an impulse using a linearized direct numerical simulation

We will take a closer look at case 3 (defined in table 2) which consists of the most efficient compensator that still produces a stable compensated system; the performance of this compensator is given by the dark blue curves in figure 14 and figure 15. We start by studying the spatio-temporal evolution of the energy integrated along lines of $x = \text{const.}$ introducing

$$e_y(x, t) = \int_{wall}^{top\ boundary} e(x, y, t) dy \quad (5.6)$$

with $e(x, y, t)$ as the pointwise energy. The x - t -diagram of e_y is shown in figure 18. Hot colors (in logarithmic scaling) indicate locations of high energy density e_y ; dark colors point to areas of no or negligible energy density. Figure 18(a) presents the propagation of an impulse of noise without control: at $t = 0$, the perturbation energy is localized in $x \in [-2, 0]$ since the initial condition B_1 is centered at $x = -1$. The initial decay of the wavepacket in the convectively stable region (in front of the separation point) is followed by an exponential amplification until the reattachment point ($x = 11$) is reached, before the wavepacket is convected and dissipated in the stable region of the flow ($x > 11$). The trailing and leading edge of the wavepacket exhibit different propagation speeds, affirming the dispersive properties of the perturbation. The equivalent scenario for the compensated configuration is shown in figure 18(b). The control action is visible along the line $x = 0.5$ (due to the placement of the actuator B_2) and introduces structures of smaller wave-lengths than those present in the uncontrolled case. These structures destructively interfere with the original wave-packet, and attenuation of the perturbation is corroborated by the successful suppression of high-energy (red) areas. We recall that

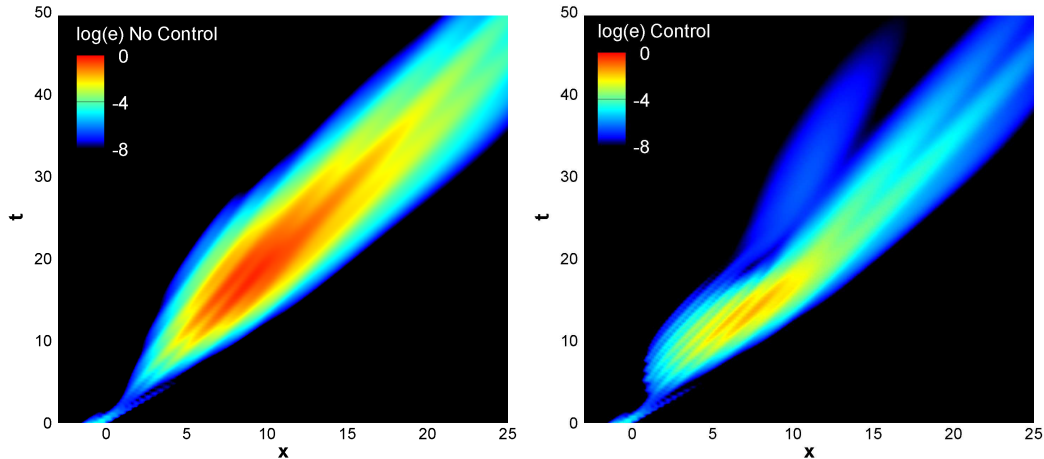


FIGURE 18. Contours of the energy integrated along lines $x = \text{const.}$ in an x - t -diagram. (a) Uncontrolled linearized simulation; (b) compensated linearized simulation (case 3).

for this case a 90%-reduction in the perturbation energy can be achieved (see the last column in table 2). Interestingly, the leading edge of the wave packet appears unaffected by the control; only the trailing edge region shows signs of control action. This may be explained by the fact that the wave packet has to first reach sensor C_1 before the state can be estimated and the control law can be applied. During this time the leading-edge of the wave packet has passed the actuator location, and only the trailing edge is subject to control action.

5.3. Control of random noise in a linearized direct numerical simulation

Even though controlling the impulse response triggered by the noise terms gives important insights into estimator and control action as well as into performance measures of the compensated system, a more realistic setup is the control of a flow that is continuously forced by random noise $w(t)$. Despite the fact that, due to linearity, the two cases are theoretically equivalent, we consider a plant governed by equation (2.3 a) where $w(t)$ now stands for a continuous source of white noise.

Figure 19(a) juxtaposes the temporal evolution of energy for the uncontrolled simulation (in red) with the evolution of energy for the compensated simulation (in green), where the same excitation sequence $w(t)$ has been used to ensure a fair comparison. Starting from a zero initial state, a transient phase is observed that quickly evolves into a statistically stationary state. At $t = 400$ the compensator is switched on (green curve). The energy rapidly decreases: nearly one decade smaller than in the uncontrolled simulation. For completeness, the measurement signal $m_p(t)$ is displayed in figure 19(b) for the uncontrolled (red) and compensated (green) simulation. Again, a noticeable reduction in variance can be observed.

The third column of table 3 contains the performance measures P_e and P_m corresponding to the above simulation (see “long” dataset on the left). As expected, the values are identical to the ones obtained for the reduced-order model (the values from table 2 have been reproduced in the second column). It is seen that the overall perturbation energy P_e and the perturbation measurement energy P_m have been reduced by a factor of 0.157 and 0.292, respectively.

Finally, figure 20 shows contours of the pointwise mean-energy for the uncontrolled (a) and controlled (b) simulations. The perturbation energy increases along the shear-layer

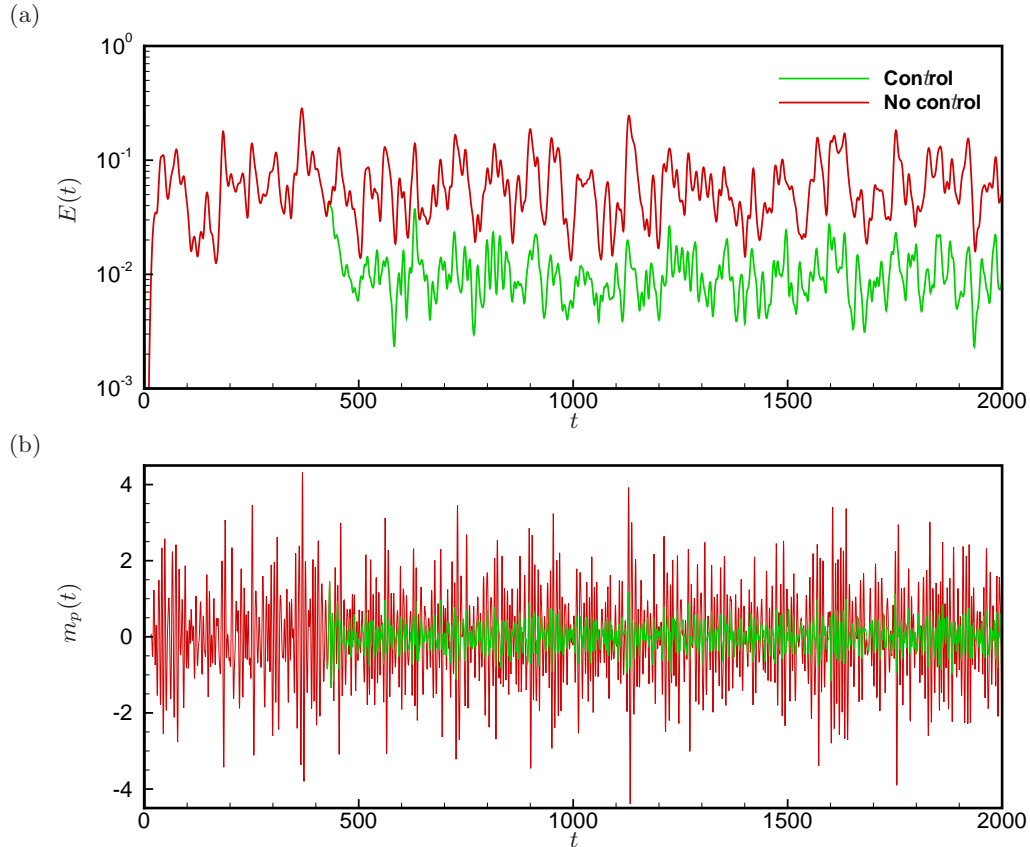


FIGURE 19. Temporal evolution of the energy based on a linearized numerical simulation continuously forced by random noise. The compensator has been designed under linear assumptions based on the ROM₁₅₀ model (case 3). (a) Perturbation energy for the uncontrolled (red) and controlled (green) case, (b) measurement energy for the uncontrolled (red) and controlled (green) case.

due to a convective instability; its maximum is reached near $x = 10$. This pointwise mean-energy distribution for the uncontrolled case is closely related to the optimal response given in figure 2(c). The mean-energy contours for the controlled simulation deviate significantly, as the effectiveness of the compensator is clearly demonstrated by the greatly reduced mean-energy in the shear-layer region. Table 3 (column 3, long dataset) shows that the maximum mean perturbation energy is reduced by a factor of 0.138. Figure 20 is of interest for experimental studies of flow control in amplifier flows as it provides a direct comparison of local turbulence levels throughout the recirculation bubble for the uncontrolled and controlled case.

6. Nonlinear effects

We will now dispense with the assumption of a linear plant and apply the linear compensator, designed to diminish perturbations governed by the linearized Navier-Stokes equations, to the nonlinear Navier-Stokes equations in the hope of attaining similar reductions in noise levels. By gradually increasing the amplitude of the incoming perturbations and the variance W^2 , we can progressively introduce nonlinear effects and can study their

	linear (ROM)	linear (long/short)	nonlinear (small amp.)	nonlinear (medium amp.)	nonlinear (large amp.)
P_e	0.157	0.157/0.132	0.136	0.209	0.406
P_m	0.292	0.292/0.278	0.291	0.504	0.741
u_{max}^2/U_∞^2 (%)			0.0125	0.793	4.53
$u_{max c}^2/U_\infty^2$ (%)			0.00144	0.158	2.11
$u_{max c}^2/u_{max}^2$		0.138/0.111	0.116	0.199	0.464

TABLE 3. Performance evaluation of linear and nonlinear simulations. Column 2: based on the reduced-order model (§4), column 3: based on linear simulations with random noise (§5 for long dataset and §6 for short dataset), columns 4, 5, 6: based on nonlinear simulations with random noise with $W = 0.1$, $W = 1$ and $W = \sqrt{10}$ (§6).

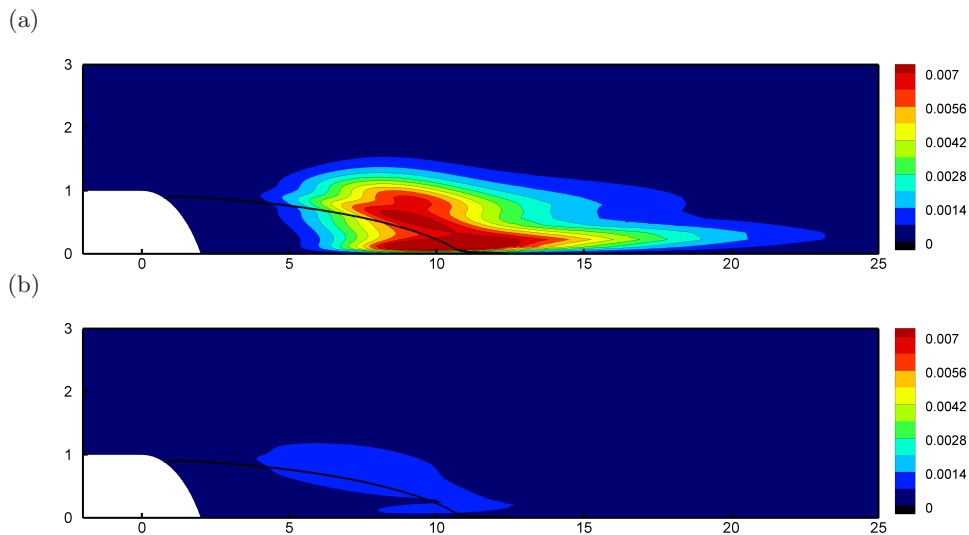


FIGURE 20. Pointwise mean perturbation energy of simulations with random forcing. (a) Uncontrolled linearized DNS; (b) compensated linearized DNS (case 3).

impact on the overall performance of the linear compensator under off-design conditions. A similar test has been conducted by Ilak (2009) for impulsive initial conditions.

6.1. Control of a noise impulse

Following the previous experiment, we compute the temporal response of the nonlinear system to an impulse of noise B_1 (with $w(t)$ set to zero). The degree of nonlinearity in the system can be adjusted using the amplitude of the initial perturbation. Figure 21 displays the system energy for the uncontrolled simulation (in black) and for controlled simulations (red curves) starting from three different initial amplitudes. Results from a linear simulation, properly normalized to match the respective initial amplitudes of the nonlinear runs, have been added by dashed lines. Discrepancies between the dashed and continuous curves can thus be attributed to nonlinear effects. The evolution of energy starting from a low-amplitude initial condition is shown in figure 21(a). Both the uncontrolled case (in black) and the compensated case (in red) show only minor nonlinear

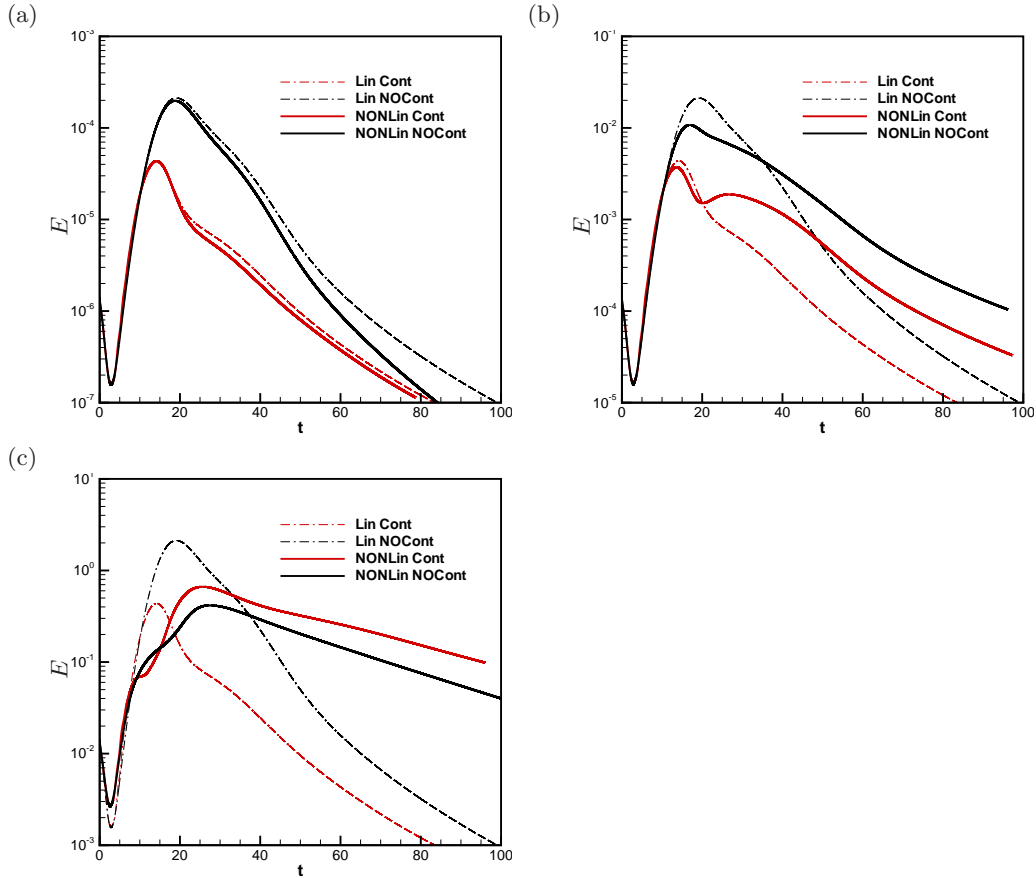


FIGURE 21. Energy versus time for the uncontrolled (black) and controlled (red) simulations using different initial amplitudes of the perturbation: (a) small amplitude, (b) medium amplitude, (c) large amplitude. In each plot, the linear simulation has been normalized at $t = 0$ for comparison.

effects, and the performance of the compensator is not compromised appreciably; only small deviations are noticeable near the maximum of the energy curve ($t \approx 20$). For medium-amplitude initial conditions (figure 21(b)) discrepancies between the linear and nonlinear simulations become apparent during the initial amplification of the perturbation and affect the energy peak as well as the disturbance propagation in the convectively stable region (for $t > 20$). In this case, the control is still effective. The early stages of the energy evolution ($t < 10$), however, behave largely linear and the control is well-designed for this regime. A second transient amplification of energy is visible in the controlled simulation (in red) for $t \approx 30$ which may be caused by nonlinearly triggered structures. Finally, figure 21(c) presents the energy curves for the large-amplitude initial conditions. In the uncontrolled simulation, nonlinear effects are already visible at $t \approx 3$, suggesting that the perturbation entering the convectively unstable region is already different from the linear one. Saturation of the energy is observed before the linear peak is reached, but a strong second amplification occurs in the controlled and uncontrolled case. After a maximum in energy is reached, a far lower decay rate during the advection through the stable region is encountered. Unlike the previous cases, the exerted control efforts influence the flow and generate structures that raise the energy levels above the uncon-

trolled case. Evidently, this final case reveals and surpasses the limits of our linear control strategy.

6.2. Control of random noise

The control of a random noise source is studied next. Whereas no new insight compared to the noise impulse response is expected for the linear case, the nonlinear response to continuous stochastic forcing is unrelated to the nonlinear response to a noise impulse since no superposition principle can be invoked. In spite of that, the control of high-amplitude random noise as a test to explore the limits of linear control design and performance is seldom undertaken. In figure 22, the temporal evolution of the total energy is displayed for different amplitudes of the noise variance W^2 ; uncontrolled simulations are shown in red, compensated simulations in green. The amplitudes of the noise variance are increased from figure 22 (a) to (c). In each of the presented cases, the mean energy level of the perturbation has been reduced by the linear compensator, but a noticeable loss in performance can be observed for the high-amplitude case.

The performance measures P_e and P_m corresponding to these cases are reported in table 3 (columns 4, 5 and 6). The simulations have been run up to $t = 600$, which is sufficiently long to observe general trends in the curves, even though full convergence would require longer simulations. The random noise sequence from the linear case has been used, which allows a direct comparison with the linear results (reported in column 3 and labeled “small” dataset). In table 3, the maximum pointwise energy (normalized by U_∞) of the uncontrolled and controlled (indicated by $|_c$) simulations are listed together with their ratio. For a small noise variance (figure 22(a)) the evolution of the uncontrolled perturbation is quasi-linear, and the performance of the compensator is nearly the same as in the linear case (compare columns 3 and 4 of table 3). As nonlinear effects play an increasingly important role, the oscillations of the energy curves for the uncontrolled case are less pronounced. The same observation can be made in the compensated simulations; the compensator in this case is also less effective. The performance measures P_e and P_m gradually deteriorate as the noise variance W^2 increases (compare columns 4, 5 and 6 of table 3). If W^2 is increased beyond a critical value, the compensated simulations become unstable.

As before, the pointwise mean-perturbation energy gives further insight into the temporal evolution of the energy as the disturbances advect along the shear layer. In figure 23(a) and (b) the pointwise mean-perturbation energy from the nonlinear simulation with random noise is displayed where a moderate variance has been used. The colormap has been adjusted to permit direct comparison with the equivalent linear results given in figure 20; significant differences to the linear case can be observed. Figure 23(a), illustrating the uncontrolled case, displays saturation effects caused by nonlinearities; the overall shape of the maximum energy contours are, however, similar to the linear case — concentrating on the dynamics in the shear layer and the reattachment area. In contrast, the amplitudes are higher in the convectively stable region ($x > 10$) for the nonlinear simulation. For the compensated case (figure 23(b)) the energy is maximal in the shear-layer but is, again, lower than the linear equivalent; in contrast, the energy is higher than in the linear case for $x > 10$, indicating the appearance of nonlinear structures which are more difficult to control. The pointwise mean perturbation energy from nonlinear simulations based random noise of high variance is shown in figure 23(c) and (d). The uncontrolled case (figure 23(c)) is similar to figure 23(a), even though higher amplitudes are reached. For the compensated case (figure 23(d)), we observe that the energy could be less attenuated by control efforts: in table 3 (column 6), a maximum mean perturbation energy of 4.53% is observed in the uncontrolled simulation which reduces to 2.11% as the compensator is

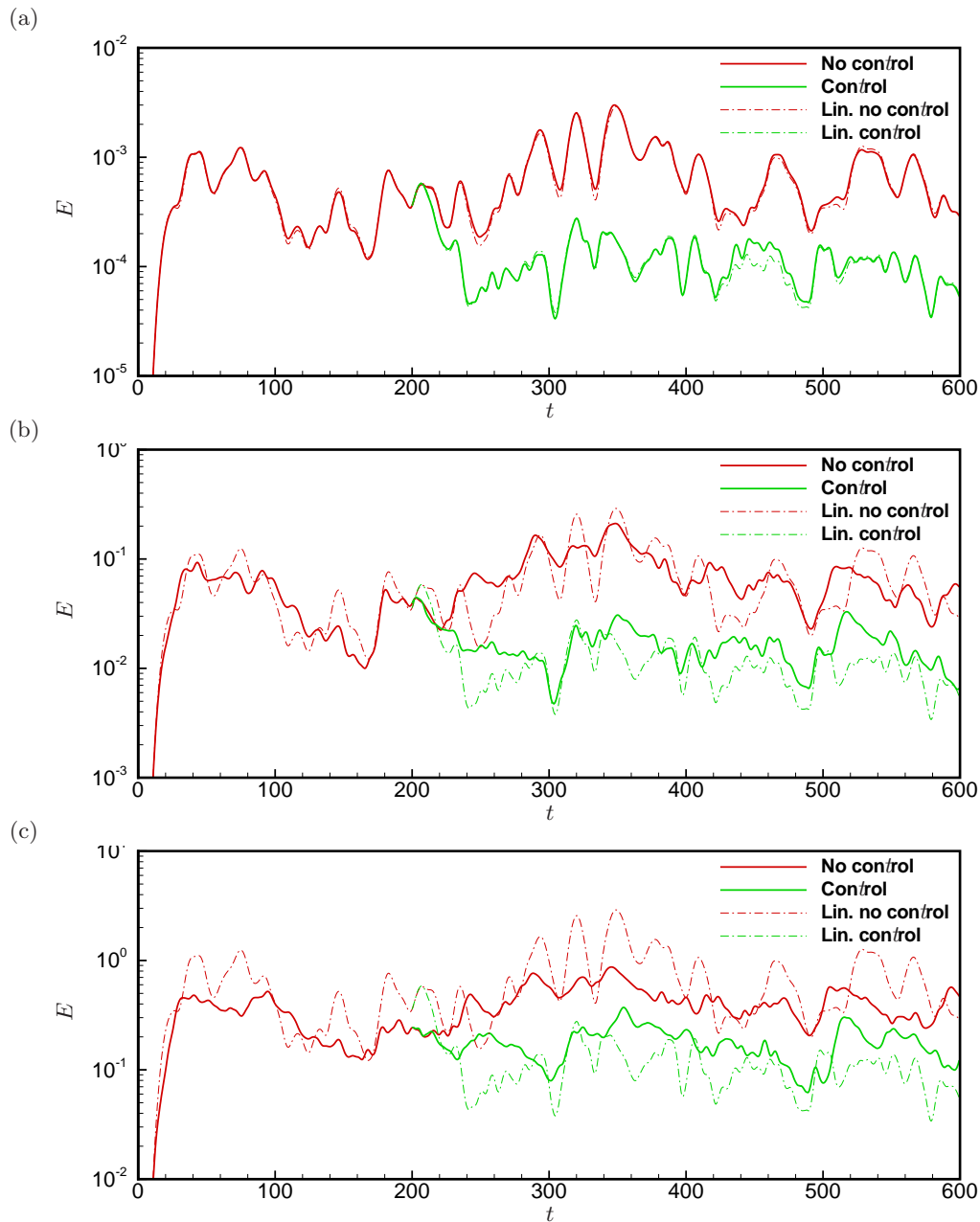


FIGURE 22. Temporal evolution of the perturbation energy based on a nonlinear numerical simulation continuously forced by finite-amplitude noise. The compensator has been designed under linear assumptions based on the ROM₁₅₀ model (case 3). (a) Low-amplitude case, (b) medium amplitude case, (c) high-amplitude case. The linear case has been added by dashed lines and scaled to the initial energy of the nonlinear simulations.

switched on. The turbulent kinetic energy is thus diminished by a more modest factor of 0.464 (compared to a factor of 0.116 for the small variance simulations, see column 4).

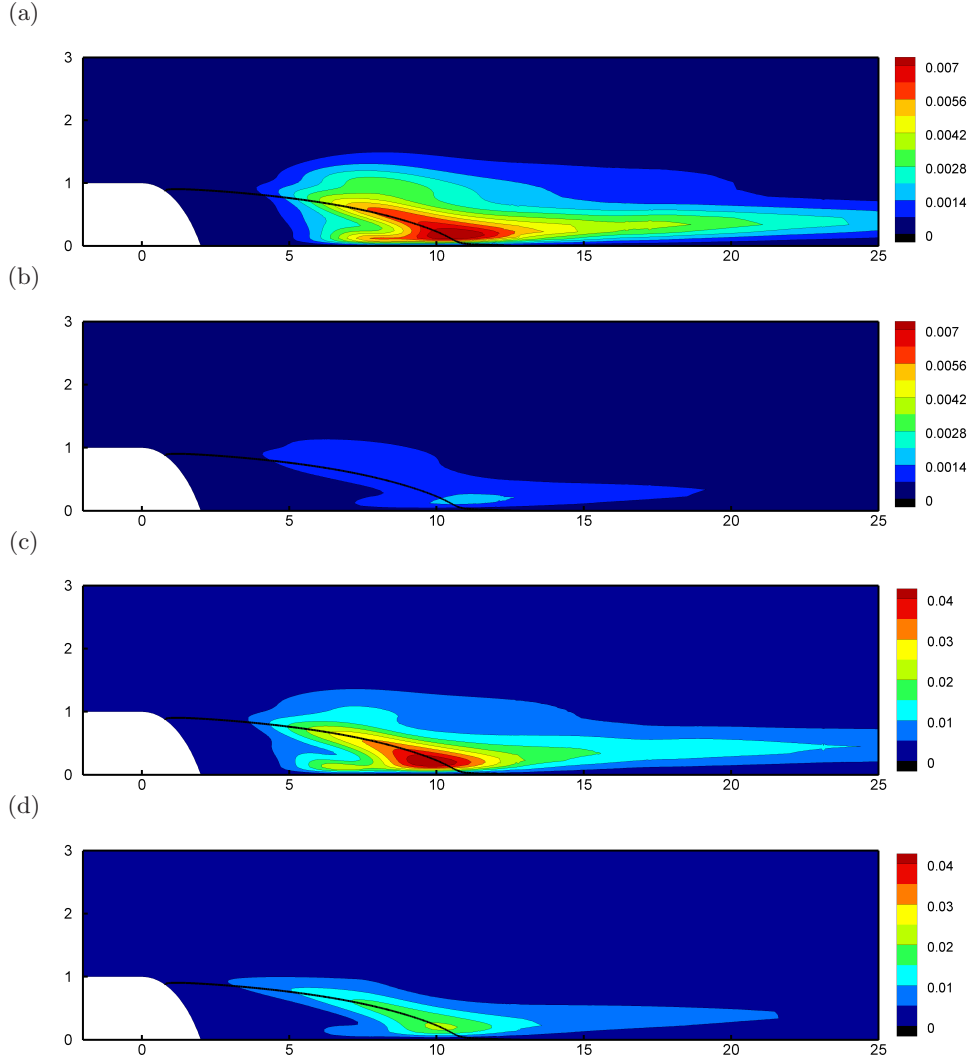


FIGURE 23. Pointwise mean perturbation energy of simulations with random forcing. (a) Uncontrolled direct numerical simulation for $W = 1$. (b) Compensated direct numerical simulation for $W = 1$ (case 3). (c) Uncontrolled direct numerical simulation for $W = \sqrt{10}$. (d) Compensated direct numerical simulation for $W = \sqrt{10}$ (case 3).

7. Summary and conclusions

Two-dimensional incompressible flow over a rounded backward-facing step, a canonical configuration showing noise-amplifying behavior, has been controlled by feedback control strategies. Specifically, the LQG-framework has been employed in conjunction with POD-based reduced-order models for the plant. Similar techniques have previously been studied (see Ilak & Rowley 2008; Bagheri & Henningson 2010), but with the main emphasis on model reduction aspects. Important issues related to the practical implementation of feedback control laws for amplifier flows have been left unaddressed, which motivated this present investigation.

The analysis of the feedback control setup first concentrated on the estimation process. A placement of sensors throughout the convectively unstable region of the flow

revealed a distinct advantage of measurement input from the most upstream sensor. It further showed that the speed of estimation is more important than the accuracy of the estimation, while keeping in mind that upstream sensor measurements are more easily corrupted by noise since the signal has not yet been amplified by the flow. Low-quality sensors should be placed further downstream where the amplitude of the detected signal prevails over the added inherent measurement noise; the resulting delay in estimation, however, will ultimately cause a loss in compensator performance. The noise-to-signal ratio of the sensor thus plays an important role and has been linked to the estimation parameter for the computation of the Kalman gain.

Continuing with the best (most upstream) sensor, the performance of the compensated system has been studied under the idealistic assumptions that the reduced-order model accurately mimics the plant. The noise-to-signal ratio (or estimation parameter) G/W and the cost-of-control parameter l have been varied to cover a range of control scenarios from the small gain limit (SGL), where the compensator is ineffective, to the large gain limit (LGL), where the compensator operates at its maximal performance. An excess in the total energy can be observed when the measurement energy is the control objective and the design parameters are chosen close to the large gain limit; this phenomenon, caused by the high sensitivity of the compensator in this parameter regime, can be overcome by basing the cost functional for the controller design on the total energy.

The idealized match between reduced-order and original model has been relaxed by considering various levels of truncation for the POD-based reduced-order model, thus varying the accuracy up to which the plant is represented. Even if the compensator is stable for the model it was design for, the stability of the compensator is no longer guaranteed when applied to a slightly different plant. It has been found that the compensated system becomes unstable in the large gain limit. Moreover, as the accuracy of the reduced-order model decreases, the unstable $(G/W, l)$ -parameter region becomes larger and imposes limitations on performance. Finally, based on a stable compensated system, a detailed study of noise attenuation by feedback control has been performed for an impulse of noise and for continuous stochastic forcing in the DNS solver. In either case, a substantial reduction in perturbation energy could be accomplished, as predicted by the reduced-order model analysis.

Nonlinear effects have been reintroduced to the closed-loop control problem by applying the compensator, designed under linear assumptions, to the nonlinear Navier-Stokes equations and attempting to suppress impulsive and continuous noise sources of progressively higher amplitudes and noise variance W^2 . Minor deviations have been detected for small-amplitude initial conditions; in the large-amplitude case, however, compensator performance deteriorated due to the appearance of nonlinearly triggered structures. These structures cause a second rise in perturbation energy that remains unattenuated by the control.

It can be concluded from our study that designing closed-loop control strategies for amplifier flows is significantly more involved than the equivalent design for oscillator flows. While in this latter case instabilities are generally narrow-banded in frequency and thus more easily detectable/controllable, a noise-amplifier produces more broadband signals and magnifies physical and non-physical perturbations alike. For this latter reason, a comprehensive study of the sensitivity of the compensator performance with respect to various noise sources is inevitable for a successful closed-loop control design. Transfer functions, i.e., frequency-based input-output relations, are particularly helpful in pinpointing strong sensitivities, in placing sensors efficiently, and in avoiding undesirable parameter regimes. It is hoped that the present study has introduced and demonstrated

effective tools that — despite the inherent challenges — aid in the design of effective closed-loop control strategies for amplifier flows.

REFERENCES

- AHUJA, S. & ROWLEY, C. W. 2010 Feedback control of unstable steady states of flow past a flat plate using reduced-order estimators. *J. Fluid Mech.* **645**, 447–478.
- ÅKERVIK, E., HÖPFNER, J., EHRENSTEIN, U. & HENNINGSON, D. S. 2007 Optimal growth, model reduction and control in a separated boundary-layer flow using global modes. *J. Fluid Mech.* **579**, 305–314.
- ALIZARD, F., CHERUBINI, S. & ROBINET, J.-CH. 2009 Sensitivity and optimal forcing response in separated boundary layer flows. *Phys. Fluids* **21**, 064108.
- ARCHAMBAUD, J.P., ARNAL, D., HEIN, S., DE SOUZA, J. MELO, HANIFI, A., GODDARD, J.L., KRIER, J. & DONELLI, R. 2008 Use of laminar flow technologies for supersonic drag reduction - results of FP project SUPERTRAC. *5th Eur. Cong. Comp. Meth. Appl. Sci. Eng (ECCOMAS)*.
- BAGHERI, S., BRANDT, L. & HENNINGSON, D. S. 2009 Input-output analysis, model reduction and control of the flat-plate boundary layer. *J. Fluid Mech.* **620**, 263–298.
- BAGHERI, S. & HENNINGSON, D. S. 2010 Simulation of transition delay in boundary layers. *Phil. Trans. Roy. Soc. A* (submitted).
- BARBAGALLO, A., SIPP, D. & SCHMID, P. J. 2009 Closed-loop control of an open cavity flow using reduced-order models. *J. Fluid Mech.* **641**, 1–50.
- BARBAGALLO, A., SIPP, D. & SCHMID, P. J. 2010 Input-output measures for model reduction and closed-loop control: application to global modes. *J. Fluid Mech.* (submitted).
- BEWLEY, T. R. & LIU, S. 1998 Optimal and robust control and estimation of linear paths to transition. *J. Fluid Mech.* **365**, 305–349.
- BOIKO, A.V., DOVGAL, A.V. & HEIN, S. 2008 Control of a laminar separating boundary layer by induced stationary perturbations. *Eur. J. Mech. B/Fluids* **27** (4), 466–476.
- BURL, J. B. 1999 *Linear optimal control. \mathcal{H}_2 and \mathcal{H}_∞ methods*. Addison-Wesley.
- CHOI, H. 2008 Control of flow over a bluff body. *Ann. Rev. Fluid Mech.* **40**, 113–139.
- EHRENSTEIN, U., PASSAGGIA, P.-Y. & GALLAIRE, F. 2010 Control of a separated boundary layer: Reduced-order modeling using global modes revisited. *Theor. Comp. Fluid Dyn.* pp. DOI 10.1007/s00162–010–0195–5.
- GHARIB, M. & ROSHKO, A. 1987 The effect of flow oscillations on cavity drag. *J. Fluid Mech.* **177**, 501–530.
- HECHT, F., PIRONNEAU, O., HYARIC, A. LE & OHTSUKA, K. 2005 *Freefem++, the book*. UPMC-LJLL Press.
- ILAK, M. 2009 Model reduction and feedback control of transitional channel flow. PhD thesis, Princeton University, Mechanical and Aerospace Engineering.
- ILAK, M. & ROWLEY, C.W. 2008 Modeling of transitional channel flow using balanced proper orthogonal decomposition. *Phys. Fluids* **20**, 034103.
- JOSHI, S.S., SPEYER, J.L. & KIM, J. 1997 A systems theory approach to the feedback stabilization of infinitesimal and finite-amplitude disturbances in plane Poiseuille flow. *J. Fluid Mech.* **332**, 157–184.
- JOSLIN, R.D. 1998 Overview of laminar flow control. *NASA TP* **208705**.
- KIM, J. 2003 Control of turbulent boundary layers. *Phys. Fluids* **15**, 1093–1105.
- KIM, J. & BEWLEY, T.R. 2007 A linear systems approach to flow control. *Ann. Rev. Fluid Mech.* **39**, 383–417.
- LIN, J.C. 2002 Review of research on low-profile vortex generators to control boundary-layer separation. *Prog. Aerosp. Sci.* **38**, 389–420.
- MARQUET, O., SIPP, D., CHOMAZ, J.-M. & JACQUIN, L. 2008 Amplifier and resonator dynamics of a low-Reynolds number recirculation bubble in a global framework. *J. Fluid Mech.* **605**, 429–443.
- ROSSITER, J.E. 1964 Wind tunnel experiments on the flow over rectangular cavities at subsonic and transonic speeds. *Aero. Res. Council. R&M* **3438**.

- SARIC, W.S., REED, H.L. & WHITE, E.B. 2003 Stability and transition of three-dimensional boundary layers. *Ann. Rev. Fluid Mech.* **35**, 413–440.
- SIPP, D., MARQUET, O., MELIGA, P. & BARBAGALLO, A. 2010 Dynamics and control of global instabilities in open flows: a linearized approach. *Appl. Mech. Rev.* **63**, 030801.
- SIROVICH, L. 1987 Turbulence and the dynamics of coherent structures. *Quart. Appl. Math.* **45**, 561–590.